Cyclic lateral design for offshore monopiles in weak rocks

Anaïs Lovera

UNIVERSITÉ PARIS-EST

EDF

Thèse

soumise pour l'obtention du grade de
Docteur de l'Université Paris-Est
Ecole Doctorale Sciences, Ingénierie et Environnement (SIE)

par

Anaïs Lovera

Cyclic lateral design of offshore wind turbines monopiles in weak rocks

---

Spécialité : *Géotechnique*

Thèse préparée au laboratoire Navier

Soutenue le 27 septembre 2019

Prof. Fabrice Emeriault	ENS3	Rapporteur
Prof. Luc Thorel	IFSTTAR	Rapporteur
Prof. Jean-Michel Pereira	Ecole des Ponts ParisTech	Président
Prof. Mark Randolph	COFS	Examinateur
Mme. Elisabeth Palix	EDF Renouvelables	Examinatrice
Prof. Jean Sulem	Ecole des Ponts ParisTech	Directeur de thèse
Dr. Siavash Ghabezloo	Ecole des Ponts ParisTech	Co-encadrant de thèse

Abstract

The European Union sets ambitious agreement of producing 20 % of its total energy needs from renewable sources by 2020. In response, the French government has launched tenders for offshore wind. The consortium that includes EDF Renouvelables won three of them for a total of 1.5 GW. Two of these projects concern wind turbines founded on monopiles installed in soft rock. One of the main objectives for EDF Renouvelables is to secure offshore wind turbines (OWT) design as well as the design of their foundation. Although monopiles represent 75 % of foundations installed offshore, their design can be optimised especially for the type of ground encountered in these particular projects. OWTs are subjected to specific design requirements such as tight tolerances concerning their natural frequencies and permanent rotation at the end of their lifetime. The monopile response plays an important role to assess these requirements. Therefore, in situ pile tests were carried out in a former quarry with similar soft rock properties as the ones encountered in the offshore projects.

The pile dimensions are selected to reproduce the ratio between the pile embedded length and the pile diameter of typical monopiles. Testing programe ensures that the applied loads represent well those relevant for offshore conditions. The stiffness evolution during cyclic loading is analysed as it is a key factor for the natural frequency requirement. The accumulated rotations are looked at for the long-term rotation requirement. Since the piles are installed in soft rock, two phenomena are highlighted: the creation of a crushed zone around the pile due to the driving process and the onset and propagation of cracks in the surrounding rock mass.

Based on these observations, a semi-analytical modelling is developed. The most commonly used procedure for prediction of the behaviour of laterally loaded piles is the $P - y$ curves formulation which gives an efficient framework to predict the response of the pile. The semi-analytical modelling is based on this framework and is extended to take in account the particularities of both monopiles design requirements and the fact that monopiles are installed in soft rock. Emphasis is given to the modelling of the response at small lateral displacements. To account accurately for the initial response, the soft rock zone appears to play an important role. The classical $P - y$ curves framework accounts neither for multi-directional loading nor for irreversible displacement and accumulated displacement due to cyclic loading. Unloading paths with or without gapping are introduced to account for irreversible displacements. To account for multi-directional loading, we propose to model several springs around the pile circumference. Analytical solutions are given in order to

calculate the $P-y$ curves for multi-directional loading from the various existing $P-y$ curves for unidirectional loading. Similarly, to creep tests, cyclic loading exhibits three main types of response: stabilisation of accumulated displacements, ratcheting and unstable increase of accumulated displacements up to failure. Therefore, we use existing creep models for simulating the cyclic response. This procedure is validated by comparing the numerical results with data recorded in field pile tests performed in soft rock.
Last of all, numerical finite element modelling is implemented using Code_Aster. The different phenomena are first analysed in a 2D configuration. This helps to understand and quantify the impacts of each phenomenon: the creation of the crushed zone, the gapping behind the pile and the onset and propagation of cracks. Then the same phenomena are analysed in a 3D configuration to understand the effect of the size difference between the piles tested in the field and those for offshore monopiles.

Résumé

L'Union Européenne a fixé des objectifs nationaux consistant à porter à 20 $\%$ la part des énergies renouvelables dans la consommation d'énergie totale à l'horizon 2020. Pour y répondre, le gouvernement français a notamment lancé des appels d'offre pour l'éolien en mer. Le consortium porté entre autre par EDF Renouvelables a remporté trois de ces appels d'offres pour un total de 1.5 GW utilisant des éoliennes posées. Deux de ces projets concernent des monopieux installés dans la roche tendre. L'un des principaux objectifs d'EDF Renouvelables est de sécuriser le dimensionnement de ces éoliennes ainsi que celui de leur fondation. Bien que les monopieux représentent autour de 75 $\%$ des fondations installées en mer, leur dimensionnement peut être optimisé en particulier pour le type de sol rencontré. Les éoliennes en mer sont soumises à des critères de dimensionnement spécifiques tels que des critères sur leurs fréquences propres et sur leur rotation permanente en fin de vie. La réponse du monopieu joue un rôle important dans la vérification de ces critères. C'est la raison pour laquelle des essais de pieux in-situ ont été réalisés dans une ancienne carrière où les propriétés de la roche sont similaires à celles des projets en mer.
Les dimensions des pieux sont choisies de sorte que leur élancement soit comparable à celui des monopieux en mer. La méthodologie utilisée pour définir le programme d'essais permet de justifier la bonne représentativité de ces essais. L'évolution de la raideur au cours du chargement cyclique ainsi que l'évolution de la rotation accumulée sont analysées puisqu'il s'agit de facteurs déterminants pour le dimensionnement. Deux phénomènes dus au fait que les pieux soient installés dans de la roche tendre sont mis en évidence: la création d'une zone de roche broyée autour du pieu lors du processus d'installation et l'apparition et la propagation de fissures dans le massif rocheux environnant.
Sur la base de ces observations, une modélisation semi-analytique est développée. La procédure la plus utilisée est la méthode des courbes $P-y$ qui permet de calculer la réponse d'un pieu sous chargement latéral. La modélisation semi-analytique est basée sur cette méthode et est étendue afin de tenir compte à la fois des critères de dimensionnement des monopieux et du fait que les monopieux soient installés dans de la roche tendre. Une attention particulière est portée sur la modélisation de la réponse initiale et la zone de roche broyée semble jouer un rôle important dans cette réponse. La méthodologie classique des courbes $P-y$ ne prend en compte ni le chargement multidirectionnel, ni les déplacements irréversibles. Pour tenir compte du chargement multidirectionnel, nous proposons de modéliser plusieurs ressorts autour de la circonférence du pieu et des solutions analytiques sont données afin de calculer les courbes $P-y$ pour le chargement multidirectionnel à

partir des courbes $P - y$ existantes pour un chargement unidirectionnel. Comme pour les tests de fluage, le chargement cyclique présente trois types de réponse: la stabilisation des déplacements cumulés, le phénomène de rochet et l'augmentation instable des déplacements cumulés jusqu'à la rupture. Nous utilisons donc des modèles de fluage pour modéliser la réponse cyclique. Cette procédure est validée en comparant les résultats numériques avec les données enregistrées lors des essais in-situ.
Enfin, la modélisation numérique par éléments finis est implémentée à l'aide de Code_Aster. Les différents phénomènes sont d'abord analysés dans une configuration 2D. Cela permet de comprendre et quantifier les impacts de chaque phénomène: création de la zone de roche broyée, décollement derrière le pieu et apparition et propagation des fissures. Ensuite, les mêmes phénomènes sont analysés dans une configuration 3D afin de comprendre le changement de taille des monopieux d'essais sur le terrain aux monopieux en mer.

Acknowledgements

Throughout my thesis, I had the chance to work in various stimulating environment and was always very well welcomed. The people I met in all these places have largely supported me and helped with the realisation of this thesis and I would like to express my deep gratitude to all the people involved.

First and foremost, I would like to thank my supervisors Jean Sulem, Siavash Ghabezloo, Mark Randolph and Elisabeth Palix for their support and guidance throughout my thesis. I would like to thank Jean for encouraging me to apply for this thesis in the first place and from whom I have learnt a lot. The clarity of his explanations and the pertinence of his remarks were very much appreciated. Many thanks to Siavash who has always encouraged me and found the way to motivate me. I have sincerely enjoyed working with him and was very lucky to be one of his students. I have also been privileged to work with Mark Randolph, I have learnt a lot during my stay at COFS and with the numerous exchange of emails. Thank you for taking the time to answer my questions all along the project and even before. Many thanks to Elisabeth Palix whose enthusiasm and passion made it possible to launch and carry out this project. My thanks also go to Elisabeth Duranteau, who taught me a lot during the first year of the thesis. Finally, I would like to thank Marc Kham and Stefano Cherubini who took over from Elisabeth, for their time and advices.

I would like to thank Fabrice Emeriault, Luc Thorel and Jeam-Michel Pereira for accepting to be part of my jury.

I had the chance to follow up Onshore Pile Tests and I would like to thank all the people involved on site and especially Youssef from EDF Energies Nouvelles, Ibrahim from Balineau and all the team from Fugro.

At UWA, I would like to thank the doctoral students without whom this experience far from home would not have been so great: Monika, Guy, Manu, Marc, Djuna, Nicole, Andrew, Maria, Maxim, Serena and Mirko.

My very deep gratitude go to my colleagues in EDF R&D of ERMES department whose help, enthusiasm and support have helped me at every stages of this thesis. I am very glad to continue working with you.

At Navier Laboratory, I would like to thank the tremendous technical team namely Emmanuel, Marine, Baptiste, Loïc and Xavier for their help during the various tests done at the laboratory. I would like to thank Sabrina for her great help in organising the different trips to conferences. It was great to be able to discuss with Roger Frank whose remarks and advice were very much appreciated. Many thanks to the amazing team of doctoral students: Xiu, Benjamin, Youssouf, Tan, Alexandre, Sophie and May with special mention to Axelle, it will certainly be very different not to share the same path with you from now!

Finally, I am grateful to my parents, my sister, my family and my friends for their support and love, and for always encouraging me during this thesis with a special thank to Serge, Nelly and Sara for coming all the way to assist to the defense. Last but by no means least, Thomas has been eternally patient with me and I could not have achieved this without his support and encouragement and I thank him for everything.

Contents

Nommenclature

Abbreviations

API	American Petroleum Institute
FEM	Finite Element Modelling
FLS	Fatigue Limit State
G.L	Ground Level
LVDT	Linear Voltage Differential Transducer
MEP	Multiannual Energy Plan
OPT	Onshore Pile Tests
OWT	Offshore Wind Turbine
RNA	Rotor-Nacelle Assembly
RQD	Rock Quality Designation
SLS	Serviceability Limit State
UCS	Unconfined Compressive Strength
ULS	Ultimate Limit State

List of symbols

Latin alphabet

For each parameter the unit is indicated between square brackets: F refers to a unit of force; L to a unit of length and T to a unit of time.

D	[L]	Diameter of the pile
c	[F L^{-2}]	Cohesion
e	(1) [L]	Load eccentricity
	(2) [L]	Thickness of the joint elements
E	[F L^{-2}]	Young's modulus
E_d	[F L^{-2}]	Eodometric modulus
E_e	[F L^{-2}]	Effective Young's modulus
E_s	[F L^{-2}]	Young's modulus of the soil for a uniform soil
E_p	[F L^{-2}]	Young's modulus of the pile
$E(y)$	[F]	External work per unit legnth in the unidirectional model
$\tilde{E}(y)$	[F]	External work per unit legnth in the unidirectional model
E_1 & E_2	[F L^{-2}]	Stiffness of the different Kelvin-Voigt models

f	[T^{-1}]	Natural frequency of the structure
f_{FB}	[T^{-1}]	Natural frequency of the structure in the case of a fixed base
F	[F]	Lateral force
F_{max}	[F]	Maximum force of a series of cycles
F_x	[F]	Force in X-axis
F_y	[F]	Force in Y-axis
F_{ult}	[F]	Ultimate load
G	[F L^{-2}]	Shear modulus
G_s	[F L^{-2}]	Shear modulus of the soil
G^*	[F L^{-2}]	Equivalent shear modulus
G_c	[F L^{-3}]	Critical strain energy release
H	[F]	Shear force
h	[L]	Height of the load application from the ground surface
I_p	[L^4]	Second moment of area of the pile
$I_{\rho H}$ & $I_{\theta H}$	[-]	Influence factors
k	[F L^{-2}]	Initial stiffness of a given $P-y$ curve
k_y	[F L^{-3}]	$P-y$ modulus gradient
K	[F L^{-2}]	Bulk modulus
K_L	[F L^{-1}]	Lateral stiffness
K_R	(1) [F L]	Rotational stiffness
	(2) [-]	Pile flexibility factor
K_{LR}	[F]	Cross-coupling stiffness
K_{Ic}	[F L$^{-3/2}$]	Fracture toughness
L	[L]	Embedded length of the pile
L_{tot}	[L]	Total pile length
M	[F L]	Bending moment
M_x	[F L]	Moment about X-axis
M_y	[F L]	Moment about Y-axis
m	[-]	Power in a power law $P-y$ curve
N	(1) [-]	Number of cycles
	(2) [-]	Total number of springs that subdivide the perimeter of the pile
N_h	[-]	Rate of increase of the Young's modulus of the soil with depth
P	[F L^{-1}]	Lateral force per unit length applied by the soil on pile edge
P_u	[F L^{-1}]	Ultimate soil reaction
R	[L]	Outer radius of the 2D FEM
t	[L]	Thickness of the pile wall
t_c	[L]	Thickness of the crushed rock
t_p	[L]	Thickness of the pile wall
T_b	[-]	Dimensionless empirical parameter (power law)
V	[F]	Vertical force
x	[L]	Displacement of the pile along X-axis
y	[L]	Displacement of the pile along Y-axis
z	[L]	Depth down the pile

Greek alphabet

α	(1) [-]	Dimensionless empirical parameter (power law fitting)
	(2) [-]	Parameter defining the tangential behaviour of the cohesive joints
β	[-]	Dimensionless empirical parameter (logarithmic)
θ_j	[rad]	Angle between spring j and X-axis
θ_S	[rad]	Rotation that would occur in a monotonic test when the appiled load is equal to the maxium cyclic load
$\Delta\theta$	[rad]	Accumulated rotation of the pile
θ_x	[rad]	Rotation of the pile about X-axis
θ_y	[rad]	Rotation of the pile about Y-axis
δ	[L]	Thickness of the crushed rock
δ_{ref}	[L]	Reference thickness
δ_n	[L]	Opening of the joints
ν_s	[-]	Poisson's ratio of the soil
ϕ	[rad]	Friction angle
η_1 & η_2	[F L^{-1} T]	Viscosities in the various Kelvin-Voigt models
η_L	[-]	Non-dimensional lateral stiffness
η_R	[-]	Non-dimensional rotational stiffness
η_{LR}	[-]	Non-dimensional cross-coupling stiffness
σ_n	[F L^{-2}]	Normal stress
σ_t	[F L^{-2}]	Tangential stress
σ_{max}	[F L^{-2}]	Rupture threshold
ζ_b	[-]	Ratio between the maximum load (or moment) in a load cycle over the ultimate load (or moment)
ζ_c	[-]	Ratio between the minimum load (or moment) in a load cycle over the maximum load (or moment) in a load cycle
γ	[F L^{-3}]	Unit weight
γ‘	[F L^{-3}]	Effective unit weight

1 General introduction

1.1 Context

1.1.1 Offshore wind industry in France and in Europe

The European Union sets ambitious agreement of producing 20% of its total energy needs from renewable sources by 2020. More recently the law on energy transition for green growth sets an objective of increasing the contribution of renewable energies to total final energy (electricity, gas, heat) consumption to 32% in 2030. Offshore wind appears to be an effective mean to help achieving these goals for several reasons. First, going offshore offers several advantages compared to onshore wind such as a lower visual impact, the possibility to install bigger turbines (blades lengths are less limited by the transportation) and also higher and steadier wind speeds (Rodrigues et al., 2015). The capacity factor for offshore wind represents the ratio between the actual electrical energy output over a certain amount of time and the electrical energy output assuming a production at full power during the same amount of time. The capacity factor for new offshore wind projects is around 50 %. As steadier wind speeds are encountered offshore, it is higher than expected onshore wind capacity factor. Some northern European countries have invested in fixed offshore wind projects since the 1990's (Rodrigues et al., 2015), and it has been a booming sector in Europe since 2008 (cf. Figure 1.1). Consequently, nowadays fixed offshore wind industry is mature, the risks have been minimized and the first fixed offshore wind projects served as proof of concept. The aim of this section is to present an overview of the offshore wind industry in Europe with a focus on French projects.

At the European scale, Europe's cumulative installed offshore wind capacity reached around 18 GW at the end of 2018. This capacity is however very unequal from one country to another, with 98 % of the total capacity hold by the top five countries: United Kingdom 44 %, Germany 34 %, Denmark 7 %, Belgium 6.4 % and the Netherlands 6 % (WindEurope, 2019).

On the national scale, in response to these directives, the French government launched several calls for tenders for both fixed and floating offshore wind projects. The first call for tenders for fixed offshore wind was launched in 2011 for a total capacity of 3 GW shared into five zones: off the coasts of Le Tréport, Fécamp, Courseulles-sur-Mer, Saint-Brieuc and Saint-Nazaire. This production capacity represents about 360 wind turbines, which should provide the equivalent of the annual consumption of 3.5 million of people. A second call for

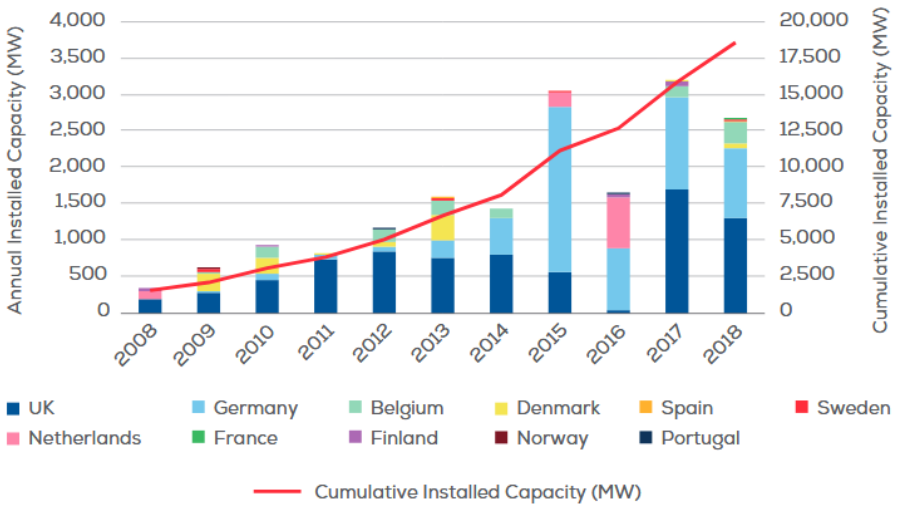

Figure 1.1.: Annual offshore wind installations by country and cumulative capacity (WindEurope, 2019)

tenders for fixed offshore wind was launched in March 2013 for a total capacity of 500 MW between the islands of Yeu and Noirmoutier. A third call for tenders for fixed offshore wind was launched in April 2016 off the coast of Dunkirk for a total capacity of 500 MW. The allocation of this project is postponed until mid-2019. The floating wind industry is the subject of several demonstration projects and a call for tenders for the deployment of four pre-commercial farms was launched in August 2015. These four projects total a capacity of 24 MW and only 3 to 4 wind turbines per each project. It can be noted that three of these demonstration projects are in the Mediterranean Sea while none of the fixed offshore tender concern this area. Although, today, no turbine of the previously mentioned projects is installed yet. The French government have published the first version of the Multiannual Energy Plan (MEP) early 2019, which is a strategic plan for energy policy in France over the next few years: 2019-2023 and 2024-2028. This plan establishes the means necessary to achieve one of the objectives of the law on energy transition for green growth. Concerning the electricity production, the plan counts on the first six offshore projects to be operational at the beginning of the second period of the MEP. Capitalising on the industrial sector thus created during the first period of the MEP, new calls for tender are planned for a total capacity of 3.25 GW: three for fixed offshore wind turbines and three for floating ones.

1.1.2 Different types of substructure but a predominance of monopiles

Many engineering bodies are involved in offshore wind turbine (OWT) design: civil and structural engineering as well as ocean engineering and electronic engineering. The engineering of interest to us herein is the design of the support substructure. Foundation costs around $25 - 35\%$ of the capital expenditure (Bhattacharya, 2014). Therefore, optimising

OWT design may lead to consequent profits. Moreover, foundations are site specific depending on site conditions whereas turbines are generic. It is therefore possible to work on design optimisation on these substructures.
Different types of foundations are possible in offshore support structures. Figure 1.2 shows different types of foundation, with their share in Europe (proportion and number of each type are indicated). It can be noted that in Figure 1.2 no distinction is done on the different concepts of substructure for floating wind turbines: ballast stabilised floater (spar buoy), buoyancy stabilised floater (semi-submersible) and mooring stabilised floater (tension leg platforms). Fixed OWT substructures can be divided in three parts depending on how the soil is loaded (Doherty et al., 2014). Gravity base foundation is a shallow foundation which loads the soil near the surface. It consists of concrete base structure and its weight assures the stability. Monopile is a deep foundation, consisting of a large diameter pile. The forces are transferred to the soil, and the soil is mostly loaded laterally. Monopiles used in offshore wind are typically 20-30 meters length into the sea bed and 4-6 meters diameter, which corresponds to a slenderness ration around 4-6 (Doherty et al., 2014). Tripile, tripode and jacket structures are similar to each other, the horizontal forces are transferred to the piles at the seabed through the truss action. Thus, the piles transferred mostly axial loading to the soil.
The choice of a foundation concept depends on the site conditions such as water depth and geotechnical data (Arany et al., 2017). Gravity base foundation needs a competent soil and a homogeneous soil profile (Doherty et al., 2014). In simplified terms, it can be said that the choice of a monopile substructure is an economically efficient solution for water depths that do not exceed 30-35 m, although floating wind turbines solutions start to be competitive for water depth higher than 60 m. In between, tripods, tripiles and jackets are generally chosen (Doherty et al., 2014).
Nevertheless, monopile is by far the most common foundation type encountered for OWT. This is due to its numerous advantages: simple and robust design, well suited for mass fabrication and simple installation method in certain soil like sandy soils which concerns most locations in the North Sea (Kallehave et al., 2015). It can be noted that this tendency is still predominant for new farms. Indeed, in 2018, monopile substructures still contributed for 66% of foundations installed for OWT in Europe (WindEurope, 2019).

1.1.3 Trends in the future for offshore wind industry

Figure 1.3 shows the different components of an OWT founded on monopile and gives the vocabulary encountered for OWT. The support structure that holds the rotor-nacelle assembly (RNA) consists of: a foundation (in this case a monopile) that enables to transmit the load to the ground, a transition piece that connects the foundation to the tower, and a tower itself. The different dimensions of the components depend on both the wind turbine and the site conditions. As the turbine size and water depths increase (WindEurope, 2019), larger monopile diameters are required. Up to 10 meters diameter monopiles

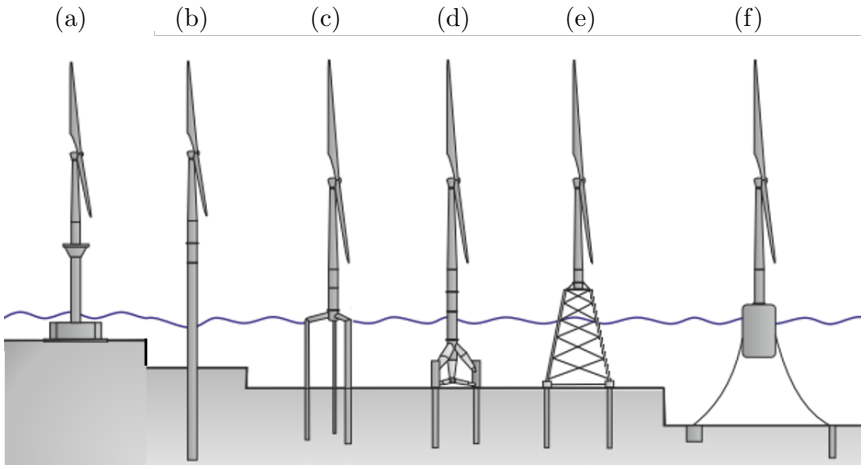

Figure 1.2.: Different types of foundations for offshore wind turbine after Abadie (2015) with their respective share in Europe for grid-connected wind turbines at the end of 2018 (a) Gravity Base (301, i.e. 6 %), (b) Monopiles (4 062 i.e. 80.9 %), (c) Tripile (80, i.e. 1.6 %), (d) Tripode (126, i.e. 2.5 %), (e) Jacket (446, i.e. 8.9 %), (f) Floating (9, i.e. 0.2 %) (WindEurope, 2019)

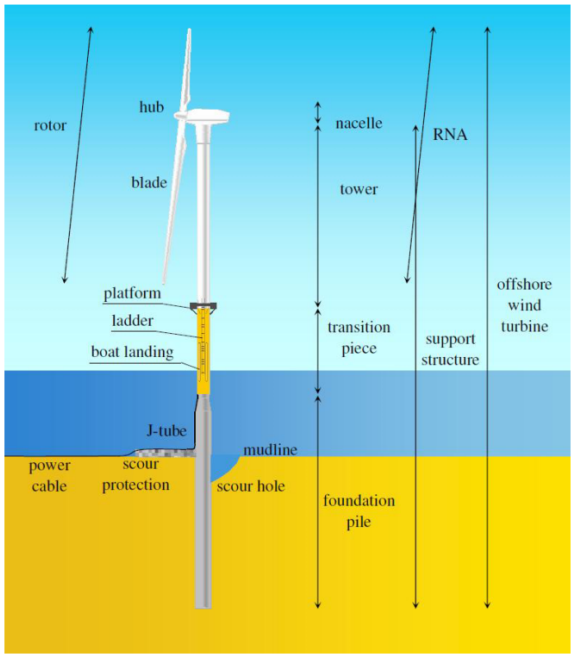

Figure 1.3.: Offshore wind turbine components (Velarde, 2016)

(called XL monopiles) are being envisaged both to go further offshore and to use higher capacity turbine. However, to go further offshore is not as simple as to increase monopile diameter. Issues due to manufacturing, storage, transportation and installation will need to be alleviated. Indeed, for instance, existing installation vessels and driving or grouting equipment are not sufficient for monopiles greater than 7 meters diameter (Doherty et al., 2014). XL monopiles are possibly identified to be an economical solution up to 60 meters water depth. Thus, the range of water depth for which jackets, tripodes and tripiles were identified to be more economic than monopile (see section 1.1.2) vanishes. In a near future, monopiles can be used for water depths corresponding to the transition from fixed offshore wind turbine to floating offshore wind.

1.2 Knowledge gaps

Current design practices for the offshore wind industry are based on feedback from the offshore oil and gas industry and follow recommendations from American Petroleum Institute (API). These recommendations are based on the subgrade reaction method which define the soil with a set of independent springs. This method can also be called, the $P-y$ curves method, the local method, the load transfer approach or the Winkler approach. In this thesis, this method is called the $P-y$ curve method (see section 2.2.2). However, there are some differences between oil and gas foundations and OWT monopiles. The three main differences are: the type of loading in stake in the two industries, the different pile behaviours that can be encountered in pile design and the different ground conditions encountered in some French projects. Therefore, the assumptions of the methods used in oil and gas industry are out of scope for OWT monopiles. Besides, some simplifying assumptions are done to account for the cyclic loading and the multi-directional loading. Even if these assumptions were suitable for the design of offshore oil and gas structures they are insufficient for optimising specific design criteria for OWT monopiles. This section focuses on the knowledge gaps concerning the design of monopile for OWT.

1.2.1 Specific design criteria

Design regarding the natural frequency

The response of the structure depends closely on the first natural frequency f_0 (Kallehave et al., 2015). Indeed, OWT are dynamically loaded structures subjected to operational and environmental loads. Operational excitations consist of the excitations of the rotor f_{1P} and of the three blades f_{3P} (blade passing frequency). Environmental excitations consist of those of waves and wind. OWT are commonly designed so that their first natural frequency avoids frequencies of operational and environmental loads. This can be very challenging because of the many constraints (Figure 1.4). As resonance leads to a decrease of fatigue

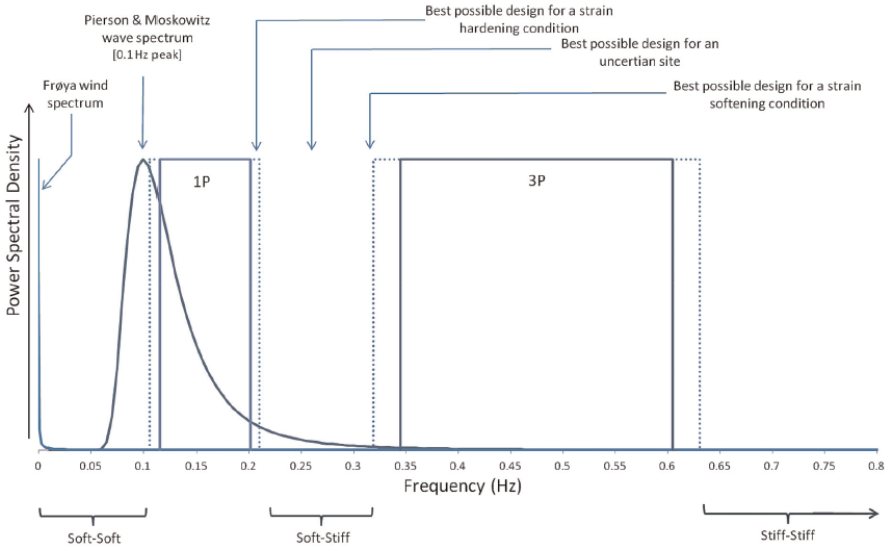

Figure 1.4.: Frequency spectrum of the dynamic loads showing design choice (Bhattacharya, 2014)

lifetime, leading to an early decomissioning, it is very important to take in account these constraints. Theoretically, three types of design are possible (Bhattacharya, 2014):

- **soft-soft design** in which natural frequency is below the rotor frequency. However, it leads to very flexible structure;
- **soft-stiff design** in which natural frequency is between the rotor frequency and the blade-passing frequency. It is the most common design nowadays;
- **stiff-stiff design** in which natural frequency is above blade-passing frequency. This design leads to larger tower or a change in foundation concept (rigid jacket piles).

As can be seen (Figure 1.4), frequency windows are very narrow. On some sites, wave spectrum may be wider or even shifted to higher frequencies making the design even harder. Finally, new turbines are larger and tend to turn more slowly, decreasing significantly the minimum "3P" value compared to what is shown in Figure 1.4. In addition, due to the increasing diameter of monopiles and the installation in very stiff soils (such as rocks), the excitation deriving from the blades 6P and 9P harmonics could be of importance in the design (Berthelot et al., 2019). Consequently, even small errors on design frequency can strongly impact the results. From Kallehave et al. (2015), current design models fail to reproduce the natural frequency although it is a key parameter for the design. Most of models underestimate the natural frequency although a correct design would have led to a lighter structure. Another issue is the impact of the soil-pile stiffness on the estimation of this natural frequency. This point has been discussed in recent papers as described in the following (Kallehave et al., 2015; Arany et al., 2015; Schafhirt et al., 2016). A sensitivity study performed in Kallehave et al. (2015) on a given wind turbine explores the impact of various parameters on the natural frequency estimation. These authors showed that the variation of the soil-pile stiffness is the parameter that impacts mostly the natural frequency

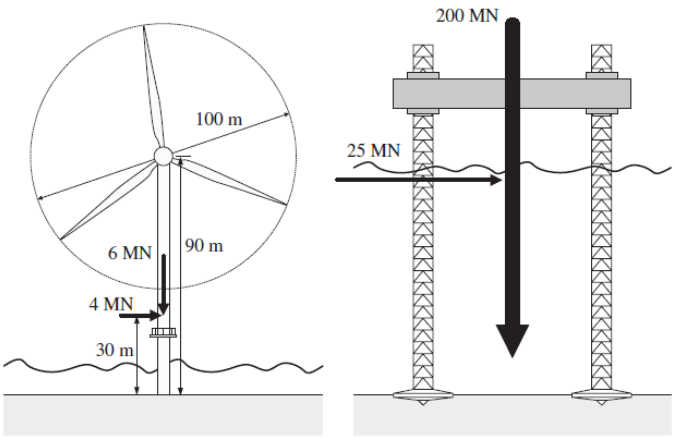

Figure 1.5.: A 3.5 MW offshore wind turbine and a jack-up rig drawn to the same scale showing typical loads applying on each structure (Byrne and Houlsby, 2003)

value. Consequently, a good estimation of the natural frequency of the OWT requires an accurate soil-structure modelling.

Threshold for cyclic accumulation at the mudline

OWT are subjected to tight tolerances concerning the accumulation of rotation and displacement at the end of the lifetime of the turbine. Indeed, long-term displacements and rotations of the foundation have a substantial impact on the turbine itself and other components. Regarding rotation, tolerances are fixed at 0.5° rotation at the mudline at the end of the lifetime. Knowing that there is already 0.25° of tolerance on the mudline rotation during the installation procedure, cyclic loading should not induce more than 0.25° of additional rotation. Typical OWT are designed against fatigue considering 10^7 cycles (Leblanc et al., 2010a). The generic method in DNV-GL (2014) to take account of load cycles uses cyclic $P - y$ curves (see section 2.2.2). These depend neither on the level of the loading cycles nor on the number of cycles. Although some works exist to account for cycles in OWT monopile design (see section 2.3.3), they do not cover all types of soil. As a result, to fulfil the cyclic rotation accumulation criterion at the mudline, an accurate estimation of the cyclic accumulation is required.

1.2.2 Different types of loading

Figure 1.5 compares a 3.5 MW OWT and a large jack-up rig (a typical offshore oil and gas structure). The quantity of interest herein is the ratio of the horizontal load over the vertical load. For OWT, this ratio is around 60 % whereas it is rarely more than 15 % for oil and gas structures (Byrne and Houlsby, 2003). Therefore, the pile lateral capacity turns out to be a critical design parameter for the monopiles although the axial capacity is not. A significant lever arm between the application point of the load and the monopile top leads to an important bending moment at the mudline (Byrne et al., 2015b).

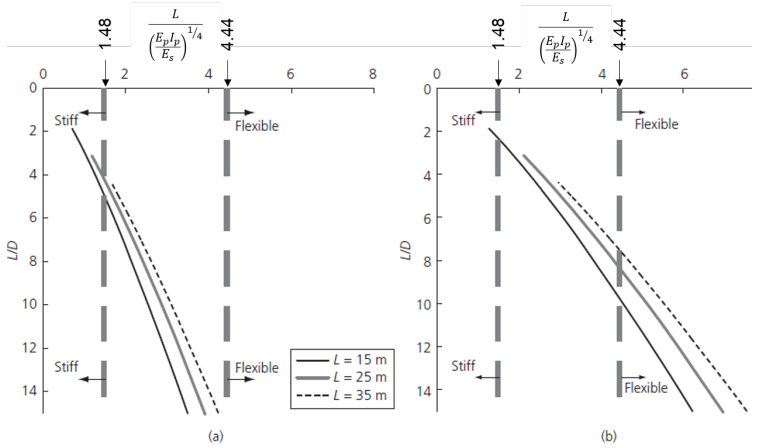

Figure 1.6.: Pile failure mechanisms for soils with (a) Es=10 MPa and (b) Es=100 MPa (Doherty and Gavin, 2011)

1.2.3 Different pile response

The $P-y$ curves were initially developed for long and slender piles up to 1 meter diameter that behave in a flexible way (DNV-GL, 2014). However, Leblanc et al. (2010a) and Doherty and Gavin (2011) analysed the possibility to encounter a rigid behaviour for a typical monopile (slenderness ratio around 4-6) and for plausible elastic moduli of the soil. Both articles used the formula given by Poulos and Hull (1989) to confirm the possibility of having rigid foundation behaviour. Figure 1.6 illustrates the analysis done by Doherty and Gavin (2011) showing that rigid pile behaviour is likely to be enountered in loose sands but less likely in stiff sands. According to Leblanc et al. (2010a) analyses, the transition from rigid behaviour to flexible behaviour occurs for Young's moduli of sands between 14 MPa and 1 121 MPa. For the case of soft rock (encountered in some offshore French projects) the behaviour of the pile is expected to be intermediate between the totally rigid behaviour and the totally flexible behaviour. In any case, for any soil conditions (soft sand, stiff sand or soft rock) the behaviour is different from piles in oil and gas industry which are undoubtedly flexible. New models accounting for rigid pile behaviour should be considered (see section 2.4.1).

1.2.4 New type of ground encountered: soft rock

Since in most cases rock is encountered at a certain depth below a sufficient thickness of soil which resistance already balances most of the applied loading, there are few studies about laterally loaded piles in rock materials. Consequently, the rock below is thus only lightly loaded and a precise knowledge of how the rock behaves under lateral loading is not needed (Reese, 1997). However, in the case of some of the French OWT projects, the rock is encountered directly at the mudline and thus a precise estimation of how the rock behaves

is needed to optimise and secure the design. Since it is rock and not soil, several features can be listed:

- **Gap behind the pile**
  As opposed to some soils, rocks and even soft rocks behind the laterally loaded pile do not ”follow” the movement of the pile. This leads to a development of a gap behind the pile. The presence of a gap implies a modification of the stress distribution around the pile. In the area where there is no more contact between the surrounding rock and the pile, the stresses are null until contact is found again.
- **Creation of crushed zone during installation procedure**
  Piles can be driven or drilled and grouted into the ground. In both situations, the installation procedure disturbs the surrounding rock. When the pile is driven, the rock beneath the area of the pile section will break as the pile goes down into the ground. The broken or crushed rock will remain all around the pile. When the pile is drilled and grouted, the drilling tool will disturb and break a thin layer of rock all around the hole. This crushed rock generated during the installation procedure has a strong impact on the response of the pile.
- **Cracks**
  Many rocks have a brittle behaviour, particularly under low confining pressures. Cracks can appear during the installation procedure (mostly for driven piles), but also during the loading.
- **Creep**
  For many rocks, creep effects in relation with the viscous behaviour of the rock mass and/or subcritical crack propagation cannot be disregarded. It can significantly affect the long-term response of the pile, and even more when considering a large number of loading cycles.

None of these considerations have yet been addressed in offshore wind projects.

1.3 Thesis objectives

1.3.1 Industrial and design goals

Since foundations contribute to about 25-30 % of offshore wind capital expenditure, it is important for the development of future wind farms to secure and optimise their design. Therefore, EDF Renouvelables decided to perform in situ tests (static and cyclic) in similar ground conditions as offshore projects. In that context, this thesis has been launched. The final aim is to improve the methodology developed in norms which is mosty inspired from oil and gas industry assumptions.
This first chapter sets the knowledge gaps concerning offshore wind turbine monopiles

design under cyclic lateral loading in soft rock. This review highlights some points of interest that need to be assessed to fulfil the aim of having a secure and optimised design (Table 1.1).

Table 1.1.: Thesis objectives

Knowledge gap	Industrial and design goal	Motivations
Foundation stiffness is a key parameter in the frequency analysis that is usually underestimated	Better estimation of the foundation stiffness	Guide the choice of the diameter of the monopile to ensure that the criteria on the natural frequency is respected
Long-term rotation at the mudline is a design criterion for which there is not a clear methodology to estimate a rotation after about 10^7 loading cycles applied during OWT lifetime	Better estimation of the displacements and rotations accumulation	Guide the choice of the length to ensure that the tolerances are respected
Rigid/flexible behaviour	Better estimation of the load distribution along the pile	Validate pile design
Rock ground conditions are rarely seen in offshore projects	Better knowledge of failure modes	Check carrying capacity
Unidirectional is considered in the design	Better estimation of the multi-directional effect	To ensure that the design criteria are still respected when considering multi-directional loading

1.3.2 Methodology and means

The work relies on onshore pile tests results. Onshore pile tests results were carried out and interpreted in order to identify the significant mechanisms to be taken in account in the modelling. The potential effects of significant phenomena on the design of OWT are quantified. A semi-analytical modelling of a laterally loaded pile is implemented and validated. The validation is done comparing the numerical simulation using the tool and the onshore pile tests results wherever possible. Then, finite element modelling confirms the modelling and validates the transposition of results from onshore pile tests to future offshore monopiles dimensions.

1.4 Thesis Structure

The outline of the thesis is structured around the three main tasks described above.

Chapter 2: describes the state of the art for the design of offshore wind monopiles and identifies the different means to model laterally loaded piles. It also gives an overview of the different research projects and other field works.

Chapter 3: presents the general tests conditions of onshore pile tests. It also gives an overview of the key mechanisms observed during these tests and describes the potential implications on OWT design.

Chapter 4: presents the development of a semi-analytical model for laterally loaded pile which permits accounting for the observations from onshore pile tests. The validation of these different developments are shown.

Chapter 5: presents the finite element modelling framework in both 2D and 3D configurations. The results of the finite element modelling are compared to the onshore pile tests results. Then, some calculations are done by varying some pile dimensions to see the impact for offshore monopiles.

Finally, the concluding chapter summarises the key findings of the thesis and proposes future directions of research.

2 State of the art

Summary

The state of the art presented herein permits to highlight some points of interest that need to be assessed to fulfil the aim of securing and optimising OWT monopiles design. The design procedure is presented succinctly giving the types and nature of loading acting on the foundation. It appears that the foundation stiffness is one of the driving parameters in the natural frequency analysis and thus needs to be assessed accurately during the whole lifetime of the turbine. Three main methods for calculating the response of laterally loaded piles are described. Emphasis is given to show the pros and the cons of each method. The different types of response to cyclic loading are presented at the material scale. A non-exhaustive review of results of some laboratory tests is given. An overview of existing methods to account for cyclic loading is presented and the various methods are analysed in the light of the context of monopiles design. Two projects involving field tests on piles are presented and the advances that they have made in the field are highlighted.

Résumé

L'état de l'art présenté ici permet de mettre en évidence certains points d'intérêt qui doivent être pris en compte pour remplir l'objectif d'un dimensionnement optimisé pour les monopieux d'éoliennes en mer. Une procédure simplifiée pour le dimensionnement de la fondation est présentée en donnant les types de charges qui s'appliquent. Il apparaît que la raideur de la fondation est un paramètre clé dans l'analyse fréquentielle et doit donc être évaluée avec précision pendant toute la durée de vie de l'éolienne. Trois grandes méthodes pour calculer la réponse d'un pieu chargé latéralement sont décrites et l'accent est mis sur les avantages et les inconvénients de chaque méthode. Les différentes réponses sous chargement cycliques sont présentées à l'échelle du matériau et une revue non exhaustive des résultats d'essais de pieux en laboratoire est donnée. Un aperçu des méthodes existantes permettant de prendre en compte le chargement cyclique est présenté et les différentes méthodes sont analysées à la lumière du contexte particulier du dimensionnement des monopieux. Deux projets d'essais de pieux in-situ sont présentés ainsi que les avancées qu'ils ont permises dans le domaine.

2.1 Design of the monopile of an offshore wind turbine

This section describes the current geotechnical design of a OWT monopile. Recommendations for the design procedure are given by the International Electrotechnical Commission (IEC, 2009), by Det Norske Veritas and Germanischer Llyod (DNV-GL, 2014) and by the Comité Français de Mécanique des Sols et de Géotechnique (Berthelot et al., 2019).

2.1.1 Types and nature of loading acting on the foundation

Design requirements for OWT are given in IEC (2009) international standard. In this standard, loads acting on OWT are described:

- **Gravitational and inertial loads** of the structure;
- **Aerodynamic loads** caused by the airflow and its interaction with the structure;
- **Actuation loads** resulting from the operational and control of wind turbines (pitch and yaw actuator loads, mechanical breaking loads). The blade pitch refers to turning the angle of attack of the blades to adjust rotational speed and the generated power. The yaw consists of keeping the rotor facing into the wind as the wind direction changes;
- **Hydrodynamic loads** caused by the waves and the current and their interaction with the support structure;
- Other loads can be considered such as sea ice loads, impact loads or earthquake.

As various physical phenomena are involved in OWT design, having an integrated design tool is essential. Besides, it can be noted that the magnitude of aerodynamics loads depends mostly on wind speed and actuation loads that come from control strategies. Magnitude of hydrodynamic loads mostly depends on wave height and wave period (Bhattacharya, 2014). Typical loads are schematically illustrated in Figure 2.1 for a wind turbine of 3.5-5 MW in water depth of 20-50 meters. The contribution of the aerodynamic and the hydrodynamic loads to the total lateral loading applied at the mudline is of 25 % and 75 % respectively. Considering the eccentricity of the loading, the contribution of hydrodynamic loads to the bending moment applied at the mudline is of 40 % and of 60 % for the aerodynamic loads. It can be noticed that with increasing water depth for future OWT projects (see section 1.1.3), the hydrodynamic contribution in the lateral loading will increase.
For a preliminary design the parameters of the monopile are:

- **The length** which is a key parameter for the overturning ultimate capacity and the long-term displacements and rotations.
- **The diameter** which is the main design parameter to respect the natural frequency criteria (see section 1.2.1).

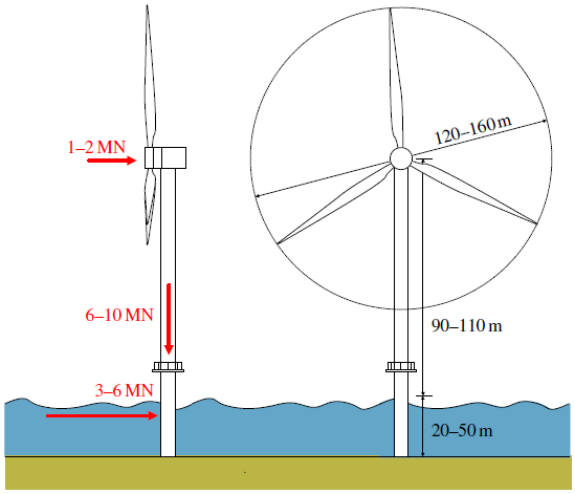

Figure 2.1.: Typical loads for a 3.5-5 MW turbine in water depth from 20-50 m (Byrne and Houlsby, 2003)

- **The thickness** which is chosen to fulfil fatigue requirements and installation constraints such as buckling (Kallehave et al., 2015).

Even at an early state of design, these three simple parameters are calculated in an iterative process (Figure 2.2).

2.1.2 Estimation of the kind of pile behaviour (flexible or rigid)

Several researchers have postulated that the response and the failure mechanisms of a pile under lateral loading varies depending on whether the pile is rigid or flexible in a given ground condition (Doherty and Gavin, 2011). Leblanc et al. (2010a) defines a rigid pile as a pile that develops a “toe kick” under lateral loading. Poulos and Hull (1989) defines a flexible pile as a pile with a length greater than a critical length, defined as the length beyond which any further increase of pile length does not influence the pile head response. There are different approaches in the literature to qualify the behaviour of the piles: flexible (slender or long), rigid (stiff or short) or intermediate. Table 2.1 lists the different criteria qualifying pile behaviour. In this table, the following notations are used: L represents the embedded length, D is the pile diameter, E_p is the Young's modulus of the pile, I_p is the second moment of area of the pile, E_s is the Young's modulus of the soil for a uniform soil, N_h is the rate of increase of the Young's modulus of the soil with depth, E_s then equals $N_h\ z$, G_s is the shear modulus of the soil, ν_s is the Poisson's ratio of the soil, $E_e = (E_p I_p)/(\pi D^4/64)$ is the effective Young's modulus and $G^* = G_s(1 + (3/4)\nu_s)$ is the equivalent shear modulus. However, these approaches only apply to a homogeneous elastic soil with linearly varying modulus with depth which is a questionable hypothesis. Therefore, within the framework of SOLCYP project a new approach is defined. Puech and Garnier (2017) proposed that the rigid or the flexible behaviour of a pile should be determined by studying the variation of the

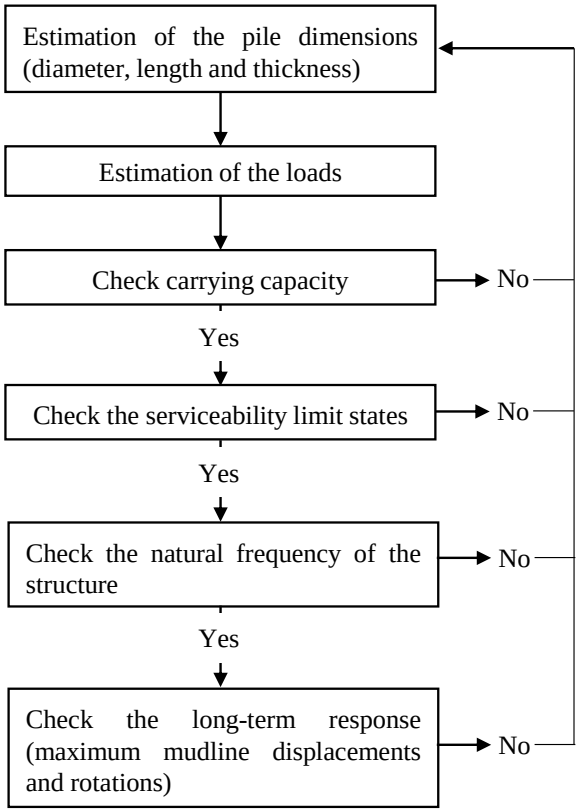

Figure 2.2.: Flowchart of a simplified design procedure after Arany et al. (2017)

Table 2.1.: Different ranges of transition from flexible to rigid pile behaviour found in the literature

	Soil profile	Rigid	Flexible
Poulos and Hull (1989)	Uniform	$L \leq 1.48 \left(\frac{E_p I_p}{E_s}\right)^{1/4}$	$4.44 \left(\frac{E_p I_p}{E_s}\right)^{1/4} \leq L$
	Increase linearly	$L \leq 1.10 \left(\frac{E_p I_p}{N_h}\right)^{1/4}$	$3.30 \left(\frac{E_p I_p}{N_h}\right)^{1/4} \leq L$
Carter and Kulhawy (1992)	Uniform	$\begin{cases} \frac{L}{D} \leq 0.05 \left(\frac{E_e}{G^*}\right)^{1/2} \\ 100 \leq \left(\frac{E_e}{G^*}\right) / \left(\frac{D}{2L}\right)^2 \end{cases}$	-
Randolph (1981)	Uniform	-	$\left(\frac{E_e}{G^*}\right)^{2/7} \leq \frac{L}{D}$
Frank (1999)	Uniform	$L \leq \left(\frac{4E_p I_p}{E_s}\right)^{1/4}$	$3 \left(\frac{4E_p I_p}{E_s}\right)^{1/4} \leq L$

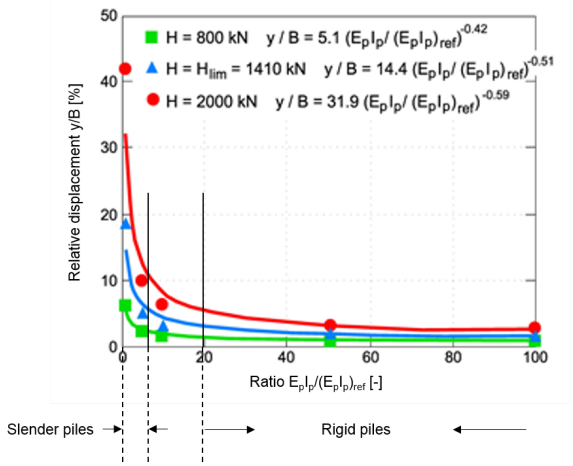

Figure 2.3.: Example of pile relative stiffness influence on pile head relative displacement (Puech and Garnier, 2017)

displacement at the pile head function of the relative stiffness of the pile (cf. Figure 2.3). For a fixed pile geometry (embedded length L and pile diameter B are fixed) installed in a given soil profile, the relative displacement at pile head (compared to pile diameter) is plotted as a function of the bending stiffness for a given load (by convention the ultimate load). One distinguishes two behaviours: when the displacement strongly depends on the bending stiffness the behaviour is flexible, whereas the behaviour is rigid in the other case (results confirmed by Peralta (2010)). These approaches allow to define the type of behaviour for given dimensions of a pile and given ground conditions although it is shown that the type of behaviour depends on the load (or displacement) applied. Zhang and Andersen (2019) presented finite element computations of laterally loaded monopiles showing the transition from flexible to rigid as the load (or the displacement) increases.

2.1.3 Impact of the soil behaviour on the natural frequency

It is to be noted that two reasons can explain the difficulty in assessing the natural frequency. Firstly, it is difficult to assess precisely the soil stiffness, particularly over a whole farm (using a restricted number of ground investigations). Secondly, even if the soil stiffness is precisely assessed during the design stage, laboratory tests on pile installed in sand exhibit an evolution of the pile stiffness with time and with the accumulated loading cycles (Leblanc et al., 2010a). Various studies focus on either: sensitivity study on the impact of frequency shift (due to miscalculation or ageing) or modelling of the softening or the stiffening of the surrounding soil. Laboratory tests and pile testing enable to assess whether softening or stiffening behaviour occurs. Long and Vanneste (1994) introduced a degradation parameter to reproduce the softening observed during the cyclic tests results on piles installed in sand. On the contrary, two studies in sandy soils based on centrifuge tests (Leblanc et al., 2010a; Abadie, 2015) showed an increase of the foundation secant stiffness with cycles.
The impact of a pile-siol stiffness change (both softening and stiffening) on OWT design

was studied in Arany et al. (2015) and Schafhirt et al. (2016). Arany et al. (2015) carried out a sensitivity study on the change of foundation stiffness on the first natural frequency of OWT founded on monopiles. The sensitivity study was done by modelling the tower as a beam and the foundation with a macro-element (see section 2.2.1). Three stiffness terms are considered in the stiffness matrix of the macro-element: a lateral stiffness, a rotational stiffness and a cross-coupling stiffness (which couples displacements and rotations). Non-dimensional stiffness is introduced as follows:

$$\begin{cases} \eta_L = \dfrac{K_L L^3}{E_p\, I_p} \\ \eta_R = \dfrac{K_R L}{E_p\, I_p} \\ \eta_{LR} = \dfrac{K_{LR} L^2}{E_p\, I_p} \end{cases} \tag{2.1}$$

where η_L, η_R and η_{LR} are the non-dimensional stiffness (respectively, the lateral, the rotational and the cross-coupling stiffness), K_L, K_R and K_{LR} are the lateral, the rotational and the cross-coupling dimensional stiffness, L represents the embedded length of the pile and $E_p\, I_p$ the equivalent bending of the pile. In Figure 2.4, the natural frequency is plotted as the ratio of the first natural frequency of the OWT and the natural frequency estimated if the tower is considered as a cantilever beam (f_{FB} for fixed base frequency) on the y-axis and on the x-axis the non-dimensional stiffness is plotted. The shape of the relative frequency function of foundation stiffness curves is always the same. The relative frequency starts to increase with a high slope and then stabilizes on a plateau. Relative frequency is highly dependent on the values of stiffness of the macro-element that models the foundations. For a given OWT with the lateral and the rotational stiffness fixed, the adding of a cross-coupling stiffness can move the relative frequency in the high-slope zone. While from a design point of view one can assess that this high-slope zone is to be avoided to prevent shifting of natural frequency towards forcing frequencies (environmental and operational frequencies) since softening or stiffening will occur with cyclic loading and ageing. Schafhirt et al. (2016) carried out an investigation on the impact of changes in the soil parameters on the fatigue lifetime for OWT founded with monopile in loose sand. They also studied the impact on modal analysis. One of the considered soil parameters in the variations of the soil conditions is the pile-soil stiffness. This parameter appears to be one of the key parameters in the investigation. Indeed, for a given soft-stiff OWT design, a decrease of 70% of the stiffness implies a decrease of 3% of the natural frequency, and an increase of 30% of the stiffness implies an increase of 2% of the natural frequency. A variation of 2-3 $\%$ could have significant effect if the designed natural frequency is situated close to the edges of the window of allowed values of the natural frequency.

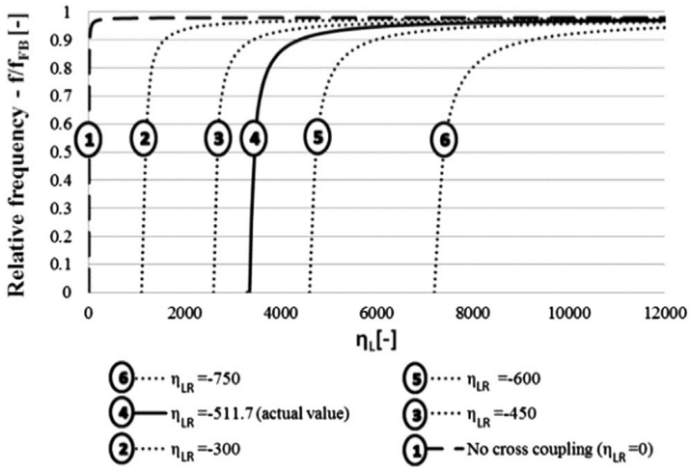

(a) Relative frequency as a function of non-dimensional lateral stiffness for several values of cross-coupling stiffness (Arany et al., 2015)

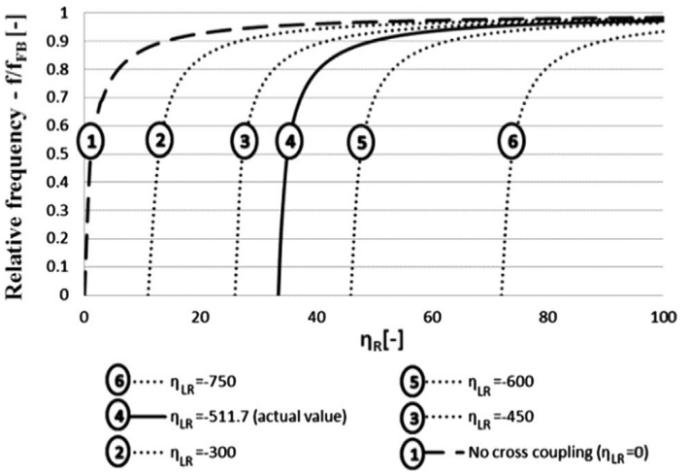

(b) Relative frequency as a function of non-dimensional rotational stiffness for several values of cross-coupling stiffness (Arany et al., 2015)

Figure 2.4.: Results of a sensitivity study on the natural frequency depending on the lateral, rotational and cross-coupling stiffness performed in Arany et al. (2015)

2.1.4 Impact of the multi-directional loading on design criteria

One particularity of the OWT loading is that it is multi-directional. Nevertheless, the design of pile foundations for these structures is generally carried out assuming that the load is acting in only one direction (DNV-GL, 2014). Figure 2.5 shows that the loading from wind and waves at Hornsea wind farm in the North Sea is far from being unidirectional and indicates the range of possible misalignments between two loadings. These data are of course site dependent.

The effects of multi-directional loading on pile behaviour have been explored in some experimental studies. In the context of seismic loading, a new testing device that generates data to calibrate multi-directional $P - y$ curves for soft clays is described in Mayoral et al. (2005). During these tests, the piles were translated in the ground over their whole length. The particular test procedure was designed to deduce a full set of $P - y$ curves and is not representative of the in-situ loading conditions in which the loading is applied at the head of the pile or, more generally, at some distance above the ground level. The results presented by Mayoral et al. (2016b) showed that applying multi-directional loading to a pile in an isotropic medium resulted in anisotropic response of the pile. Also in the context of seismic loading, and with a focus on the global response of the pile, Su (2012) carried out laboratory pile testing in sand with various multi-directional loading paths applied at the head of the pile. Peralta (2010) and Rudolph et al. (2014) performed centrifuge tests in cohesionless soil, modelling the cyclic lateral loading response of large diameter piles acting as foundations of offshore wind turbines. Both studies focused on the impact of multi-directional loading on the accumulation of displacements due to a large number of cycles. Rudolph et al. (2014) showed that multi-directional loading led to an increase in the accumulation of displacements compared with uni-directional loading. On the other hand, Peralta (2010) showed that multi-directional loading resulted in less significant accumulation of displacements than for uni-directional loading. This diversity in the conclusions is perhaps due to the fact that the loading regimes considered were quite different.

The effects of multi-directional loading on pile behaviour have been explored in some numerical studies. Among the few existing studies, Levy et al. (2007) presented a method to take into account multi-directional loading using an energy-based variational approach. Considering elasto-plastic behaviour of the soil and adopting local yield surfaces along the pile, they showed that changes in lateral loading direction altered the global stiffness of the pile. An extension of the model proposed in Levy et al. (2007) was presented in Levy et al. (2009) to account for cyclic loading in addition to multi-directional load paths. Besides Levy's work, Su and Yan (2013) and McCarron (2016) proposed methods to account for multi-directional loading as well as cyclic loading using a bounding surface plasticity model, based on finite-element methods. Mayoral et al. (2016a) proposed a discrete model, based

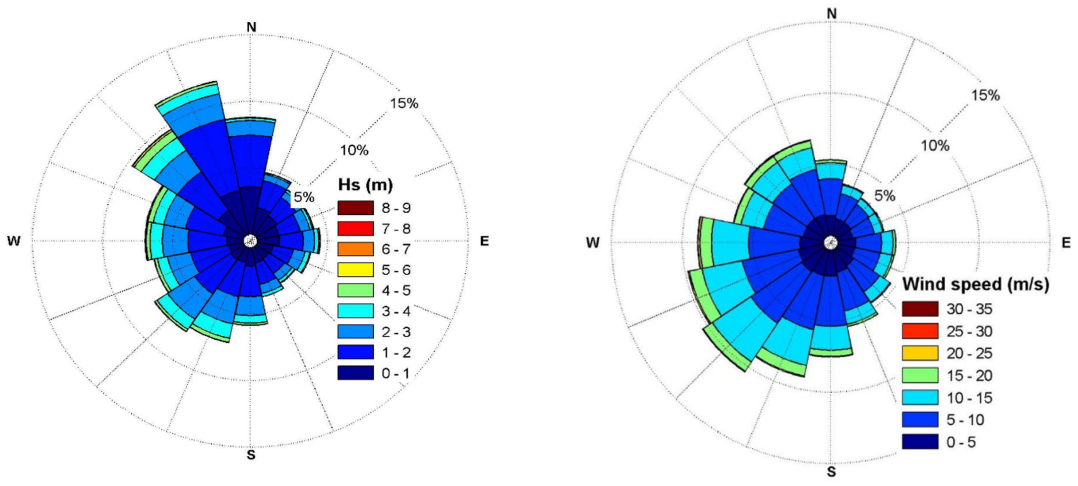

Figure 2.5.: Wave rose (a) and wind rose (b) at Hornsea wind farm, from National Infrastructure Planning (https://infrastructure.planninginspectorate.gov.uk/)

on an assembly of elasto-plastic springs, to reproduce the $P - y$ curves derived from the laboratory tests (Mayoral et al., 2016b). In the case of the methods proposed by Su and Yan (2013) and McCarron (2016), further calibration is needed for the parameters defining the yield and the bounding surfaces (5 parameters for the model proposed by Su and Yan (2013) and 10 for that proposed by McCarron (2016)). For the method proposed by Mayoral et al. (2016a), four additional parameters are needed to define the $P - y$ curves. Consequently, accounting for multi-directional loading effects needs further studies in order to secure the design criteria.

2.2 Methodologies to model laterally loaded pile response

Depending on the accuracy of the soil description one can distinguish three main methodologies to compute the response of a laterally loaded pile:

- **The global approach** models the pile as a structural element. It gives access to the deflection and the rotation but only at the ground surface.
- **The local approach** replaces the soil by a system of springs and only permits an estimation of the deflections, rotations and internal forces along the pile without any output on the ground response. This method is commonly used in foundation engineering and is known as $P-y$ curves approach.
- **Three-dimensional finite element modelling** enables to accurately model the pile and the surrounding ground but requires a detailed knowledge of the ground properties. It gives access to the stress and the strain fields in the ground and to the deflections, rotations and internal forces in the pile.

These three methodologies are illustrated in Figure 2.6 and compared in Table 2.2 in terms of their capability to model monotonic, cyclic and multi-directional response, computing efficiency, accuracy and the possibility of implementation into an integrated design tool. Potential improvements are also listed for each method. It can be noted that the local approach is a good compromise in terms of modelling speed and accuracy. It can be relatively easily extended by considering additional springs to account for the distributed moments along the pile and the ground reaction at the pile toe. Besides, it is the method preferred in the industry for monopile design. For these reasons, the local modelling will be described in detail, while the global approach and the finite element modelling will be only briefly mentioned in the following.

2.2.1 Macro-element modelling

Principles and implementation

The macro modelling consists in representing the whole foundation response below ground level with one stiffness matrix. This stiffness matrix contains diagonal terms corresponding to a stiffness associated with each degree of freedom and non-diagonal coupling terms (Equation 2.2). In the case of OWT monopiles subjected mainly to lateral loading, the stiffness terms related to the degrees of freedom of vertical displacement and torsion are usually disregarded. The stiffness matrix of the macro-element (Equation 2.2) is symmetric and includes coupling terms between displacement in a given direction and the corresponding rotation. These coupling terms have a non-negligible effect on the response

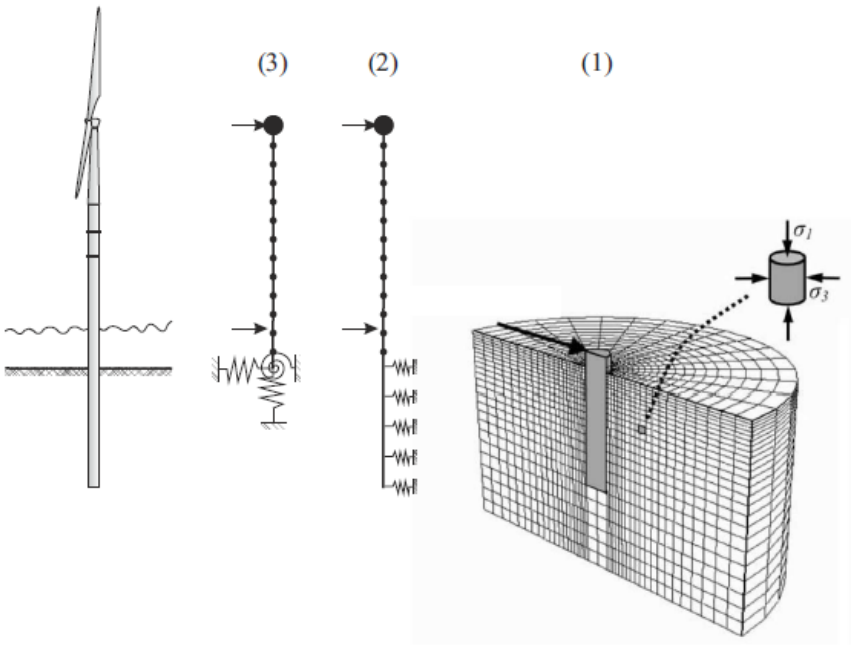

Figure 2.6.: Schematic representation of the possible pile design methodologies (Abadie, 2015)

Table 2.2.: Comparison of different design practices on different criteria

	(1) Global approach (macro-element)	(2) Local approach ($P-y$ curves)	(3) Finite Element Method (FEM)
Monotonic modelling	✓	✓	✓
Cyclic modelling	✓	✓	Very complex
Multi-directional loading	yes with non-symmetric stiffness matrix of the macro-element	yes with calibration for the parameters defining the yield and the bounding surfaces	✓
Speed	$+++$	$++$	$+$
Accuracy	$+$	$++$	$+++$
Integrated design	$+++$	$+++$	$-$
Improvement	-	Add other springs along the depth (rotational springs) see section 2.4.1 for more details	Research project to take into account cycles

(Arany et al., 2015). Considering the x and y directions as the horizontal directions, the stiffness matrix of the macro-element can be written as follows:

$$\begin{bmatrix} F_x \\ F_y \\ M_x \\ M_y \end{bmatrix} = \begin{bmatrix} K_L & 0 & 0 & -K_{LR} \\ 0 & K_L & K_{LR} & 0 \\ 0 & K_{LR} & K_R & 0 \\ -K_{LR} & 0 & 0 & K_R \end{bmatrix} \begin{bmatrix} u_x \\ u_y \\ \theta_x \\ \theta_y \end{bmatrix} \tag{2.2}$$

where K_L, K_R and K_{LR} are the lateral, rotational and cross-stiffness terms, F_x and F_y represent the lateral forces that are applied on the macro-element whereas M_x and M_y are the bending moments, u_x, u_y, θ_x and θ_y are the four degrees of freedom considered for the macro-element.

Linear elastic stiffness matrix expressions for the macro-element modelling

There are various linear elastic stiffness matrix expressions given for different pile rigidity (slender or rigid), for different soil profiles (homogeneous, linear in-homogeneous or parabolic in-homogeneous) and for different types of soils. Arany et al. (2017) listed various formulations (Poulos and Davis, 1980; Carter and Kulhawy, 1992; Shadlou and Bhattacharya, 2016).

Advantages and limitations

This methodology is very simple at first sight and it is possible to make it far more complex. One advantage of the method is the possibility to implement complex advance constitutive laws (non-linear and hysteretic response (Page et al., 2018)) keeping its efficiency in terms of computation time. Its limitation is that only the displacement and the rotation at the mudline can be evaluated without any information on their distribution along the pile. Moreover, the soil beneath ground surface is in most cases assumed to be homogeneous even if one can mention the works of Poulos and Davis (1980) and Shadlou and Bhattacharya (2016) who have considered soils stiffness varying with depth. More complex soil behaviour requires a calibration of the stiffness terms based on finite element computations.

2.2.2 Semi-analytical modelling

Although initially developed to model soil-structure interaction of slender piles, the $P-y$ curves method is the most commonly used method for monopile design. It is implemented in numerous software (e.g OPILE, Bladed, PILATE...). It can be noted that Bladed is an integrated design tool that enables to take the foundation into account at the same time as the tower. Considering a cross-section of the pile that moves in a rigid manner in the direction of the loading, the soil reaction can be decomposed in a normal reaction and a tangential reaction (Baguelin et al. (1977) gave analytical solutions of this problem). However, most of the time, these two components are not separated, and the soil reaction

P is uniformly applied on the projected width of the pile (i.e. on its diameter for circular pile).

Principles

For simplicity, the pile is modelled as an Euler beam element subjected to loads at the head of the pile and soil reaction along its length (cf. Figure 2.7). It should be noted that the Timoshenko beam model is more adequate for rigid monopiles but the differences remain small when comparing these two beam models (below 8 %). The $P-y$ curve (or load-transfer) approach models the soil as a discrete set of independent springs along the length of the pile (i.e. springs operate in the horizontal plane, with no interaction between them). Springs are usually non-linear, describing the local lateral reaction (P) with lateral displacement (y). It can be noted that axial friction along the pile is not considered herein, and consequently the axial force is constant with depth. We consider a 2D coordinate system with y-axis in the direction normal to the pile and z-axis in the direction of the pile axis. Writing equilibrium equations for an infinitesimal element of the pile of length $\mathrm{d}z$ gives three equations traducing equilibrium of bending moment, shear force and axial force:

$$\begin{cases} M-(M+\mathrm{d}M)+H\mathrm{d}z-P\mathrm{d}z\dfrac{\mathrm{d}z}{2}-V\mathrm{d}y=0 \\ H-(H+\mathrm{d}H)-P\mathrm{d}z=0 \\ V-(V+\mathrm{d}V)=0 \end{cases} \tag{2.3}$$

where M is the bending moment, H the shear force, V the vertical force applied on the top of the pile and P is the reaction mobilised by the spring. The lateral reaction P corresponds to a force per unit length applied along a pile element of height $\mathrm{d}z$, and its value is given by the so-called $P-y$ curve. The bending moment M is linked to the lateral displacement y (in the direction of the spring) according to:

$$M=E_pI_p\frac{\mathrm{d}^2y}{\mathrm{d}^2z} \tag{2.4}$$

where E_p is the Young's modulus of the pile and I_p is the second moment of area of the pile. Neglecting second-order terms and combining Equations 2.3 and 2.4, the following governing differential equation is obtained (Reese and Van Impe, 2011):

$$\frac{\mathrm{d}^2}{\mathrm{d}z^2}\left(E_pI_p\frac{\mathrm{d}^2y}{\mathrm{d}z^2}\right)+V\frac{\mathrm{d}^2y}{\mathrm{d}z^2}+P=0 \tag{2.5}$$

The non-linear differential Equation 2.5 is commonly solved by using finite difference or finite element numerical schemes. In this form, the differential equation only involves the lateral displacement y, but other unknowns such as rotations, shear forces and bending moments along the pile can be deduced once the lateral displacements along the pile are known. The equation deals with: a layered profile of soil (or rock) by modifying the function P with the depth, a non-linear behaviour of the soil by implementing a non-linear load-transfer curve, a non-linear behaviour of the pile (usually in the case of bored pile)

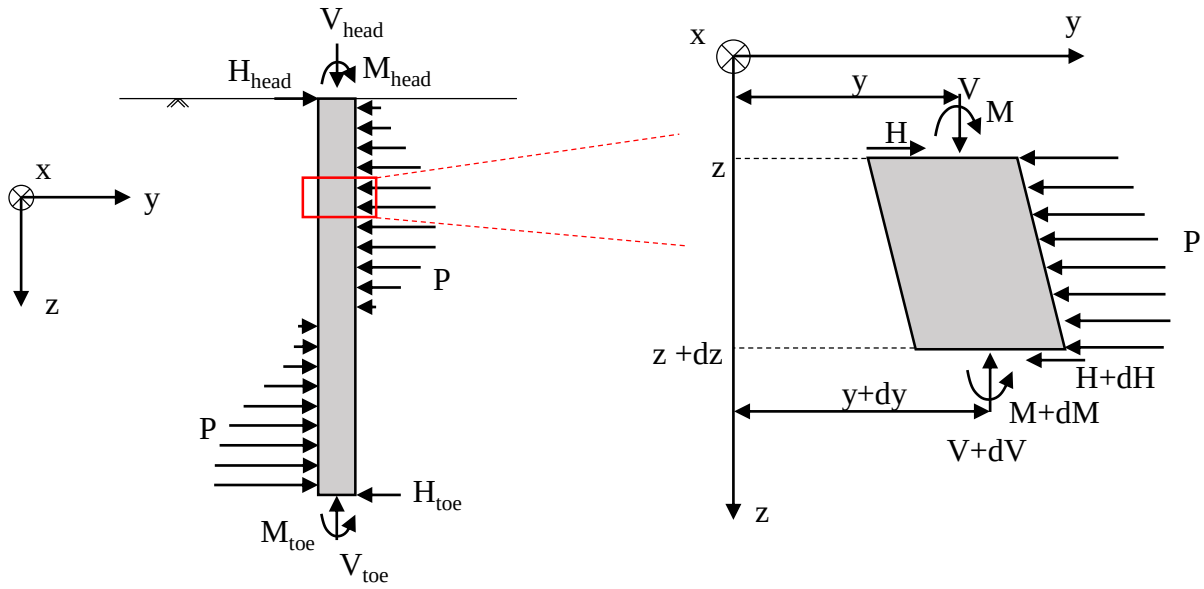

Figure 2.7.: Schematic representation of forces acting on the pile

by considering a non-linear bending stiffness (Reese, 1997) and an axial load. It can be noted that in the particular case of elastic linear models, the differential equation obtained above can be solved analytically. These analytical solutions can be found in Frank (1999) for various boundary conditions. As in most of the time, the soil behaviour is non-linear, this fourth-order differential equation is solved numerically in design tools.

2.2.3 Existing $P - y$ curves

Different $P - y$ methodologies exist in the literature for various ground conditions. A focus is done here for soft rocks. The mathematical expression of the $P - y$ curves and the input parameters are given in Appendix A from Abbs (1983), Fragio et al. (1985), Reese (1997), and Erbrich (2004). They all have in common to be dedicated for weak rock. Considering that within the French offshore wind projects weak carbonate rocks are encountered, we also refer to the work of Dyson and Randolph (2001) who considered cemented calcareous sands. Table 2.3 describes the principal differences between the methodologies described in Appendix A, in terms of theoretical background, parameters used, cycling effect and assumed failure modes. It can be noticed that most methodologies give the same global shape of $P - y$ curves.

Table 2.3.: Comparison of different $P - y$ methodologies

	Theoretical background	Used parameters	Effect of cycles on $P - y$ curves	Failure modes
Abbs (1983)	Validated with full scale tests (even if only the elastic part is validated)	Shear strength	Strength degradation Same degradation is applied regardless cycle's level of loading and number of cycles	Brittle near the surface and ductile deeper
Fragio et al. (1985)	Validated with full-scale tests	Shear strength	None	Brittle near the surface and ductile deeper
Reese (1997)	Validated with full-scale tests	Unconfined compressive strength	None	Ductile
Dyson and Randolph (2001)	Deduced from centrifuge test results	Cone tip resistance	None	Ductile
Erbrich (2004)	Finite element modelling (2D and 3D) + plasticity analysis + centrifuge tests	Cone tip resistance	Shifting $P - y$ curves (done cycle by cycle)	Brittle near the surface and ductile deeper

2.2.4 Computing $P - y$ curves from pile tests

Computing $P - y$ curves from pile tests is possible provided that the pile is sufficiently instrumented. Strain gauge measurements along the pile are indeed needed to deduce $P - y$ curves. The measured quantity is the axial strain (usually on the tensile side of the pile) and assuming that the pile is linear elastic the corresponding axial stress is deduced. Then, considering the beam theory the bending moment in the section is determined. In order to have sufficient data to compute $P - y$ curves from tests, the minimum number of sensor locations should be equal to the order of the polynomial used to fit the data plus one (Xue et al., 2016). For each load applied on the pile, the lateral deflection y and the corresponding soil reaction per unit length P are deduced at each depth of measurements. Assuming an elastic behaviour of the pile, the profiles of the deflection and the soil reaction along the pile are determined numerically as follows (Rosquoët, 2004):

$$\begin{cases} \dfrac{\mathrm{d}^2 y}{\mathrm{d}z^2} = \dfrac{M}{E_p\, I_p} \\ \\ P = -\dfrac{\mathrm{d}^2 M}{\mathrm{d}z^2}(z) \end{cases} \tag{2.6}$$

Boundary conditions are the measured lateral displacements at two different locations.

Deriving deflection versus depth profile technique

The measured bending moments along the pile can be interpolated by a polynomial. Usually, a seven-order polynomial is used, and then analytical integration is performed. The two integration constants are determined with two boundary conditions. Attention is paid to the boundary conditions adopted, since they may have a significant influence on the accuracy of the double integration (Rosquoët, 2004). Usually, the displacement at the head of the pile, or near the ground level is measured allowing the determination of one integration constant. The choice of the second integration constant depends on the pile behaviour. A flexible pile has a zero-toe displacement. For rigid piles another measurement is needed, such as the rotation at the head of the pile (Xue et al., 2016). It can be noted that lateral deflection profile along the depth can also be deduced from rotations measured by inclinometers. In this case, the measured rotations can be approximated with a polynomial and the deflection profile is deduced with single integration involving only one integration constant. Yang and Liang (2007) have compared two profiles: one determined from strain measurements and one from rotation measurements and showed that both measurements lead to the same deflection profile.

Deriving soil resistance per unit length technique

Since the double derivation of discrete data points results in error amplification (Yang and Liang, 2007), various methodologies are proposed in the literature for soil reaction evaluation:

- **Approximation of the bending moment profile with polynomial functions**:
  - → Piecewise cubic polynomial curve fitting is used by Matlock and Ripperger (1956), Dunnavant (1986), and Dyson and Randolph (2001);
  - → High order global polynomial curve fitting is used by Reese and Welch (1975) and Wilson (1998);
  - → Cubic or quintic spline curve fitting is described by Mezazigh and Levacher (1998), which can be seen as a form of piecewise polynomial curve fitting.
- **Weighted residuals method** (Wilson, 1998):
  The moment profile is approximated by using shape functions which coincide with the measurements at the nodal point. This approximation is then derived, and an approximation of the derivative of the moment as a piecewise linear function is searched by minimising the residue. The same procedure is done to deduce the second derivative of the profile of moment as a piecewise linear function.
- **Approximation of the soil reaction profile with a polynomial function** (Xue et al., 2016):
  The soil resistance profile is approximated with a fourth-order polynomial and the shear force acting on the base is also considered. Under the constraints that equilibrium equations are fulfilled (global equilibrium of horizontal and vertical forces and moments) the coefficients of the fitted polynomial and the value of the base shear are deduced by minimising the difference between the calculated and measured moment profile. These authors used a genetic algorithm optimisation technique.

Note that in the two first methods the equilibrium is checked afterwards. The unbalanced forces and moments should not exceed 10 $\%$ of the applied loads (Rosquoët, 2004).

2.2.5 Finite element modelling

In general, it can be noted that finite element studies (Erbrich, 2004; Achmus et al., 2009; Liang et al., 2009; Zdravkovic et al., 2015) are used to justify analytical design methods (local method with $P-y$ curves, design charts...). Finite element methods enable to study the impact of various parameters (pile geometries, loading characteristics...) on the results. Due to geometric and loading symmetry for laterally loaded pile studies, there is no need of modelling everything; only half of the geometry is sufficient (Zdravkovic et al., 2015).

Pile modelling

For driven piles, the pile is a steel tube pile. The pile can either be modelled with 3D elements as a tube or as a solid cylinder. In the latter case, the section of the pile is not respected so the Young's modulus of the pile must be changed to ensure constant bending stiffness (Achmus et al., 2009). Otherwise, the pile can be modelled with structural elements (beam elements or shell elements). The advantages of using structural elements are to

decrease the number of elements in the model and to facilitate post-processing as the rotations and the internal forces are directly available for these elements. The pile is usually modelled with as linear elastic. One should ensure that pile stresses remain in the elastic range of steel grade considered (Velarde, 2016). In the case of drilled and grouted piles, the pile is modelled as a solid cylinder with an equivalent bending stiffness (bending stiffness of grouted section and steel tube). The modelling of the drilled shaft is more complicated to model than the steel tube pile as the grout stiffness can vary which implies incorporating in the model a non-linear constitutive law. However, the ground behaviour is of primary interest in the analysis and the drilled shaft can be modelled with a linear elastic law (Liang et al., 2009).

Ground modelling

Various constitutive models are used in the literature for ground behaviour. Erbrich (2004) has modelled the rock using a Von Mises yield criteria. Achmus et al. (2009) have taken into account a stiffness degradation model. Liang et al. (2009) have modelled the rock with modified Drucker-Prager yield criteria. Finally, Zdravkovic et al. (2015) have simulated stiff clay using Modified Cam Clay model and sand using a bounding surface plasticity model based on Taborda et al. (2014).

Interface modelling

Depending on the soil, there are two options to model the interface, either the soil follows the pile movement, or a gap is allowed between the pile and the surrounding ground. In the second case, there are two major methods to model the soil-structure interface: zero-thickness elements and thin layer elements. Among these two possibilities, sliding and friction behaviours can also be accounted for. In Zdravkovic et al. (2015) the interface is modelled differently depending on the type of soil. For example, interface in sandy soils is modelled using a Mohr-Coulomb criteria with no cohesion, so that the gap opens when the effective normal stress is in tension. Interface in clay soils is modelled using a Tresca model. It can be noted that Erbrich (2004) used small strain interface elements available in Abaqus finite element code.

Various parametric studies undertaken

Erbrich (2004) undertook finite elements modelling to calibrate a local approach. It can be seen in this study that whatever the pile roughness is, failure is reached at smaller displacements for two-sided mechanism than for one-sided mechanism. In the same spirit, Zdravkovic et al. (2015) conducted various finite element analysis to justify a new design method validated with in-situ large scale pile tests (see section 2.4.1). They demonstrated the impact of slenderness ratio (length over diameter), lever arm and diameter over thickness of the pile tube on the global response of a monopile in stiff clays.

2.3 Cyclic behaviour

2.3.1 General considerations

First, the different terms that can be encountered in the field of cyclic behaviour are defined:

- **dynamic / quasi-static loadings**
  The loading of a rock sample can be considered as dynamic if the inertial forces generated in the material are significant relative to the loading force. Conversely, these forces of inertia are negligible during a quasi-static loading. However, there is no widely agreed threshold limiting these two types of loading (Cerfontaine and Collin, 2018), but one can mention Zhao (2010) who defined a loading rate of 0.05 MPa/s and Cho et al. (2003) who defined a deformation rate threshold around 0.1 and 1 s^{-1}.
- **cyclic / monotonic loadings**
  Cyclic loadings are defined by an imposed time-dependent stress or displacement signal that has a repeated pattern, as opposed to monotonic loading for which stress or displacement increases or decreases continuously. The cyclic loading is defined by the mean value and the amplitude of the cycles.
- **high cycle / low cycle loadings**
  For cyclic loadings, one can distinguish high cycle loading and low cycle loading depending on the number of cycles applied. Once again, there is no strict definition of the threshold between these two types of loading. Cerfontaine and Collin (2018) considered that this threshold is about one thousand cycles.
- **fatigue / damage-controlled tests**
  The mean and the amplitudes of the stress (or displacement) signal can be constant or variable during the cyclic test. Tests with constant mean and amplitude values with a high number of cycles are mainly used to determine the fatigue limit of rock materials which are called fatigue tests. Conversely, tests with increasing mean and amplitude values are called damage-controlled tests.
- **stress / strain controlled loading**
  For cyclic loadings, the controlled variable can be either the stress (similarly the load) or the strain (similarly the displacement).
- **one-way / two ways loadings**
  The sign of the controlled variable during the cyclic loading defines the type of cycles (one-way or two-way). If the sign of the controlled variable is constant within a cycle, it is called one-way loading whereas if the sign changes within a cycle it is called two-ways loading.

There are five main responses that can be distinguished for **stress controlled cycles** (or load controlled cycles). Figure 2.8 shows these five possible responses on a strain-stress plot

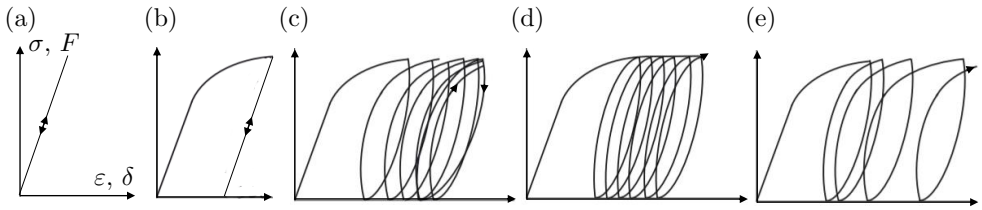

Figure 2.8.: Sketch of typical cyclic behaviour encountered during stress (or load) controlled cyclic tests (a) Purely elastic (b) Adaptation (c) Accomodation (d) Perfect ractcheting (e) Unstable ractheting after Di Prisco and Muir Wood (2012)

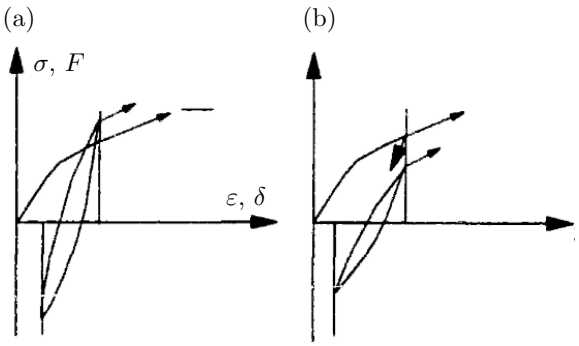

Figure 2.9.: Sketch of typical cyclic behaviour encountered during strain (or displacement) controlled cyclic tests (a) Cyclic hardening (b) Cyclic softening after Dupla (1995)

(or displacement-force plot). It can be noticed that among these categories, there are three categories (a, b and c) that lead to a stabilised state, which means that there is a time (or number of cycles) after which there is no more strain accumulation. Among these stabilised states, there are:

- **Accommodation** when the amplitude of the strains reduces during each new cycle to finally stabilise on a loop, which accounts for a dissipative behaviour without increase of strain accumulation.
- **Adaptation** is similar to accommodation but instead of stabilising on a loop it stabilises on a straight line that accounts for a non-dissipative behaviour.

Ratcheting phenomenon regroups the three categories (c, d and e), which differ by the rate of accumulation: for sketch (c) the rate of accumulation decreases towards 0 and leads to a stabilised state, whereas for sketch (d) the rate of accumulation is constant (sometimes called perfect ratcheting), finally for sketch (e) the rate of accumulation increases and usually leads to failure in few cycles. Other terms are encountered in Levy et al. (2009), in which adaptation behaviour is called shakedown, accommodation behaviour is called plastic shakedown or alternating plasticity and ratcheting is called incremental collapse. Concerning **strain controlled cycles** (or displacement controlled cycles) two cases can be distinguished (Figure 2.9): **cyclic hardening** can be recognised as the cycles tend to get straighter whereas **cyclic softening** is observed on the opposite case.

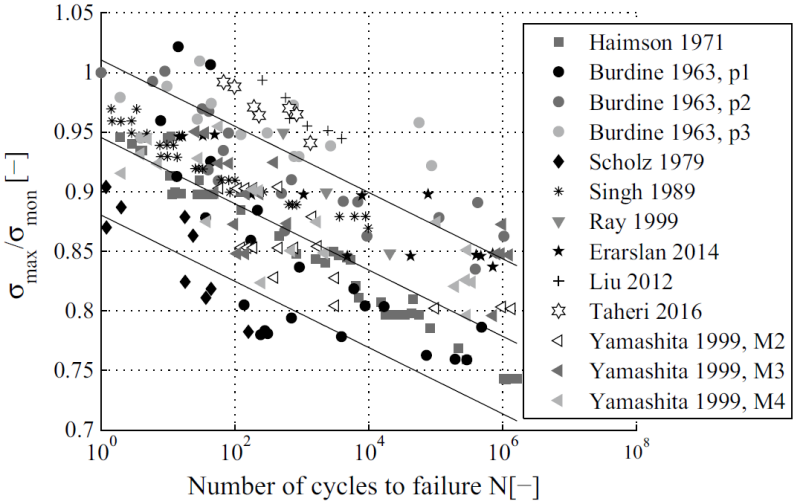

Figure 2.10.: S-N curves from different material and types of tests, constant amplitude (Cerfontaine and Collin, 2018)

2.3.2 Cyclic behaviour at the scale of the material

In this thesis, we are interested in cyclic behaviour of rock materials because monopiles-based OWT installed in soft rock are submitted to a high number of cycles during their lifetime. However, there are many other structures involving rocks that are submitted to cyclic loadings. We already mentioned wind and waves but one can also mention earthquakes and traffic induced wave propagation or freeze-thaw cycles (Cerfontaine and Collin, 2018).

$S-N$ curves

Fatigue is the weakening of a material caused by repeated cycles. One effect of fatigue is that under cyclic loading a sample fails at a lower stress level than under monotonic loading. One way to represent this effect is to plot an $S-N$ curve also known as a Wöhler curve. This is a graph that shows on the y-axis the cyclic stress (usually divided by the failure stress considering a monotonic loading) and on the x-axis the corresponding number of cycles leading to failure (usually in logarithmic scale). Figure 2.10 taken from Cerfontaine and Collin (2018) summarises $S-N$ curves obtained on different rocks in the literature. It can be noted that $S-N$ curves can be obtained for any type of experiment (uniaxial, triaxial...), the choice of the type of test will obviously impact the results. What appears ini this graph is that there is a linear trend in log-scale between the stress level of constant amplitude cyclic loading and the number of cycles leading to failure. Generally, if failure is not reached after one million of cycles, the test ends and assuming one million of cycles as the number of cycles leading to failure is conservative.

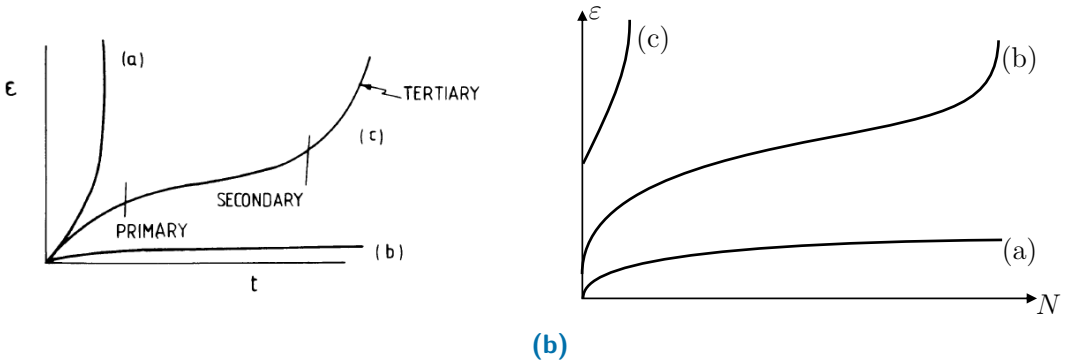

Figure 2.11.: Comparison between mechanism of deformation under (a) creep loading (Farmer, 1983) (b) cyclic loading after Xiao et al. (2009)

Link between creep phenomenon and fatigue

Deformations under cyclic loading and creep are shown to share some similarities (Farmer, 1983; Airey and Fahey, 1991; Cerfontaine and Collin, 2018). Under both creep and cyclic loadings, the sample is weakened and can fail at a lower level of loading than under monotonic loading. For creep loading, the long-term strength represents the level of stress above which failure can be reached and it ranges around 50-70 % of the ultimate monotonic stress for rocks (Farmer, 1983). For cyclic loading, the fatigue strength represents the level of stress above which a certain number of cycles (usually below one million) can lead to failure, and the fatigue strength ranges also around 60-70 % of the ultimate strength for rocks (Farmer, 1983). Besides, for both creep and cyclic loading, the three same main mechanisms of deformation are identified (cf. Figure 2.11). For high maintained load (respectively for high maximum cyclic load), the strain accumulates faster and faster leading quickly to failure. For low maintained load (respectively for low maximum cyclic load), the strain accumulates at the beginning and then stabilises. For intermediate maintained load (respectively for intermediate maximum cyclic load), three phases can be identified in the strain evolution. These three phases are commonly known as primary creep, secondary creep and tertiary creep. These deformation mechanisms are commonly linked to the development of cracks for rock materials. There are several rheological models that enable to model creep phenomenon (Maxwell model, Kelvin-Voigt model, Zener model, Burgers model or Bingham model). Using this framework to model cyclic loading is also relevant. Besides, to model cyclic loading with a time dependent model is also justified by some experimental observations: the elapsed time appears to be a more relevant parameter than the number of cycles (Cerfontaine and Collin, 2018).

2.3.3 Cyclic behaviour at the pile scale

Various cyclic lateral load tests on piles were performed by (Little and Briaud, 1988; Long and Vanneste, 1994; Lin and Liao, 1999; Leblanc et al., 2010a; Abadie, 2015). Some of these studies (Lin and Liao, 1999; Leblanc et al., 2010b) also focused on defining a procedure in order to superpose cycles at different load amplitude. The framework of these approaches is briefly described in Table 2.4. It can be noted that two studies (Leblanc et al., 2010a; Abadie, 2015) are specially tailored for rigid monopiles for OWT. These approaches described simple cyclic loading cases whereas OWT are loaded with extremely complicated loading. Briefly, a cyclic lateral loading can be described with the three following parameters (cf. Figure 2.12):

- number of cycles N;
- ratio between maximum load (or moment) in a load cycle over the ultimate capacity (ultimate load or ultimate moment) ζ_b;
- ratio between the minimum load (or moment) applied in a load cycle over the maximum load (or moment) applied in a load cycle ζ_c

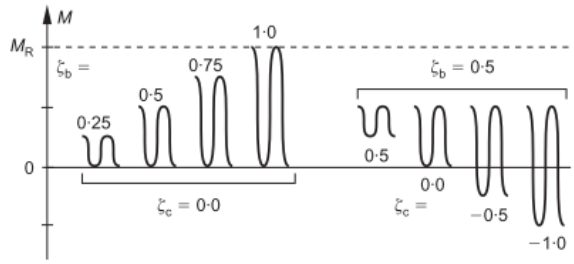

Figure 2.12.: Characteristics of cyclic loading defined in terms of ζ_b and ζ_c (Leblanc et al., 2010a)

Other parameters are important to define the tests such as the nature of soil, the scale of tests and the nature of the pile. In these studies the authors do not consider the effect of the installation method. By way of comparison, the characteristics of cyclic lateral loading of these different approaches is given in Table 2.4 as well as orders of magnitude of parameters for OWT. It is noted from this table that the number of cycles for OWT is much higher than the number of cycles for the other references. One can question using these laws of approximation for higher number of cycles than those considered during the test. This is why a physical understanding of what is going on at the scale of the material is needed.

Table 2.4.: Framework of approximation of a quantity accumulation for cyclic lateral loading studies

References	Pile type	Installation	Soil Type	Tests type	N	ζ_b	ζ_c	Parameters used	**Law of approximation**
Little and Briaud (1988)	Slender piles	Drilled	Sand	Full scale	~ 20	-	[0 ; 0.5]	Stiffness	$\propto N^{-a}$
Long and Vanneste (1994)	30 slender piles / 4 rigid piles	Drilled Driven Vibrated	Sand	Full scale	<100 (3 tests with 500 cycles)	-	[0 ; -1 ; -0.25 ; 0.5]	Soil reaction modulus (R_n)	$R_n = N^{-t}$
Lin and Liao (1999)	Slender piles	Drilled Driven Vibrated	Sand	Full scale	<100	-	[0.5 ; 0.1 ; 0 ; -0.25 ; -1]	Strain (ϵ_N)	$\varepsilon_N = \varepsilon_1 \ [1 + t\, ln(N)]$
Rosquoët (2004)	Slender piles	Driven	Sand	Lab. tests	≤ 45	0.2, 0.3 or 0.4	[0;0.5]	Displacement (y_N)	$y_N = y_1 + b \ln N$
Rakotonindriana (2009)	Slender piles	Driven	Sand	Lab. tests	$\sim 25\,000$	0.1, 0.2 or 0.3	[-1;0.33]	Displacement (y_N)	$\begin{cases} y_N = a_1 \ln N + b_1 \text{ , if } N \leq N_{init} \\ y_N = a_2 \ln N + b_2 \text{ , if } N \geq N_{init} \end{cases}$
Leblanc et al. (2010a)	Rigid piles	Driven	Sand	Lab. tests	~ 10000	[0.20 ; 0.27 ; 0.34 ; 0.40 ; 0.53]	[0.50 ; 0.33 ; 0 ; -0.33 ; -0.67 ; -0.98]	Rotation ($\Delta\theta$) Stiffness (k_N)	$\Delta\theta = \theta_S \, T_b \, T_c \, N^{-\alpha}$ $k_N = k_0 + A \, ln(N)$
Abadie (2015)	Rigid piles	Driven	Sand	Lab. tests	~ 10000 ~ 100000	[0.31 ; 0.42 ; 0.47]	[0.13 ; 0.18 ; 0.24]	Rotation ($\Delta\theta$) Stiffness (k_N)	$\Delta\theta = \theta_S \, T_b \, T_c \, N^{-\alpha}$ $k_N = k_0 + A \, ln(N)$
OWT	-	-	-	-	10^7	$< 5\%$	Random loading + multi-directional	-	-

2.3.4 Taking into account cyclic behaviour in the design

Table 2.5 gives an overview of the different methods to take into account cyclic modelling in the context of laterally loaded piles. The pros and the cons of these methods are listed in this table. On the one hand, to assess the response for a given cycle using a cycle by cycle analysis, the response of all the cycles applied before needs to be calculated. Even assuming sufficient computer capacity, attention should be paid to the accuracy of those methods. In the case of OWT monopiles, the accumulated strains as well as the strain rates are expected to be small. Thus, cumulative systematic numerical errors might not be negligible anymore (Lesny and Hinz, 2007; Achmus et al., 2009). On the other hand, modified monotonic analyses using cyclic parameters comprise those analyses for which the response at a given cycle is calculated directly without needing to calculate the response of the previous cycles. However, these empirical laws are usually based on a particular set of experimental results, and attention should be paid to the area of validity of these kinds of laws.

2.4 Field works

There are very few field tests for laterally loaded piles in the literature as it is very expensive to design, carry out and interpret them. Though, one can mention two field tests in various ground conditions: PISA project (in sand and clay) and Wind Support (in chalk). Both field tests lead to an improvement of the classical $P-y$ curves approach (see section 2.2.2). Table 2.6 gives the main parameters of both field tests.

2.4.1 PISA (PIle Soil Analysis)

PISA is a joint industry project which aimed at establishing a new design method for large monopiles under lateral loading in sandy soils and stiff clays. It took place between August 2013 and January 2016. This project was specially tailored for OWT monopiles. The results are based on numerical modelling and field tests. Field tests were realised onshore in sandy and clays soils similar to the soil that can be encountered in the North Sea with smaller pile dimensions than the ones encountered offshore for OWT but similar slenderness ratios (see Table 2.6). Both numerical analyses and field testing were needed to validate the new design method (Byrne et al., 2015b) as it will be applied at a larger scale for OWT monopile. The load eccentricity corresponds to the lever arm between the level of application of the loading and the ground surface (i.e. ratio M/F). Byrne et al. (2015a) highlighted the importance of applying a lateral loading with a certain load eccentricity in order to apply also a bending moment at the ground level. This is done in order to be representative of how the ground is loaded in offshore conditions (loading due to the waves and the wind). Currently, in the existing $P-y$ method only the lateral pressure developed in the ground

Table 2.5.: Comparison of different methods to take into account cyclic loading for laterally loaded piles

		References	Principle	Limitations	Advantages
Cycle by cycle analyses	Macro-modelling	Houlsby and Puzrin (2006), Abadie (2015), and Houlsby et al. (2017)	Hyper-plasticity framework	Complex parameters calibration Require cyclic pile tests results	Numerical efficiency Applicable for OWT
	Local modelling	Levy et al. (2009)	Energy-based numerical model		Capture all cyclic behaviours and multi-directional effects
		API (2000) and DNV-GL (2014)	Degraded static $P-y$ curves	Independent of the number of cycles and the level of loading	Numerical efficiency Implemented in integrated design tool
		Puech and Garnier (2017) and Heidari et al. (2014)	Definition of a backbone curve (static $P-y$ curve) an unloading curve and reloading curve	High computational cost	Versatility of the type of behaviours
		Erbrich et al. (2011)	Definition of a new $P-y$ curve at each cycle	Limited to few cycles Developed for carbonate soils	Based on rigorous link to laboratory testing Used for the design of industrial piles Can be implemented in integrated design tool
	FEM	Achmus et al. (2009)	Complex constitutive law	Limited to number of cycles below 50	-
Modified monotonic analyses	Macro-modelling	Puech and Garnier (2017)	Equation 2.7 *	Not validated for high number of cycles (around 100)	Numerical efficiency
		Leblanc et al. (2010b)	Cyclic lateral pile testing at reduced scale and the Miner's rule	Not validated for higher number of cycles (around 10 000)	Numerical efficiency Take into account random cyclic loading
	FEM	Achmus et al. (2009)	Empirical laws on degradation of certain parameters	Not validated for high number of cycles (around 10 000)	Numerical efficiency
		Page Risueno et al. (2013)	Contour diagrams	Require extensive laboratory testing programme	Implemented in commercial FEM programs Numerical efficiency

$$* \frac{y_N}{y_1} = 1 + \frac{0.235}{CR} \ln(N) \left(\frac{H_c}{H_{max}}\right)^{0.35} \tag{2.7}$$

where y_N is the lateral is the lateral displacement after N cycles, y_1 is the lateral displacement at the same load if the loading would have been static, CR is rigidity coefficient, H_c is the maximum level of load within a cycle and H_{max} is the pile static ultimate load.

Table 2.6.: Parameters of two field tests PISA and Wind Support

	PISA	Wind Support
Type of soils	sand and clay	chalk
Number of piles tested	14 at each site	5
Monotonic loading	✓	✓
Cyclic loading	✓	✓
Eccentricity of the loading	5-10 m	1 m
Diameter of the pile	0.273 m / 0.762 m / 2 m	0.762 m
L/D	3-10	5-13
D/t	30-80	17-30

is modelled. Soil reaction may not be restricted to lateral pressure, other mechanisms can occur. Four different components of the soil reaction are considered in the new design method proposed by Byrne et al. (2015b): the distributed lateral pressure function of the lateral deflection, the distributed moment function of the rotation, the base shear function of the pile tip deflection and the base moment function of the pile tip rotation. The effect of adding one by one the four components of the soil reaction was studied and showed that the already existing $P-y$ modelling is insufficient to describe the global response and the effect of the three new components depend on the nature of the soil. The response is compared with the 3D finite element modelling and give a very good results. Finally, the existing $P-y$ method was extended in the new design method proposed in PISA project. This new design method was validated through numerical analyses and pile tests. However, this project only concerned sand and clay. Even if cyclic tests were undertaken, it was mostly to give guidelines but no cyclic design methodology was expected from this project.

2.4.2 Wind Support

Since current design practice for monopiles in chalk was very conservative as there was limited data on this topic in chalk, the Wind Support project was launched (Muir Wood et al., 2015). Field tests were carried out (between November 2011 and March 2012) in a former quarry with properties close to the ones of the chalk at the Westermost Rough Offshore Wind Farm located in the North Sea to optimise the monopile design. The field tests and the design process were described in Muir Wood et al. (2015). It appeared from these tests that the remoulded chalk created during the pile installation is of importance in the design. Further tests were performed in order to understand the extension of the remoulded zone around the pile. As the monopiles installed offshore are large-diameter piles, it was assumed that from the perspective of the chalk the monopile can be seen as a plate more than a cylinder. Some steel plates were installed in the chalk and then excavated to see the extent of the remoulded chalk. To take into account the impact of the remoulded zone, two $P-y$ curves in series are considered, one $P-y$ curve that represents the behaviour of the remoulded chalk and the other represents the intact chalk. This new method enables

to assess more precisely and more rigorously the monopile lateral stiffness. The method deduced from these field tests was used for the design of an industrial offshore wind farm in the UK and the method was validated by the certifier. Even a small-scale field testing enabled to identify a method to optimise the design of an offshore wind project.

2.5 Conclusions

The nature and the behaviour of the surrounding ground have an impact on the overall behaviour of the monopile (flexible or rigid), on the natural frequency (over the time) and on the effects of the multi-directional loading. The three major methods to calculate the response of a pile submitted to lateral loading are described. Even if it is difficult to avoid finite element analysis as it is usually used to validate the macro-modelling and the $P-y$ curves approach, it is the latter that is used in practice for the monopile design. Describing the cyclic behaviour of the monopile is very complicated and various approaches based on various assumptions exist. A compromise has to be found between the accuracy of the description of the cyclic loading effects and the applicability of the method when 10^7 cycles are considered. For rock materials, the similarities between the creep and the cyclic phenomena offer a wide range of possible modelling that can be applied to the industrial design. Cyclic and monotonic laboratory tests performed on samples representative of the surrounding ground in which the monopile would be installed are essential. Piles tested at reduced scale are also a good means to understand the pile-soil interaction during cyclic loading, and can be used to validate different approaches. Field testing aims to provide results to identify key phenomena and to calibrate and validate numerical methods.

3

Onshore pile tests (OPT)

Summary

One of the aims of the experimental program of onshore field tests performed in Gouvieux is to understand the response of piles installed in soft rock under lateral monotonic and cyclic loading. A description of the site soil conditions and of the choice of the pile characteristics and installation methods is given as well as an explanation of how the load is applied and how the piles are instrumented. Testing programme ensures that the applied load represent well those relevant for offshore conditions. The main results of these tests are presented. The stiffness evolution in due course of cyclic loading is analysed as it is a key factor for the natural frequency requirement. The accumulated rotations and the rotation threshold are looked at for the long-term rotation requirement. Since the piles are installed in soft rock, two phenomena are highlighted: the creation of a crushed zone around the pile due to the driving process and the onset and propagation of cracks in the surrounding rock mass.

Résumé

L'un des objectifs des essais de pieux réalisés à Gouvieux est de comprendre la réponse des pieux installés dans la roche tendre sous chargement latéral monotone et cyclique. La description des conditions de sol, des caractéristiques géométriques des pieux et de leur méthode d'installation est donnée ainsi que la description de comment la charge est appliquée et comment les pieux sont instrumentés. La méthode utilisée pour définir le programme d'essais est présentée et permet une bonne représentativité des essais en comparaison d'un chargement en mer et de tenir compte des limitations expérimentales. Les principaux résultats de ces essais sont présentés. L'évolution de la raideur en raison du chargement cyclique est analysée puisqu'il s'agit d'un paramètre déterminant pour le respect du critère sur la fréquence propre. L'accumulation des rotations et le seuil de rotation sont analysés en raison du critère sur la rotation à long terme. Deux phénomènes dus au fait que les pieux soient installés dans de la roche tendre sont mis en évidence: la création d'une zone de roche broyée autour du pieu due au battage et l'apparition et la propagation de fissures dans la roche.

3.1 General test conditions

3.1.1 Site selection and soil stratigraphy

To simplify the procedure and the interpretation of the pile testing, it was important to select a site with unfractured flat rocky ground. A free field would have required significant work to remove the backfill and the upper rock layer fractured with roots. Therefore, during the site selection quarries were specially looked at. The rock properties encountered in the site should be similar to the ones of the two offshore projects (Courseulles-sur-Mer and Saint-Nazaire). Table 3.1 summarises the rock properties which were targeted for site selection. The selected site is a former quarry located at Gouvieux in the Oise department north of Paris. The regional geology within the Gouvieux site consists of a calcareous substratum from the Middle Eocene period (Lutetian). This substratum consists in a pale-yellow fine to medium grained calcarenite with few fine sand sized shells and shell fragments. The stratigraphy is summarised in the Table 3.2.

Table 3.1.: Rock properties targeted for site selection

Soil property	Criteria
Unconfined Compressive Strength (UCS)	5 MPa $\leq$UCS$\leq$ 15 MPa
Porosity (ϕ)	$20\ \% \leq \phi \leq 35\ \%$
Rock Quality Designation (RQD)	$40\ \% \leq$ RQD without a strong anisotropy of fractures
Carbonate content ($CaCO_3$)	$70\ \% \leq CaCO_3$

Table 3.2.: Stratigraphy

Type	Layer thickness	Description
Calcarenite	3.5 - 4.1 m	Unfractured weak limestone with UCS ranging from 5 to 11 MPa
Limestone	0.3-0.8 m	Moderately strong limestone with UCS higher than 20 MPa
Dense sand	-	Dense sand alternating with cemented sand and thin layers of moderately strong limestone

A set of triaxial experiments have been performed on samples of rock from OPT site under dry conditions (details on the device used are given in Appendix C). For the laboratory tests, the samples (40 mm in diameter and 80 mm in height) have been prepared from cores retrieved in-situ at a depth between 2 and 3 meters. One hydrostatic test, one uniaxial test, two triaxial tests at a confining pressure of 2 and 6 MPa and two Brazilian tests have been performed. The critical pressure for the onset of pore collapse is obtained from the hydrostatic compression test (Figure 3.1a) and is of about 15 MPa. This limestone shows a brittle to ductile transition at a rather low confinement of 6 MPa. The triaxial tests under

a confinement of 6 MPa exhibits an elastic perfectly plastic response. From the uniaxial and triaxial tests (Figure 3.1b) one can obtain the elastic moduli: the average Young's modulus deduced from these three tests equals around 5 GPa and the Poisson's ratio equals around 0.3. From these values, one can deduce the bulk modulus $K = E/(3(1-2\nu))$ which equals 4.2 GPa. On the other hand, the obtained bulk modulus from the initial slope of the hydrostatic test is of 4.7 GPa. This shows a good agreement between the different tests. Besides, Figure 3.1c shows the Mohr circles at failure which permits a Mohr-Coulomb failure envelope with a cohesion of 1.66 MPa and a friction angle of 32°. The tensile strenght obtained from the Brazilian tests is of 1.57 MPa.

3.1.2 Pile characteristics and installation procedure

11 piles with pile diameter of either 0.762 m (medium diameter piles) or 1.2 m (large diameter piles) were installed and 10 piles were loaded laterally. The pile layout shown in Figure 3.2 illustrates that the large diameter piles were tested two by two whereas the medium diameter piles were tested in reaction to one of the large diameter piles. The minimum distance between two piles was chosen to be equal to 13 m to ensure that the pile group effect is negligible both during the installation and the loading procedure. Pile dimensions were selected to reproduce the ratio between the pile embedded length and the pile diameter (L/D) of typical monopiles for OWT (ranging between 2.7 and 4). However the ratio between the pile diameter and the pile thickness (D/t) was not similar to those relevant for OWT monopiles. However, this compromise was done as the thickness was not expected to be a key parameter in the pile lateral response. Piles equipped with optical fibre gauges are 35 mm thick, whereas the two piles without this instrumentation are 25 mm thick. The tube is in steel with a grade of 420 MPa (i.e. a minimum yield stress that equals 420 MPa). Four major types of pile installation procedure were tested:

- Full driving until reaching the full penetration depth. Some piles were drilled internally (large diameter piles) after driving to install extensometer chains and inclinometer chains in the casings;
- Pre-drilling of a fraction of the internal pile steel diameter followed by driving until the targeted depth;
- Drilled, driven and grouted sequence;
- Drilled and grouted sequence.

One aim of the experimental programme is to test installation procedures that would be used offshore. Another challenge was to maintain the pile vertical during installation. Since no self-penetration or initial vibro-installation were possible, two installation frames were specifically designed and built for the project. They were fixed to the ground through drilled and grouted micropiles to avoid movement during driving. No driving refusal was reached during the installation procedure which is also an important information for the limit of

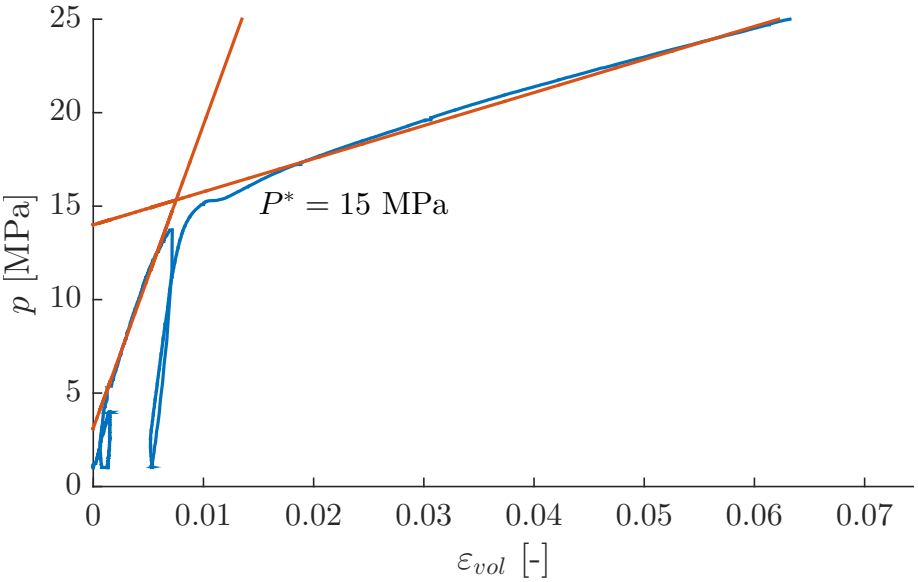

(a) Confining pressure function of volumetric strain deduced from a hydrostaic compression test performed on a rock sample from OPT site.

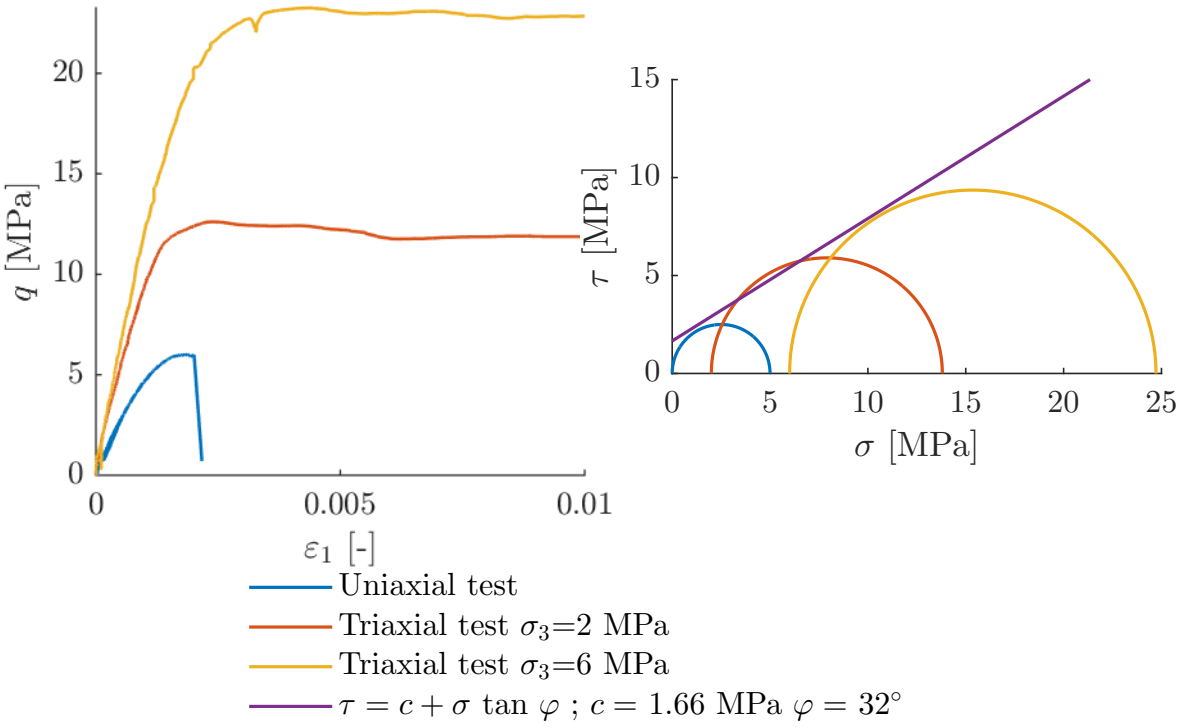

(b) Differential stress function of axial strain for experiments at various confinement pressures

(c) Mohr circles representation of the two dry triaxial tests and the uni-axial test

Figure 3.1.: Results and interpretation of one uniaxial test and two triaxial tests perfomed on samples from OPT site

drivability in such rocks.

Table 3.3 summarises the different piles tested giving their key dimensions and their installation method. Table 3.4 summarises for each pile the installation procedure and the corresponding type of test.

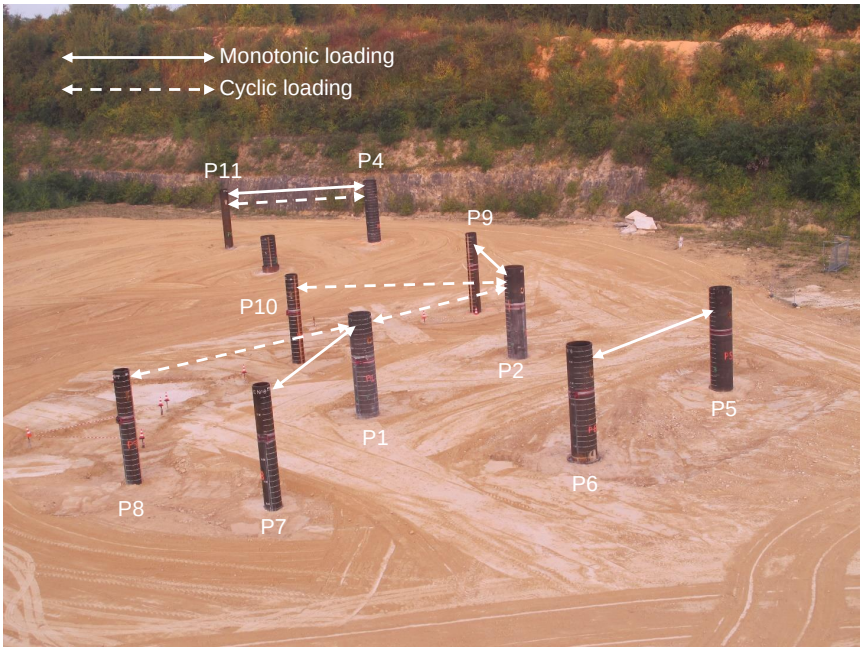

Figure 3.2.: Piles layout

Table 3.3.: Pile characteristics

	P1*	P2*	P3	P4	P5*	P6**	P7***	P8	P9	P10	P11****
D [m]	1.2	1.2	1.2	1.2	1.2	1.2	0.762	0.762	0.762	0.762	0.762
t [mm]	35	35	25	25	35	35	35	35	35	35	35
L [m]	4.2	3.3	6.0	4.2	3.2	3.2	2.7	2.7	2.0	2.0	3.0
L_{tot} [m]	9.7	8.7	11.2	9.7	8.7	8.7	8.2	8.2	7.5	7.5	8.5
			Driven			Drilled & Grouted			Driven		Drilled & Grouted

Notes:
D: outer diameter
t: wall thickness
L: embedded length
L_{tot}: total pile length

*: P1, P2 and P5 were drilled inside after the installation in order to install instrumentation inside the piles
**: P6 was drilled to 2.7 m then driven from 2.7 m to 3.2 m. Then, P6 was drilled inside to 3.2 m to in order to install instrumentation inside the pile
***: a pre-hole of 320 mm was performed to 2.7 m before the pile was driven
****: P11 was drilled to 3.3 m (i.e. 0.3 m of grout below the pile toe)

Table 3.4.: Summary of the tests

Tested piles	Type of test
P11 & P4	Fine tuning + Monotonic
P5 & P6	Monotonic
P9 & P2	Monotonic
P7 & P1	Monotonic
P8 & P1	Cyclic
P10 & P2	Cyclic
P1 & P2	Cyclic
P11 & P4	Cyclic

3.1.3 Load frame and monitoring

Load frame

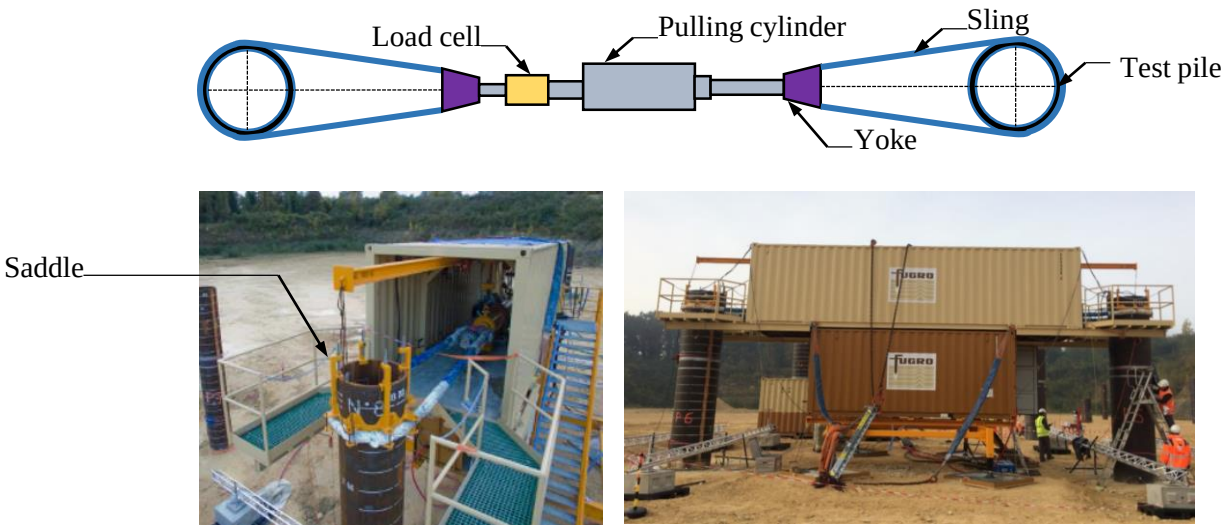

Figure 3.3.: Description of the different elements constitutive of the pulling assembly

The load frame is composed of an assembly of two containers mounted on a support frame. The pulling assembly is composed of (Figure 3.3):

- One **pulling jack** with a maximum load capacity of 2 500 kN;
- Two **yokes** that enable the pulling load to be transferred to the slings;
- Two **slings** that transfer the load to the pile, each sling going around one pile. The advantage of the use of slings is that it offers the possibility to unload the pile to almost zero loading, that it automatically aligns itself to the axis of loading and that it enables to load the pile homogeneously around the circumference of the pile;
- Two **saddles** placed on the loaded pile, defining the height of the loading application with each sling lying on one saddle.

The top container is positioned on a support frame and on four 1.5×1.5 m pads to limit the effect of the frame self-weight on the soil near the loaded piles. The nominal eccentricity of the loading is of 5 m, which in terms of normalised load eccentricity $M/(H\ D)$ leads to values ranging from 4 to 6.5 which is representative of wave loading (Byrne et al., 2015a). The as-built eccentricity are show in Table 3.5 for different tests.

Table 3.5.: As-built loading eccentricity for different tests

Tested piles	Pile → eccentricity	Pile → eccentricity
P11 & P4	P11 → 5.00 m	P4 → 4.96 m
P5 & P6	P5 → 5.05 m	P6 → 4.97 m
P9 & P2	P9 → 5.00 m	P2 → 4.89 m
P7 & P1	P7 → 5.00 m	P1 → 4.64* m
P8 & P1	P8 → 5.00 m	P1 → 5.07 m
P9 & P2	P9 → 5.00 m	P2 → 5.06 m
P1 & P2	P1 → 5.00 m	P2 → 5.01 m
P11 & P4	P11 → 5.00 m	P4 → 4.96 m

* Some backfill was still present near pile P1 so that the actual lever arm is higher than this value

Sensors

The monitoring system was designed to get the maximum information for assessing global load displacement behaviour (measurements above the ground level) and local soil structure interaction (measurements below the ground level). Figure 3.4 shows the nominal locations in the section of the different sensors; these locations can vary due to installation tolerance.

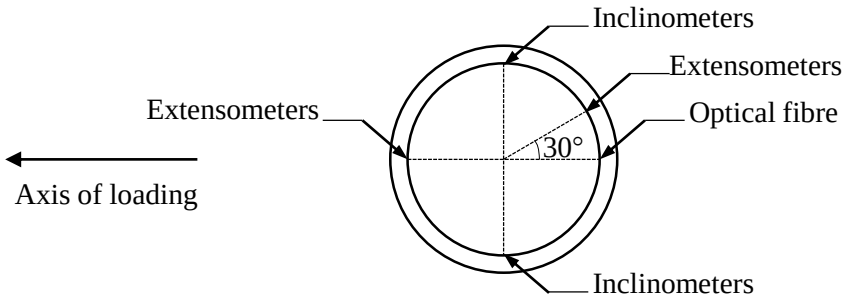

Figure 3.4.: Location of the sensors in the pile section, the optical fibre gauges are spaced every 0.5 m, the inclinometers and the extensometers are spaced every 1 m

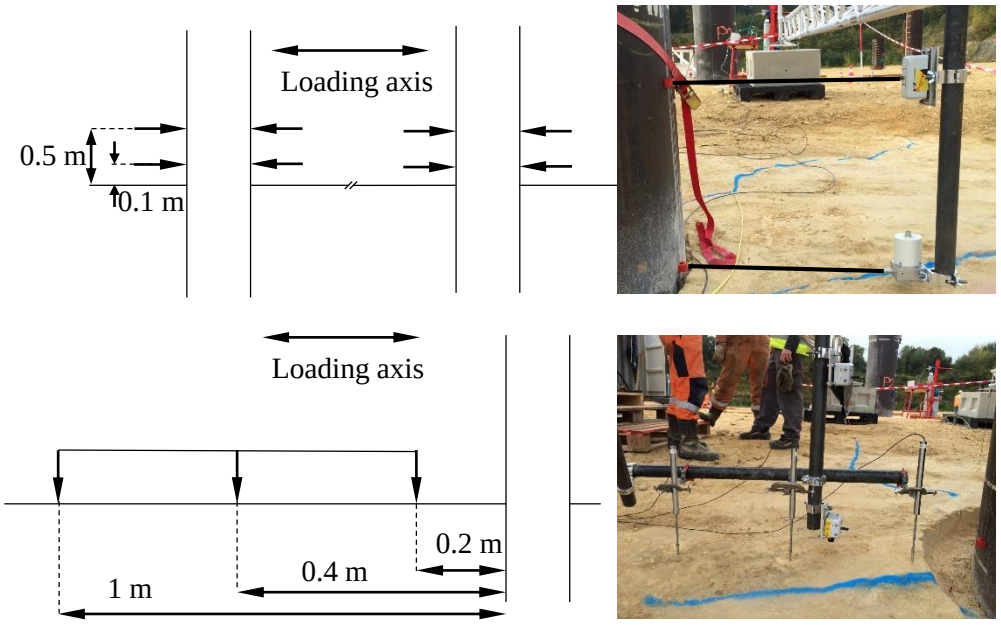

Figure 3.5.: Locations of lateral and vertical displacements measurements above the ground surface

The **vertical strains** of the pile at discrete points were measured with optical fibre gauges and extensometer chains. Optical fibre chains were installed in a 5 × 5 mm groove. Even if each chain included three temperature sensors to correct the effect of temperature changes on recorded strains, it appeared that these sensors were not working properly (the temperature measurements were affected by the loading). This is why, the measurements from the optical fibre were processed assuming a constant temperature during the test. Therefore, the measured strain values might be affected by possible temperature changes during the test. However, the variation of temperature deeper in the ground is expected to be small.

The anticipated variation in temperature should not exceed 10°C above the ground level, and 5°C below the ground level. For the considered optical fibre gauges a variation of 5°C (respectively 10°C) leads to a variation of the measured stress of 8 MPa (respectively 16 MPa). Thus, for a given pile the errors can be estimated and they decrease with increasing lateral force applied. The orientation of the optical fibre compared to the loading axis can vary depending on the pile tested, but for most of the piles the optical fibre is located on the tensile side of the pile. The optical fibre gauges were spaced every 0.50 cm. The purpose of the extensometer chains was to control the strains in the pile recorded by the optical fibre. The extensometers were used only for two tests with the chains located on the compression side of the pile with sensors installed every meter. Three different methods described in section 2.2.4 were implemented in order to deduce the $P-y$ curves from the measurements of the optical fibre gauges (the high order polynomial curve fitting, the cubic and quintic spline method and the weighted residuals method). Howeer, for all these implemented methods, when back-calculated the equilibrium of forces and bending moments from the calculated reaction, the relative errors were higher than 10 $\%$ for different piles. Thus, there was no confidence in the $P-y$ curves deduced from these methods, and they cannot be used in the $P-y$ curves approach. The feedback from this work is that there was not enough measurements along the length of the pile (one measurement every 50 cm).

The **inclinations** of the pile at discrete points were measured with the inclinometers. The chain of inclinometer sensors were inserted in casings fixed inside the pile at 90° and 270° of the loading axis (i.e. on the neutral axis). The sensors were placed every meter with the first inclinometer located at 50 cm above the bottom of the pile. It must be noted that the inclinometers were only used for two tests.

The **lateral displacements** of the pile above the ground level were measured with four potentiometer sensors per pile and with the topographic measurements. Figure 3.5 shows the nominal locations of the LVDTs; it was not always possible to place the sensors at the required locations and the acutal positions of the sensors (i.e. as-built positions) are specified in the graphs if they differ from the nominal locations. The four potentiometer sensors were attached to an aluminium frame resting on concrete blocks and fixed to the pile with magnets. The aim of the sensors was to monitor horizontal displacements of the pile in the direction of the loading axis on both sides (tensile side and compression side) near the ground level (around 10 cm and 50 cm above the ground level). Due to the rotation of the pile, the displacements measured by potentiometers are a combination of the horizontal and the vertical displacements of the pile (cf. Figure 3.9). Yet, the scale of the displacements measured (usually below 10 mm and always below 100 mm) allowed to reasonably ignore the vertical component of the displacement. The range of the sensors selected for the data measurement were 50 mm, 125 mm and 250 mm with a repeatability of 0.15 $\%$ of the full scale (i.e. 0.1 mm, 0.2 mm and 0.4 mm respectively). Three optical targets were installed on each pile near ground level, at mid-level and near the point of application of the load.

The **vertical displacements** of the rock near the pile were measured using 3 LVDTs at around 20 cm, 40 cm and 1 m away from the pile edge on the compression side (see Figure 3.5).

The **applied lateral load** was measured with the load cell mounted on the axis of the jack and the **axial displacement** of the jack axis was also monitored. The load applied to the piles is recorded with an accuracy of 5 kN.
Almost all the sensors were logged in real time using the data logger acquisition units allowing to synchronise all the records. The LVDT for the vertical displacement measurements of the rock near the pile were not synchronised with the rest of the measurements. Finally, the sign convention used for the different sensors is given in Table 3.6.
In this thesis a focus is done on the interpretation of the potentiometers measurements (i.e. the global response).

Table 3.6.: Sensors sign convention

Measurement	Positive	Negative	Remark
Elevation	Below the ground level	Above the ground level	-
Orientation	Anticlockwise	Clockwise	0° refers to the tensile side of the pile and 180° to the compression side
Lateral displacement	Towards the load frame	-	Displacements are initialised to zero at the start of the test
Inclination	Towards the load frame	-	All the inclinations are positive
Strain	Compression	Tension	-

3.1.4 Testing programme

The monotonic tests aimed at assessing the initial stiffness response and the ultimate response (i.e. failure). The main purpose of the cyclic tests was to load the pile in similar ways as in offshore conditions and assess the susceptibility of such rocks to cyclic degradation.

Offshore loading conditions

To ensure that loads applied on the onshore piles are representative of the offshore loads, time series from Saint-Nazaire project have been studied. Loads and moments in the time series were considered at the mudline. The design situations and load cases are defined in IEC (2009). The design load cases are defined in the norm in which for each design load case the conditions to consider are specified (wind, marine, electrical and other external conditions). The analysis showed that the design load case (DLC) 6.2a_idling gives the highest values of moment and force. It is the ultimate loading considered thereafter. The ultimate loading of the pile is considered to correspond to the factored highest value encountered in DLC 6.2a_idling with a safety factor that equals 1.35 (i.e. $F_{ult} = 1.35\ F_{\text{DLC 6.2a}}$), which

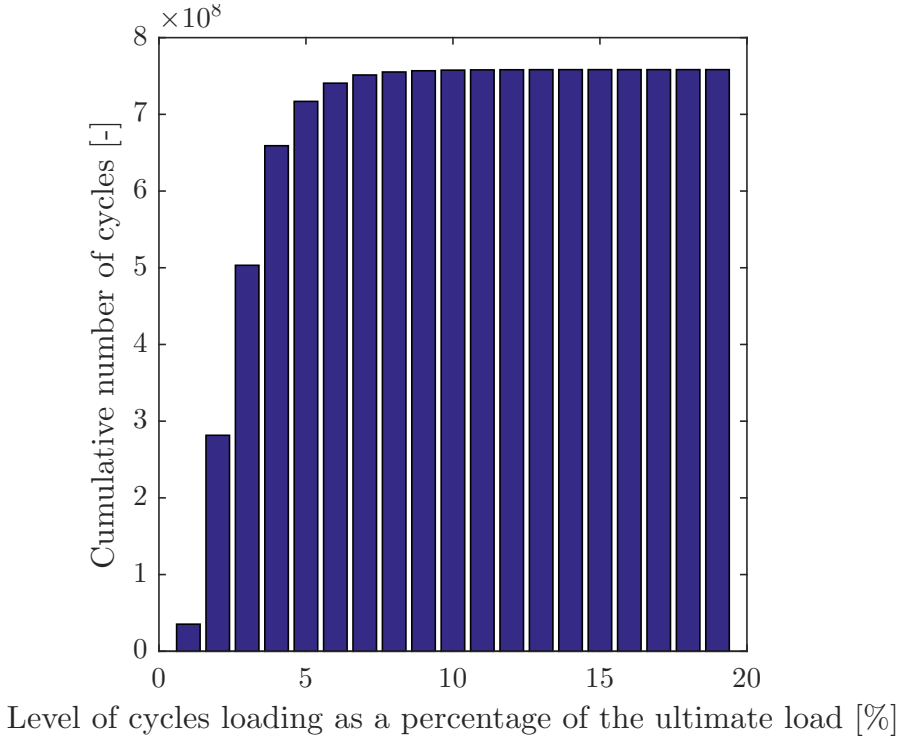

Figure 3.6.: Cumulative number of cycles for different level of loading expressed as a percentage of the defined ultimate load (rainflow analysis SLS)

is a conservative assumption. Then, the DLC 1.2 is identified as the DLC that represents operational conditions of the OWT and is considered as the serviceability limit state (SLS). This DLC considers a power production of the turbine with a normal turbulence model, a normal sea state and a normal water level range above the mean sea level. For these two DLC the moments around the fore-aft direction and the side-side directions (see Figure 4.21) are identified as the reference for the testing programme. As the load applied during the OPT is unidirectional, and as the two moments are of the same order of magnitude, only one of them is considered in the following.

Rainflow analysis is commonly applied to count cycles in a complex and irregular loading in which cycles are defined as close-loops (Downing and Socie, 1982). Usually, the outputs are presented in the form of a Markov matrix that gives the number of cycles counted for a given list of the mean value and a given list of the amplitude value that define a cycle. A Weibull distribution for wind speeds is assumed to deduce the probability of occurence for different scenario of the SLS (assuming that this SLS occurs during all the lifetime of the turbine: 25 years). The rainflow analysis was made on one of the overturning moments. The quantity of interest is the level of loading of the cycles which equals the mean value plus half of the amplitude expressed as a percentage of the ultimate loading of the monopile. Figure 3.6 shows the result of this rainflow analysis. The figure shows that most of the cycles occur done for levels of loading below 5 % of the ultimate load. It can also be noted that for the levels of loading that equal 17 % and 18 % of the ultimate load, the corresponding numbers of cycles equal 760 and 125 respectively for all the turbine lifetime.

In order to be able to draw useful conclusions at the end of the OPT, it is necessary to compare operational offshore conditions (see above) and what is doable during OPT. Indeed, it is impossible to reproduce the whole lifetime loading (25 years) during the tests. Consequently, an equivalent damage with higher load amplitude was targeted to reproduce the operational conditions. The formulation given in Puech and Garnier (2017) and recalled in Equation 2.7 is used to deduce the level of loading targeted during OPT. Assuming that the operational conditions apply during all the wind turbine lifetime, the structure will be loaded with around 10^9 cycles and the ratio considered in Equation 2.7 H_c/H_{max} is around 5 %. However, during the OPT a limited number of cycles can be achieved (around 5 000). Thus, to reach the same order of magnitude of the accumulated displacements as for OWT with fewer cycles, the levels of loading of the cycles have to be higher and ranging between 10-30 % of the ultimate load. This assumption was assessed retrospectively (see section 3.2.1) in order to validate the testing programme.

Monotonic testing programme

Figure 3.7 illustrates an example of a monotonic testing programme. The load was increased in steps equal $1/10^{th}$ of the predicted ultimate load. The load was maintained constant during a certain amount of time to see if some creep phenomenon occurs and at which extent. The amount of time for which the load is maintained is expressed in minutes in Figure 3.7. This period was also necessary to perform the topographic measurements. To explore the increase in soil stiffness during loading, three unloading-reloading loops were performed during each monotonic test. These loops were performed at milestone loads around 30 % and 70 % of the predicted ultimate load and at the maximum load. It was assumed that by performing relatively few loops, the ultimate strength was not significantly altered. A small displacements unloading-reloading loop was also imposed to assess the instrumentation performance at the beginning of the test. Monotonic tests were carried out until reaching one of the following thresholds: either the displacement at the ground level reached 10 % of the pile diameter or 80 % of the steel yield stress was reached somewhere in the pile. The loading/unloading minimum rate imposed by the load frame equals 2 mm/s. Considering this value, monotonic test duration is around 2 hours, which is not too long. The minimum loading rate was thus used. The objective was to have at least one measure per millimetre of displacement at the level of loading. Thus, a sampling frequency was taken at 2 measures per second in order not to miss the displacement variation at the ground level. The Abbs (1983) method (see Appendix A.1) was used to calibrate the loading programme and the range of measurement of some sensors. Three analyses were made using OPILE software according to three different soil modelling (upper bound, best estimate and lower bound).

Cyclic testing programme

The load frame imposed that only one-way loading was possible. The pulling jeack imposed the shape of the cycles (triangular shape). For each load stage, the maximum cyclic load

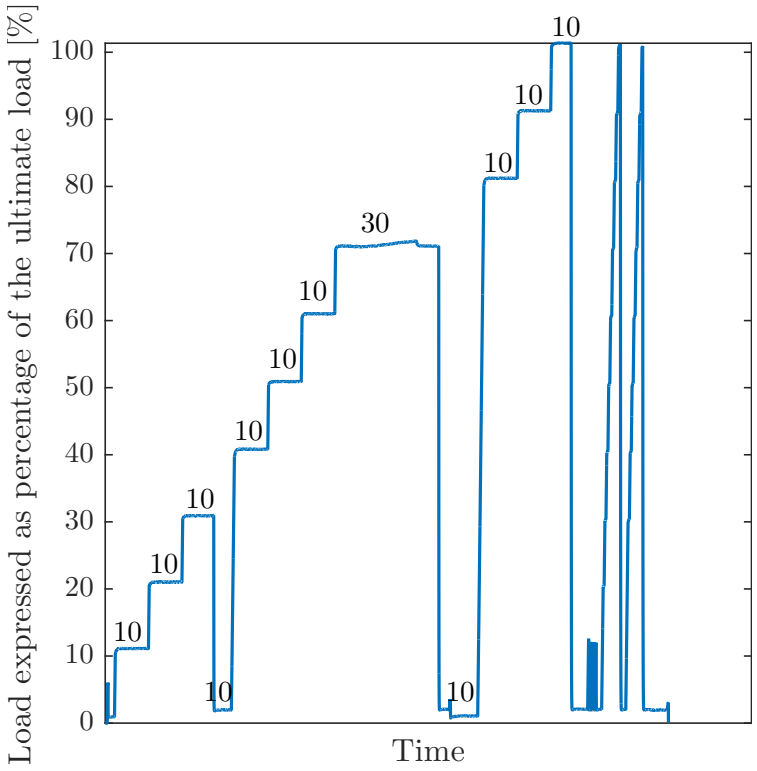

Figure 3.7.: Example of static testing programme, duration for which the load is maintained is expressed in minute on the graph.

is expressed as a percentage of the estimated ultimate load from the corresponding monotonic test performed on a similar pile (same dimension and same installation procedure). Figure 3.8 illustrates an example of a typical cyclic testing programme. However, some variations can be observed for each individual tests. Several types of response were tested during the cyclic tests:

- Response under loading equivalent to SLS loading, around 20-30 % of the ultimate load as identified during the study of offshore loading. The idea is to perform most of the cycles under this value and see how displacements accumulate.
- Response under loading equivalent to a storm event, corresponding to a ULS loading unfactored with a safety factor that equals 1.35. As it is not representative of the lifetime of the wind turbine, few cycles were made at this level.
- Response after the storm event, with the load decreasing to level equivalent to the SLS loads.
- Finally, once a cyclic test was completed the pile was tested monotonically in a similar fashion to the procedure described before but without the unloading-reloading loops and the load maintaining periods. This permitted to assess if the ultimate load was impacted by the previously experienced cycles.

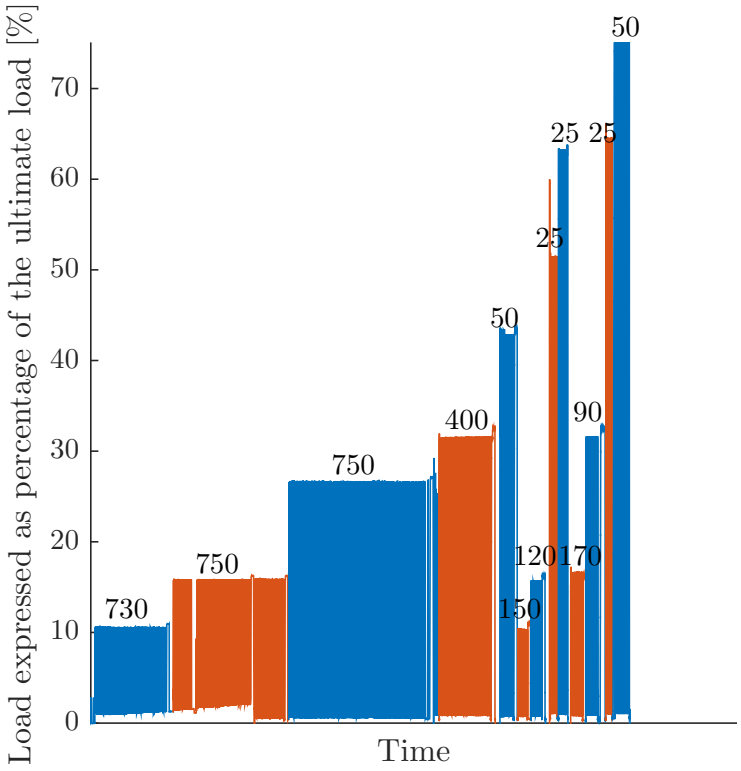

Figure 3.8.: Example of cyclic testing programme, number of cycles are expressed for each series of constant amplitude cycles

After a few series of constant amplitude cycles, the level of loading at maximum load was maintained for sufficient time to perform the topographic measurements. Period of loading observed offshore is not specially targeted even if the periods applied were similar. The objective was to perform as many cycles as possible in a fixed time allowed for the cyclic tests (i.e. 24 hours) and with the jack characteristics. The cycles period is fixed depending on the level of loading: for small levels of loading the periods will be smaller than the periods for higher levels of loading, which is representative of offshore conditions. To combine the limitations of the loading application system and the objective of doing the maximum number of cycles, the period of cycles ranges between 10 and 60 seconds. The principle was to have at least twenty measures per cycle. In accordance with the period of cycles, a sampling frequency being equal to 2 measures per second enables to achieve this goal. The number of cycles at each load stage was estimated accordingly to limit the testing time at 24 hours. The time for each cycle was evaluated by considering the time needed to reach the load targeted at each stage. The limitation of the jack was given as a maximum displacement rate. The displacements of both loaded piles and the elongation of the slings were considered to calculate the time needed for each cycle depending on the level of the loading. The displacements of both loaded piles were calculated assuming non-linear $P - y$ curves given by Abbs (1983) (see Appendix A.1) with various values of the shear strength to have an envelope and assess the variability. The elongation of the slings was calculated using the load elongation curve provided by the manufacturer.

3.2 General observations from OPT and the potential impacts on the design of a monopile

3.2.1 Description of the accumulated rotations for the fatigue design

Rotations are deduced from the potentiometers measurements with the following relation (Figure 3.9):

$$\theta = \arctan\left(\frac{y_2 - y_1}{z_2 - z_1}\right) \tag{3.1}$$

where y_1 and y_2 refer to the measurements of the two potentiometers above the ground level on the same side of the pile (tensile or compression) and z_1 and z_2 correspond to the distance from the ground level of each potentiometers considered. The various sources of errors are the position of the sensors (z_1 and z_2) and the accuracy of the measurement of the displaements (y_1 and y_2). The precision of the LVDT measurements is of 0.2 mm and no information is provided on possible operational errors. Considering only the error in the displacement measurements would lead to an error of about 0.02° on the evaluated rotation.

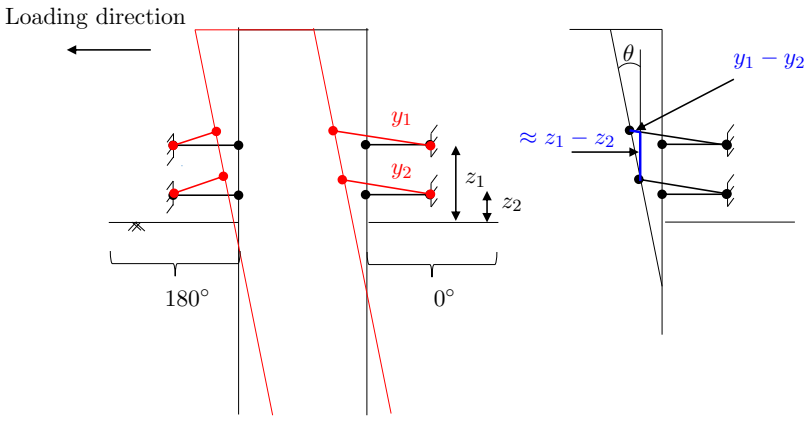

Figure 3.9.: Sketch of the potentiometers measurements above the ground level and calculation of the pile rotation from these measurements

The evolution of the accumulated rotation is evaluated in terms of the following dimensionless ratio as in Leblanc et al. (2010a):

$$\frac{\Delta\theta\,(N)}{\theta_S} = \frac{\theta_N - \theta_1}{\theta_S} \tag{3.2}$$

where θ_1 corresponds to the rotation at the maximum loading of the first cycle, θ_N refers to the rotation at the maximum loading of the N^{th} cycle and θ_S is the rotation that would occur in a monotonic test at a level of loading equivalent to the maximum loading of the

cycles. This accumulated rotations are described for the cyclic test P10-P2. P10 is a medium diameter pile while P2 is a large diameter pile, but they have similar L/D ratios. For pile P10, θ_S is obtained from the rotation measured during the corresponding monotonic test (i.e. pile P9). For pile P2, θ_S is obtained from the rotation measured of pile P2 when it was tested towards pile P9. The values of θ_S are given in Table 3.7 for both piles and for the different series of cycles considered in the following fittings. The maximum level of loading for each series of cycles corresponds to different ratios when considering the dimensionless ratio F_{max}/F_{ult} in which F_{max} refers to the maximum level of loading of cycles and F_{ult} refers to the monotonic ultimate loading. For P9, the test was performed up to failure and the ultimate load F_{ult} is 1 000 kN. Assuming a hyperbolic tangent $P-y$ curves (i.e. $P(y) = P_u \tanh k\, y/P_u$), the ultimate reaction P_u is determined as the value which leads to the same ultimate load as those observed in P9 monotonic test. It is assumed that this value essentially depends on the ground and in a lesser extent to the diameter of the pile and the installation process. For simplicity it is thus assumed that these $P-y$ curves can be considered for all the pile and are used to estimate the ultimate load F_{ult} of each pile. This quantity is only used for presenting the results in dimensionless form F_{max}/F_{ult}. The ultimate load estimated with this method for pile P2 is around 3 000 kN.

Table 3.7.: Values of θ_S for piles P10 and P2

Pile	Angle	Elevation (above G.L)	Level of loading 100 kN	200 kN	300 kN
P10	0°	0.30 m	0.09 °	0.19°	0.29°
P2	0°	0.30 m	0.02 °	0.05°	0.08°

Logarithmic fitting

The formulation suggested by Lin and Liao (1999) and modified by Puech and Garnier (2017) (see Equation 2.7) gives an evolution of the accumulated displacements proportional to $\ln N$. The cyclic testing programme was based on this formulation. Accordingly, the accumulated rotation is fitted with the following expression:

$$\frac{\Delta\theta\ (N)}{\theta_S} = \beta \ln N \tag{3.3}$$

The results of this approximation are shown in Figure 3.10 for two different piles tested together. For each series of cycles and for each pile, the values of the parameter β fitted and the coefficient of determination are given in the legend. As can be seen in Figures 3.10, a good fit is obtained for $N < 25$ but the extrapolation for higher number of cycles leads to an underestimation of the accumulated rotations except for the first series of cycles for P2. It can be seen that the dimensionless parameter $\Delta\theta/\theta_S$ is higher for pile P2 than for pile P10. This is explained by the fact that θ_S for pile P2 is lower than for pile P10 by around 70 %. Consequently $\Delta\theta$ is, as expected, higher for pile P10 than for pile P2. Besides, Leblanc et al. (2010a) showed that the logarithmic approximation was valid for

$N < 100$ but underestimated the results for $N > 500$ for similar ratios of F/F_{ult} explored. When considering the OPT results the logarithmic approximation is valid for $N < 25$ with a coefficient of determination (R^2) above 90 % but falls around 50 % when considering the first 100 cycles. Thus, this means that the used of a logarithmic law is not a good approximation for those conditions. Finally, these plots show that the previous series of cycles have an impact on the results, as the parameter β decreases for increasing values of F/F_{ult}.

Fitting with a power-law function

Similarly to what was achieved by Leblanc et al. (2010a), a better fit is obtained if the accumulated rotations are modelled as a power function of the number of cycles N:

$$\frac{\Delta\theta\ (N)}{\theta_S} = T_b\ (N-1)^{\alpha} \tag{3.4}$$

where T_b and α are the two fitting parameters.
First, the estimation is done considering that T_b and α can vary with the applied maximum load. The results of this first fitting are shown in Figure 3.11 for the same piles as before. For each series of cycles and for each pile, the values of the fitted parameters Tb and α and the coefficient of determination R^2 are given in the legend. This figure illustrates that the approximation fits very well the data ($R^2 > 90$ %). Similarly to what was observed when considering the logarithmic fitting, the successive series of cycles seem to have an impact on the following cycles. Indeed, the α parameter increases whereas the T_b parameter decreases with increasing values of F/F_{ult}. Considering only the first series of cycles for each pile (to avoid the loading history effects), the mean value of α of 0.27 is considered and a new fitting is obtained. For comparison, the value of α fitted by Leblanc et al. (2010a) is 0.31. Strains appear to accumulate less rapidly in terms of number of cycles in soft rocks as compared to sand. Figure 3.12 shows the results of this second fitting assuming a constant value of α, leading to a reasonable approximation for the first two series of cycles but not for the third one. The power law fitting permits the accumulated rotation to be assessed for $N > 100$.

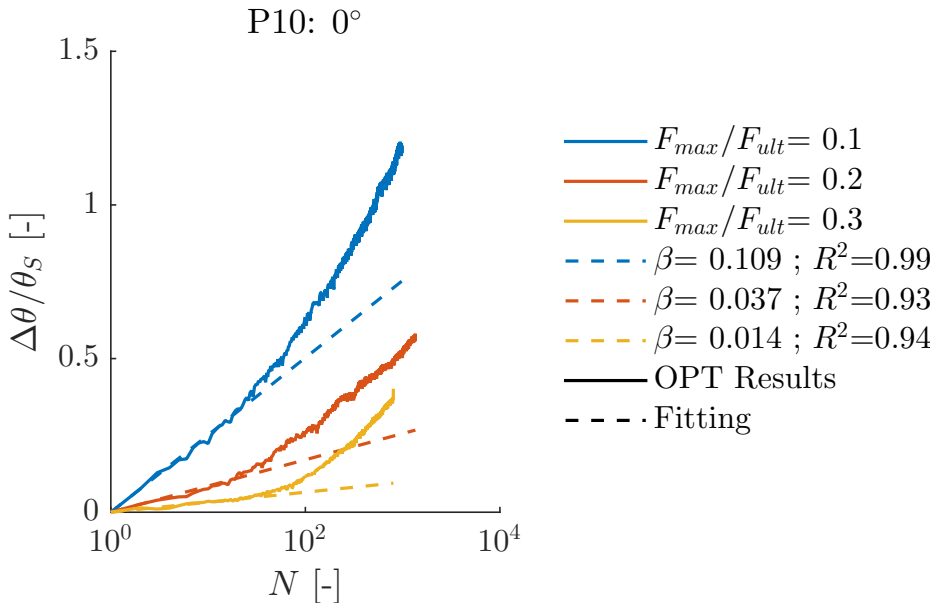

(a)

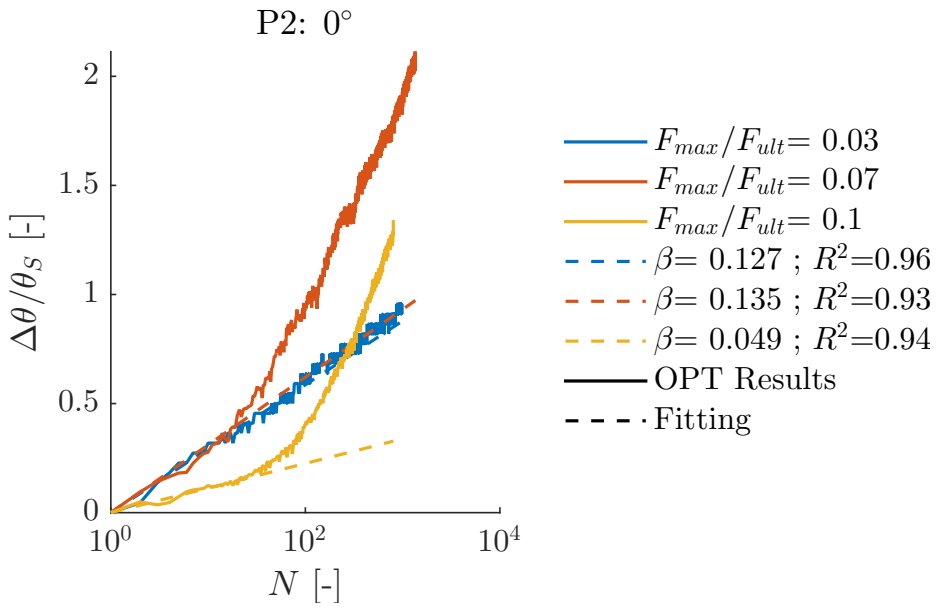

(b)

Figure 3.10.: Results of the fitting using Equation 3.3 for the accumulated rotations measured for pile P10 (top) and pile P2 (bottom)

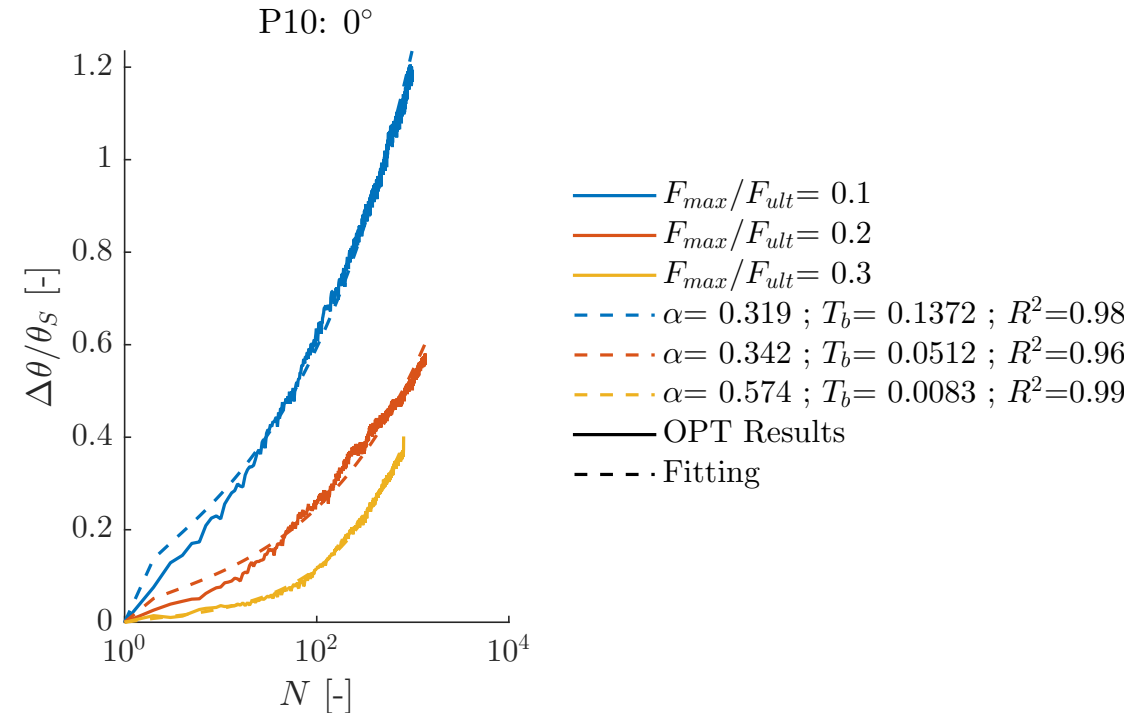

(a)

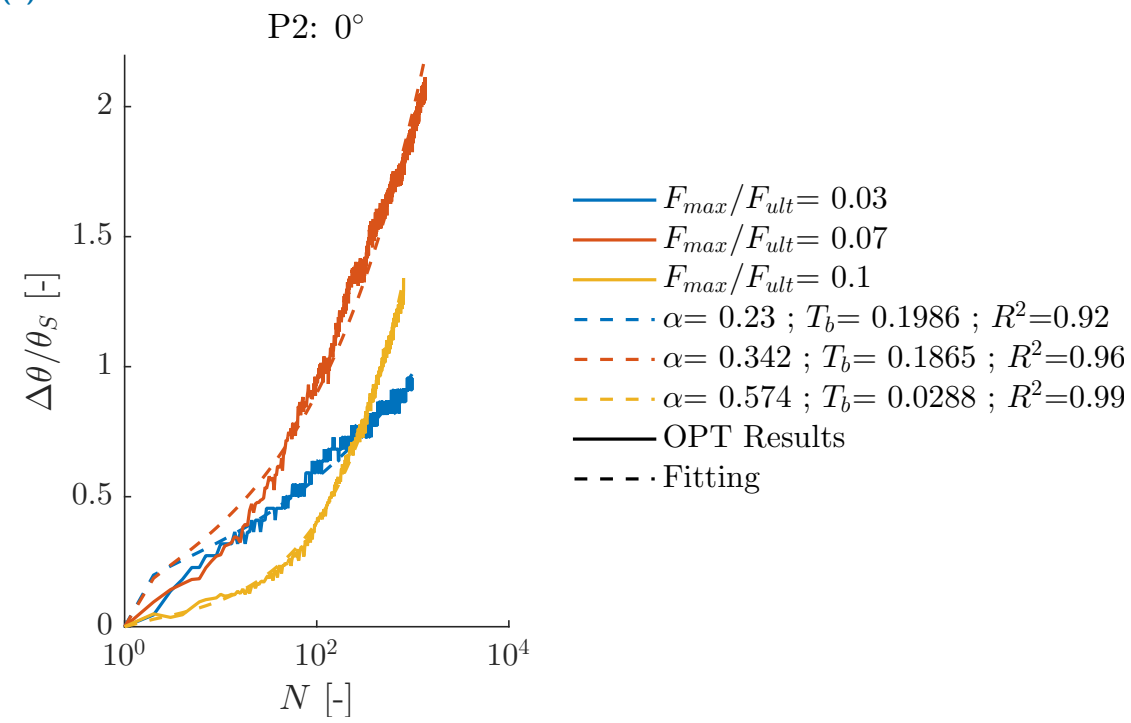

(b)

Figure 3.11.: Results of the fitting using Equation 3.4 for the accumulated rotations measured for pile P10 (top) and pile P2 (bottom)

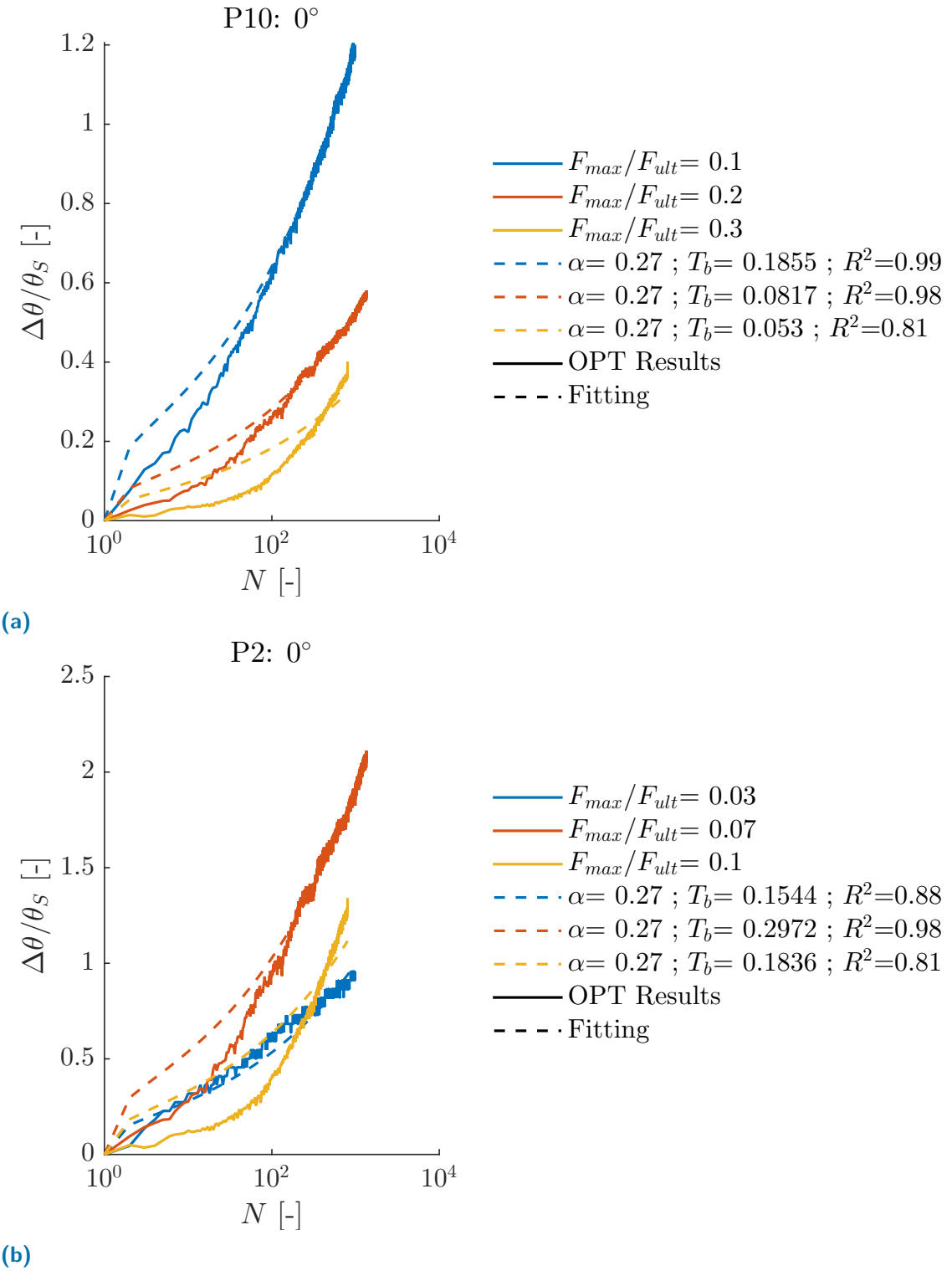

Figure 3.12.: Results of the fitting using Equation 3.4 and $\alpha = 0.27$ for the accumulated rotations measured for pile P10 (top) and pile P2 (bottom)

Validation of the cyclic testing programme

During the definition of the cyclic programme, the logarithmic function was used. Although according to the OPT accumulated rotations, the logarithmic fitting leads to an underestimation of the accumulated rotations. This is why the power law fitting is used afterwards to validate the cyclic programme. A posteriori a number of cycles of 10^9 seems a bit high. Leblanc et al. (2010a) recommended a number of cycles of 10^7 for the fatigue design, which is considered thereafter. T_b is assumed to be proportional to the ratio of the ultimate load as it is found in Leblanc et al. (2010a). Using the previously fitted power-law for P2: 10^7 cycles at around 5 $\%$ of the ultimate load would be equivalent to few thousands cycles at around 30 - 40 $\%$ of the ultimate load. Nevertheless, the cyclic tests were performed with few thousands cycles at around 10 - 30 $\%$ of the ultimate load which would be equivalent of applying 5×10^5 cycles at 5 $\%$ of the ultimate load. Thus, it can be said that the cyclic testing programme is roughly representative of what will be encountered offshore.

3.2.2 Crushed zone induced by the driving process

During the driving procedure a ring of highly compacted crushed rock is created all around the pile. Field observations only allow observation of the crushed rock at the surface and no information is provided on the repartion of this crushed rock with depth. It is observed at the ground surface that the thickness of this zone is of the same size as the thickness of the pile and it is constant around the pile. Some samples were taken from the site in order to characterise their mechanical properties in the laboratory. Figure 3.13 shows the crushed rock retrieved on site. Note that the retrieved samples have been previously subjected to

Figure 3.13.: Picture of the crushed rock retrieved on site

one lateral load test. The crushed rock appears as a cohesionless material with very small particles (few microns). For the tests the material was sieved in order to keep only the particles with a size smaller than 1.6 mm, to be consistent with the size of the testing device. As the tests were performed in dry conditions the samples were first dried in an oven during 24 hours at 60°C. The grain size distribution is shown in Figure 3.14 (see also Table 3.8).

Table 3.8.: Passing diameter for the crushed rock deduced from the grain size distribution test

Passing diameter
$D_{10\ \%} = 0.054$ mm
$D_{50\ \%} = 0.303$ mm
$D_{90\ \%} = 1.100$ mm

The in situ density of the crushed rock is unknown. Laboratory tests have been performed on reconstituted dense samples, a density of 1 600 kg/m^3 for oedometric tests and densities of 1 550 and 1 800 kg/m^3 have been used for direct shear tests. Specimens were prepared in a oedometric cell with a diameter of 38 mm and a height of 20 mm. A uniaxial strain test was performed at a controlled displacement rate of 6×10^{-3} mm.s^{-1} with unloading and reloading loops to evaluate the current oedometric modulus in the unloading part of each loop (see Figure 3.15) up to a maximal axial stress of 23 MPa. In Figure 3.15,

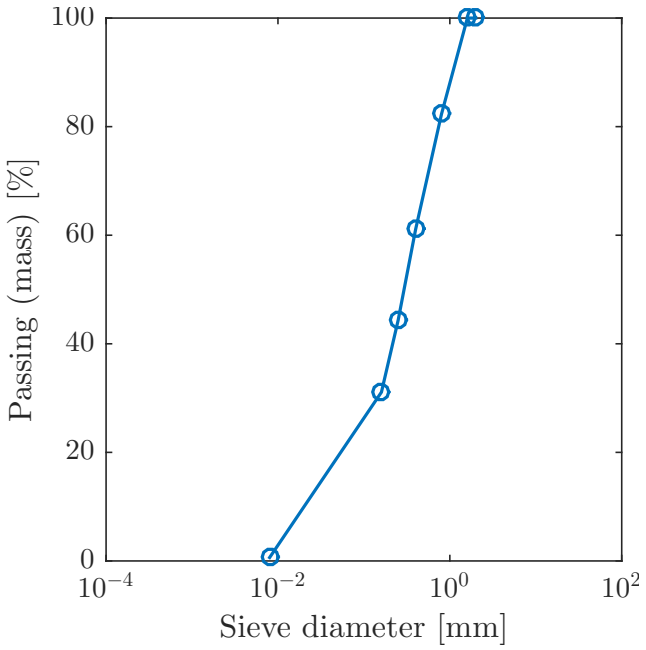

Figure 3.14.: Grain size distribution results of the crushed rock

3.16 and 3.17 compression stresses and compression strains are considered positive. This modulus is representative of the lateral stiffness of the crushed zone around the pile. The oedometric test shows the highly noon-linear character of the stress-strain curve. The tangent oedometric modulus values at low normal stresses are evalutaed and showed in Figure 3.17. The test is performed in a much larger range of stresses than what is expected around piles for serviceability limit state. Assuming a Poisson's ratio of 0.3, the Young's modulus of the crushed rock for an axial stress of 2 MPa equals 210 MPa. Thus, the ratio between the elastic modulus of the crushed rock over the elastic modulus of the intact rock is around 0.04 (assuming a Young's modulus of the rock of 5 GPa cf. section 3.1.1). The representativity of the crushed rock modulus is discussed in chapter 4. Taking samples of crushed rock around different piles and performing several oedometric tests would have permitted a better characterisation of the material.

Direct shear tests are also undertaken on the crushed rock. The aim of these tests is to have an estimation of the crushed rock friction angle. Two sets of tests are done at two different initial densities (1550 and 1800 kg/m^3). For a given initial density, three direct shear tests were done at different normal stresses, to calibrate the failure envelope (Figure 3.18). For each set of test the three data points are quite well aligned (R^2 around 80 %) and the fitted friction angle slightly increases with the initial density.

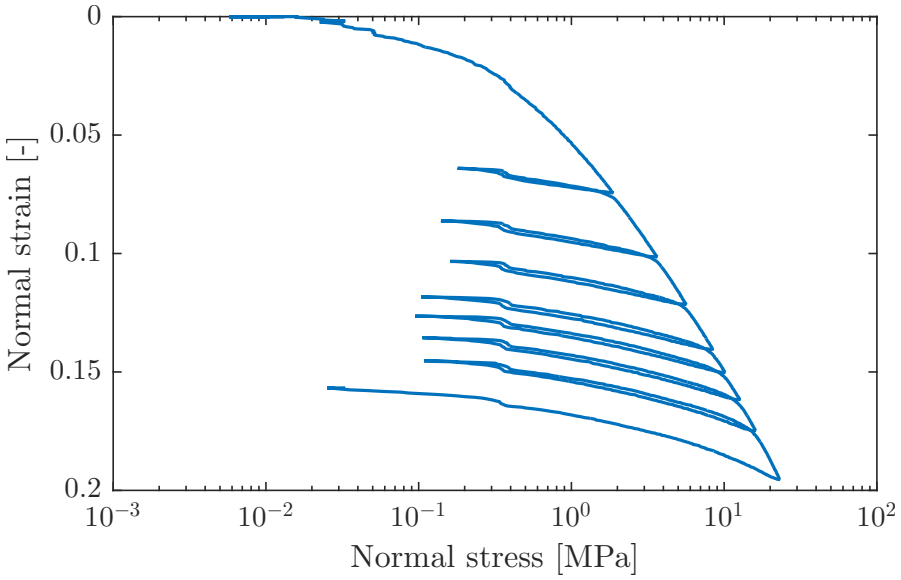

Figure 3.15.: Oedometer test results on the crushed rock

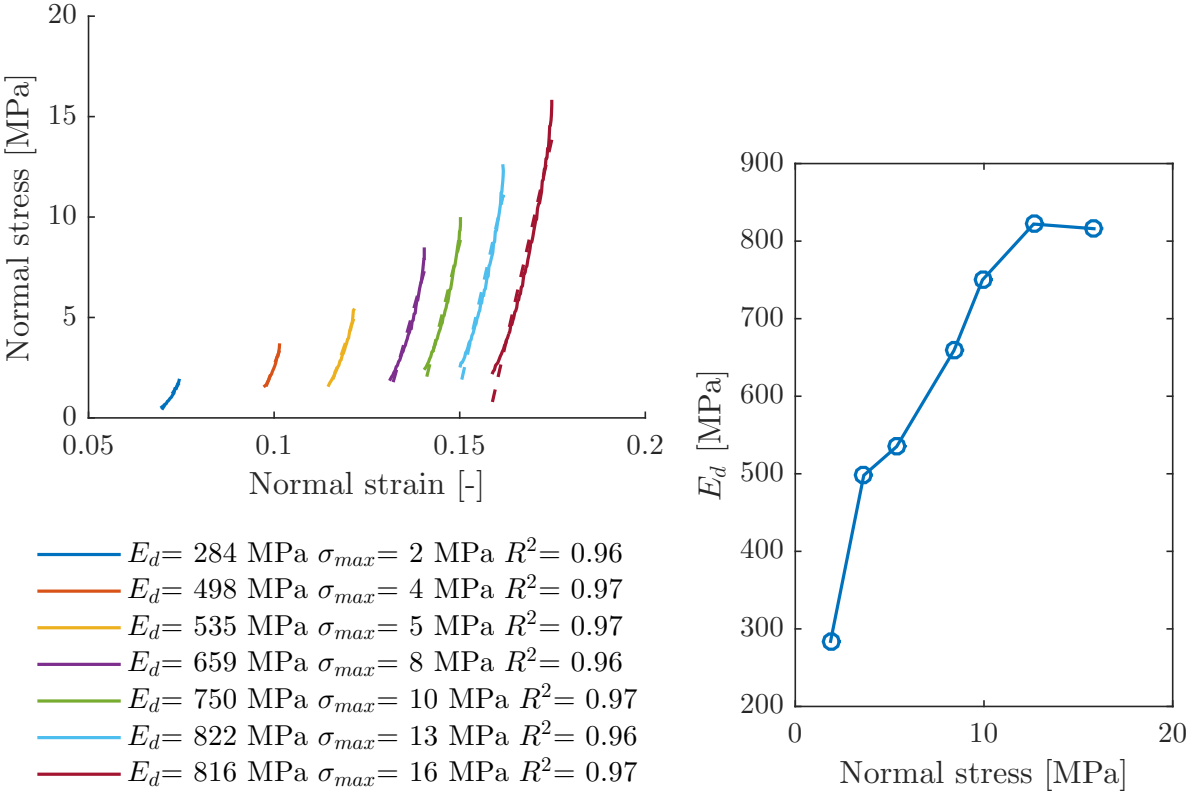

Figure 3.16.: Evaluation of the eodometric modulus of the crushed rock at various loads

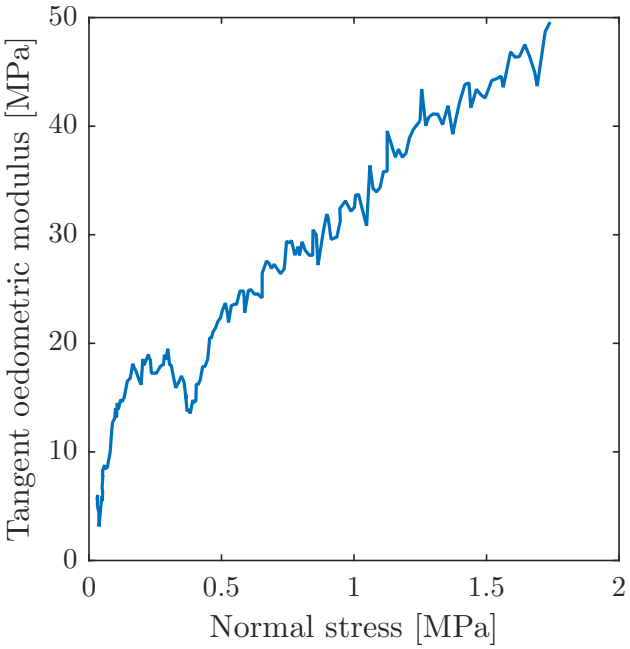

Figure 3.17.: Evaluation of the tangent oedometric modulus of the crushed rock at lows normal stresses

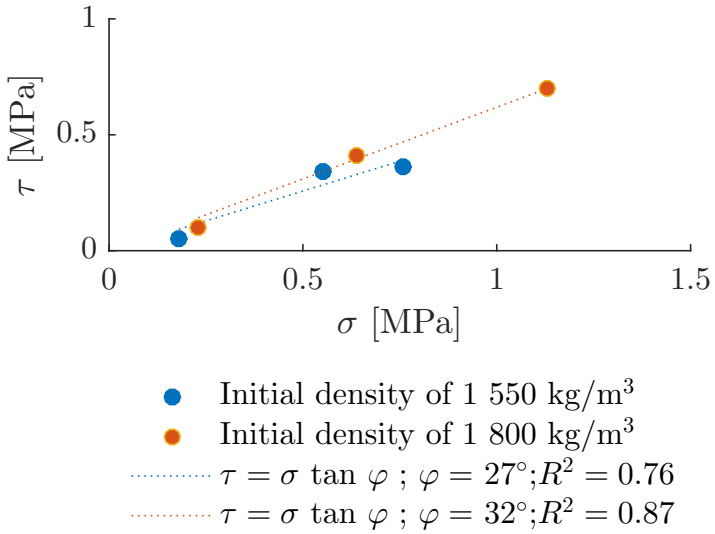

Figure 3.18.: Shear box tests results

3.2.3 Description of the stiffness evolution for the natural frequency requirement

When first looking at the cyclic tests results, it is noticed that the shape of the cycles evolved with the number of the cycles and the level of loading. Therefore, the stiffness evolution is evaluated on each unloading-reloading loop.

Methodology

The fluctuations in the experimental data make the evaluation of the derivative somewhat challenging. The force dependency of the tangent lateral stiffness can be fitted with a very good approximation (cf. Figure 3.19a) using the following equation:

$$\frac{1}{K_L} = \frac{1}{K_\infty} + \left(\frac{1}{K_i} - \frac{1}{K_\infty}\right) e^{-F/F_0} \tag{3.5}$$

where F is the lateral force applied, K_i is the tangent lateral stiffness at $F = 0$, K_∞ is the maximum tangent lateral stiffness, K_L is the tangent lateral stiffness at the corresponding force F and F_0 is a parameter controlling the non-linearity of the curve. The tangent lateral stiffness is the derivative of the lateral force applied with respect to the lateral displacement $K_L = \mathrm{d}F/\mathrm{d}y$. The expression of the function giving the force-displacement curve can be evaluated by integrating Equation 3.5:

$$y(F) = \int \frac{1}{K_L}\,\mathrm{d}F = y_{ref} + \frac{F - F_{ref}}{K_\infty} + \left(\frac{1}{K_i} - \frac{1}{K_\infty}\right) F_0 \left(e^{-F_{ref}/F_0} - e^{-F/F_0}\right) \tag{3.6}$$

where the integration constant can be evaluated by knowing one point of the data $y(F_{ref}) = y_{ref}$. The three model parameters (K_i, K_∞ and F_0) can be fitted separately for both the unloading and the loading part of the force-displacement cycle. This is done by using a Matlab integrated non-linear numerical solver. Following the same procedure for all the cycles and all the series of cycles for each cyclic test, it is possible to assess how the tangent lateral stiffness evolves. Different effects on the stiffness can be looked at: the number of cycles, the level of loading and the load history. Different stiffness are defined in Figure 3.19b and the area of the loading-unloading loop is also shown in this figure.

Implementation and interpretation

This methodology is implemented for pile P10. One of the outcomes described by Leblanc et al. (2010a) is that the secant stiffness always tends to increase with the number of cycles. However, this is not observed when analysing OPT data. Figure 3.20a shows that the secant stiffness tends to decrease with the number of cycles. It can be noted that the decrease depends on the applied maximum load; most of the decrease for cycles at $10\ \%$ of the ultimate load occurs during the first cycles while for higher levels of loading ($20\ \%$ and $30\ \%$ of the ultimate load) the decrease occurs in a more progressive way. However, for the first cycles of each series of cycles, the secant stiffness are similar. The difference in the outcomes

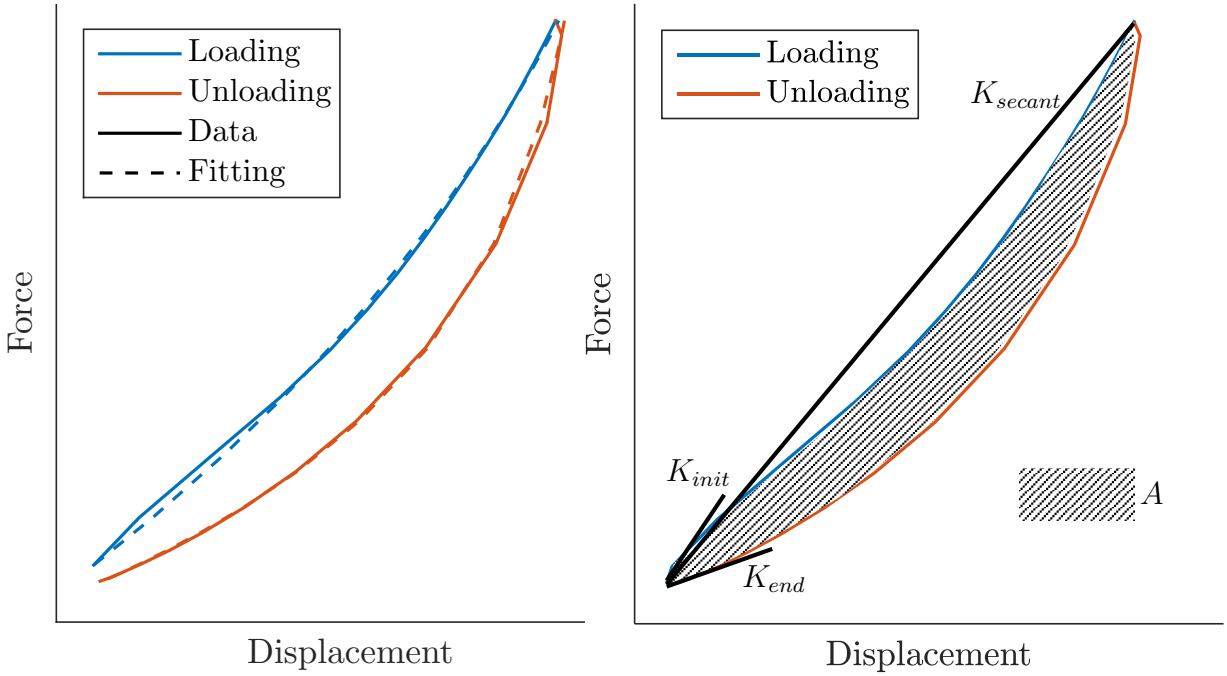

(a) Example of the comparison for one cycle between the OPT data and the fitting using Equation 3.6 for both the loading and the unloading part

(b) Definition of the secant stiffness (K_{secant}), the tangent initial stiffness (K_{init}), the final initial stiffness (K_{end}) and the area of the loading-unloading loop (A)

Figure 3.19.: Sketch for the anayses of the evolution of the different stiffness

can be explained partly by the difference of behaviours between sand and soft rock. Loose sand gets more and more compacted with increasing number of cycles corresponding to a stiffening of the response with increasing number of cycles. Even though in the OPT there is an annulus of crushed rock around the pile that could be seen as highly compacted fine sand, the rock beyond the annulus of the crushed rock degrades with increasing number of cycles. According to the results, the combination of the stiffening of the annulus of the crushed rock and the softening of the soft rock leads to a softening of the overall behaviour with increasing number of cycles. However, this softening does not occur endlessly, and a stabilisation is observed after a certain number of cycles. Besides, both the initial and the final lateral stiffness (cf. Figures 3.20b and 3.20c) tend to decrease with the number of cycles and to decrease with the applied loading. This evolution can be interpreted by the evolution of the extent of the gap behind the pile. Indeed, field oberservations (cf. Figure 3.21) allow detection of the presence of a gap at the ground surface but no information is provided on the depth of this gap. With an increasing extend of the gap, while the loading is close to zero there are some areas along the length of the pile that move without mobilising the soil reaction because of the gap. Therefore, the initial and final tangent stiffness decrease. However, even given these changes in stiffness (secant, initial and final), the area of the loading-unloading loop does not evolve much with the number of cycles but more with the levels of the applied loading (cf. Figure 3.20d). This indicates that for levels of loading looked at, the dissipation does not increase significantly with the number of cycles.

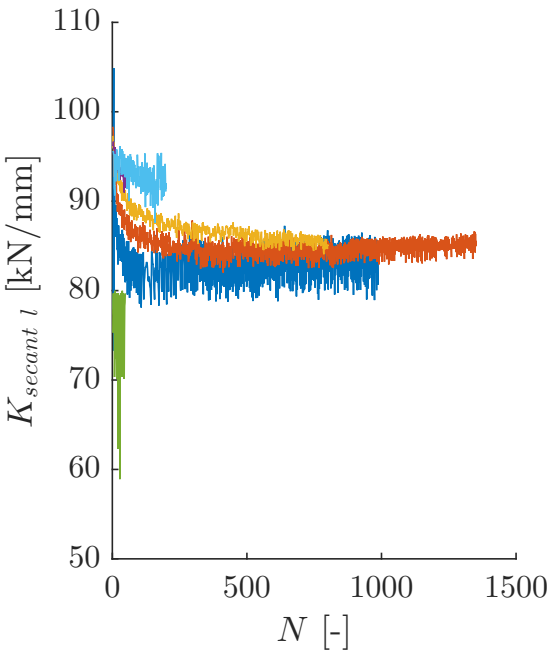

(a) Evolution of the secant stiffness

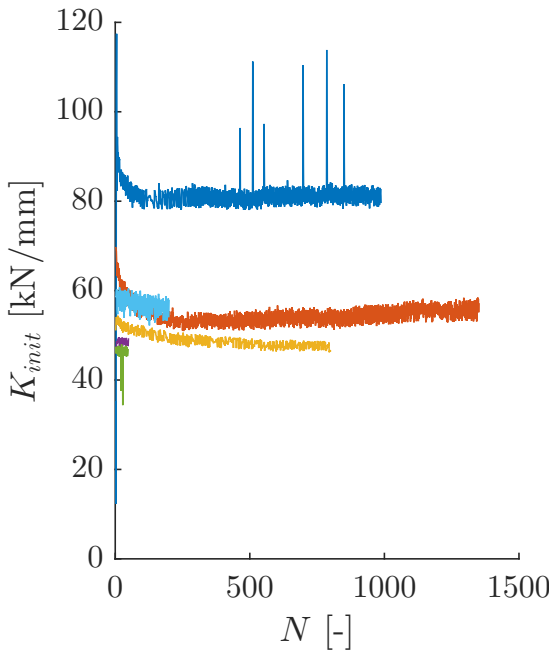

(b) Evolution of the tangent initial stiffness

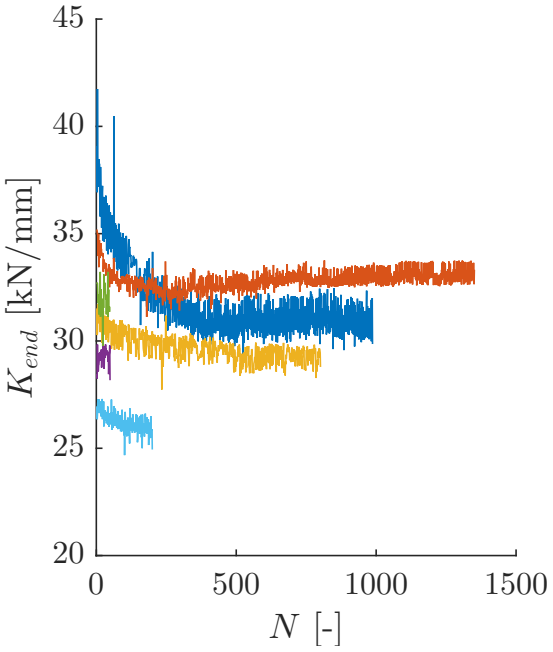

(c) Evolution of the tangent final stiffness

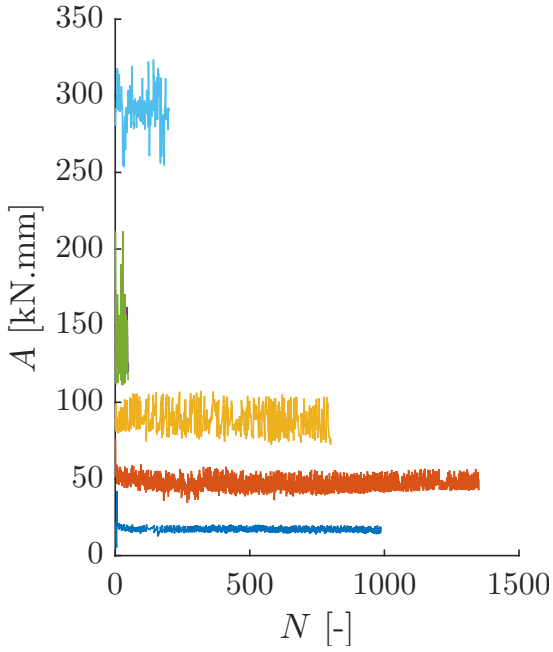

(d) Evolution of the area of the loading-unloading loops

Batch 1: F_{max}/F_{ult}= 0.1
Batch 2: F_{max}/F_{ult}= 0.2
Batch 3: F_{max}/F_{ult}= 0.3
Batch 4: F_{max}/F_{ult}= 0.4
Batch 5: F_{max}/F_{ult}= 0.3
Batch 6: F_{max}/F_{ult}= 0.4

Figure 3.20.: Evolution of different quantities of interest depending on the number of cycles for different series of cycles performed during P10 cyclic test

Figure 3.21.: Picture of the gap behind pile P2 after loading

3.2.4 Study on the rotation threshold for the long-term requirement

To respect the requirement on the long-term rotation at the mudline at the end of the OWT lifetime, a rigorous and precise evaluation of cumulative rotations generated by a very large number of cycles should be done. A brief analysis of onshore pile tests gives some useful information on:

- the kind of loading for which this threshold is achieved;
- the order of magnitude of normalised displacement corresponding to exceeding this threshold;
- the effect of cycles on exceeding this threshold.

Both monotonic and cyclic tests are looked at. Tables 3.9 (monotonic tests) and 3.10 (cyclic tests) show the order of magnitude of the loads and the lateral displacements at the ground level corresponding to exceeding the rotation threshold at the mudline during OPT. For the cyclic tests, the number of cycles after which the threshold is exceeded is also specified. It can be noted that for all the piles (except P9 and P10) the ultimate load is estimated. It can be seen from these tables that for the large piles the threshold is exceeded for higher loads than for the medium piles. It does not seem to be an effect of the L/D ratio but more an influence of the ratio of the pile diameter over the thickness of the pile tube. Though if the loads tend to be higher for the large piles, the normalised displacement at the ground level is similar. The cycles have important effects on the load corresponding to the exceeding of the threshold: the load is lower by 28 % for the cyclic test (P8) compared to the monotonic test (P7) and is lower by 50 % for the cyclic test (P10) compared to the monotonic test (P9). However, even if the cycles tend to reduce the load at which the threshold is reached, the corresponding displacements are larger by around 40 % when considering both cyclic tests.

Table 3.9.: Level of loading (expressed as a ratio of the ultimate loading) and lateral displacement at the ground level (expressed as a ratio of the pile diameter) corresponding to the exceeding of the rotation threshold of $0.25°$ at the mudline

	Threshold of 0.25° achieved for:				
Pile	F/F_{ult}	y/D	L/D	D	Installation
P5	40 %	0.50 %	2.7	1.2	driven
P6	53 %	0.44 %	2.7	1.2	drilled, driven and grouted
P7	28 %	0.45 %	3.5	0.762	driven
P9	30 %	0.46 %	2.6	0.762	driven
P11	27 %	0.35 %	4.3	0.762	drilled and grouted

Table 3.10.: Maximum level of loading of cycles (expressed as a ratio of the ultimate loading), lateral displacement at the ground level (expressed as a ratio of the pile diameter) and number of cycles corresponding to the exceeding of the rotation threshold of $0.25°$ at the mudline

	Threshold of 0.25° achieved for:					
Pile	F_{max}/F_{ult}	y/D	L/D	D	Installation	N
P8	20 %	0.64 %	3.5	0.762	driven	After 720 cycles at 200 kN and during the first cycle at 300 kN
P10	10 – 15 %	0.67 %	2.6	0.762	driven	After 980 cycles at 100 kN and during the first cycle at 200 kN

3.2.5 Cracks induced in the ground

Cracks appear during the driving procedure without obvious preferential directions. Field observations allow detection of cracks at the surface and no information is provided on the depth of the cracks. It is however not likely that the cracks extend over the entire embedment length of the pile. Some cracks appear all around the pile, as the driving procedure damages the rock all around the pile. During the lateral loading, some cracks already created during the installation procedure propagate further and some others are initiated. As opposed to the cracks created during the installation procedure the cracks due to the loading present a preferential direction. For pile P5 Figure 3.22b shows the cracks due to the pile driving in blue and the cracks induced by the lateral loading test towards P6 in orange. General $P - y$ curves approach is not suited to account for cracks onset and propagation. The approach developed by Erbrich (2004) takes into account failure at shallow depth by considering wedge cracks in front of the pile but cracks due to the installation procedure and other types of cracks propagation are ignored. Finite element modelling is necessary for exploring the effects of the cracks on the pile response.

(a)

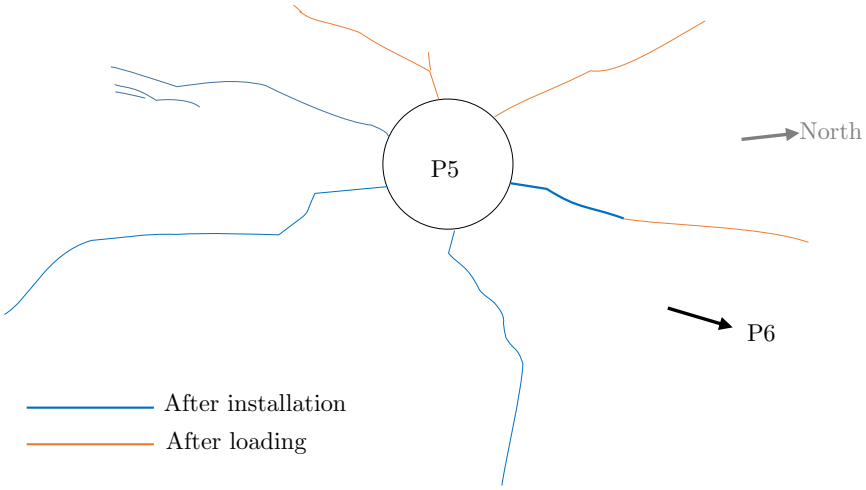

(b)

Figure 3.22.: Sketck and picture of cracks around pile P5

3.3 Conclusions

The onshore pile tests are first described in this chapter (cf. section 3.1). In general, the various instrumentations worked well except the temperature measurements of the optical fibre that would have enabled to process the vertical strain measurements. More care should have been paid to the temperature variation during the test, especially for the cyclic tests as the duration of such tests are sufficiently long to encounter non-negligible temperature variation. Besides, a new optical fibre technology exists nowadays and permits to record the vertical strain continuously. This improvement would have permitted to determine the $P - y$ curves from the tests. The methodology used to define the testing programme (for both monotonic and cyclic tests) is developed in section 3.1.4 and validated in section 3.2.1. The results presented in this chapter have highlighted the particularities of soft rock as compared to sand on the response of laterally loaded piles:

- Even though the rotation accumulation (cf. section 3.2.1) at the ground level follows the same mathematical function (power function of the number of cycles applied) in soft rock as in sand, the fitting showed that the power is lower and thus, rotations accumulate less in soft rock as compared to sand. Besides, the effect of previous loading history seems more pronounced in the case of soft rock as compared to sand.
- Driving piles in soft rock leads to the creation of an annulus of crushed rock around the pile (cf. section 3.2.2).
- Driving and loading induce cracks (cf. section 3.2.5) in the soft rock.
- Loading leads to the creation of a gap behind the pile. The extent of this gap is related to the irreversible displacements. The presence of this gap impacts the stiffness evolution (cf. section 3.2.3).

These four major phenomena have been identified as relevant to be accounted for in the design.

4 Extended semi-analytical modelling of laterally loaded pile

Summary

The semi-analytical modelling presented herein is based on the $P-y$ curves framework which is extended to account for various phenomena relevant to OWT monopile foundations. Particular emphasis is being placed on modelling the initial response accurately as the initial stiffness is a key parameter for natural frequencies analysis. Linear springs in series are assumed at each depth and this procedure is validated using OPT results for various installation procedures. The classical $P-y$ curves framework accounts neither for multi-directional loading nor for irreversible displacement and displacement accumulation due to cyclic loading. To account for multi-directional loading, the $P-y$ curves framework is extended by using multiple springs distributed around the pile perimeter. The effects of multi-directional loading are discussed using numerical results. To account for cyclic loading, the $P-y$ curves framework is enriched by adding a rheological creep model. The latter extension is validated by comparing the numerical results with data recorded in OPT.

Résumé

La modélisation semi-analytique présentée ici est basée sur la méthode des courbes $P-y$ qui est généralisée pour tenir compte des phénomènes pertinents pour les monopieux d'éoliennes en mer. L'accent est tout d'abord mis sur le calcul de la réponse initiale des pieux comme c'est un paramètre important pour les analyses fréquentielles. Une méthode considérant des ressorts linéaires en série est présentée ici et validée à l'aide des résultats d'essais de pieux (OPT). La méthode classique des courbes $P-y$ ne prend en compte ni un chargement multidirectionnel, ni des déplacements irréversibles et ni d'accumulation des déplacements due à un chargement cyclique. Pour tenir compte du chargement multidirectionnel, la méthode des courbes $P-y$ est généralisée et plusieurs ressorts autour de la circonférence du pieu sont considérés. L'étude de l'effet d'un chargement multidirectionnel est réalisée. Pour tenir compte du chargement cyclique, la méthode des courbes $P-y$ est étendue et des modèles de fluage sont considérés en série avec les courbes $P-y$. Cette dernière généralisation de la méthode des courbes $P-y$ est validée en comparant les résultats numériques avec les données enregistrées pendant les essais de pieux.

4.1 Modelling of initial stiffness

The initial part of the monotonic results is analysed to better assess the initial stiffness which is of interest for the particular case of monopiles in soft rocks. There are two quantities of interest: the global stiffness and the local stiffness (cf. Figure 4.1). The global stiffness is defined as the slope of the force versus displacement at the ground surface. Assuming a homogeneous ground along the length of the pile and linear $P - y$ curves, the local stiffness is defined as the subgrade modulus (i.e. slope of the linear $P - y$ curves) that enables the same global stiffness to be achieved as that from the OPT monotonic tests. These global and local stiffness are deduced for all the monotonic tests for which various installation procedures were done.

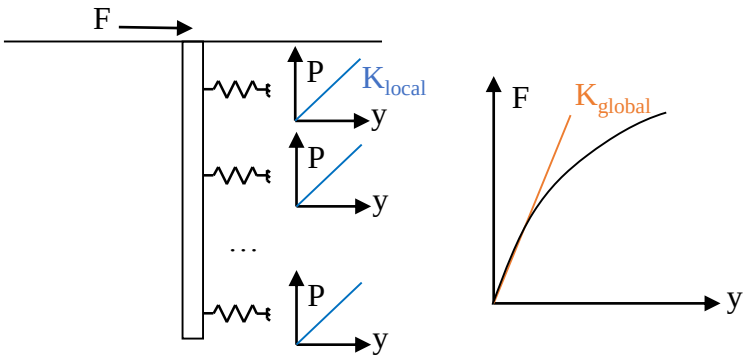

Figure 4.1.: Sketches showing the definitions of the local stiffness and the global stiffness

4.1.1 Analysis of the global stiffness

Table 4.1 summarises the global stiffness calculated from load versus displacement curve for each pile. Figure 4.2 shows for pile P7 the load versus displacement curve as well as the global stiffness calculated from this curve. The relative displacement corresponds to the measured lateral displacement divided by the pile outer diameter. It can be seen from these results that the global lateral stiffness for small relative displacements is constant for a pile relative displacement lower than 0.4 %. It should be noted that the measured lateral displacements do not correspond to the lateral displacements at the ground surface. The displacement at the ground surface is estimated by double integration of the bending moment profile above the ground surface (two boundaries conditions are given by the two levels of the lateral displacements measurements). It can be noted that the global stiffness deduced for P4 is higher than that deduced for P1 even though it is the same length over diameter ratio. This can be explain by the fact that the steel tube thickness for pile P4 is lower than those for pile P1. The lower value of the pile tube thickness implies a smaller extent of the crushed zone and thus a stiffer global response. Although both the length over diameter ratio and the pile tube thickness are the same for the piles P2 and P5, there

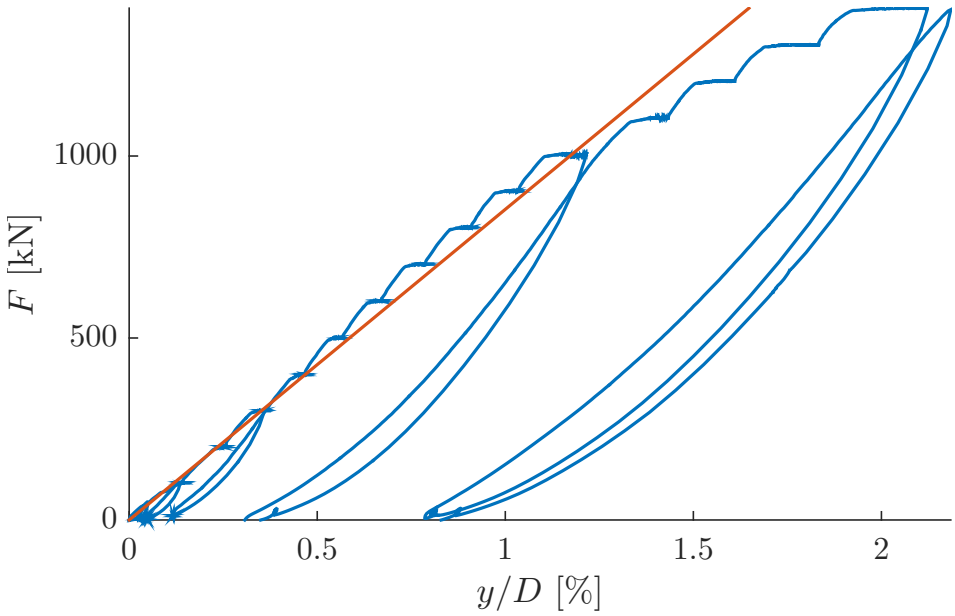

Figure 4.2.: P7 monotonic result and deduction of the global lateral stiffness (mean value of LVDTs measurement at 10 cm above the ground level)

Table 4.1.: OPT monotonic results in terms of the global stiffness

Pile	L/D	Global stiffness measured	Global stiffness deduced at the ground surface
	[-]	[kN/mm]	[kN/mm]
P1	3.5	120	133 - 137
P2	2.7	131	147 - 157
P4	3.5	288	311 - 325
P5	2.7	197	209 - 213
P6	2.4	332	372 - 395
P7	3.5	112	124 - 128
P9	2.6	103	115 - 119
P11	3.3	184	223 - 241

is a difference in the global stiffness. This difference in stiffness can be explained by the variability of the rock characteristics in space.

According to the criteria given in Carter and Kulhawy (1992) and recalled in section 2.1.2, the piles in OPT behave in a flexible manner. Carter and Kulhawy (1992) provided solutions giving the global stiffness for both flexible and rigid piles. For flexible piles the global stiffness depends on the relative modulus of the pile and the rock mass whereas for rigid piles the stiffness depends on the length over diameter ratio. According to OPT results the global stiffness seems to depend on these two parameters at the same time. In order to obtain the same global stiffness as those deduced in OPT using these formulations the shear modulus of the homogeneous ground has to be artificially small (around 50 MPa) although the shear modulus of the rock is about 2 GPa. Therefore, this comparison confirms the

fact that the crushed rock needs to be modelled and plays an important role in the initial response.

4.1.2 Comparison of the local stiffness between existing work and OPT

Assuming linear and homogeneous $P-y$ curves along the depth of the pile the subgrade reaction modulus E_s (i.e. slope of the $P-y$ curves) is back calculated in order to match the global stiffness at the ground surface deduced in the section 4.1.1. Besides, in this calculation only the steel tube is modelled (i.e. for the drilled and grouted piles the grout is considered as part of the surrounding soil). This is justified by the fact that the gap behind the pile is not between the grout annulus and the surrounding soil but between the steel tube and the grout annulus. Table 4.2 summarises the results for each pile and the ratio of the subgrade modulus over the shear modulus is also shown (considering a Young's modulus that equals 5 GPa and a Poisson's ratio that equals 0.3).

Table 4.2.: Local stiffness deduced to obtain the same global stiffness

Pile	K_L from OPT	E_s	E_s/G	K_L from $P-y$ curves
	[kN/mm]	[MPa]	[-]	[kN/mm]
P1	133-137	561	0.29	138
P2	147-157	718	0.37	153
P4	311-325	1 313	0.68	323
P5	209-213	1 033	0.54	212
P6	372-395	2 211	1.15	395
P7	124-128	914	0.48	125
P9	115-119	1 256	0.65	116
P11	223-241	2 060	1.07	238

Figure 4.3 shows the thresholds defining rigid and flexible behaviour of piles for two different criteria given by Poulos and Hull (1989) and Frank (1999) as well as the values of this quantity of interest for the piles of OPT relatively to these thresholds. Generally speaking, the piles of OPT are in between these two thresholds, consequently their behaviour is neither totally flexible neither totally rigid but somewhere in between. For low levels of loading the pile would behave in a flexible manner whereas with increasing levels of loading, the toe can start to be mobilised and the pile would behave in a rigid manner (Zhang and Andersen, 2019).

Assuming plane strain conditions, analytical solutions are given in Baguelin et al. (1977) for a circular section in translation in an elastic finite medium (R being the outer radius of the model) for two cases. In the intact model, the pile is surrounded by a homogenous elastic medium defined by a Young's modulus E and a Poisson's ratio ν (G being the shear modulus of the intact material) and the analytical solutions are exact solutions. In the disturbed model, an annulus of disturbed material is modelled between the pile and the homogeneous

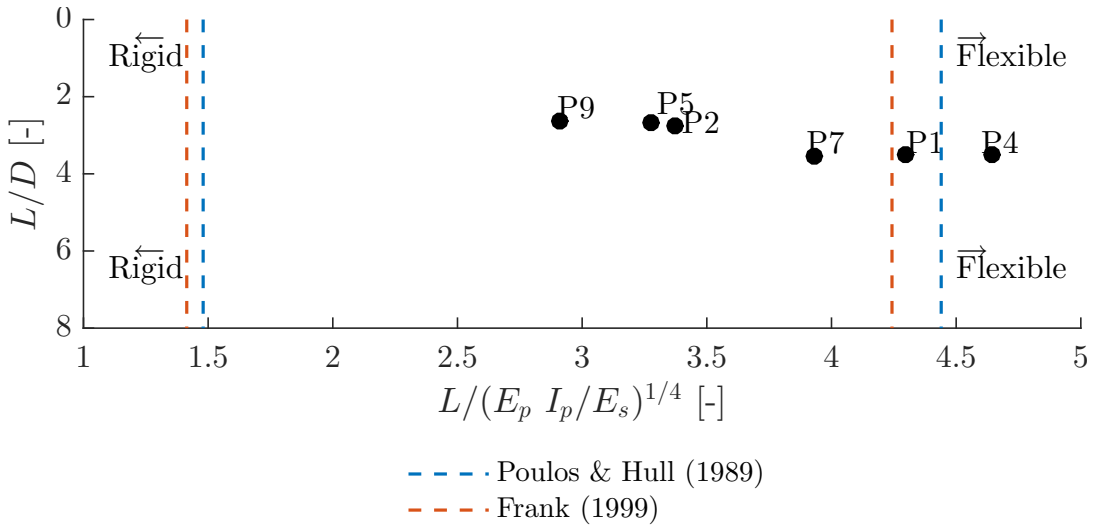

Figure 4.3.: Type of behaviour of different piles tested during OPTs applying the criterion defined by Poulos and Hull (1989) and those defined by Frank (1999) and considering a modulus value of the ground of $E_s = 5$ GPa

outer material. In the latter case, the analytical solutions are approximate. Figure 4.4 illustrates the considered models in which: T is the load per unit length applied to the pile, $E_{disturbed}$ is the Young's modulus of the disturbed zone, r_0 is the outer radius of the pile, r_1 is the outer radius of the disturbed zone, β is a parameter defined as $\beta = E_{disturbed}/E < 1$ and α is another parameter defined as $\alpha = r_1/r_0 = 1/\alpha'$. In the case of the intact model the subgrade reaction modulus is expressed as $E_s = E/s$ and s is a dimensionless parameter defined as:

$$s = \frac{1}{8\pi}\frac{1+\nu}{1-\nu}\left((3-4\nu)\ln\left(\frac{R^2}{r_0^2}\right) - \frac{2}{3-4\nu}\frac{R^2-r_0^2}{R^2+r_0^2}\right) \tag{4.1}$$

In the case of the disturbed model the subgrade reaction modulus is expressed as:

$$E_s = \frac{E}{s + \Delta s_r} \tag{4.2}$$

Where Δs_r is the increment of the parameter s caused by the disturbed zone:

$$\Delta s_r = \frac{1}{8\pi}\frac{1+\nu}{1-\nu}\frac{1-\beta}{\beta}\left((3-4\nu)\ln(\alpha^2) - \frac{2(1-\alpha'^2)^2}{(3-4\nu)(1-\alpha'^4(1-\beta))+\beta}\right) \tag{4.3}$$

In the case of driven piles these formulations are considered to account for the zone of crushed rock. Thus, the intact material corresponds to the rock mass and the disturbed material corresponds to the crushed rock. Equation 4.1 is used to calculate the value of R in order to fulfil $E_s/G = 4$. Equation 4.2 is used to deduce the ratio of the subgrade reaction modulus over the shear modulus of the rock in the case of the disturbed model assuming $E = 5$ GPa, $\nu = 0.3$, $E_{disturbed} = 70$ MPa (which is a plausible value for crushed rock (cf. Figure 3.17)) and a thickness of the crushed rock being equal to the thickness of the pile tube. Table 4.3 summarises the ratio calculated for different piles from OPT. It can

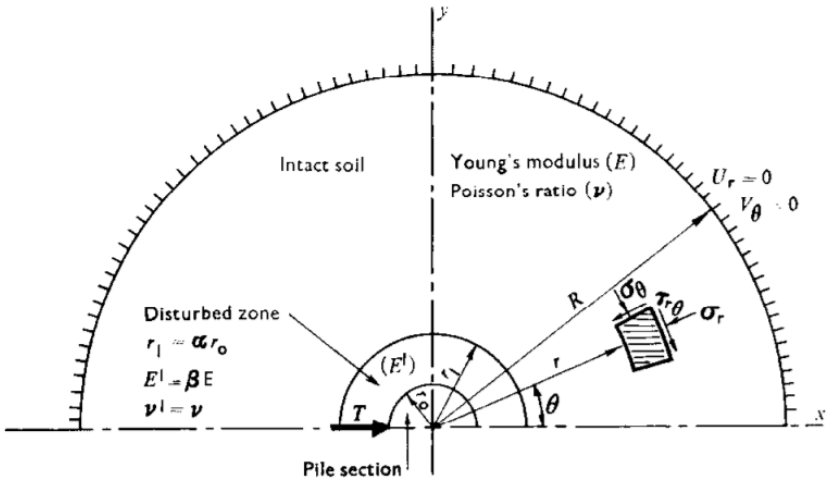

Figure 4.4.: Geometry of the considered model in Baguelin et al. (1977)

Table 4.3.: Comparison of the ratio of the subgrade reaction over the shear modulus of the rock between those back calculated using the OPT results and the solution in Baguelin et al. (1977)

Pile	E_s/G from OPT	E_s/G from Baguelin et al. (1977)
P1	0.29	1.8
P2	0.37	1.8
P4	0.68	2.1
P5	0.54	1.8
P6	1.04	2.7
P7	0.48	1.4
P9	0.65	1.4
P11	1.07	2.4

be noted that to obtain the average value of $E_s/G = 0.5$ obtained in OPT (cf. Table 4.3), the Young's modulus of the crushed rock must equal 15 MPa and this value is very low for the crushed rock even at very low stress. The difference between the analytical solutions found in Baguelin et al. (1977) and OPT results can be explained partly by the difference in the values of β. The considered values of β are higher than 0.2 in Baguelin et al. (1977) whereas for the piles tested during OPT the value of β equals around 0.015. The analytical solutions for the disturbed model are approximate solutions. They give good results for "high" values of β but are less appropriate for lower values of β as the discontinuity of the radial stress at the interface between the disturbed material and the outer material increases as β decreases although it should be continuous independently of β. Besides, another reason that can explain this difference is that in the analytical solutions given in Baguelin et al. (1977) the pile is assumed to be in full contact with the surrounding ground whereas it is not the case for the piles during OPT. The presence of the gap implies a different stress field around the pile and thus modifies the subgrade reaction modulus. Finally, the analytical solutions are given for a plane strain problem, which can also explained the differences.

4.1.3 Initial local stiffness deduced using springs in series

Methodology

The theoretical reaction of the soil can be decomposed into a frontal reaction and a tangential reaction that vary around the pile (see Figure 4.5). In the following the reaction of the soil is simplified and considered to apply uniformly. In order to have an equivalence of the resultant reaction, the uniform reaction should spread accross a reduced diameter of the pile λD, leading to $\lambda = 2/\pi \approx 0.64$ and in the following $\lambda = 0.6$ is considered.

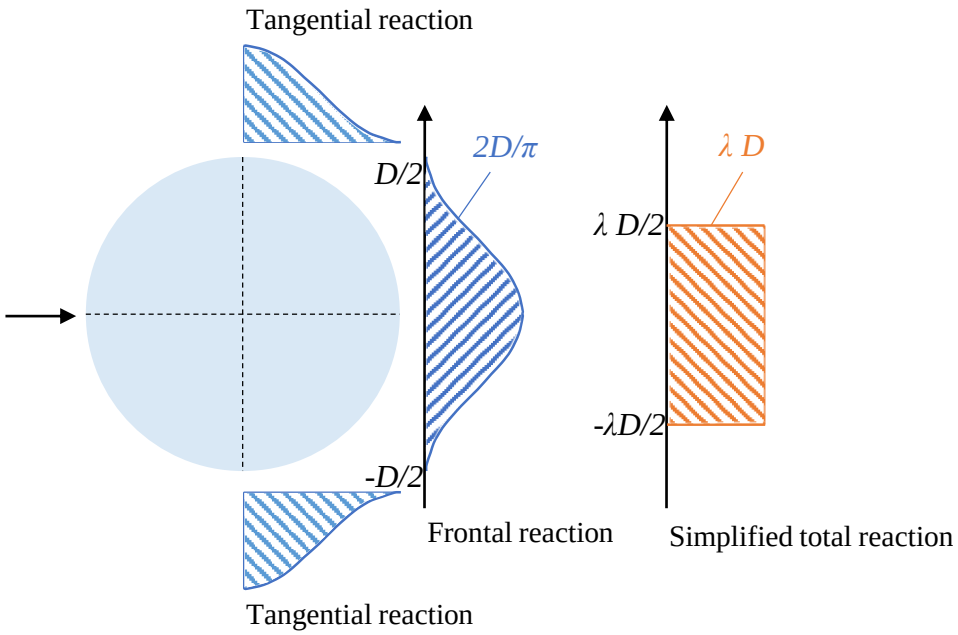

Figure 4.5.: Theoretical (blue) and simplified (orange) reaction of the soil around the pile

Figure 4.6 illustrates the model used to fit the data. Surrounding the steel tube each different layer is modelled with a spring. For springs in series, the force per unit length is

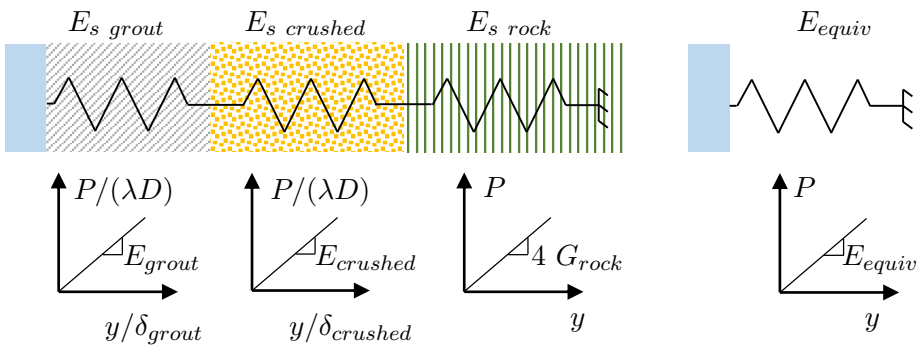

Figure 4.6.: Modelisation with three springs in series

the same in each spring, and the total strain is the sum of the strain of individual springs (cf. Equation 4.4).

$$y = \sum_i y_i = \sum_i \frac{P}{E_i} \tag{4.4}$$

where y is the total displacement, y_i is the displacement of the spring i, P the reaction of the soil and E_i the subgrade reaction modulus of the spring i. The sum implies two terms in the case of driven piles and three terms in the case of drilled and grouted piles. Classically the equivalent modulus for springs in series E_{equiv} is calculated as $1/E_{equiv} = \sum_i 1/E_i$. The subgrade reaction of the crushed rock is written as:

$$E_{s,crushed} = \frac{\lambda D E_{crushed}}{\delta_{crushed}} \tag{4.5}$$

where D is the outer diameter of the pile (either outer diameter of the steel tube in the case of driven piles and outer diameter of the drilling rig in the case of drilled and grouted piles), $E_{crushed}$ is the Young's modulus of the crushed rock and $\delta_{crushed}$ is the thickness of the annulus of crushed rock around the pile. The subgrade reaction of the soft rock is written as:

$$E_{s,rock} = 4\, G_{rock} \tag{4.6}$$

where G_{rock} is the shear modulus of the soft rock and the coefficient 4 is justified in Baguelin et al. (1977). The subgrade reaction of the grout is written as:

$$E_{s,grout} = \frac{\lambda D E_{grout}}{\delta_{grout}} \tag{4.7}$$

where E_{grout} is the Young's modulus of the grout and δ_{grout} the thickness of the annulus of grout.

Implementation for OPT results

Thus for driven piles there are three parameters ($E_{crushed}$, $\delta_{crushed}$ and G_{rock}) to determine. The shear modulus of the rock is fixed and equals 1.92 GPa, the value of $\lambda = 0.6$ is assumed and the thickness of the crushed rock is fixed and equals the thickness of the steel tube. For drilled and grouted piles there are five parameters to determine. The shear modulus of the rock is fixed and equals 1.92 GPa, the value of $\lambda = 0.6$ is assumed, the Young's modulus of the grout is fixed and equals 20 GPa and a smaller value of the thickness of the crushed rock is appropriate than that assumed for the driven piles. For both cases, the modulus of the crushed rock is back calculated to obtain the equivalent modulus E_{equiv} that matches the subgrade modulus calculated from OPT results. The back calculated Young's modulus of the crushed rock is compared to the modulus deduced from the laboratory tests, showing the consistency of the results. Table 4.4 summarises the values of the different parameters.

Table 4.4.: Values of the different parameters in the springs in series modelling

Pile	Installation	$E_{crushed}$	$\delta_{crushed}$	E_{grout}	δ_{grout}	G_{rock}	E_{equiv}
		[MPa]	[mm]	[GPa]	[m]	[GPa]	[MPa]
P1	Driven	29	35	-	-	1.92	561
P2	Driven	39	35	-	-		718
P4	Driven	55	25	-	-		1 313
P5	Driven	58	35	-	-		1 033
P6	Drilled and grouted	58	15	20	0.075		2 211
P7	Driven	79	35	-	-		914
P9	Driven	115	35	-	-		1 256
P11	Drilled and grouted	80	15	20	0.069		2 060

Relative contribution of each term

The relative contribution of a spring is defined as the proportion of the displacement of a given spring to the total displacement, thus the proportion of a given spring i is defined as the ratio E_{equiv}/E_i. Table 4.5 compares the relative contribution of each terms in the case of driven piles and drilled and grouted piles. For driven piles, the relative contribution is in average 90 % for the spring that models the crushed rock and 10 % for the spring that models the soft rock. For drilled and grouted piles, the relative contribution is around 70 % for the spring that models the crushed rock, 28 % for the spring that models the soft rock and 2 % for the spring that models the annulus of grout. This relative contribution of each spring is valid for the initial part of the response, but one can imagine that these relative contributions evolve with increasing levels of loading. Indeed, with increasing levels of loading a hardening of the crushed rock, a weakening of the soft rock as well as a softening of the grout (for drilled and grouted piles) can occur. First, only a hardening of the crushed rock is assumed. When considering a Young's modulus of the crushed rock equalling 300 MPa and assuming that all other parameters remain unchanged the relative contribution of each terms would equal for driven piles: 60 % for the crushed rock and 40 % for the soft rock (for drilled and grouted piles: 35 % for the crushed rock, 60 % for the soft rock and 5 % for the grout). The value of 300 MPa corresponds to a Young's modulus calculated using the oedometric modulus obtained during oeodometer test on the crushed rock for a maximal axial stress of 2 MPa. Finally, both crushed rock hardening and weakening of the soft rock are considered at the same time. A shear modulus of the soft rock is now half of the value initially considered (i.e. 0.96 GPa). For driven piles, the relative contributions of each term would equal 40 % for the crushed rock and 60 % for the rock (for drilled and groutes piles: 22 % for the crushed rock, 74 % for the soft rock and 4 % for the grout). It is worth noting that no term can be completely eliminated and that the relative contributions of the springs change completely with increasing levels of loading.

Table 4.5.: Relative contribution of each spring

Pile	Crushed rock	Soft rock	Grout
P1	93 %	7 %	-
P2	91 %	9 %	-
P4	83 %	17 %	-
P5	87 %	13 %	-
P6	70 %	29 %	1 %
P7	88 %	12 %	-
P9	84 %	16 %	-
P11	71 %	27 %	2 %

4.1.4 Summary of the main findings

The important difference between the solutions of Carter and Kulhawy (1992) and the results from OPT results is explained by the fact that the crushed zone is ignored in their model. This is why the local approach presented in Baguelin et al. (1977) is compared to the results. Although, this model permits to account for the crushed rock, it still gives stiffer response compared to the results. The difference can be explained by the fact that some terms neglected in the approximate solutions are no more negligible and by the fact that gapping occurs behind the pile (even at low level of loading) leading to a change in the stress field. The modelling considering several springs in series to account for the different layers around pile permits to quantify the role of each layer in the response.

4.2 Modelling multi-directional loading effects

A simple procedure is presented herein to evaluate the extension of $P-y$ curves from the classical unidirectional model to the new multi-directional one. Simple relationships are presented for commonly used $P-y$ curve expressions (linear, elasto-plastic, power-law, hyperbolic tangent and hyperbolic). The proposed method remains as simple and practical as the original $P-y$ curve method and does not need any further information or parameters. First, the extension of the $P-y$ curve method to multi-directional lateral loading is presented. The following part is dedicated to the downscaling procedure for the evaluation of multi-directional $P-y$ curves. The model verification is then presented by comparing its predictions with those of Su (2012) and those of Levy et al. (2007) as there was no usable data to validate this model using OPT results.

4.2.1 Model framework

The original unidirectional model is presented in section 2.2.2. In order to model multi-directional effects, several springs are considered around the perimeter of the pile at

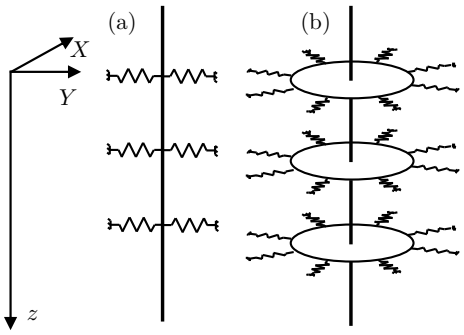

Figure 4.7.: Comparison of unidirectional and multi-directional models

each level, instead of only the single spring considered for the unidirectional model. For simplicity, the pile section is subdivided equally in a way that each spring has another spring diametrically opposed to it, which implies using an even number of springs around the pile perimeter. For practical reasons, it is preferable (but not essential) to have for each spring another one orthogonal to it; this implies using a total number of springs that is a multiple of 4 as assumed in the following. The springs are assumed to act in compression only. Consequently, a given spring and that on the diametrically opposed side cannot be activated at the same time, regardless of whether a gap is assumed to occur or not. Conceptually as the load in a given orientation changes from positive to negative, it is automatically assumed to transfer (as a positive load) to the opposing spring (Figure 4.7a). In this paper we will use the convention that compressive soil reaction is considered positive. Assuming N springs around the pile perimeter, if the loading is applied in the direction of one spring, only $n = N/2 - 1$ springs will be active along half of the perimeter (Figure 4.7b).

In the 3D configuration of the multi-directional model, the equilibrium of an infinitesimal pile element of length $\mathrm{d}z$ involves six equations instead of three for the 2D case. One equation corresponds to torsion which is neglected. One equation refers to equilibrium of vertical forces; as no axial friction along the pile is considered the axial force is constant with depth. Two equations correspond to equilibrium of shear forces in the two perpendicular directions of the section. Finally, two equations refer to equilibrium of bending moments around two perpendicular directions of the section. Using the same procedure as for the 2D problem, we obtain a system of two differential equations:

$$\begin{cases} \dfrac{\mathrm{d}^2}{\mathrm{d}z^2}\left(\left(E_pI_p\right)_x \dfrac{\mathrm{d}^2x}{\mathrm{d}z^2}\right) + V\dfrac{\mathrm{d}^2x}{\mathrm{d}z^2} + P_x\left(x,y\right)=0 \\ \dfrac{\mathrm{d}^2}{\mathrm{d}z^2}\left(\left(E_pI_p\right)_y \dfrac{\mathrm{d}^2y}{\mathrm{d}z^2}\right) + V\dfrac{\mathrm{d}^2y}{\mathrm{d}z^2} + P_y\left(x,y\right)=0 \end{cases} \tag{4.8}$$

In the above system, x and y are the displacements in two perpendicular directions of the pile section, $\left(E_pI_p\right)_x$ and $\left(E_pI_p\right)_y$ are the flexural rigidities in the corresponding two vertical planes (for a circular pile these two quantities are equal), z is the vertical coordinate along

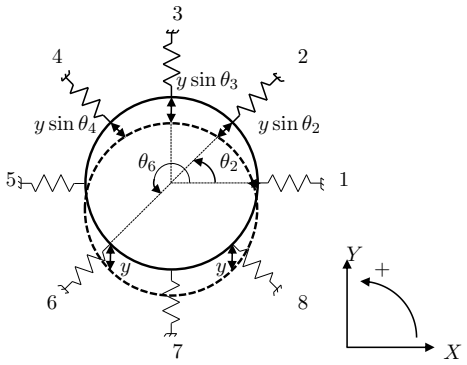

Figure 4.8.: Example of a pile section subdivided with 8 springs ($N = 8$) with a pile lateral displacement of y along Y-axis. In this example, $j \in \{2; 3; 4\}$

the pile, V is the vertical force applied on top of the pile and P_x and P_y are the soil reactions mobilised in the two corresponding directions. Equation 4.8 is valid when considering only distributed lateral loads (represented by $P - y$ curves) but new design methods for large diameter piles under lateral loading have proposed distributed moment resistance, represented by $M - \theta$ curves, in addition to the $P - y$ curves (Byrne et al., 2015b). This paper focuses on $P - y$ curves, although the principles may be extended to $M - \theta$ springs as well.

Let us consider the schematic representation of a pile section discretised with N springs around its perimeter, among which n springs are active at the same time for a given loading direction. An example of a section discretised with 8 springs and with a loading direction along the Y-axis is shown in Figure 4.8. Throughout the paper, the subscript j refers to the active springs. θ_j is the angle between the direction of spring j and the X-axis, P_j is the applied force (per unit length), u_j the resulting displacement in the spring direction. u_j can be expressed as a function of the pile displacements, x and y, in the section considered: $u_j = x \cos\theta_j + y \sin\theta_j$. The resultant soil reactions P_x and P_y can be calculated as the sums of the projections of the reactions P_j of the mobilised springs in X and Y directions: $P_x = \sum_j P_j \cos\theta_j$ and $P_y = \sum_j P_j \sin\theta_j$.

In the $P - y$ curve approach the reaction force of each spring is written as a function of its displacement $P_j = P_j(u_j)$. This results in:

$$P_x(x, y) = \sum_j P_j(x \cos\theta_j + y \sin\theta_j) \cos\theta_j \tag{4.9a}$$

$$P_y(x, y) = \sum_j P_j(x \cos\theta_j + y \sin\theta_j) \sin\theta_j \tag{4.9b}$$

Replacing the above expressions in Equation 4.8 shows the coupling effects between the displacements in the two perpendicular directions. The finite difference method is used to solve this differential equations system. This requires linearisation of the non-linear

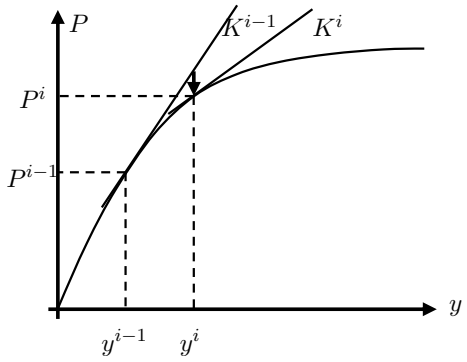

Figure 4.9.: Illustration of radial-return algorithm used to estimate soil reaction

functions $P_j\,(u_j)$ using the radial-return algorithm (Figure 4.9). The reaction of the spring j at the load-step i, noted as P_j^i, is approximated by:

$$P_j^i = P_j^{i-1} + K_j^{i-1}\left(u_j^i - u_j^{i-1}\right) \tag{4.10}$$

where K_j^{i-1} refers to the tangent modulus of spring j at load step $i-1$.

$$\begin{aligned} P_x^i\left(x^i, y^i\right) = x^i \sum_j K_j^{i-1} \cos^2\theta_j + y^i \sum_j K_j^{i-1} \cos\theta_j \sin\theta_j \\ + \sum_j \left(P_j^{i-1} - K_j^{i-1} u_j^{i-1}\right) \cos\theta_j \end{aligned} \tag{4.11a}$$

$$\begin{aligned} P_y^i\left(x^i, y^i\right) = x^i \sum_j K_j^{i-1} \cos\theta_j \sin\theta_j + y^i \sum_j K_j^{i-1} \sin^2\theta_j \\ + \sum_j \left(P_j^{i-1} - K_j^{i-1} u_j^{i-1}\right) \sin\theta_j \end{aligned} \tag{4.11b}$$

However, solving this model requires the definition of the $P-y$ function for each spring, which is discussed in the next section.

4.2.2 $P-y$ curve approach for multi-directional loading

Unidirectional $P-y$ curves have been evaluated from laterally loaded pile tests (real-scale in-situ tests or laboratory physical modelling at reduced scale). Based on such experiments various typical $P-y$ relationships have been proposed in the literature. Among these, the most commonly used are linear, bi-linear (elasto-plastic), power-law, hyperbolic tangent and hyperbolic relationships. In the multi-directional model, a given lateral loading activates several springs. Thus the $P-y$ curve for each spring depends on the number of springs around the pile.

For the sake of simplicity, we assume that the $P-y$ functions of the multi-directional model have the same mathematical expressions as for the unidirectional case. Assuming that the

$P-y$ curve for the unidirectional model is known, we aim to determine a consistent set of $P-y$ curves for different springs in the multi-directional model. For that, we assume equality of the external work (force per unit length integrated over displacement) of the single spring for the unidirectional model and the total external work for the multi-directional model (sum of the external work required for each mobilised spring) for a given pile section under an imposed horizontal displacement. This equality can be guaranteed rigorously for some simple $P-y$ functions (linear function and power-law, as will be shown later). For more complex functions, some small differences remain, as will be discussed later in this section. To determine the $P-y$ curves for multi-directional loading, we assume that the imposed horizontal displacement is applied in the direction of one of the springs. This facilitates establishing equations that remain true regardless of the direction of the horizontal displacement considered. So, strictly speaking, the $P-y$ curves of the multi-directional model are only valid for loading applied in the direction of one of the springs. In practice, for a sufficiently high number of springs around the perimeter of the pile, the following approach can be applied even though the loading is not aligned with one of the spring directions. Consequently, it is possible to spread the load between two adjacent springs allowing a gradual rotation of the loading direction using this model. The procedure is presented for different $P-y$ curves function in the following and details are given in Appendix D.

Linear $P-y$ curve

The relationship for linear unidirectional and multi-directional models is written as:

$$P(y) = ky \tag{4.12a}$$

$$\tilde{P}(y) = \tilde{k}y \tag{4.12b}$$

where k is the elastic stiffness and the tilde symbol refers to the multi-directional model.

The external work for the unidirectional model for an imposed displacement y is given by $E = \int_0^y P(v)\,\mathrm{d}v$. From Equation 4.12a, we find $E = ky^2/2$. For the multi-directional model we have $\tilde{E} = \sum_j \int_0^{y_j} \tilde{P}(v)\,\mathrm{d}v$ where $y_j = y\sin\theta_j$ is the projection of the imposed displacement y in the direction of the considered spring j. The work is thus given by $\tilde{E} = \sum_j \left(\tilde{k}y^2\sin^2\theta_j\right)/2$. By setting $\tilde{E} = E$ we find $k = \tilde{k}\sum_j \sin^2\theta_j$. For the set of active springs on half of the pile perimeter (Figure 4.8), we find $\sum_j \sin^2\theta_j = N/4$. The following relation is thus obtained between the stiffness parameters of the unidirectional and multi-directional models:

$$\tilde{k} = \frac{4k}{N} \tag{4.13}$$

Elasto-plastic $P-y$ curve

For an elastic-perfectly plastic behaviour:

$$P(y) = \min(ky, P_u) \tag{4.14a}$$

$$\tilde{P}(y) = \min\left(\tilde{k}y, \tilde{P}_u\right) \tag{4.14b}$$

where k is the elastic stiffness and P_u the ultimate reaction.

For evaluating $\tilde{k}$ and $\tilde{P}_u$ we consider the two following limit situations. If all the active springs remain in the elastic regime Equation 4.13 holds. When all the active springs are in the plastic regime, using the same procedure as for the linear model, we find:

$$\tilde{P}_u = \tan\left(\frac{\pi}{N}\right) P_u \tag{4.15}$$

The equality between the two external works E and $\tilde{E}$ cannot be fully satisfied when some of the active springs are in the elastic regime whereas others are in a plastic state. In Figure 4.10a the resultant reaction of the multi-directional model is compared to the $P-y$ curve of the unidirectional model for various values of the number of springs N. In this graph, we use dimensionless quantities yk/P_u and $P(y)/P_u$. The curves of the unidirectional model and the multi-directional ones coincide if all the active springs are in the elastic regime. They start to diverge as soon as one active spring of the multi-directional model yields. The corresponding displacement is $\tilde{y_u} = \tilde{P}_u/\tilde{k}$.

$$\frac{\tilde{y_u}}{y_u} = \frac{N}{4}\tan\frac{\pi}{N} \tag{4.16}$$

where $y_u = P_u/k$ is the displacement for which the spring of the unidirectional model reaches the plastic state. As expected, the yield state is reached first for the multi-directional model, as for $N \geq 4$ we have $\tilde{y_u}/y_u \leq 1$. For typical values of $N > 8$, we have $\tilde{y_u}/y_u \simeq \pi/4$, showing that the point at which the responses of the unidirectional and multi-directional models start to diverge becomes essentially independent of the number of springs. When all the active springs have reached the plastic limit, the curves coincide again. The corresponding displacement is $NP_u/8k$. The transition zone between the values $\pi/4$ and $N/8$ on the dimensionless axis yk/P_u becomes smoother for a greater number of springs but the resultant reaction of the multi-directional model does not depend significantly on the number of springs as long as $N > 8$. Using more springs leads to more precise results in terms of irreversible displacement around the pile and greater accuracy in the choice of the applied load angle.

Power law $P-y$ curve

Power-law $P-y$ curves are used for example in API (2000) for soft clays, in Reese and Welch (1975) for stiff clays of marine origins, in Wesselink et al. (1988) for calcareous sands,

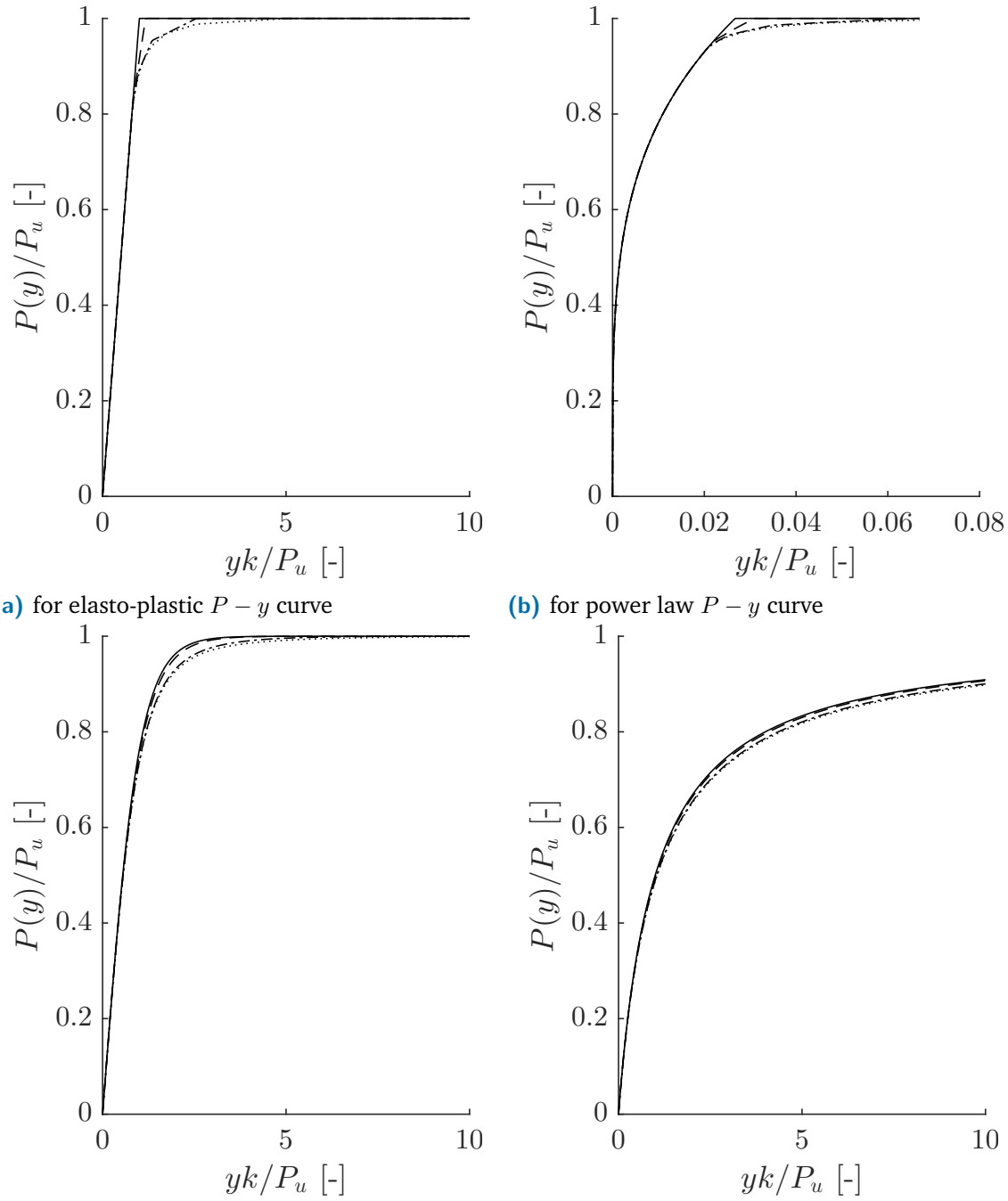

(a) for elasto-plastic $P - y$ curve

(b) for power law $P - y$ curve

(c) for hyperbolic tangent $P - y$ curve

(d) for hyperbolic $P - y$ curve

Figure 4.10.: Comparison of the unidirectional $P - y$ curve and resultant reaction of the multi-directional model for values of N

in Dyson and Randolph (2001) for carbonate sands and in Reese (1997) for weak rocks. They are expressed as:

$$P(y) = ky^m \tag{4.17a}$$

$$\tilde{P}(y) = \tilde{k}y^{\tilde{m}} \tag{4.17b}$$

where the power m usually ranges between 0.25 and 0.65. Such a function leads to an infinite initial stiffness and unlimited growth in P at large displacements. This is remedied in the previously cited papers by replacing the initial part by a specified maximum gradient and by adding an ultimate reaction. Equations 4.13 and 4.15 as established in the previous sections can be used for the linear part and the ultimate reaction. We have thus to establish the relationships between the unidirectional and multi-directional models for the section of the curve that follows the power-law function. The external work for the unidirectional model for an imposed displacement y is given by $E = ky^{m+1}/(m+1)$. For the multi-directional model we have $\tilde{E} = \sum_j k\left(y \sin\theta_j\right)^{\tilde{m}+1}/(\tilde{m}+1)$. Assuming $\tilde{m} = m$ and setting $\tilde{E} = E$, we find:

$$\tilde{k} = \frac{k}{\sum_j \left(\sin\theta_j\right)^{m+1}} \tag{4.18}$$

This transition law results in a perfect match between the results of unidirectional and multi-directional models. Similarly to Figure 4.10a, Figure 4.10b shows a comparison of the unidirectional $P-y$ curve and the resultant reaction of the multi-directional model considering a classically modified power-law $P-y$ curve, with specified maximum initial gradient and a cut-off ultimate reaction. It can be seen from this figure that there is a perfect match between the two models for the initial part (specified maximum gradient) and for the intermediate part (power-law) and for the transition between these two parts, but as already seen for the elasto-plastic behaviour the transition to ultimate reaction occurs gradually for the multi-directional model. However, the equivalence between these two models is acceptable.

Hyperbolic tangent $P-y$ curve

The hyperbolic tangent function offers the advantage of having a defined gradient at zero displacement and a finite limit at large displacement. Thus, using the hyperbolic tangent shape obviates the need to define piecewise $P-y$ functions. The expression for the $P-y$ curves is given by:

$$P(y) = P_u \tanh\frac{ky}{P_u} \tag{4.19a}$$

$$\tilde{P}(y) = \tilde{P}_u \tanh\frac{\tilde{k}y}{\tilde{P}_u} \tag{4.19b}$$

Such $P-y$ curves have been proposed for example for soft clays in Guo et al. (2014), for stiff and preconsolidated clays in Dunnavant and O'Neill (1989) and for sands in API (2000). Similarly to the elastic perfectly plastic case, this function involves two parameters: the initial stiffness k and the ultimate reaction P_u. However, the transition from unidirectional to multi-directional models is not as straightforward as for the previous models considered. Equality of the external work per unit length for the unidirectional and multi-directional models needs to be achieved regardless of the value of y. There is no simple analytical solution for this. Assuming equality of the derivative of both work input per unit length for small values of y leads to Equation 4.13 for the relation between k and $\tilde{k}$. For large values of y the asymptotic reaction is given by Equation 4.15. As for the elasto-plastic function, the equality between the two work inputs is not fully satisfied. However, as shown in Figure 4.10c, the equivalence between the two models is acceptable. The discussion presented for the comparison of unidirectional and multi-directional models for the elasto-plastic function is valid for analysis of the results presented in Figure 4.10c.

Hyperbolic $P-y$ curve

Other authors (e.g. Su and Yan, 2013) have used hyperbolic $P-y$ curves to fit experimental results of multi-directional loaded piles, according to

$$P\left(y\right)=\frac{y}{1/k+y/P_u} \tag{4.20a}$$

$$\tilde{P}\left(y\right)=\frac{y}{1/\tilde{k}+y/\tilde{P}_u} \tag{4.20b}$$

Just as for the hyperbolic tangent function, the hyperbolic $P-y$ curve offers the advantage of having a defined slope at zero displacement (k) and a finite limit at large displacement (P_u). Following the same approach as for the previous models, $\tilde{k}$ and$\tilde{P_u}$ are obtained and are given here again by Equations 4.13 and 4.15. The close agreement between the multi-directional model and the unidirectional one is shown in Figure 4.10d.

Unloading response (gapping occurs or not)

The $P-y$ curve is commonly assumed to be reversible (e.g. DNV-GL, 2014). This is generally not the case for real soils, for which irreversible displacements are observed during unloading. This irreversibility can also be accompanied by the formation of a gap between the pile and the soil behind during loading in a given direction. To keep the model simple, in the following we assume elastic unloading of the $P-y$ curve with a modulus equal to the initial slope of the loading branch E_0 (Figure 4.11).

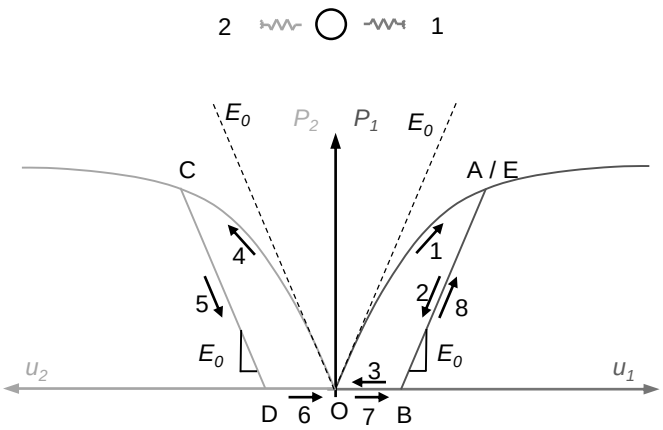

Figure 4.11.: Sketches showing the response in unloading of a generic $P - y$ curve with gapping

Depending on the soil behaviour, the pile stiffness and the stress state around the pile after installation, gapping can occur and significantly affect the response of the pile. The extent of the gap will vary with depth along the pile. For example in the pile tests for the PISA project, the extent of a gap was analysed in Zdravković et al. (2019) for stiff clay and in Taborda et al. (2019) for sand. To explain the modelling procedure in the presence of gapping, we shall first consider the case of unidirectional loading simulated with two opposite springs n°1 and n°2. Consider a loading sequence consisting of loading and unloading of spring n°1 followed by loading and unloading of spring n°2 in the opposite direction and finally reloading of spring n°1. After the first loading/unloading cycle applied on spring n°1 (paths 1 and 2 in Figure 4.11), the irreversible displacement is represented by segment OB. The pile moves towards its initial position (zero displacement) without mobilising the soil reaction (path 3). Spring n°2 starts to be compressed only when the displacement of the pile changes sign. The second loading and unloading cycle applied on spring n°2 is represented in Figure 4.11 by paths 4 and 5, which generate irreversible displacement OD. Spring n°1 is reloaded only after the pile returns to point B (paths 6 and 7). By contrast, when no gapping occurs spring n°2 is compressed directly from point B, even though the spring displacement is negative (negative load in the spring is never permitted). It is assumed that the response of spring n°2 is not affected by the previous loading/unloading cycle of spring n°1. This is a strong assumption because pile loading affects the soil behind when no gapping occurs. However, the model could be extended to account for soil remoulding due to pile loading but this would require additional complexity in the constitutive model of the soil. The same procedure can be extended to multi-directional loading. In a general loading sequence for which the direction varies, some springs might be loaded whereas others are unloaded. The response of each individual spring is analysed by considering the projection of the imposed load along the spring direction with special attention paid to whether gapping occurs or not.

Summary of the procedure

The modelling procedure can be summarised as follows:

(i) Choice of the unidirectional model parameters with or without gapping
(ii) Choice of an even number of springs distributed around the perimeter of the pile.
(iii) Evaluation of $P - y$ curves for multi-directional model from those used for the unidirectional model (Equations 4.13, 4.15 or 4.18).
(iv) Resolution of the differential equations system (Equation 4.8). At the end of this stage, the displacements in the X and Y direction of each node are known and displacements along each spring can be deduced.
(v) Calculation of the total displacement, the displacement in the direction of loading and the misalignment between the total displacement and the direction of loading.

4.2.3 Evaluation of the model performance

Comparison with experimental data

The experimental results presented by Su (2012) are used to evaluate the capacity of the proposed model to reproduce the response of a pile under multi-directional lateral loading. This experimental work consisted of laboratory load tests on reduced scale piles installed in sand. The model piles were steel tubes with an outer diameter of 38 mm, a wall thickness of 0.8 mm and embedment length varying between 350 and 500 mm. The load was applied in a displacement controlled manner with the loading point located 200 mm above the ground surface. Both unidirectional and multi-directional loading sequences were applied. Comparison between the results of the proposed model and the experimental results of Su (2012) is first carried out for unidirectional monotonic loading to calibrate the $P-y$ curves. Similarly to Su and Yan (2013) a hyperbolic function is assumed to fit the $P-y$ curves. Since the tested piles were installed in sand, we consider that gapping does not occur, although we have taken no account of the likely loosening of the soil behind the pile as it is displaced forward. Both the initial stiffness k and the ultimate soil reaction P_u are assumed to vary linearly with depth according to:

$$k = 22\ z \ \ \mathrm{MPa} \tag{4.21a}$$

$$P_u = 20\ z \ \ \mathrm{kN/m} \tag{4.21b}$$

where z is the depth below the ground surface in m. The monotonic unidirectional loading is simulated using both the unidirectional model and the proposed multi-directional model considering 40 springs around the perimeter of the pile. The results of both models and the experimental data from Su (2012) are compared in Figure 4.12. Figure 4.12a shows the results in terms of lateral load versus imposed lateral displacement at the head of the pile and Figure 4.12b shows the results in terms of bending moment along the length of the pile for different values of imposed displacement at the head of the pile (2.5, 5.0, 7.5 and 10 mm). Very good compatibility is found between the results of the unidirectional and multi-directional models and those of Su (2012). This validates the relationships found for k and P_u.

One of the multi-directional paths performed during the laboratory tests was a cross-path as shown in Figure 4.13, which has been simulated using the proposed model considering 40 springs. The results of the multi-directional model in terms of the shear force at the head of the pile are presented in Figure 4.14 and for the X (left) and Y (right) directions. The comparison with the experimental results shows good compatibility although it may be seen that the results of the proposed model overestimates the maximum load after the first loading cycle (1-2). This can be attributed to the assumption that the mechanical properties of the soil behind the pile are not affected by this first loading cycle. However, as mentioned above, even with no gapping it is expected that the soil state wil be changed all around

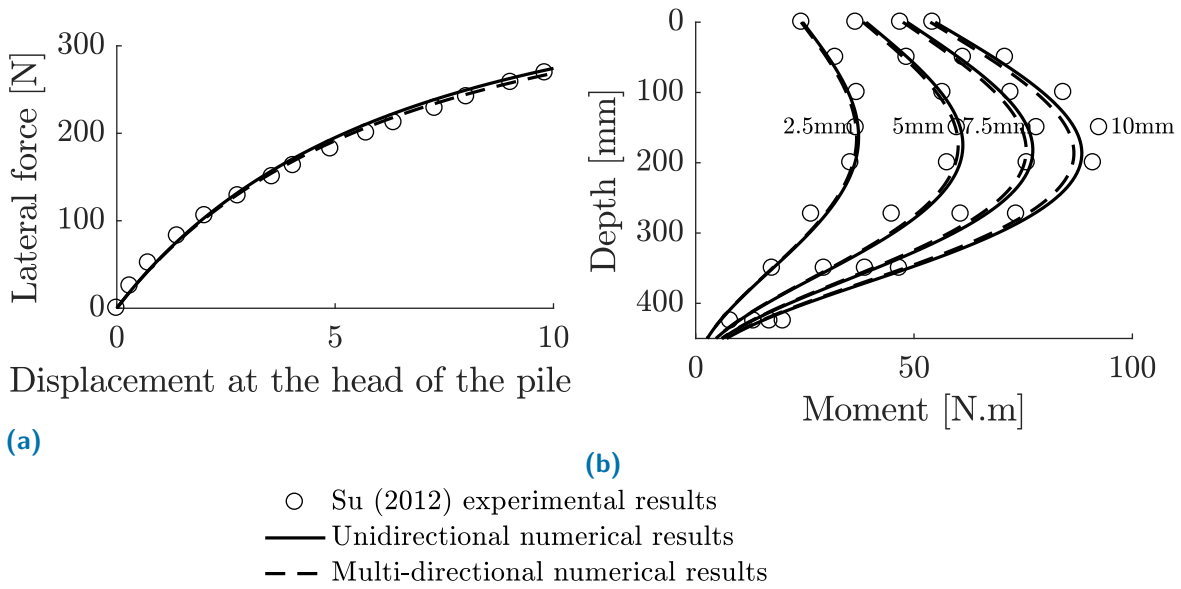

Figure 4.12.: Comparison between the numerical model and the experimental data

the pile and in particular will loosen behind the pile as the pile is displacement in a given direction. Nevertheless, the key mechanisms are well captured by the multi-directional model: the presence of a residual force in the Y-direction when the pile returned to its equilibrium position (end of 4); the decrease of this force when loading in the positive X-direction (5); and no significant further change when loading/unloading in the negative x-direction (7 and 8).

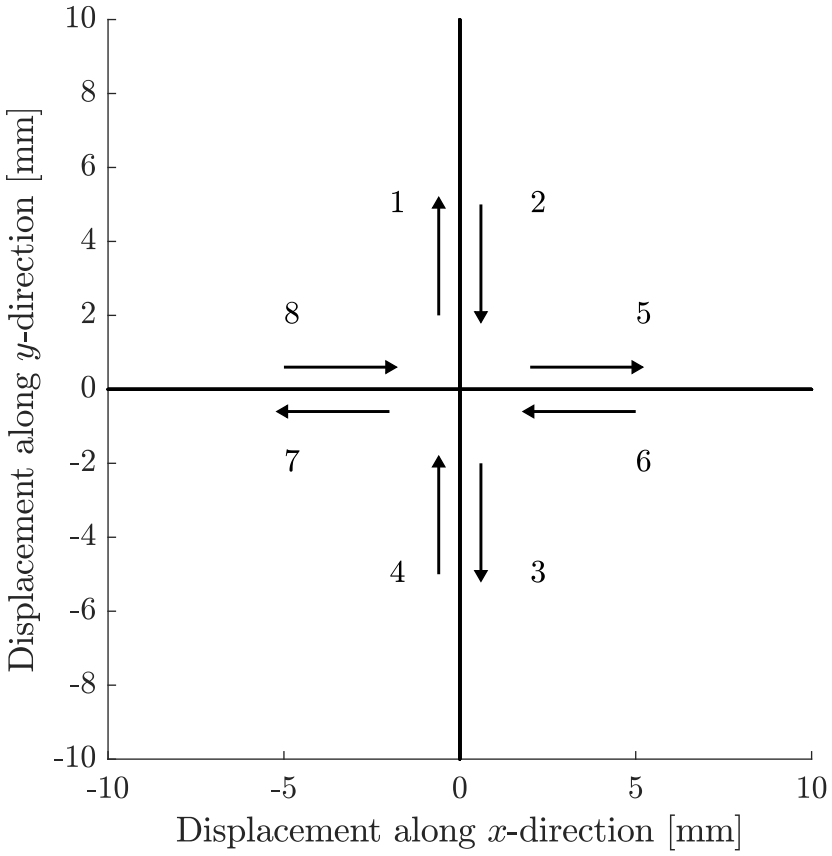

Figure 4.13.: Definition of the cross-path multi-directional loading

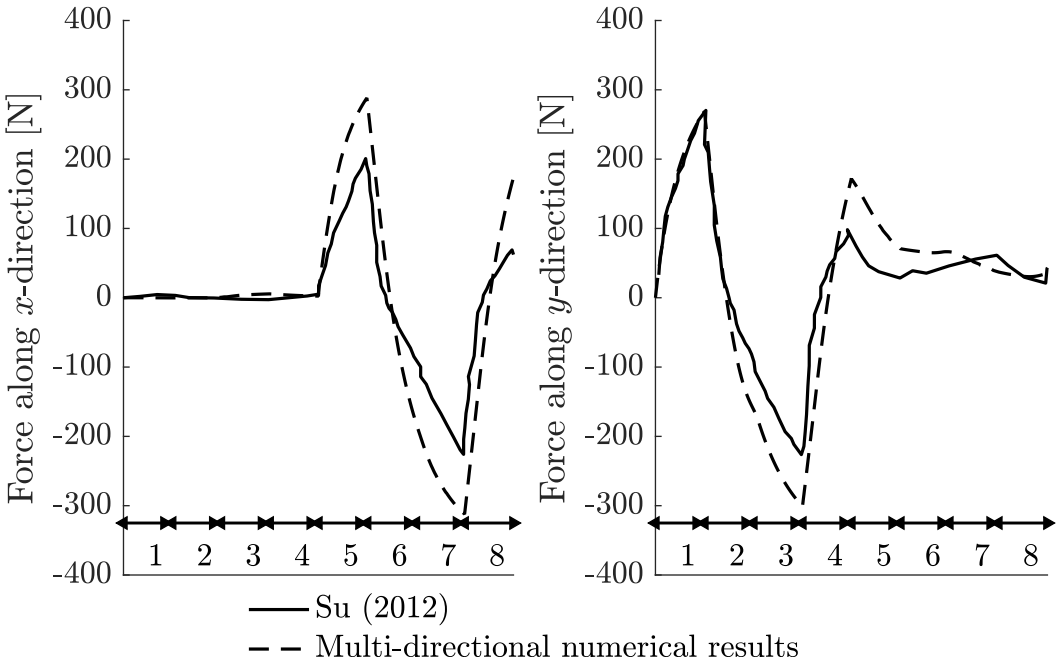

Figure 4.14.: Comparison between the numerical model and the experimental data for a cross-path multi-directional loading

Comparison with numerical results

In the following, we analyse the case study developed in Levy et al. (2007) to further evaluate the performances of the proposed model. The authors developed a theoretical numerical study of a pile under both unidirectional and multi-directional loading. A 20 m long steel pile ($E_p = 210$ GPa) was considered with two different cases: a tubular pile (2 m diameter and 20 mm thickness) and an (artificial) solid pile of 2 m diameter. The soil was assumed to be elastic, perfectly plastic with a Young's modulus increasing with depth according to $E_s = 30 + 1\ z$ MPa, with z the depth in m, and Poisson's ratio of ν=0.4. The soil strength was assumed to increase with depth according to $s_u = 20 + 4\ z$ kPa. For the $P - y$ curve, the initial gradient was derived from a relationship by Ashford and Juirnarongrit (2003) as detailed by Levy et al. (2007). The limiting resistance was taken as $P_u = 10.8\ D\ s_u$ Randolph and Houlsby (1984). Gapping is not considered in this study.

The monotonic loading described in Levy et al. (2007) consisted of a lateral load applied progressively at ground level. The same case of monotonic loading is simulated here using the proposed model considering 40 springs around the perimeter of the pile and also using the classical unidirectional model. The results of both models for this monotonic loading are compared in Figure 4.16 with the results obtained in Levy et al. (2007) in terms of the applied load at ground level versus horizontal displacement at ground level. The results show excellent compatibility between the results of unidirectional and multi-directional models and those of Levy et al. (2007). For multi-directional loading, Levy et al. (2007) considered three load cases (4-1, 4-2 and 4-3) with three loading stages: Stage I: horizontal loading to a force F, Stage II: unloading to zero in the same direction, Stage III: horizontal loading in a direction perpendicular to stage I to a force F. They are represented in Figure 4.15. These three load cases differ in the applied lateral load at ground level: for load case 4-1 F equals 25% of the ultimate load, for load case 4-2 F equals 50% and for load-case 4-3 F equals 75% of the ultimate load.

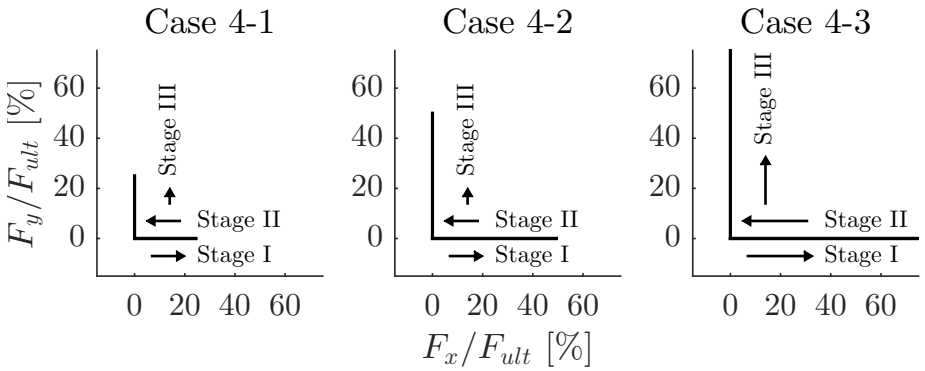

Figure 4.15.: Sketches showing considered multi-directional loading cases in Levy et al. (2007)

The same cases of multi-directional loading are simulated for the tubular pile using the proposed model. Comparison of the results of the multi-directional loading scenario is

presented in Figure 4.17 in terms of normalised horizontal force versus normalised pile head displacement. Note that the plotted displacement is the resultant of pile head displacements. Once again the comparison shows excellent compatibility between the results of the proposed multi-directional model and those of Levy et al. (2007). It should be emphasised that this comparison is achieved without any parameter fitting, but just by using the expressions of the unidirectional $P - y$ curve parameters, k and P_u, given by Levy et al. (2007). After the model verification, in the next section we present some application examples to illustrate further the effects of multi-directional loading on the pile response and the consequence for design.

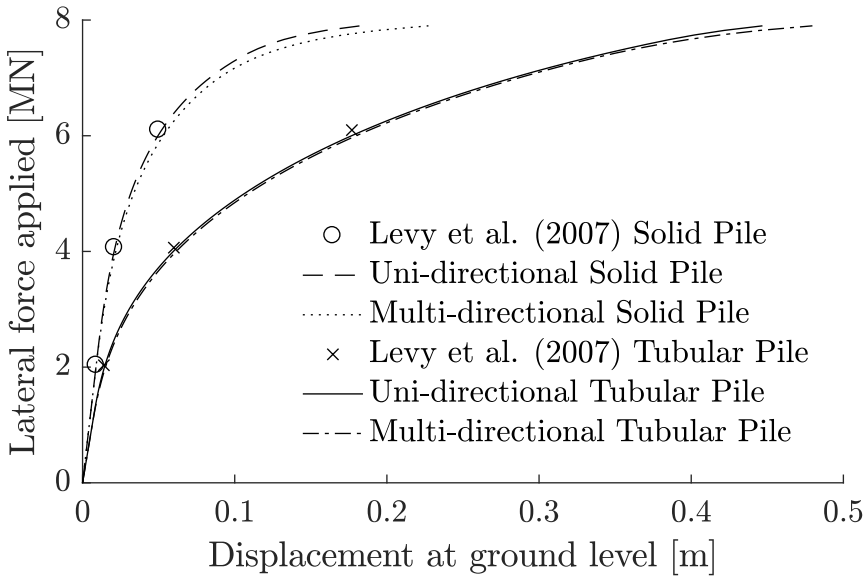

Figure 4.16.: Comparison of applied force versus deflection at the pile head for both tubular an solid piles

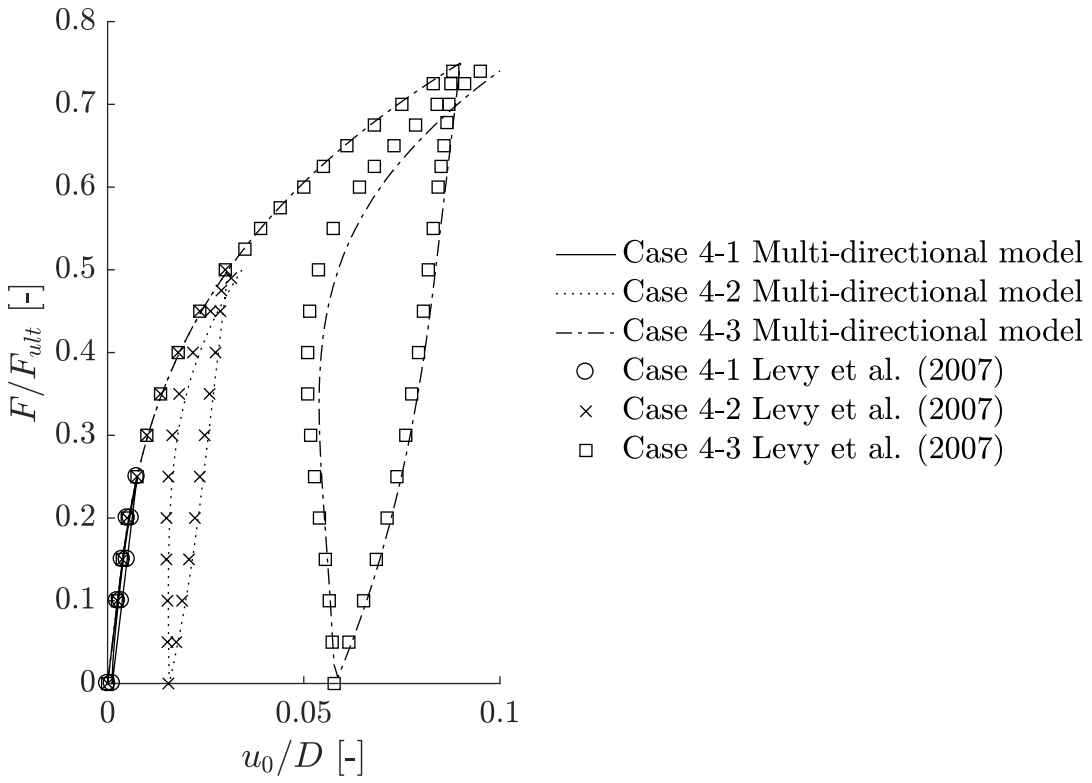

Figure 4.17.: Comparison of F/F_{ult} versus u_0/D at the pile head for Load Cases 4-1, 4-2 and 4-3

4.2.4 Impact of a change in loading direction on the misalignment between the applied load and the displacement directions

The same soil parameters and pile geometry as used in Levy et al. (2007) and a rigid pile section are considered for this application example. The elasto-plastic $P-y$ curve is replaced by a hyperbolic tangent function which permits more accurate representation of the pile behaviour due to the smooth transition between the initial phase and failure. It has been verified that the value of the ultimate load (F_{ult}) is not influenced by the change of function (from elasto-plastic to hyperbolic tangent). In the following, all the lateral loads applied at ground level are expressed as a ratio of this ultimate load. The effect of the occurrence of gapping on multi-directional loading response is analysed. A total number of $N = 36$ springs around the pile is used in order to have a smooth profile of the irreversible displacements around the pile. As it is convenient for the load to be applied in the direction of one of the springs, use of a large number of springs allows flexible choice of the loading direction. A slightly different multi-directional loading sequence is considered compared to that in Levy et al. (2007). Four loading stages are considered : Stage I : horizontal loading to a force F (given as a ratio of the ultimate load) in the direction of X-direction; Stage II : unloading to zero in the same direction; Stage III: loading to the same force F in a different direction oriented at an angle θ_{load} with respect to the previous loading direction and finally; Stage IV: unloading to zero in the same direction as the previous stage. Figure 4.18 illustrates the

multi-directional loading sequence implemented in the following numerical analyses, taking θ_{load} as 90°.

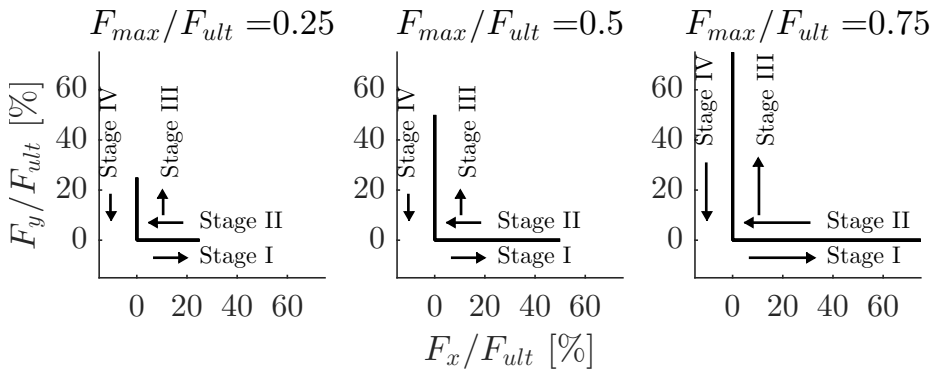

Figure 4.18.: Sketches showing considered multi-directional loading cases in the analyses

Effect of the maximum load experienced previously

Figure 4.19a shows a polar plot of the impact of the maximum load previously experienced on the profile of irreversible displacement around the pile at ground level ($z/L = 0$) at the end of stage IV. The simulations are performed considering that a gap occurs behind the pile. Several ratios of ultimate load are considered for stage I: $F/F_{ult} = 25$ %, 50 % and 75 %. Figure 4.19b illustrates the misalignment that occurs during stages III and IV between the applied load and the displacement directions. Obviously, there is no misalignment during stage I and stage II. In the figure, $\theta_{\text{load}} = 90°$ and θ_{displ} is defined as the angle of the resultant displacement with respect to the X-axis. It can be noticed that the higher the maximum load experienced previously, the greater is the effect of multi-directional loading. This misalignment reflects the fact that the pile does not move necessarily in the direction of the resultant load but moves towards the direction of least soil resistance (corresponding to the previous loading directions). This phenomenon has an impact when considering a macro-element to model the foundation in a structural design. This kind of modelling is used for example for natural frequency analysis (Arany et al., 2015). The stiffness matrix contains off-diagonal terms due not only to the coupling between displacements and rotations but also to the coupling between lateral displacements in different directions.

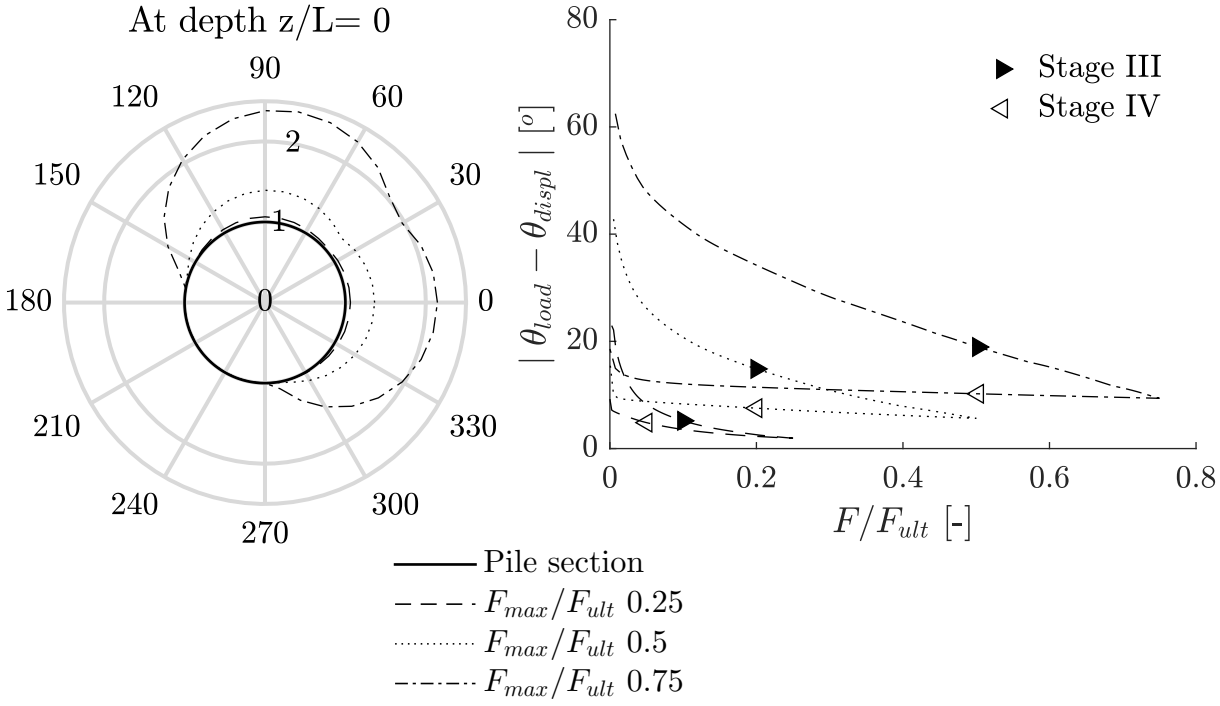

(a) Irreversible soil displacement at ground level around the pile at the end of Stage IV for various maximal load experienced previously when gapping occurs (amplified by a factor of 20 relative to the pile radius 1 m)

(b) Misalignment between load direction and total displacement direction versus F/F_{ult} for Stage III and Stage IV for various maximal load experienced previously when gapping occurs

Figure 4.19.: Numerical results of muli-directional loading sequence sketched in Figure 4.18

Effect of gapping

When gapping occurs, the pile irreversible displacement is less than the ”no gapping” case. However, the soil irreversible displacements are the same. Figure 4.20 illustrates the misalignment for both cases (with and without gapping) for two values of maximal load previously experienced: 50% and 75% of the ultimate load. It can be seen that when gapping occurs, misalignment at the beginning of stage III and at the end of stage IV depends on the maximum load experienced previously. On the contrary, when gapping does not occur, these two values do not depend on the maximum load experienced previously. A greater misalignment is found for the case without gapping.

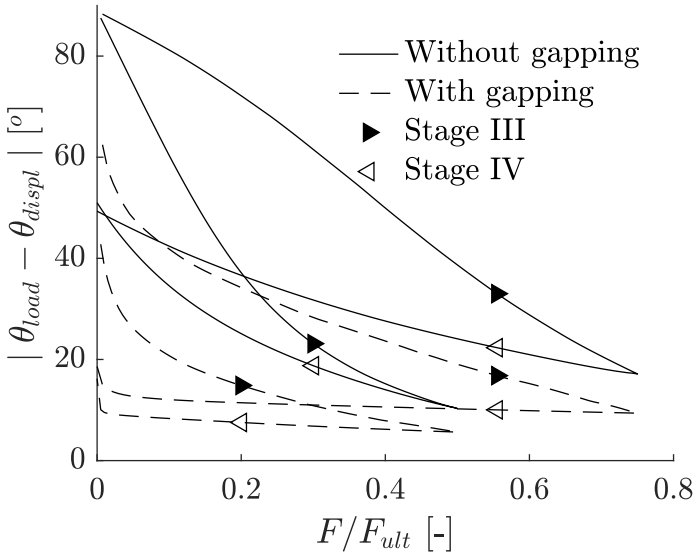

Figure 4.20.: Comparison of misalignment between load direction and total displacement direction versus F/F_{ult} for Stage III and Stage IV whether if gapping occurs or not

4.2.5 Impact of multi-directional loading on macro-element modelling and application for offshore wind turbine natural frequency analysis

The presented application case focuses on the impact of multi-directional loading on natural frequency analysis. The publicly available characteristics of the 5 MW wind turbine developed by National Renewable Energy Laboratory (NREL) are used in this application case. The monopile configuration is considered. For applications considering an integrated design (i.e. modelling the above structure and the foundation at the same time), it is common to define a macro-element which represents the response of the foundation at ground level. The methodology consists of first defining a macro-element which was subjected to a multi-directional loading sequence. In a second step, this macro-element is used as an input parameter for the natural frequency analysis. The problem is first described in terms of geometry and soil conditions. The soil conditions are used to derive the macro-element whereas the tower geometry and turbine characteristics are used for the natural frequency analysis. Then, the loading path used to derive the macro-element is presented, taking account of the impact of multi-directional loading. The assumptions for the macro-element are discussed and finally, the results of a sensitivity study are presented.

Studied problem (NREL 5 MW) geometry and soil conditions

The NREL 5 MW turbine is considered. The properties needed for the analysis can be found in Jonkman et al. (2009). The mass of the rotor-nacelle assembly (RNA) is taken to be 350 000 kg. The RNA inertias are assumed equal to 2.35×10^7 m^4 in the fore-aft plane and 4.35×10^7 m^4 for side-side motion (cf. Figure4.21). The structure is modelled using Euler beam elements with characteristics of the tower given in Jonkman and Musial (2010). The diameter and the thickness of the tower are assumed to be linearly tapered from base to top. The configuration with monopile in a sandy ground is considered here with the soil-pile-interaction model as described in Passon (2006). The layered soil conditions considered are described in Table 4.6 assuming the hyperbolic tangent formulation of the API-sand model (API, 2000). The initial stiffness and ultimate reaction vary with depth and are expressed as (API, 2000):

$$k = k_y \, z \tag{4.22}$$

$$P_u = 0.9 \min \left[(C_1 \, z + C_2 \, D) \, \gamma' \, z; C_3 \, D \, \gamma' \, z \right] \tag{4.23}$$

where k_y is the rate of increase of the subgrade reaction modulus, z the considered depth below ground level, C_1, C_2 and C_3 dimensionless constants depending on friction angle ϕ, D is the pile diameter and γ' represents the soil effective weight. These parameters are deduced for the multi-directional loading using Equations 4.13 and 4.15 and considering 36 springs around the pile periphery (one spring every 10°). For the frequency analysis, we model the macro-element considering the same loading conditions as in Passon (2006). These consist of a lateral load of 3 910 kN and a bending moment of 124 385 kN.m, and thus a lever

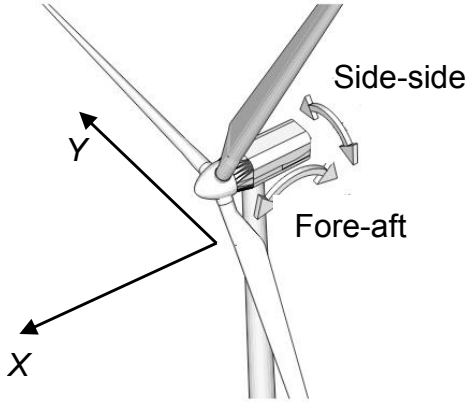

Figure 4.21.: Sketch showing directions of fore-aft and side-side modes on a wind turbine (after Knudsen et al. (2012))

Table 4.6.: Properties of the soil layered considered (Passon, 2006)

	Layer 1	Layer 2	Layer 3
Layer top	0 m	5 m	14 m
Layer bottom	5 m	14 m	∞
Effective unit weight γ'		10 kN/m^3	
Friction angle ϕ	33°	35°	38.5°
$P-y$ modulus gradient k_y [kN/m^3]	16287	24430	35288

arm of 32 m. Considering a lever arm of 32 m and the given $P-y$ curves (Equation 4.19) an ultimate lateral load of around 50 MN may be deduced with a corresponding bending moment of 1 600 MN.m. In the following the loading is expressed as a ratio of this ultimate lateral load.

Loading path

The following loading sequence is considered for the macro-element calculation (cf. Figure 4.22):

- Stage I: loading with a combined force and moment with an angle ψ with the X-direction;
- Stage II: unloading in the same direction to zero load and zero moment;

The macro-element is then calculated considering this pre-loading conditions.

Macro-element assumptions

The macro-element modelling consists of representing the whole foundation response below ground level with one stiffness matrix. In natural frequency analysis, we are only interested in small displacements and rotations (Bhattacharya and Adhikari, 2011) so that a linearisation of the response of the foundation is performed for the assumed pre-loaded

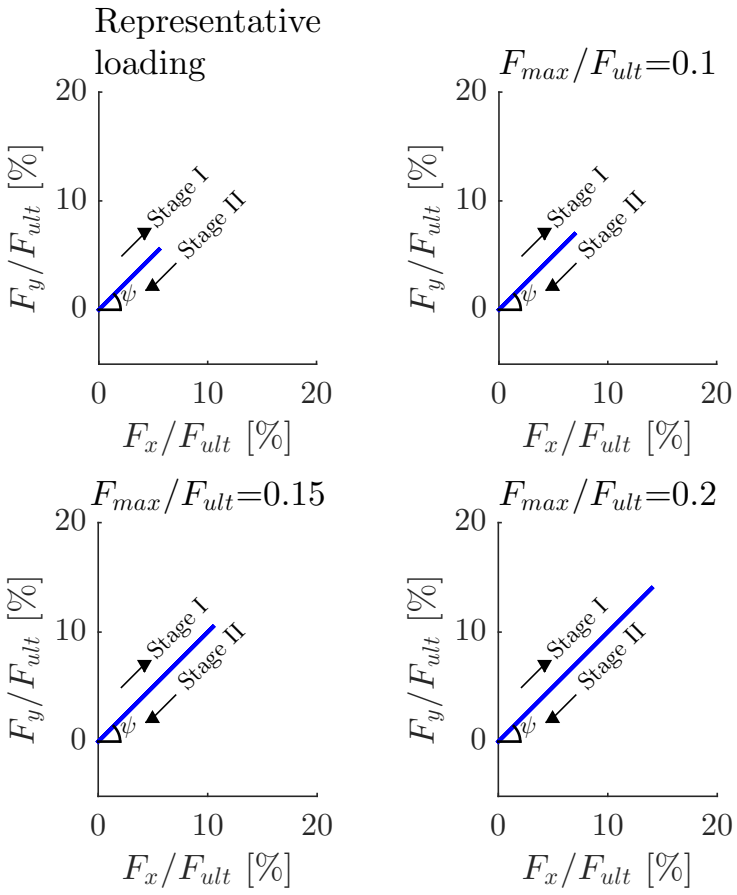

Figure 4.22.: Sketches showing considered pre-loading conditions in the analyses

conditions. In the case of monopiles for offshore wind turbines subjected mainly to lateral loading, the stiffness terms related to the degrees of freedom of vertical displacement and torsion are usually not considered. For a unidirectional loading the stiffness matrix of the macro-element (Equation 4.24) is symmetric and includes coupling terms between displacement in a given direction and the corresponding rotation. These coupling terms have a non-negligible effect on the natural frequency analysis (Arany et al., 2015). Note that for symmetry reasons the lateral stiffnesses in x and y-directions are equal as well as the rotational ones. Using the unidirectional model, the representative loads defined in Passon (2006) and the soil properties given in Table 4.6, we find $K_L = 1.87 \times 10^9$ N/m , $K_R = 1.95 \times 10^{11}$ N.m and $K_{LR} = 1.54 \times 10^{10}$ N.

$$\begin{bmatrix} K_L & 0 & 0 & -K_{LR} \\ 0 & K_L & -K_{LR} & 0 \\ 0 & -K_{LR} & K_R & 0 \\ -K_{LR} & 0 & 0 & K_R \end{bmatrix} \tag{4.24}$$

When multi-directional effects are considered, the stiffness matrix is no longer symmetric since the soil stiffness in the direction of a previous loading is altered. The general form of the stiffness matrix of the macro-element is:

$$\begin{bmatrix} F_x \\ F_y \\ M_x \\ M_y \end{bmatrix} = \begin{bmatrix} K_{xx} & K_{xy} & K_{x\theta_x} & K_{x\theta_y} \\ K_{yx} & K_{yy} & K_{y\theta_x} & K_{y\theta_y} \\ K_{\theta_x x} & K_{\theta_x y} & K_{\theta_x\theta_x} & K_{\theta_x\theta_y} \\ K_{\theta_y x} & K_{\theta_y y} & K_{\theta_y\theta_x} & K_{\theta_y\theta_y} \end{bmatrix} \begin{bmatrix} x \\ y \\ \theta_x \\ \theta_y \end{bmatrix} \tag{4.25}$$

where K_{XY} in the above matrix is equivalent to the force or moment X to apply corresponding to a displacement of 1 m or a rotation of 1 rad of the degree of freedom Y while the other degrees of freedom are equal to zero. Additional extra-diagonal terms appear when considering multi-directional loading. For example, an applied force in the x-direction, leads not only to a displacement along the x-axis and a rotation around the y-axis, but also to a displacement along the y-axis and a rotation around the x-axis.

Results and sensitivity study

The methodology presented in the previous section is implemented and a sensitivity study is performed. In the following the assumption that gapping occurs is done. The parameters that are considered to vary are: the level of loading applied during stage I, and the angle ψ of the direction of loading (counter clockwise from the X-axis). Figure 4.23 shows the dependency of the stiffness matrix of the macro-element with the angle of pre-loading for different level of loading experienced previously. For a clearer demonstration of the effects of multi-directional, each term of the stiffness matrix is normalised with respect to either K_{LL}, K_{RR} or K_{LR} as appropriate. It can be seen that the evolution of the lateral stiffness K_{xx} and K_{yy} with the loading direction are identical and just shifted by 90°. The same observation holds for the evolution of $K_{\theta_x\theta_x}$ and $K_{\theta_y\theta_y}$, and for the evolution of $K_{x\theta_y}$ and $K_{y\theta_x}$. Note that the terms corresponding to X and Y directions are different as opposed to the unidirectional case. Consequently, the fore-aft and the side-side natural frequency evolve differently. The effect of the multi-directional loading experienced during the loading sequence is a decrease of all the terms of the stiffness matrix as compared to the unidirectional model. For example, considering an initial loading during stage I of 20 % of the ultimate load, and depending on the loading direction, the lateral stiffness can be reduced up to 50 %, the cross-coupling terms up to 70 % and the rotational stiffness up to 88 %. The frequency analysis is performed on the macro-element obtained for given loading conditions as described above. As an example, we consider an applied loading in phase I that corresponds to either the representative loads or to 10, 15 and 20 % of the ultimate loading for an arbitrary direction ψ and evaluate the natural frequencies of the OWT. Figure 4.24 shows the dependence of 1st and 2nd mode natural frequencies (for-aft and side-ide) with the loading direction. We observe that the minimum side-side frequencies are shifted of 90° as compared for the fore-aft frequencies. Therefore, for a given loading direction ψ, one frequency is more altered than the other. For example, a previous applied loading of 20 %

of ultimate can lead to a decrease of fore-aft (respectively side-side) frequency of around 3.5 % (resp. 2 %) for the first mode and around 4.5 % (resp. 1 %) for the second one. The figure also shows that the fore-aft natural frequency is more impacted than the side-side frequency, which is due to the fact that the turbine is non-symmetric.

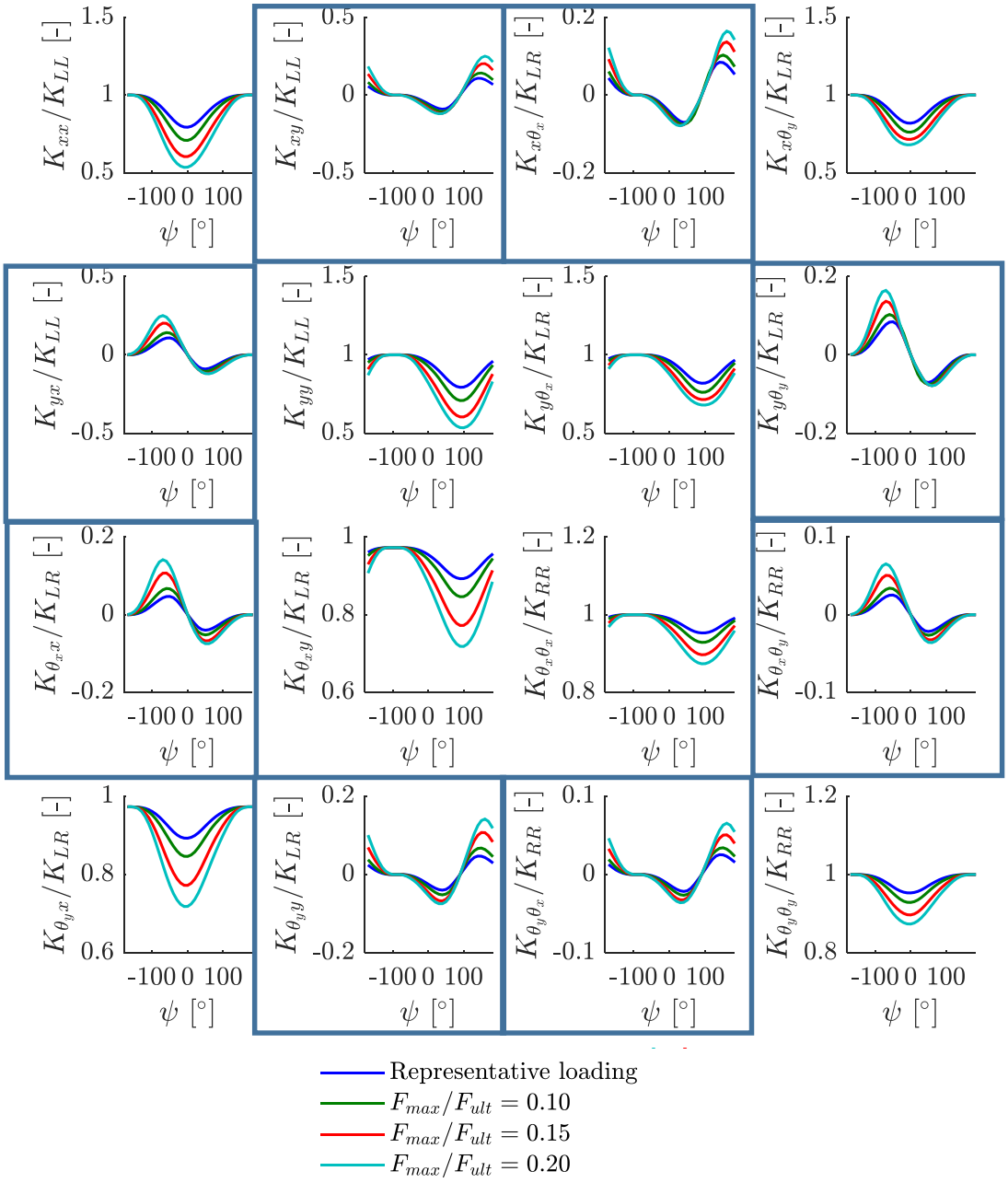

Figure 4.23.: Stiffness matrix of the macro-element: Effect of the angle of loading in stage III on the stiffness matrix terms of the macro-element for various maximum loads previously experienced in stage I. Solid frames correspond to the additional coupling terms due to multi-directional effects.

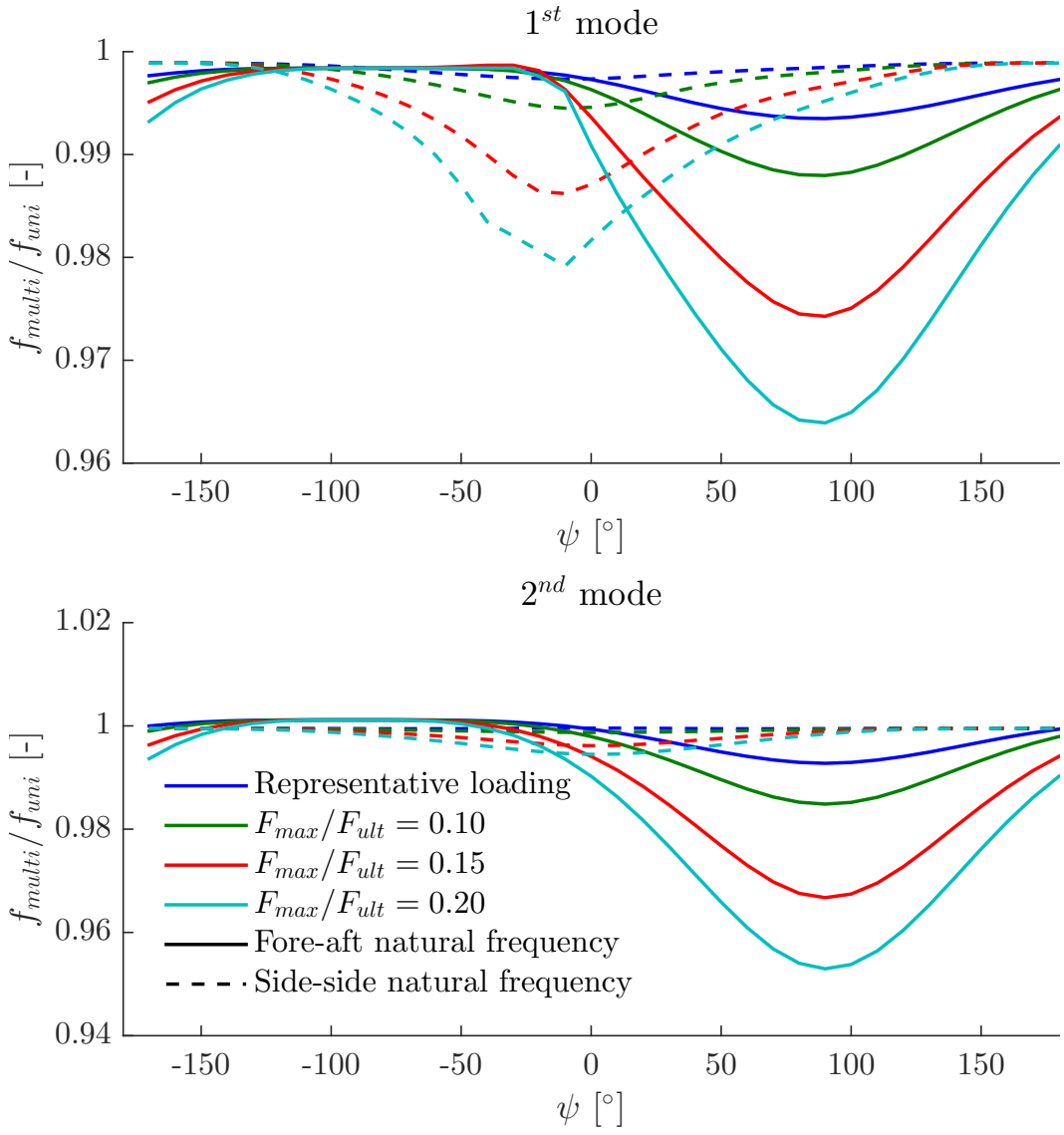

Figure 4.24.: Evolution of first (top) and second (bottom) mode for fore-aft (solid lines) and side-side (dashed lines) natural frequencies with angle of multi-directional loading for various maximum load levels experienced

4.2.6 Summary of the main findings

In this section, a new model is presented that enables better characterisation of multi-directional laterally loaded piles. The model is based on the classical approach of $P-y$ curves used to calculate laterally loaded pile response and extended to consider multi-directional loading. The advantage of the approach is its simplicity, as it provides a semi-analytical method that only requires information from unidirectional $P-y$ curves. The $P-y$ curves for multi-directional loading are deduced from the $P-y$ curves for unidirectional loading by assuming equality of the external work required for the two models. The model permits taking into account irreversible non-linear $P-y$ curves and the phenomenon of gapping. Its performance has been studied by comparing model predictions with experimental data presented by Su (2012) on reduced scale piles. The model parameters were first calibrated from the experimental results of unidirectional loading tests. The predictions for multi-directional loading have shown close agreement with the experimental data. The proposed model has been further validated by comparing with the numerical results of Levy et al. (2007). The Levy et al. (2007) model followed an energy-based variational approach and an elasto-plastic soil behaviour. The comparison presented here shows good agreement between the two approaches. The proposed model allows the key mechanisms involved in multi-directional loading to be captured, in particular the development of misalignment between the direction of loading and the lateral displacement of the pile. The advantages of the proposed model are the simplicity of the approach (with no further calibration of parameters required), its computational efficiency (similar to the unidirectional approach) and its ability to be implemented in an integrated design tool. In the present version of the model, soil remoulding around the pile due to loading is not considered. This should be addressed in future work as well as its extension to cyclic and hysteretic behaviour. Moreover, the present work only considers the effects of multi-directional loading for the response in translation (i.e. $P-y$ springs) but could be extended relatively simply to degrees of freedom in rotation ($M-\theta$ springs).

An application example is given herein, to assess the impact of taking into account multi-directional effects in calculating the stiffness matrix of a macro-element in an integrated structural design. We explore the effects of multi-directional loading on the natural frequencies of OWT using an extension of the load transfer ($P-y$ curve) approach to include the effects of multi-directional loading. The frequency analysis is based on the definition of a macro-element which accounts for pre-loaded conditions. This application case demonstrates that multi-directional loading leads to a reduction of a few percent of the 1st and 2nd modes frequencies. This could be (at least to some extent) a possible explanation of the shifting of the natural frequency as mentioned by Arany et al. (2015) during the first few months after installation, in addition to softening effects of the surrounding soil. A variation of 2-3 $\%$ could have significant effect if the designed natural frequency is situated close to the edges of the window of allowed values of the natural frequency.

4.3 Modelling cyclic behaviour

A simple procedure is presented herein for the extension of the classical $P-y$ curves framework to permit modelling cyclic behaviour. The classical $P-y$ curves framework considers reversible $P-y$ curves and does not permit modelling of irreversible displacements. The two different unloading paths implemented and shown in the previous section (see Figure 4.11) permit modelling of irreversible displacements but not cyclic accumulation. As creep and fatigue share important similarities, we explore the use of existing frameworks used to model creep response for cyclic response. There are several rheological models that enable modelling creep phenomena in more or less complex ways (Maxwell model, Kelvin-Voigt model or there stages creep model...). In this section, we implement rheological models in series with $P-y$ curves in order to model the cyclic response.

4.3.1 General methodology

First, the extension of the classical $P-y$ curves framework using rheological model in series to model the cyclic response is presented considering a simple Kelvin-Voigt model (cf. Figure 4.25). This rheological model permits modelling of an accumulation that reaches a stabilised state (i.e. a certain number of cycles after which the accumulation stops) similar to the sketch (c) in Figure 2.8. The Kelvin-Voigt model involves two parameters: a stiffness (E_1) that controls the maximum accumulated displacement when the stabilised state is reached and a viscosity η_1 that controls the rate at which the stabilised state is reached (the higher η_1 is, the slower the stabilised state is reached). The lateral displacement of the Kelvin-Voigt model y_1 and the soil reaction P are linked with the following differential equation:

$$P = E_1\, y_1 + \eta_1 \frac{\mathrm{d}y_1}{\mathrm{d}t} \tag{4.26}$$

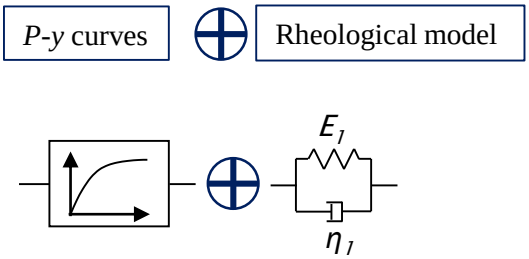

Figure 4.25.: Framework of the extension of the classical $P-y$ curves method to account for cyclic behaviour by adding time dependent rheological modelling (example presented with a single Kelvin-Voigt model in serie with the $P-y$ curve)

The finite difference method is used for solving the pile equilibrium equation (cf. Equa-

tion 2.5) and to express the lateral reaction of the soil P as a linear combination of the unknown (the lateral displacements at each node of the pile).

As the rehological model is time dependent, the loading is given as a function of time and each time step corresponds to a load step. For $P-y$ curves in series with a rheological model the soil reaction is applied to each of them and the total displacement is the sum of the displacement of each of them. As the $P-y$ curve is non-linear some iterations are needed at each time step. The following system of equations permits to express the soil reaction P_i at the iteration i of the time step $t+\mathrm{d}t$:

$$\begin{cases} P_i = P_{i-1} + E_{0,i-1}\ (y_{0,i} - y_{0,i-1}) \\ P_i = E_1\ y_{1,i} + \dfrac{\eta_1}{\mathrm{d}t}\ (y_{1,i} - \tilde{y_1}) \\ y_i = y_{0,i} + y_{1,i} \end{cases} \tag{4.27}$$

where for a quantity of interest X, X_i is the value of X at the iteration i of the time step $t+\mathrm{d}t$ and $\tilde{X}$ is the value of X at the previous time step. The various quantities of interest are: the total displacement y, the displacement corresponding to the $P-y$ curve element y_0 , the displacement of the visco-elastic element (Kelvin-Voigt model) y_1 , the force per unit length applied by the soil on the pile P, the tangent stiffness of the $P-y$ curve element $E_0(y_0)$, the stiffness of the visco-elastic element E_1 and the viscosity of the visco-elastic element η_1. This is a system of three independent equations with four unknowns, it is thus possible to express three of the unknowns as a function of the remaining unkown (the total displacement y_i). Introducing $\Delta = 1 + (E_1 + \eta_1/\mathrm{d}t)/E_{0,i-1}$, the reaction at iteration i of time step $t+\mathrm{d}t$ is expressed as a linear combination of the unknown y_i and variables that are known from the previous time step or from the previous iteration:

$$P_i = \frac{1}{\Delta}\left(1 + \frac{\eta_1}{\mathrm{d}t}\right)\ y_i + \frac{1}{\Delta}\left(1 + \frac{\eta_1}{\mathrm{d}t}\right)\left(\frac{1}{E_{0,i-1}}\ P_{i-1} - y_{0,i-1} - \frac{\eta_1}{\mathrm{d}t}\tilde{y_1}\right) \tag{4.28}$$

Figure 4.26 shows the flowchart of the extension of the classical $P-y$ curves in order to model the cyclic behaviour. It can be noticed that the $P-y$ curves are modified at the beginning of each time step depending on the solution at the previous time step, but remain the same during the iterations. Once the total displacement at iteration i is known at each node of the pile, the values of P_i, $y_{0,i}$ and $y_{1,i}$ are determined by solving the system of equations 4.27.

4.3.2 Implementation for OPT

For driven piles, the crushed rock plays an important role in the response and needs to be modelled. Similarly to what is done in section 4.1.3 two Kelvin-Voigt models are considered in series with the $P-y$ curve (cf. Figure 4.27). The first Kelvin-Voigt model is used to model the cyclic accumulation due to the crushed rock around the pile whereas the second

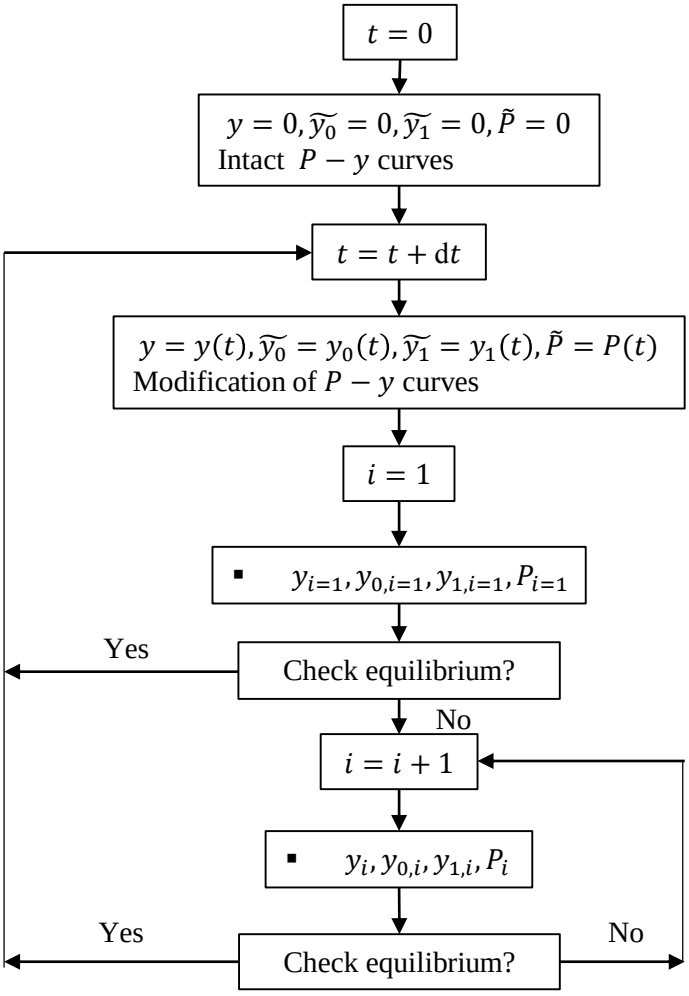

Figure 4.26.: Flowchart of the extension of the $P - y$ curves method for accounting of cyclic behaviour

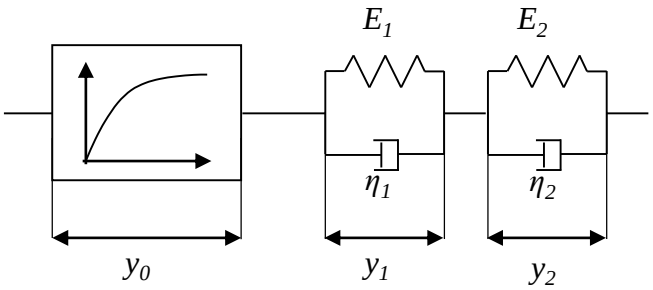

Figure 4.27.: Sketch of the rheological model considered for driven piles

Kelvin-Voigt model is used to model the accumulation due to the rock mass behaviour. For each element the following symplifying assumptions are done:

- For the $P-y$ curve a hyperbolic tangent function and an unloading path with gapping are considered. The $P-y$ curves are homogeneous along the pile depth. The $P-y$ curve is of the form of:
$$P(y) = P_u \tanh\left(\frac{ky}{P_u}\right) \tag{4.29}$$
where $k = 1\ 000$ MPa is taken as the average value of the stiffness determined in section 4.1.3 for driven piles of 35 mm of thickness and $P_u = 6$ MN/m (i.e. nominal pressure $P_u/D = 7.9$ MPa for a 0.762 m diameter pile) is determined as the value of maximum soil reaction that leads to the observed ultimate loading for the only pile that reached failure (pile P9) during monotonic loading.
- For the Kelvin-Voigt that models the crushed rock the two parameters are noted E_1 and η_1. They are considered constant along the depth of the pile. The compaction and the hardening of the crushed rock leads to limited accumulation which leads to a low value of η_1. The corresponding displacement y_1 of the Kelvin-Voigt model is assumed to only increase in absolute value.
- For the Kelvin-Voigt that models the soft rock the two parameters are noted E_2 and η_2. They are considered constant along the depth of the pile. Significant and long-term accumulation are expected for the soft rock which leads to a relatively higher value for η_2. The displacement y_2 of the Kelvin-Voigt model is assumed to only increase in absolute value.

Since the displacements (y_1 and y_2) are assumed to only increase, unloading would rise to a larger gap compared to non-cyclic loading sequence. There are thus four parameters to calibrate. Results of the cyclic tests done during OPT are used to determine these four parameters. As the Kelvin-Voigt models lead to a stabilised state only the first two or three series of cycles are considered (corresponding to cyclic maximum lateral load lower than 30 % of the ultimate load). The following procedure is adopted for the fitting and the validation:

i. Fit the four parameters (E_1, η_1, E_2 and η_2) for one of the 35 mm thickness steel tube driven piles for the first three series of cycles.
ii. Verify that the four parameters fitted at the step (i) lead to acceptable results for other driven piles with 35 mm thickness steel tube.
iii. Considering that the value fitted corresponds to the reference stiffness $E_{1,ref}$ for a reference thickness δ_{ref} of the crushed rock (i.e. a thickness of the pile tube), the stiffness of the Kelvin-Voigt model E_1 representing the accumulation due to the crushed rock for a given thickness of the crushed rock δ is determined with the following equation:
$$E_1 = \frac{\delta_{ref}\ E_{1,ref}}{\delta} \tag{4.30}$$

iv. Verify that the four parameters applied to another pile with a different pile tube thickness using Equation 4.30 lead to acceptable results.
v. Verify that the two parameters of the Kelvin-Voigt model representing the soft rock lead also to a good representatity of the results for a drilled and grouted pile.

This procedure permits to give good confidence in the values of the four parameters fitted. The quantity of interest fitted during this procedure is the displacement accumulated at the cylic maximum load. In the following, the relative displacement (displacement accumulated at the cyclic maximum load divided by the outer diameter of the pile) is plotted versus the number of cycles applied.

Validation for steel tube of 35 mm thickness

Figures 4.28a, 4.28b and 4.29 show the result of the calibration of the numerical modelling for three different piles with the same thickness of the steel tube for different successive series of cycles. It can be seen from these graphs that the numerical results and the results from OPT are in good accordance.

Validation for steel tube of 25 mm thickness

Figure 4.30 shows the results of the calibration of the numerical modelling for pile P4 that was not instrumented with an optical fibre and thus was thiner than the other piles. The stiffness of the Kelvin-Voigt model representing the crushed rock is calculated using Equation 4.30 and considering $E_{1,ref} = 100$ MPa and $\delta_{ref} = 35$ mm, which lead to $E_1 = 700$ MPa. The graph shows a good match between the experimental data and the numerical results.

Validation for drilled and grouted piles

Figure 4.31 shows the result for a cyclic test performed on a drilled and grouted pile. The numerical modelling consists of only one Kelvin-Voit model representing the behaviour of the soft rock. The same stiffness E_2 and the same viscosity η_2 determined during the calibration of driven piles are considered. The graph shows a good accordance between experimental data and numerical results. It should be noted that no fatigue behaviour of the grout is considered herein.

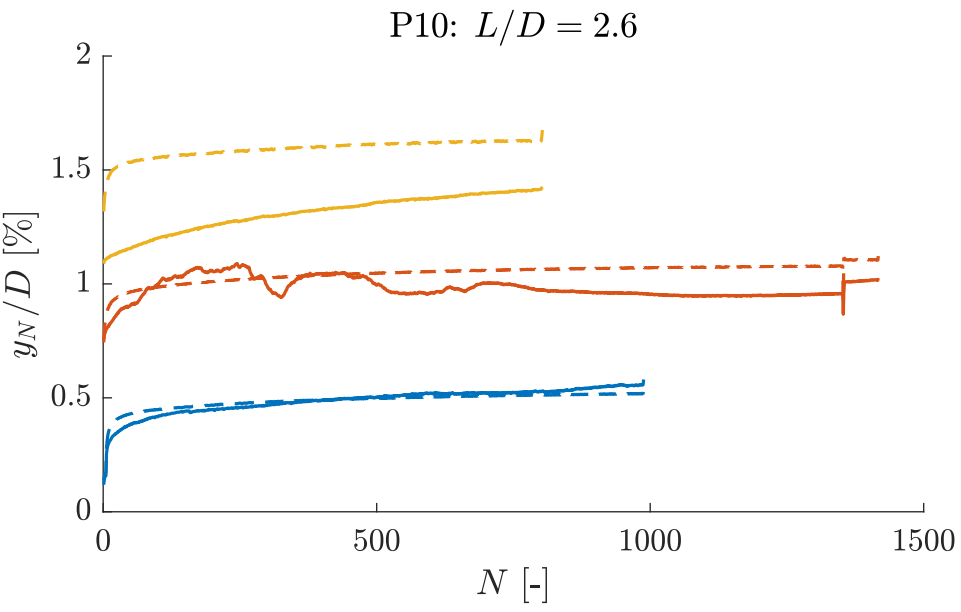

(a)

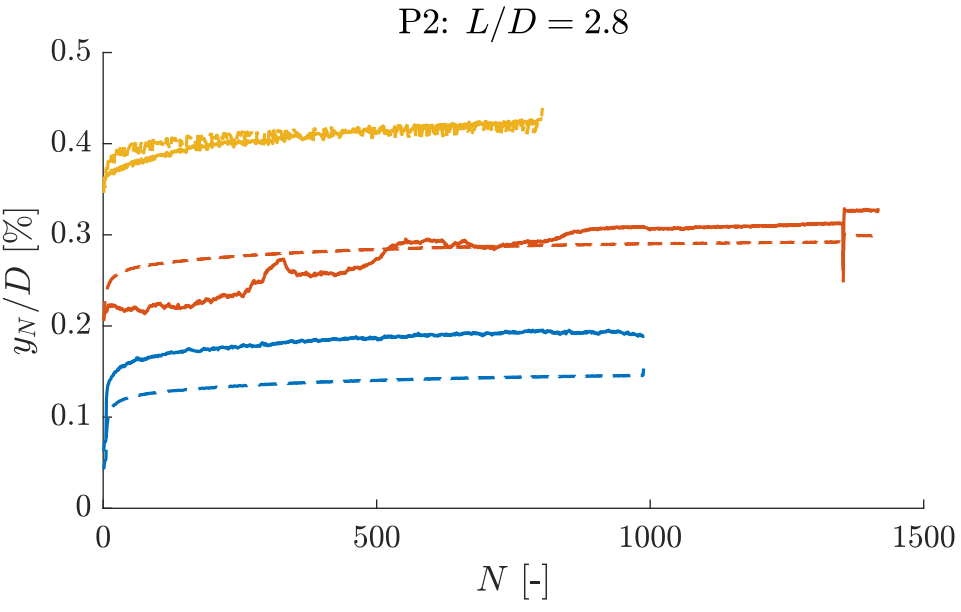

(b)

Figure 4.28.: Comparison between the OPT results in terms of relative displacement accumulated at the maximum cyclic load and the results of the numerical modelling considering two Kelvin-Voigt models in series with a hyperbolic tangent $P-y$ curve with $E_1 = 500$ MPa, $\eta_1 = 6 \times 10^3$ MPa.s, $E_2 = 1\,000$ MPa and $\eta_2 = 1.5 \times 10^6$ MPa.s

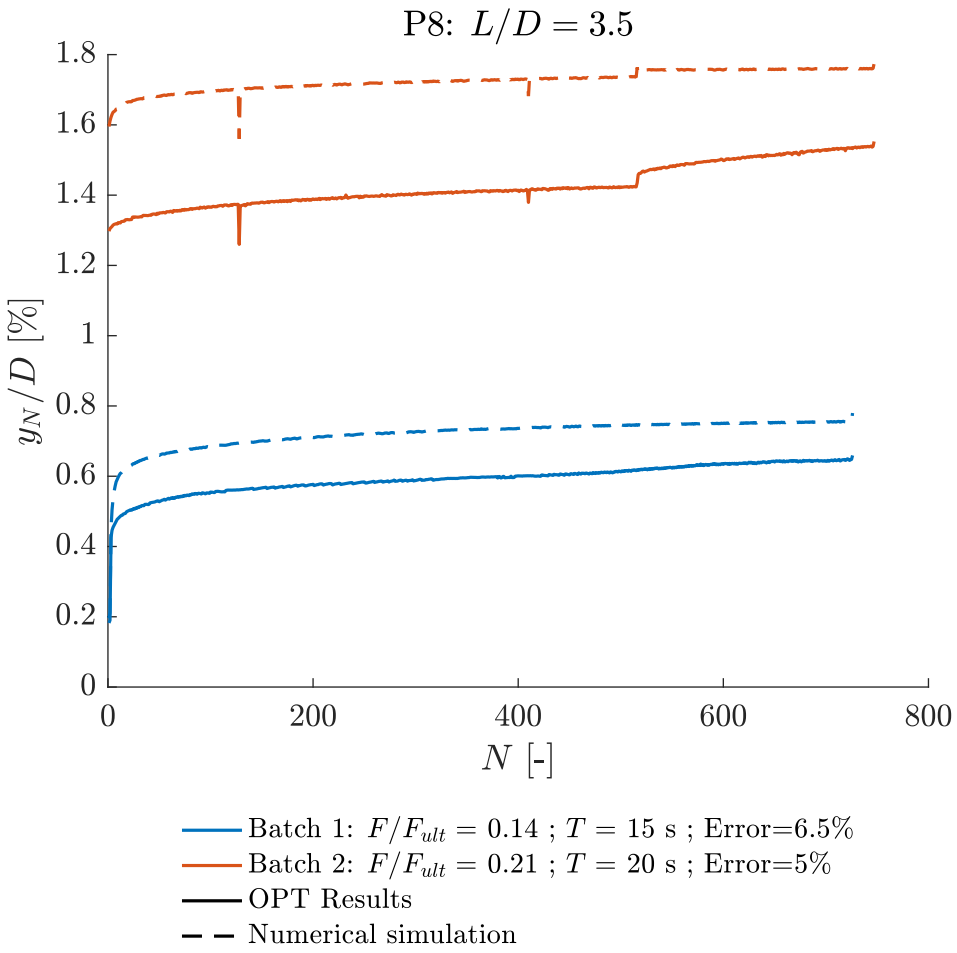

Figure 4.29.: Comparison for pile P8 between the OPT results in terms of relative displacement accumulated at the maximum cyclic load and the results of the numerical modelling considering two Kelvin-Voigt models in series with a hyperbolic tangent $P - y$ curve with $E_1 = 500$ MPa, $\eta_1 = 6 \times 10^3$ MPa.s, $E_2 = 1\,000$ MPa and $\eta_2 = 1.5 \times 10^6$ MPa.s

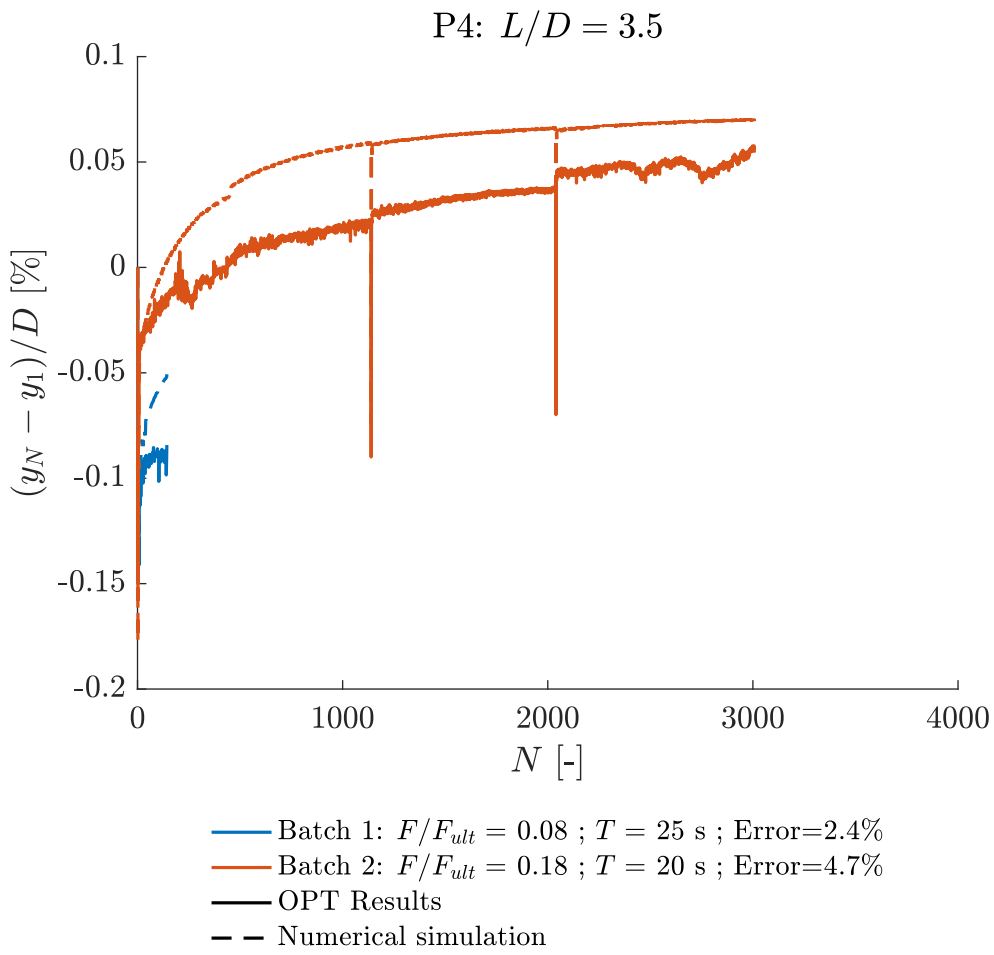

Figure 4.30.: Comparison for pile P4 between the OPT results in terms of relative displacement accumulated at the maximum cyclic load and the results of the numerical modelling considering two Kelvin-Voigt models in series with a hyperbolic tangent $P - y$ curve with $E_1 = 700$ MPa, $\eta_1 = 6 \times 10^3$ MPa.s, $E_2 = 1\,000$ MPa and $\eta_2 = 1.5 \times 10^6$ MPa.s

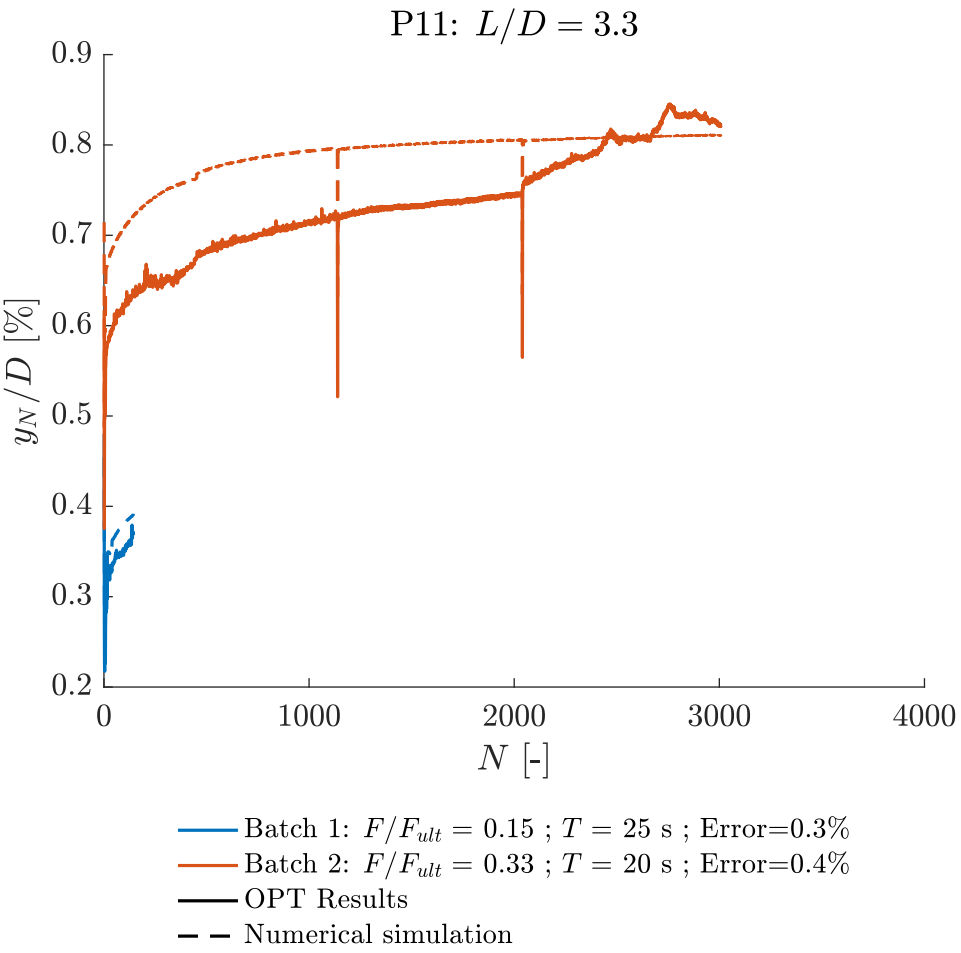

Figure 4.31.: Comparison for pile P11 between the OPT results in terms of relative displacement accumulated at the maximum cyclic load and the results of the numerical modelling considering one Kelvin-Voigt model in series with a hyperbolic tangent $P - y$ curve with $E_2 = 1\ 000$ MPa and $\eta_2 = 1.5 \times 10^6$ MPa.s

4.3.3 Summary of the main findings

The extension of the $P-y$ curves method to account for the cyclic behaviour is presented. The parameters of the different Kelvin-Voigt models (one for the crushed rock and one for the rock) are calibrated using one of the cyclic test results of a driven pile. Considering the same calibrated parameters for other cyclic tests leads to good accordance between the numerical results and the recorded data. Thus, the procedure undertaken allows good confidence in the values of the different parameters. It can be noted that this model is validated for different series of cycles with cyclic periods ranging from 8 to 25 s. Theses values are similar to cycles period encountered for cyclic loading due to waves. These developments are applicable for OWT design and it can be implemented in an integrated design tool. For example, equivalent $P-y$ curves can be deduced after a given cyclic loading and can be used as input $P-y$ curves in a natural frequency analysis (similarly to what is done in Erbrich et al. (2011)). At present, maintaining the load a certain amount of time or applying loading cycles will lead to the same stabilised state. However, this is not seen experimentally as greater accumulated displacements are shown for cyclic loading than for a maintained load at the same level. A non-linear modulus of the Kelvin-Voigt model would allow the model to address this observation but was not necessary to provide an adequate fit to the results of OPT. Finally, following the analogy with creep, the use of creep damage models would allow the model to account for unstable behaviour.

5 Finite element modelling

Summary

The numerical study using finite element modelling permits to account for the different phenomena identified during in-situ pile testing and to assess their potential effects on the response of the pile. The different physical mechanisms are first analysed in a 2D configuration in which a cross-section of the pile is modelled. This helps to better understand, in a qualitative manner, the impacts of each one: the creation of the crushed zone, the gapping behind the pile, the onset and propagation of cracks and the non-linear and irreversible response of the surrounding ground. The same mechanisms are then analysed in a 3D configuration. First, the numerical simulations are compared with the monotonic tests of the OPT, this allows validation of the main physical mechanisms at stake. Then, a sensitivity analysis is performed in order to assess the effect of the ratio of the diameter of the pile over the thickness of the pile.

Résumé

L'un des objectifs de l'étude numérique par éléments finis est de prendre en compte les différents phénomènes observés lors des essais de pieu et d'en quantifier les effets sur la réponse du pieu. Les différents mécanismes physiques sont d'abord analysés dans une configuration 2D dans laquelle une section transversale du pieu est modélisée. Cela permet de comprendre de manière qualitative, les impacts de chaque phénomène: la création de la zone de roche broyée, le décollement du pieu, l'apparition et la propagation des fissures dans le massif rocheux environnant et la réponse non-linéaire et irréversible du massif environnant. Ensuite, les mêmes mécanismes sont modélisés dans une configuration 3D. D'abord les simulations sont comparées aux résultats des essais de pieux statiques, ce qui permet de valider les mécanismes en jeu identifiés. Ensuite, une analyse est menée pour comprendre les effets d'un paramètre adimensionnel: le rapport entre le diamètre et l'épaisseur du pieu.

5.1 Model set up

The finite element code Code_Aster (www.code-aster.org) is used for numerical simulation in association with Salome-Meca for geometry and mesh building. The 2D finite element (FE) modelling is aimed at quantifying the influence of major phenomena identified during the OPT on the global response: (i) the creation of crushed rock annulus during the driving process; (ii) the creation of gapping behind the pile; (iii) the onset and propagation of cracks; (iv) the non-linear response of the ground. Each phenomenon is added step by step in the model to quantifiy the corresponding effect on the global response.

5.1.1 Geometry of the 2D model

The considered geometry in the 2D FE modelling is a cross-section of a laterally loaded pile (see Figure 5.1). The pile section is a tube. The different geometric dimensions used in the following are given in Table 5.1. Plane strains are assumed. For lateral loading of the pile, it has been identified in Baguelin et al. (1977) that the solution depends on the size of the model. This is an artefact of the 2D approach which is observed both for the analytical solution and the numerical one. This point is discussed in Appendix F. Nevertheless, even if the results from 2D FEM modelling are qualitative, they are useful for understanding the effects of the various mechanisms involved.

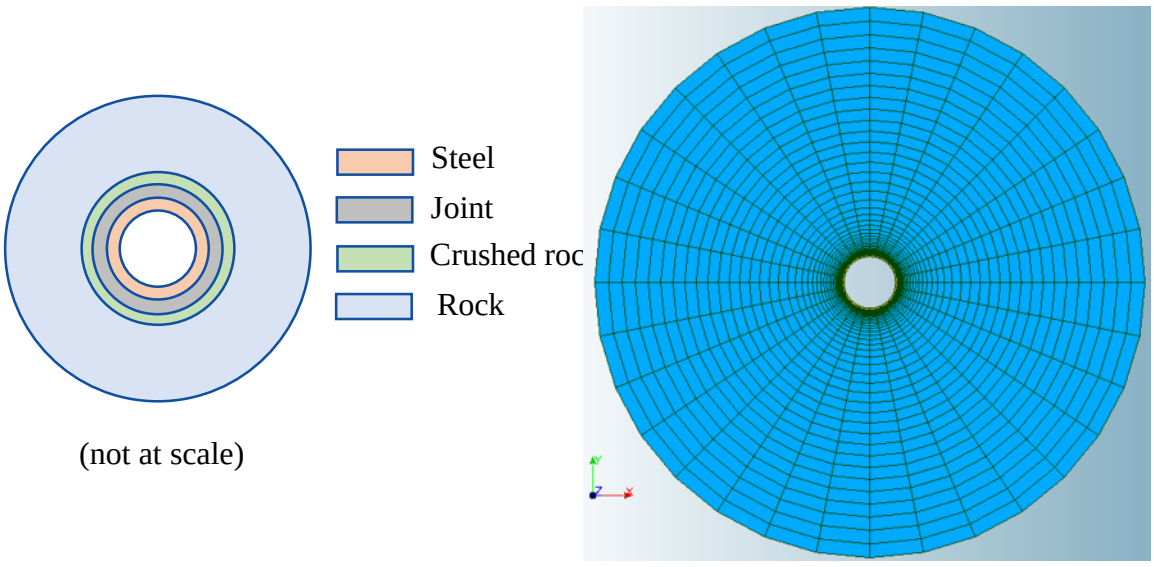

Figure 5.1.: FE geometry and mesh for the 2D analyses

Table 5.1.: Parameters of the geometry of the 2D model

Description	Symbol	Value	
Outer diameter of the pile	D	1.2	m
Thickness of the pile tube	t	35	mm
Thickness of the joints elements	e	1	mm
Thickness of the crushed rock	t_c	35	mm
Outer radius of the 2D model	R	30	m

5.1.2 Boundary conditions

An isotropic initial stess field σ_0 is imposed. The horizontal load is applied in a displacement-controlled manner, by prescribing increments of uniform displacement to all the nodes belonging to the pile cross-section. The corresponding lateral load is obtained as a reaction to the applied horizontal displacements. Far field boundary conditions are applied by setting to zero the displacements on the outside boundary of the model.

5.1.3 Material behaviour

Four different zones are considered in the FE mesh corresponding to different materials: the steel pile, the pile-soil interface, the crushed rock and the rock. These zones are discretised with linear hexagonal isoparametric finite elements. The pile is considered to be linear elastic with a Young's modulus of 210 GPa and a Poisson's ratio of 0.3. The pile-soil interface is simulated using Mohr-Coulomb joint elements for which the constitutive behaviour is described in section 5.1.4. The radial cracks in the rock are simulated using cohesive joint elements with the constitutive behaviour described in section 5.1.5. For modelling the non linear behaviour of the crushed rock and the surrounding rock, a Drucker Prager elasto-plastic model with an associate flow rule is assumed. The mechanical properties of the rock and of the crushed rock are given in Table 5.2. Drucker-Prager yield criterion can be written as follows (R7.01.16, 2013):

$$f(\sigma, \gamma^p) = \sqrt{3\ J_2} + A\ I_1 - R(\gamma^p) \leq 0 \tag{5.1}$$

where σ is the Cauchy stress tensor, γ^p is the accumulated plastic strain, J_2 is the second invariant of the deviatoric part of the Cauchy stress, I_1 is the first invariant of the Cauchy stress, A is a given friction coefficient and R is a hardening function of the accumulated plastic strain of linear type:

$$R(\gamma^p) = \sigma_y + h\ \min\left(\gamma^p, \gamma^p_{ult}\right) \tag{5.2}$$

In our case, no hardening or softening are considered for both the rock and the crushed rock but these parameters can be used for computational efficiency of the numerical calculations

Table 5.2.: Parameters of the rock and the soft rock for the two kinds of model (elastic and elasto-pastic)

Material behaviour		Rock	Crushed rock
Elastic	E	5 GPa	60 MPa*
	ν	0.3	0.3
Drucker Prager elasto-plastic	A	0.42	0.36
	σ_y	3.43 MPa	0 MPa

*60 MPa corresponds to the average value of the crushed rock modulus calibrated in section 4.1.2 in order to fit the inital response of the OPT

provided that it does not affect the response (i.e h chosen as large as possible without the response being impacted when considering the numerical results for $h = 0$). A and σ_y can be expressed as functions of the friction angle φ and the cohesion c:

$$\begin{cases} A = \dfrac{2 \sin \varphi}{3 - \sin \varphi} & \text{(5.3a)} \\ \sigma_y = \dfrac{6\, c \cos \varphi}{3 - \sin \varphi} & \text{(5.3b)} \end{cases}$$

More details on how this constitutive behaviour is implemented in Code_Aster are given in R7.01.16 (2013).

5.1.4 Modelling of the gap behind the pile

In order to model the gapping behind the pile, the points belonging to the interface between the pile and the surrounding soil must satisfy the conditions of unilateral contact. These conditions are generally known as the Signorini conditions and can be written as follow:

$$\begin{cases} \delta_n \geq 0 & \text{(5.4a)} \\ \sigma_n \leq 0 & \text{(5.4b)} \\ \delta_n\, \sigma_n = 0 & \text{(5.4c)} \end{cases}$$

Where δ_n is the gap between the pile and the soil and σ_n the normal reaction at the interface. Inequality 5.4a prevents inter-penetration of the pile and the soil, and if the pile and the soil are in contact ($\sigma_n < 0$) the normal displacement is 0 according to Equation 5.4c. Inequality 5.4b sets that gapping occurs as soon as the normal reaction reaches 0, and once gapping occurs the normal reaction equals 0 according to Equation 5.4c. In addition, a constitutive behaviour for the tangential components of the interface (δ_t tangential displacement and σ_t the tangential reaction of the interface) can be considered. Mohr-Coulomb friction law which depends on only the friction coefficient μ is considered.

$$|\sigma_t| = \mu\, \sigma_n \tag{5.5}$$

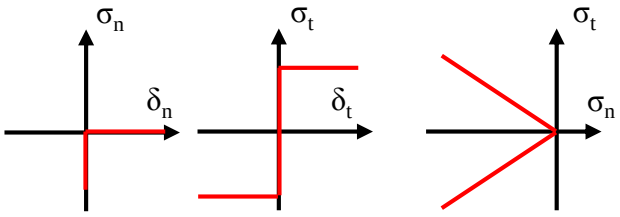

(a) Ideal Signorini conditions and Mohr-Coulomb criterion

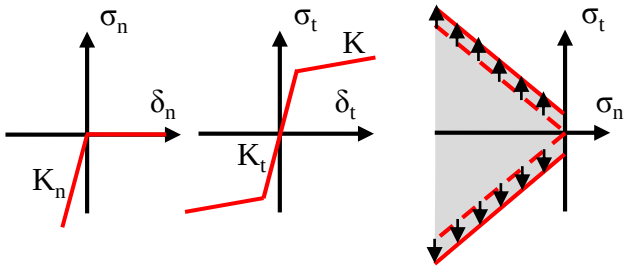

(b) Penalty method for the numerical implementation of the Signorini conditions and hardening of the Mohr-Coulomb criterion

Figure 5.2.: Graphical representation of the normal components and the tangential components after R7.01.25 (2016)

Figure 5.2 shows how the Signorini conditions (Equations 5.4) are implemented numerically. In Code_Aster, the penalty method is used and the implemented law is called JOINT_MECA_FROT. More details can be found in R7.01.25 (2016). The 2D formulation is written as follows:

$$\begin{cases} \delta_t = \delta_t^{el} + \delta_t^{pl} & \text{(5.6a)} \\ \sigma_t = K_t\ \delta_t^{el} = K_t\ \left(\delta_t - \delta_t^{pl}\right) & \text{(5.6b)} \\ \sigma_n = \min\left(K_n\ \delta_n; 0\right) & \text{(5.6c)} \end{cases}$$

where K_n is the normal rigidity, K_t is the tangential rigidity with the assumption that the response of the interface is elastic before gapping occurs. The yield surface and flow rule of the model are expressed as:

$$\begin{cases} f(\sigma, \lambda) = |\sigma_t| + \mu\ \sigma_n - K\ \dot{\lambda} & \text{(5.7a)} \\ f\ \dot{\lambda} = 0 \text{ with } \dot{\lambda} \geq 0 & \text{(5.7b)} \\ \delta_t^{pl} = \dot{\lambda}\ \dfrac{\sigma_t}{|\sigma_t|} & \text{(5.7c)} \end{cases}$$

where K is a hardening parameter introduced to regularise the tangential sliding slope and $\dot{\lambda}$ is a plastic multiplier. It can be noted that elasto-plastic behaviour is only implemented for the tangential displacement and that the normal displacement is always elastic. This constitutive law is implemented for joint elements that need to be oriented and meshed as quadrilateral surface elements (with a given thickness and a single element in the thickness). A thickness of 1 mm is considered for these joints elements around the pile. The values of $K = 10^7$ Pa/m and $K_n = K_t = 10^{12}$ Pa/m are calibrated (see details of the calibration in

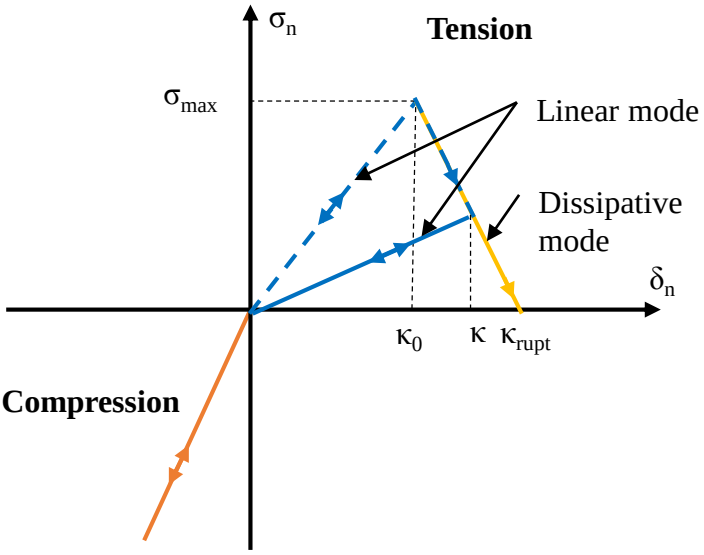

Figure 5.3.: Normal and tangential behaviour of a cohesive formulation of the rupture after R7.01.25 (2016)

Appendix E.1). The value of the friction coefficient μ equals 0.35 (a sensitivity study on this parameter is presented in the Appendix E.2).

5.1.5 Modelling the onset of radial cracking

In order to model potential onset of cracking around the pile one possibility is to introduce pre-existing cohesive joints (cf. Figure 5.3). The normal behaviour of the cohesive joints is defined in Figure 5.4a. Under compression the response is elastic (i.e $\sigma_n < 0$). Under tension, the normal stress depends on the normal displacement jump of the lips of the crack δ_n and on the internal variable κ which is the maximum normal displacement δ_n experienced during the opening. Two parameters control the normal behaviour: the rupture threshold σ_{max} (reached for $\delta_n = \kappa_0$) and the critical strain energy release G_c. The tangential behaviour of the cohesive joints is defined in Figure 5.4b and the parameter α defines how the tangential stiffness varies with the normal behaviour of the joint. In Code_Aster the implemented law is called JOINT_MECA_RUPT and more details about its numerical implementation can be found in R7.01.25 (2016). A thickness of 1 cm is taken for these cohesive joints. A first calculation is done considering a normal stiffness that equals 2.5×10^{10} Pa/m and a rupture threshold of 100 MPa, purposely high, in order to verify that the radial cohesive joints do not damage or open and that the lateral stiffness is not affected by these radial joints compared to the elastic modelling. Here, a thickness of 1 cm and a normal stiffness of 2.5×10^{10} Pa/m are used in the following. A tensile threshold σ_{max} of 1 MPa is considered. The crititical strain energy release can be expressed depending on the fracture toughness and the Young's modulus of the rock as $G_c = K_{Ic}^2/E$. Considering a fracture toughness ranging between 0.8 and 1 MPa.$\sqrt{\text{m}}$ (current values for carbonate rocks) and a Young's modulus of 5 GPa leads

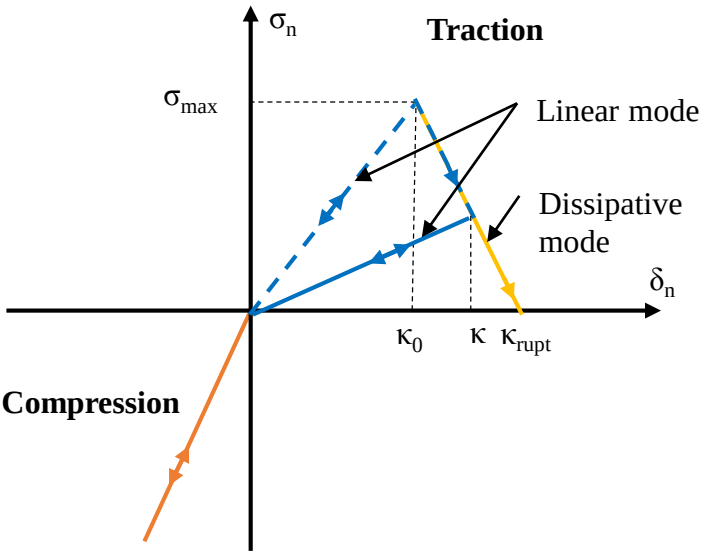

(a) Normal stress function of the normal jump between the two lips of the crack

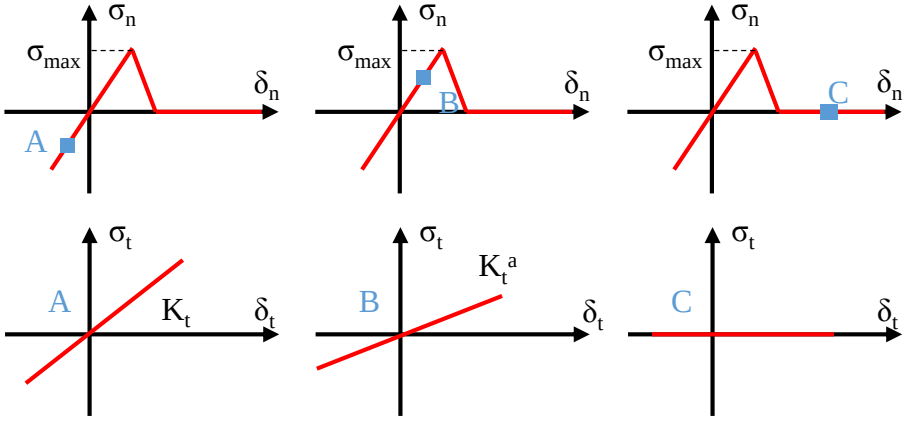

(b) Graphical reprensetation of the coupling between the normal opening of the joint and the tangential component with $K_t^a = \left(1 - \frac{\delta_n}{\kappa_{\text{rupt}} \tan \alpha\pi/4}\right)$ with $\alpha \in]0, 2]$

Figure 5.4.: Graphical representation of the normal components and the tangential components for the cohesive formulation after R7.01.25 (2016)

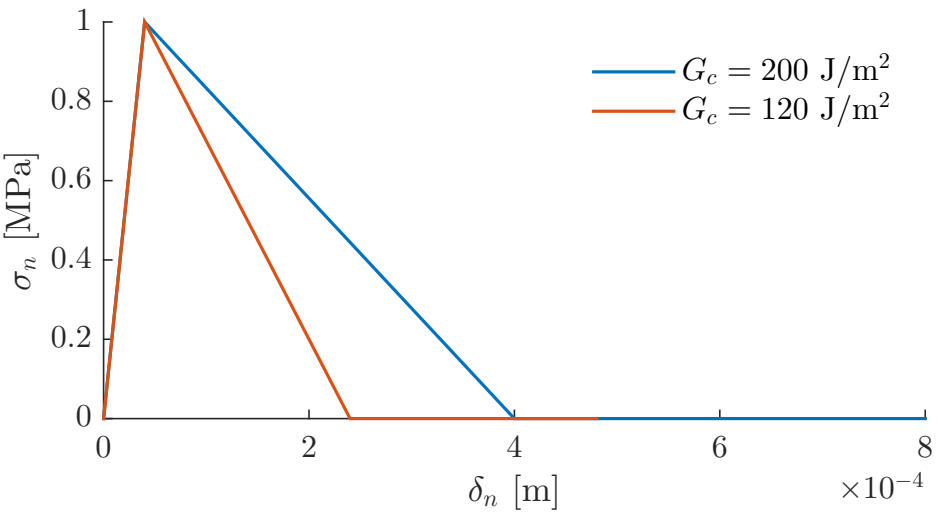

Figure 5.5.: Different normal behaviour of the radial cracks depending on the critical strain energy release

to a crititcal strain energy release ranging between 120 and 200 J/m^2. Figure 5.5 shows the corresponding normal behaviour for these two values. Two different values of parameter α (see Figure 5.4b) are considered in the following ($\alpha = 1$ or 2).

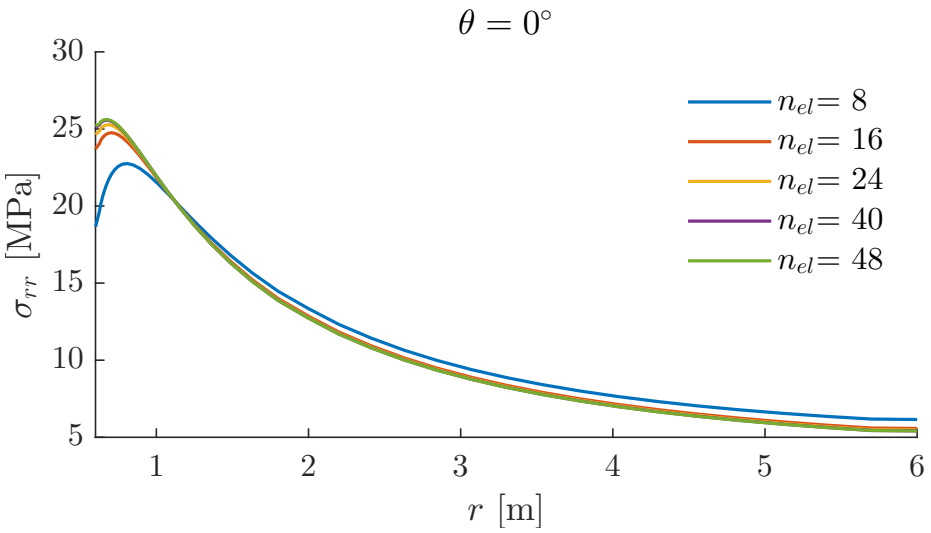

Figure 5.6.: Mesh dependency

5.2 2D numerical results

5.2.1 Validation

Mesh dependency

Even though the numerical results depend on the extent of the model (see Appendix F), for a given size of the model the results should not depend on the discretisation. A mesh sensitivity analysis is therefore performed on the intact configuration without gapping. The driving parameter is the number of elements n_{el} on the circumference. Figure 5.6 shows the radial stress along the axis of loading for various values of n_{el}, showing that above 40 elements mesh dependency vanishes. This value of n_{el} is fixed for the following computations.

Accuracy

The accuracy of the 2D numerical model is assessed by comparison of the numerical results to the analytical solutions given by Baguelin et al. (1977). Figures 5.7, 5.8 and 5.9 show the comparison of the model with the analytical solutions for the radial, the tangential and the shear stress in the case of the intact ground (i.e without crushed rock around the pile) and without gapping.

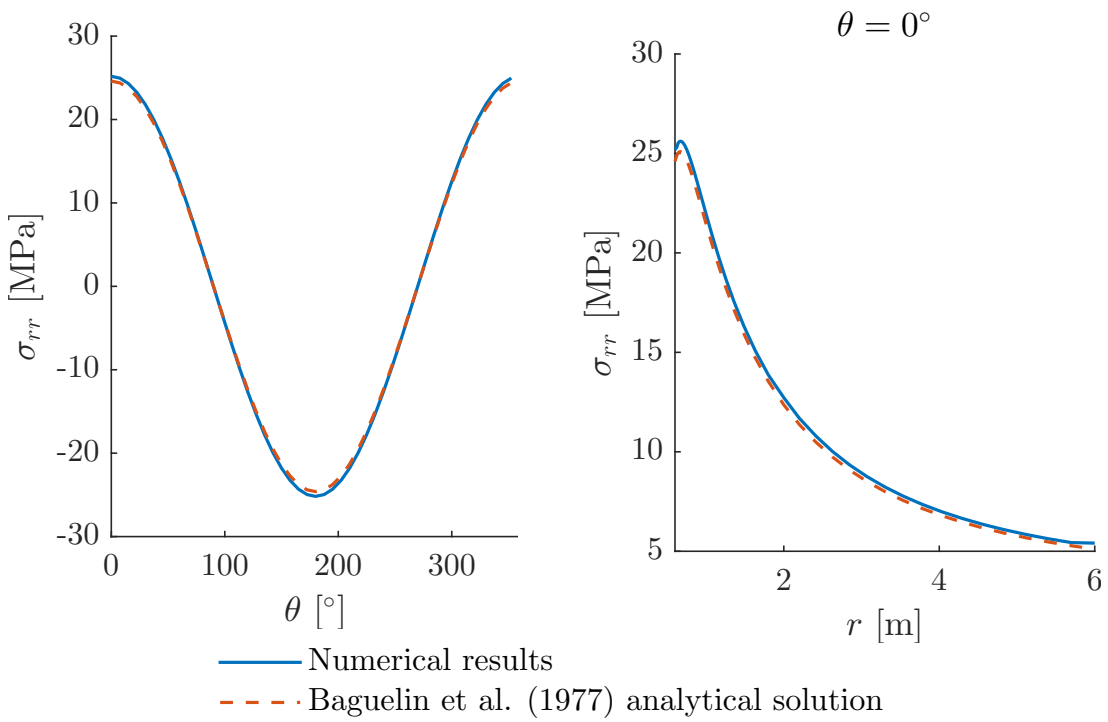

(a) Stress profile around the pile **(b)** Stress profile along loading axis

Figure 5.7.: Comparison of the radial stress

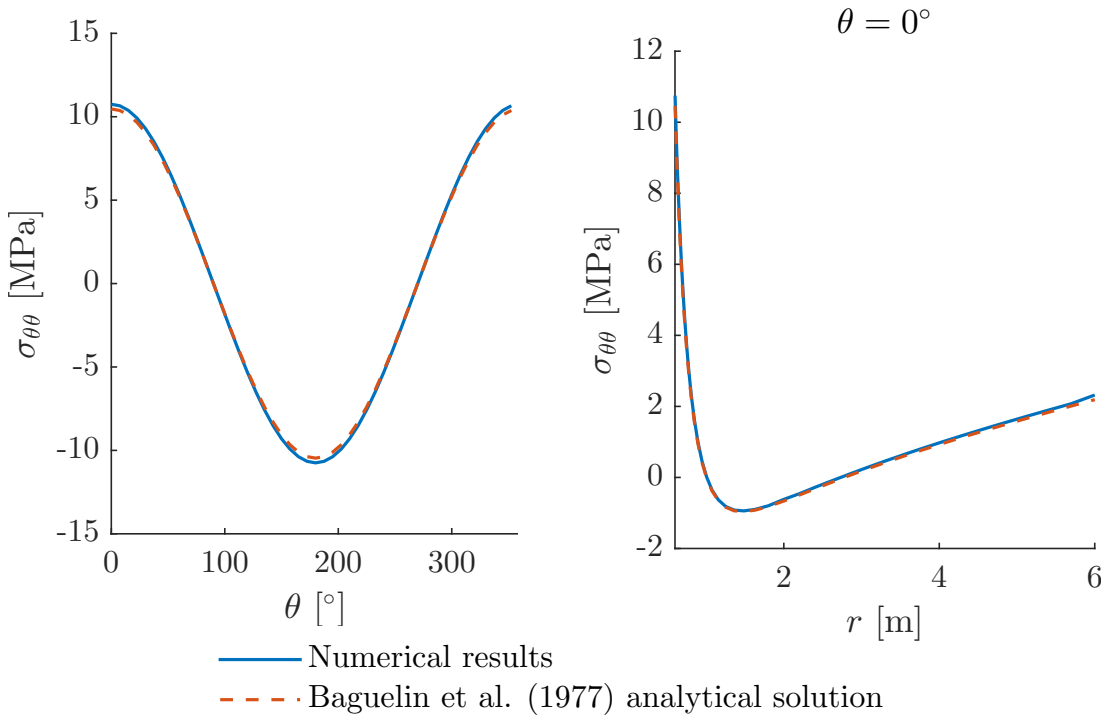

(a) Stress profile around the pile **(b)** Stress profile along loading axis

Figure 5.8.: Comparison of the tangential stress

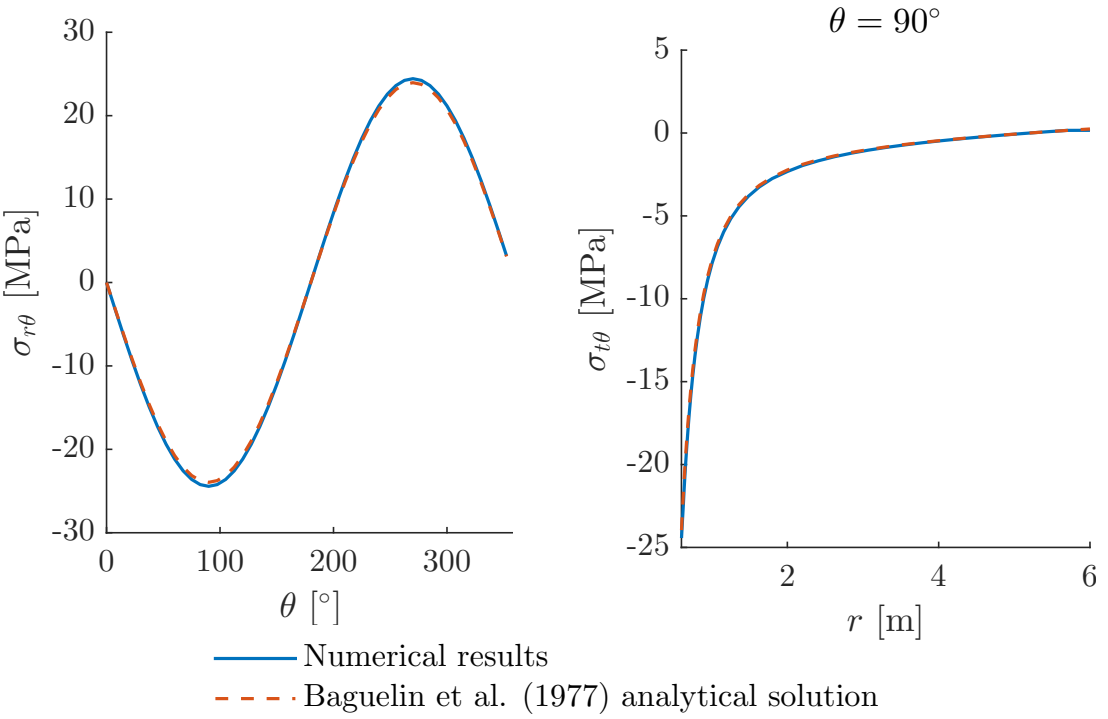

(a) Stress profile around the pile

(b) Stress profile perpendicular to the loading axis

Figure 5.9.: Comparison of the shear stress

5.2.2 Effects of the crushed rock and of the gap behind the pile on the global response

Comparison between the four models

In the following, four models are compared: with and without crushed rock around the pile, initially taking $t_c/t_p = 1$, and for each of these two models two cases are considered: with or without gapping. For the models considering gapping behind the pile there is an effect of the initial confinement σ_0. Indeed, for low confinement (cf. Figure 5.10a) the sliding regime of the joint elements is reached at the first calculation step whereas for higher initial confinement (cf. Figure 5.10b) the sliding regime of the joint elements is reached after a given lateral displacement and thus two slopes are seen in the global response. The first slope corresponds to the pile-soil stiffness without sliding whereas the second slope corresponds to the pile-soil stiffness with sliding occuring along the joint elements. In terms of evolution of the $P - y$ stiffness (slope of the global response), the following observations can be made: for models without crushed rock, considering gapping leads to a decrease of 40 % of the $P - y$ stiffness. For models without gapping, considering crushed rock leads to a decrease of 55 % of the stiffness. For the model with crushed rock and with gapping compared to the model without crushed rock and without gapping, the decrease of the stiffness is around 80 %. The total reaction $F_{tot} = F_f + F_{tg}$ at a given radius r_0 can be

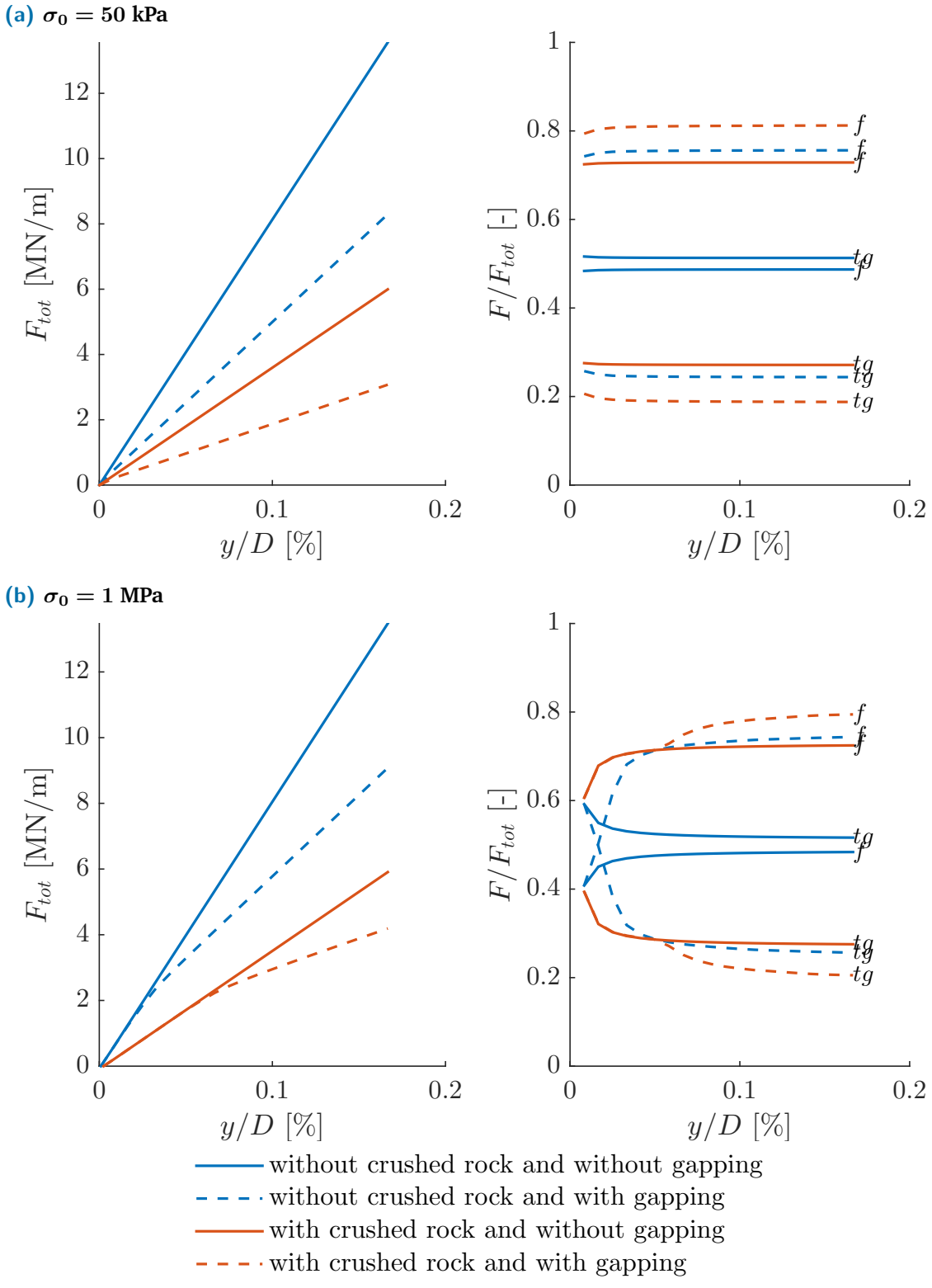

Figure 5.10.: Comparison of the global response (left) and the frontal (noted f) and tangential (noted tg) proportions in the total reaction (right) for various values of initial confinement

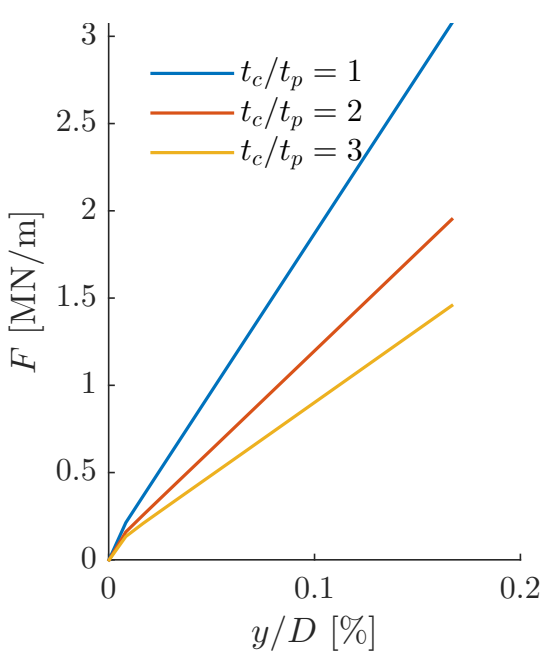

(a) Forve versus lateral displacement curve for various values of the thickness the crushed rock

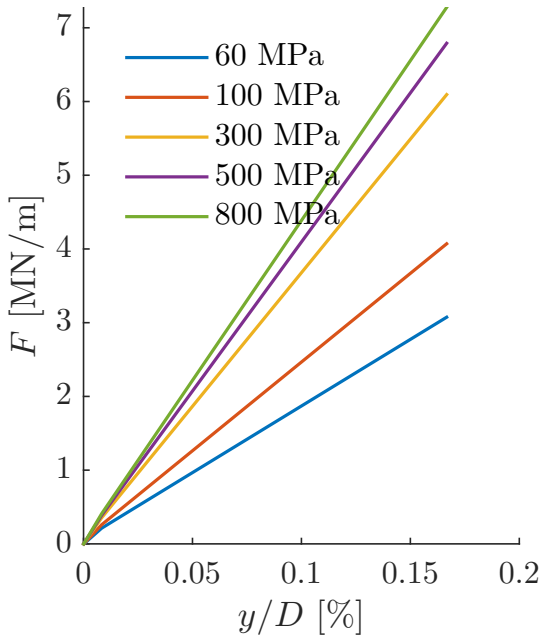

(b) Forve versus lateral displacement curve for various values of the Young's modulus of the crushed rock

Figure 5.11.: Sensitivity study of numerical parameters of the crushed rock (thickness of the zone and Young's modulus)

separated in two terms: the frontal reaction F_f and the tangential reaction F_{tg} calculated as follows:

$$F_f = \int_0^{2\pi} r_0 \sigma_{rr}(r_0;\theta)\cos\theta \mathrm{d}\theta \tag{5.8a}$$

$$F_{tg} = -\int_0^{2\pi} r_0 \sigma_{r\theta}(r_0;\theta)\sin\theta \mathrm{d}\theta \tag{5.8b}$$

It can be seen that for the model without crushed rock and without gapping, both reactions (frontal and tangential) contribute to approximately the same amount to the total reaction (50 % - 50 %). The creation of the crushed rock around the pile and the creation of gapping behind the pile lead both to a decrease of the proportion of tangential reaction in the total reaction with a proportion around 70 % for the frontal reaction and thus 30 % for the tangential one. Not only accounting for the crushed zone as well as the gapping changes the lateral stiffness of the system but also the way the ground is loaded for the same imposed lateral displacement.

Sensitivity study on the thickness of the crushed rock

The thickness of the crushed zone is not a well-constrained parameter. Figure 5.11a shows the global response for various ratios of thickness of the crushed rock t_c compared to the thickness of the pile t_p. This parameter has a strong impact on the results, with the lateral stiffness decreasing by around 55 % as t_c/t_p is increased from 1 to 3.

Sensitivity study on the mechanical properties of the crushed rock

An estimation of the modulus can be obtained from an oedometer test performed on the crushed rock (see Figure 3.15 in section 3.2.2). However, one can imagine that the properties of the crushed rock created during the driving process during the installation procedure can vary with the type of rock, the geometry of the pile and the level of loading. It is thus an uncertain parameter and a sensivity study is undertaken in order to assess the influence of this value on the lateral stiffness. The range of values explored during this study is the range of values of oedometer modulus calculated for various displacement, for the case of $t_c/t_p = 1$. Figure 5.11b shows the results in terms of force versus lateral displacement. It can be noticed that, as expected, an increase of the modulus leads to an increase of the lateral stiffness. From a value of 60 MPa to a value of 100 MPa (i.e an increase of 66 $\%$), the lateral stiffness increases by 33 $\%$. However, for higher modulus the effect is less pronounced, which is explained by the fact that the controlling parameter is actually the ratio between the modulus of the crushed rock and the modulus of the surrounding rock.

5.2.3 Effect of radial cracks on the global response

The geometry with the radial joints consists of the cross-section of the pile, the joints around the pile that permits gapping to occur, the crushed rock zone and the surrounding rock. What differs from previous numerical simulations, is that in the rock, some radial cohesive joints are added which permits the radial cracks to potentially open. Figure 5.12 shows the considered geometry; different configurations of radial cracks are shown in which θ is the angle between two neighbouring radial cracks. The behaviour of these radial cracks is those described in section 5.1.5.

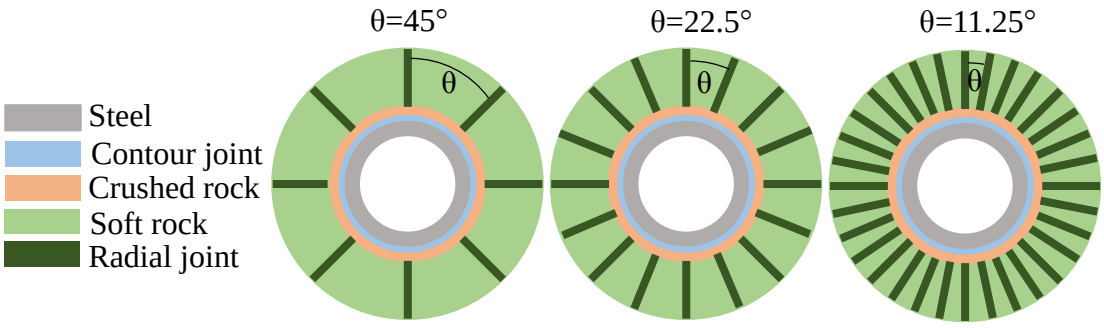

Figure 5.12.: Different modelling

Figure 5.13 shows the sensitivity study done on the cohesive joints and in each figure there is only one parameter of the cohesive joints that varies. The effect of the onset of cracking is shown in Figure 5.13a. Since some cracks open, the lateral stiffness decreases by about 16 $\%$ when compared to the elastic case. The higher value of G_c ($G_c = 200$ J/m^2) leads to a slightly stiffer response when compared to the smaller value of G_c ($Gc = 120$ J/m^2) as in the latter case the opening of the cracks occurs for slightly smaller displacements. This

observation is illustrated in Figure 5.13b. The two values of strain energy release considered give very similar results which is satisfactory as it is an uncertain parameter. Since when considering the different configurations (i.e. different values of θ) the same number of radial cracks open, there is no effect of the value of θ on the global response (see Figure 5.13c). The numerical simulations with more radial cracks only permit a finer location of where the radial cracks open. Finally, the effect of the tangential behaviour of the cohesive joint elements is shown in Figure 5.13d and there is no influence on the global response.
Figure 5.14 illustrates the location of the cracks that open during the loading. The angle between the loading axis and the direction of the crack is 78.75°. Figure 5.15 illustrates the length of the opened crack. This numerical observations (location and length of the cracks) are in accordance with the cracks due to loading detected during OPT (see Figure 3.22 in section 3.2.5).

5.2.4 Effect of elasto-plasticity of the rock and the crushed rock

In the following numerical simulations, the crushed rock and the rock are modelled with an elasto-plastic constitutive behaviour using the yield criterion of Drucker-Prager. The response is compared to the elastic response for both the soft rock and the rock. The internal variable $V3$ in this section is an indicator of plasticity; if it equals to 0 it means that the material behaves in a elastic way whereas if it equals to 1 it means that the yield criterion is reached. A decrease of $11\ \%$ of the lateral stiffness when comparing the elastic calculation wih the elasto-plastic one (cf. Figure 5.16a) is observed. Figure 5.16b shows where the yield criterion is reached.

5.2.5 Summary of the 2D results

The 2D FE modelling allows assessment of the influence of major phenomena identified during the OPT on the global response. By order of importance, accounting for the creation of the crushed rock and the gapping leads to substantial decrease of the lateral stiffness, then radial cracks and non-linear response of the crushed rock and the rock also lead to a decrease of the lateral stiffness but to a lesser extent. Now, the work done for the 2D configuration can be transposed to the 3D configuration.

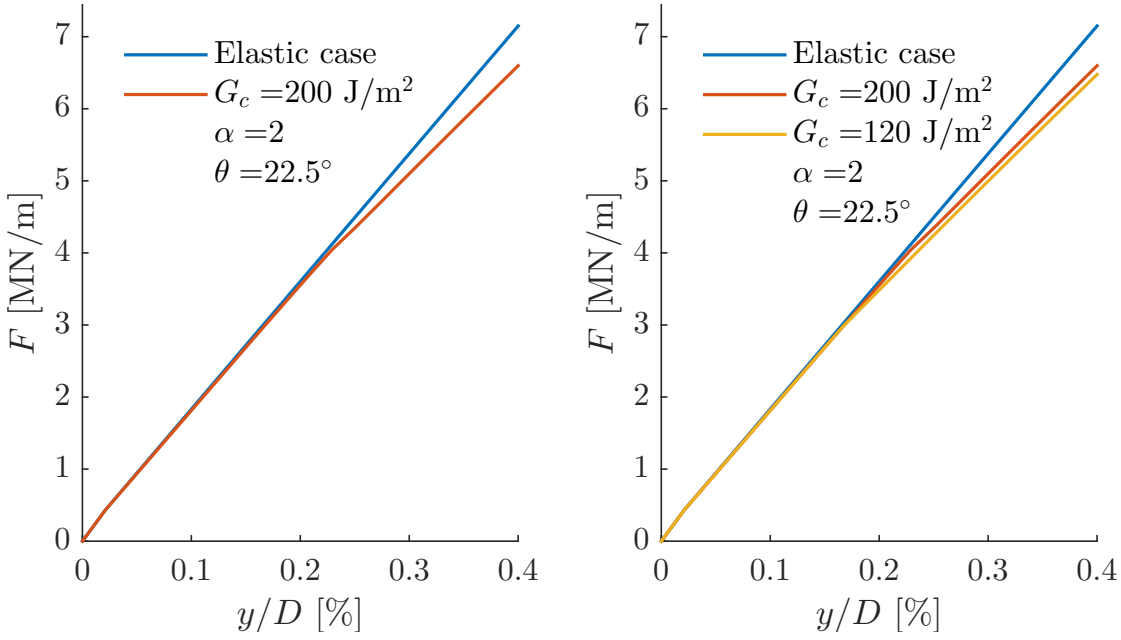

(a) Effect of the onset of cracks

(b) Effect of the strain energy release value G_c

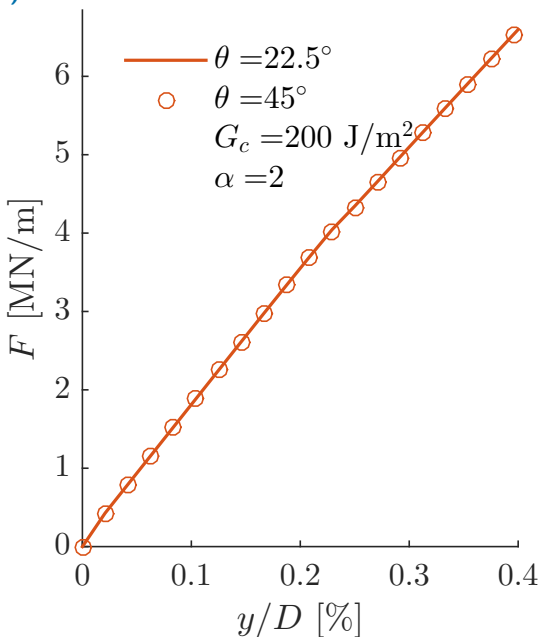

(c) Effect of the angle between two neighbouring joints θ

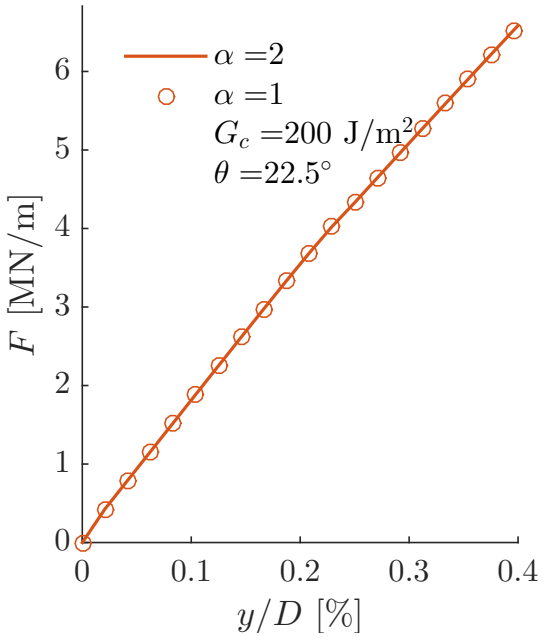

(d) Effect of the parameter α

Figure 5.13.: Sensitivity study on the cohesive joints parameters

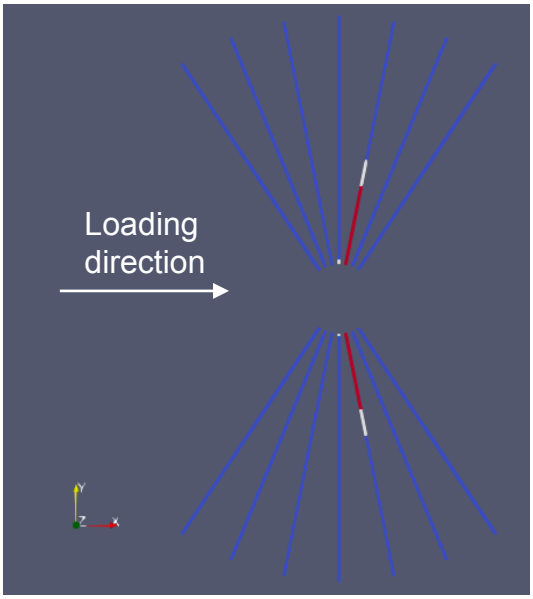

Figure 5.14.: Fracturation of the rock mass around the pile: internal variable $V3$ of the cohesive joints intact joint $V3 = 0$ (blue), damaged joint $V3 = 1$ (white) and open joint $V3 = 2$ (red)

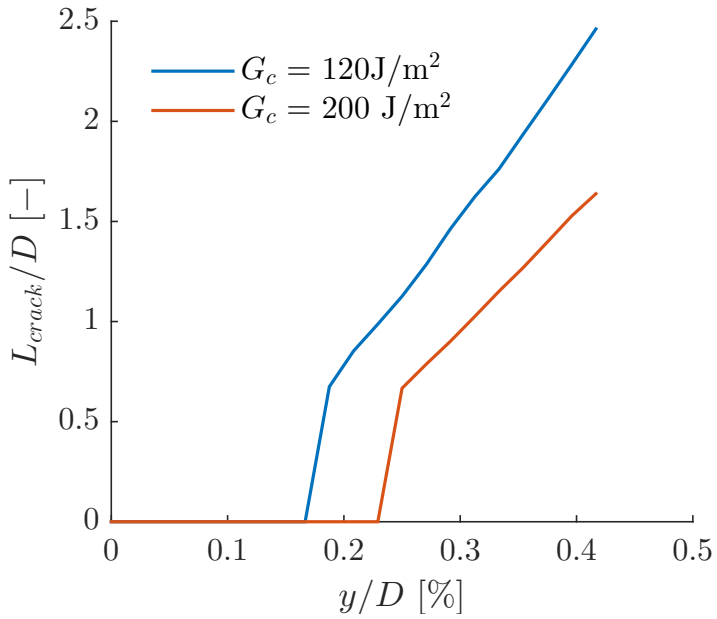

Figure 5.15.: Length of the crack depending on the applied lateral displacement for two values of energy strain release G_c

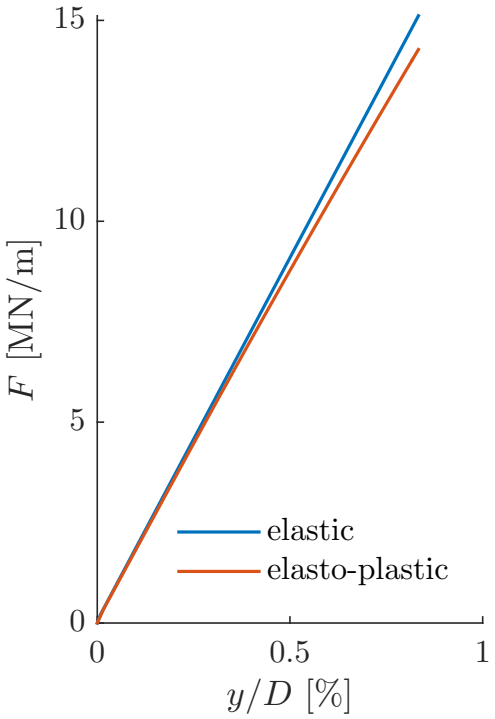

(a) Comparison of the global response when considering an elastic and an elasto-plactic behaviours in both the soft rock and the crushed rock.

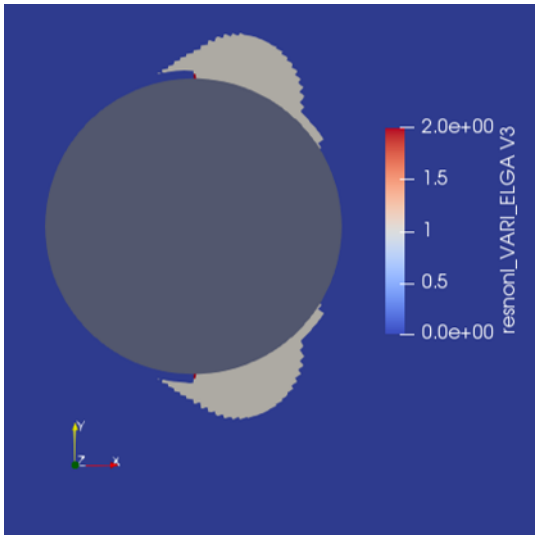

(b) Internal variable indicating where the yied criterion is reached at the final calculation step (corresponding to a lateral displacement that equals 1 cm)

Figure 5.16.: Results of the numerical simulation considering elasto-plastic behaviour in both the crushed rock and the rock

5.3 3D finite element modelling

The 3D FE modelling aims at accounting for the phenomena identified as influent in 2D into the 3D configuration. Numerical results are compared to the initial response of OPT and some calculations are done by varying a non-dimensional parameter to see the impact for offshore monopiles.

5.3.1 Model set up and validation

Geometry

The considered geometry in the 3D FE modelling (see Figure 5.17) is a laterally loaded pile with geometric characteristics listed in Table 5.3. Table 5.2 summarises the mechanical properties of the rock and of the crushed rock. A bulk unit weight of 20 kN/m^3 is considered and no influence of water is accounted for in the following studies. It is assumed that a crushed zone with a thickness equal to the thickness of the pile exists around the pile. From symmetry, only half of the model is discretised (see typical mesh in Figure 5.18).

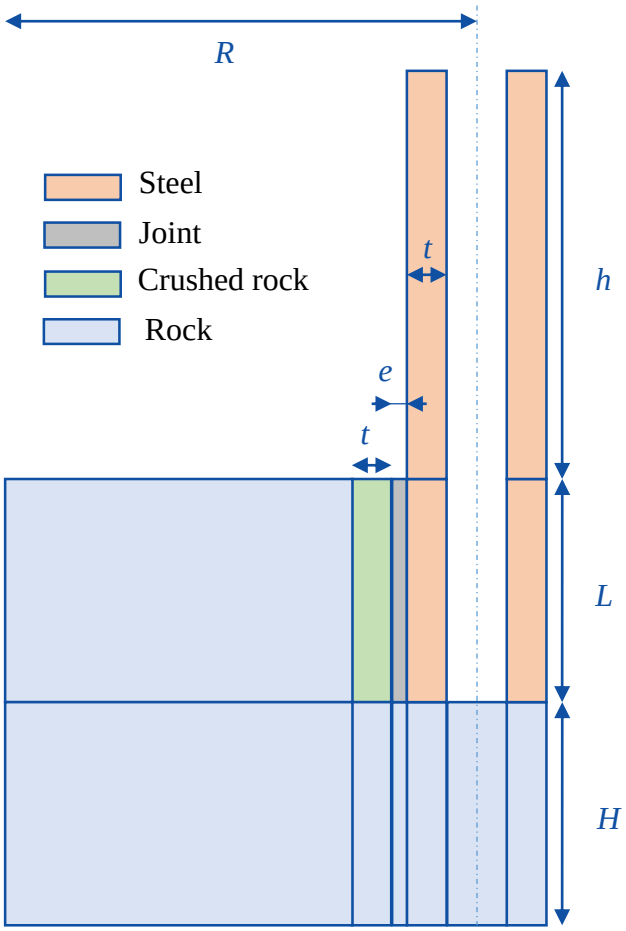

Figure 5.17.: Geometry for the 3D model

Table 5.3.: Parameters of the geometry of the 3D model

Description	Symbol	P7	P5
Outer diameter of the pile	D	0.762 m	1.2 m
Thickness of the pile tube	t	35 mm	35 mm
Length of the pile	L	2.7 m	3.2 m
Thickess of the joint elements	e	1 mm	
Outer radius of the 3D model	R	30 m	
Height of the model	H	12 m	
Height of the load application from the ground surface	h	5 m	

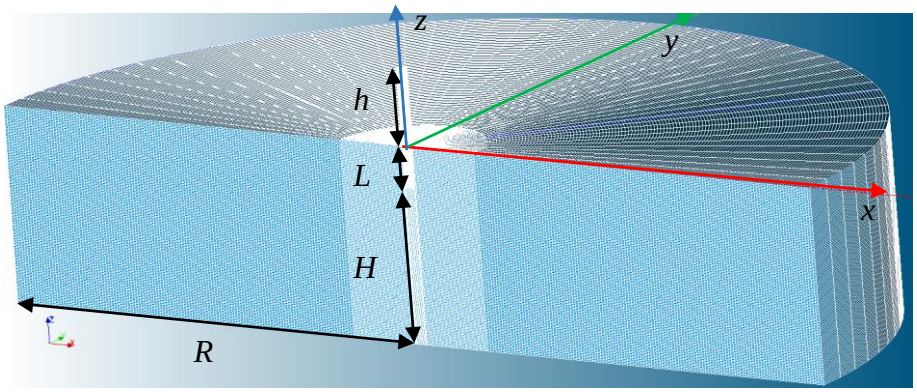

Figure 5.18.: Typical FE mesh for the 3D modelling

Boundary conditions

Far field boundary conditions are applied by setting to zero the vertical displacement at the base of the mesh and to zero the horizontal displacement at the outer cylindrical boundary of the model. Zero normal displacements are applied in the plane of symmetry. The horizontal load is applied at the pile top in a displacement-controlled manner, by prescribing increments of uniform displacement to all the nodes belonging to the pile top cross-section. The corresponding lateral load is obtained as a reaction to the applied horizontal displacements. An initial stress field is applied corresponding to vertical stresses due to gravity $\sigma_{zz} = \rho\, g\, z$ (ρ is the bulk density of the soil, g is the gravity acceleration and z the depth from the ground surface) and horizontal stresses $\sigma_{xx} = \sigma_{yy} = K_0\, \sigma_{zz}$ (K_0 is the earth pressure at rest and a value of 0.5 is considered).

Comparison with existing works for elastic ground

We first check the trends of the numerical solutions in the case of elastic homogeneous ground by comparing to some existing works. Explicit expressions of the displacement and the rotation of a free-headed pile (considering the soil as an elastic continuum) as functions of the lateral force and bending moment are proposed by Poulos (1971) using a semi-analytical solutions and by Randolph (1981), Carter and Kulhawy (1992), Pender and of Auckland. School of Engineering (1993), and Shadlou and Bhattacharya (2016) using

finite element numerical simulations. The 3D FE modelling is compared to these solutions in Figure 5.19. The results are presented as functions of the pile flexibility factor defined as:

$$K_R = \frac{E_p\, I_p}{E_s\, L^4} \tag{5.9}$$

where E_p is the Young's modulus of the pile, I_p is the inertia of the pile, E_s is the Young's modulus of the surrounding soil and L the embedded length. Using the same formulations as those in Poulos (1971) the lateral displacement and the rotation of a free head pile are expressed as:

$$\begin{cases} \rho = I_{\rho H}\, \dfrac{H}{E_s\, L} + I_{\rho M}\, \dfrac{M}{E_s\, L^2} & \text{(5.10a)} \\ \theta = I_{\theta H}\, \dfrac{H}{E_s\, L^2} + I_{\theta M}\, \dfrac{M}{E_s\, L^3} & \text{(5.10b)} \end{cases}$$

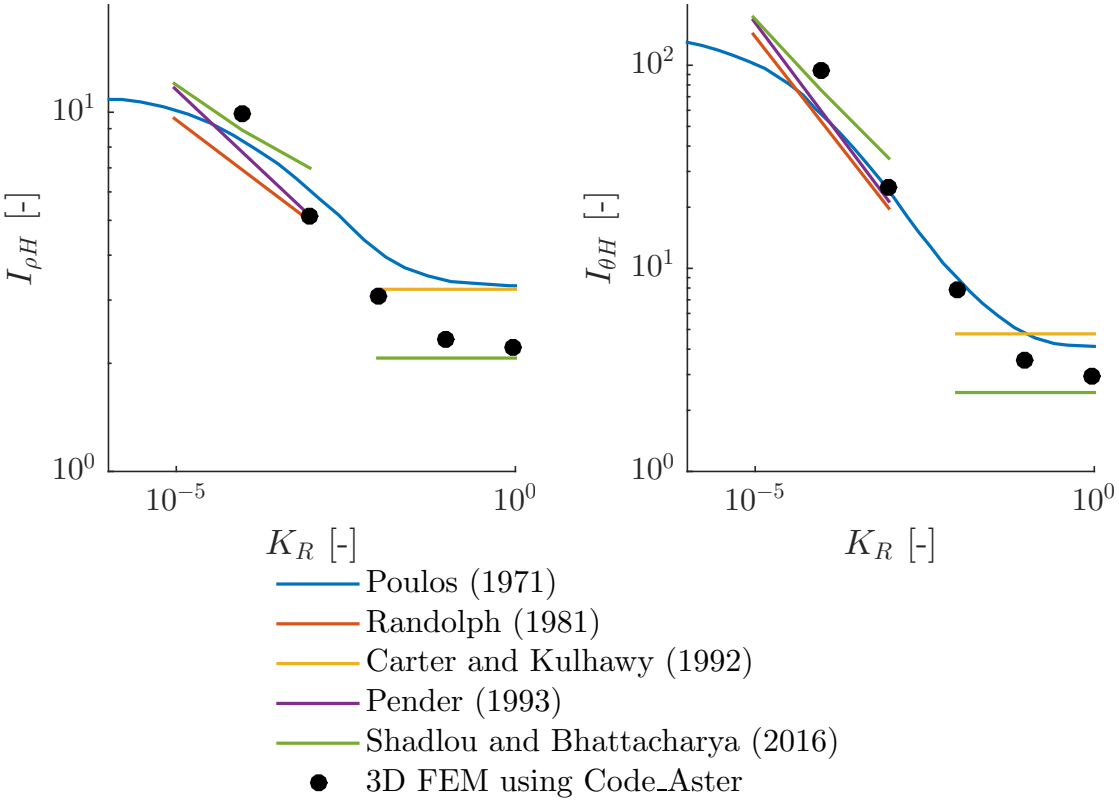

Figure 5.19.: Comparison of 3D FEM simulations using Code_Aster with existing solutions

For this comparison, the length over diameter ratio equals 5 and the different values of the flexibility factor are obtained by varying the Young's modulus of the soil. This comparison allows checking in a qualitative way the validity of the 3D model. The same evolution of the influence factors $I_{\rho H}$ and $I_{\theta H}$ with the flexibility factor are shown when comparing the different studies.

5.3.2 Comparison with OPT results

The 3D FE model are compared to OPT results for two different piles: P7 (small diameter pile) and P5 (large diameter pile). We can observe that the numerical results are in good accordance with the field data for both the small (Figures 5.20) and the large (Figure 5.21) diameter pile. These results are obtained without further calibration of the model parameters (i.e. same parameters of the rock mass, the crushed rock (see Table 5.2) and the joints around the pile as in the 2D configuration). In these figures, we highlight the effect of gapping. As already shown for the 2D study, the presence of gapping leads to a stiffness which can be reduced by about 45 % as compared to the case without gapping.

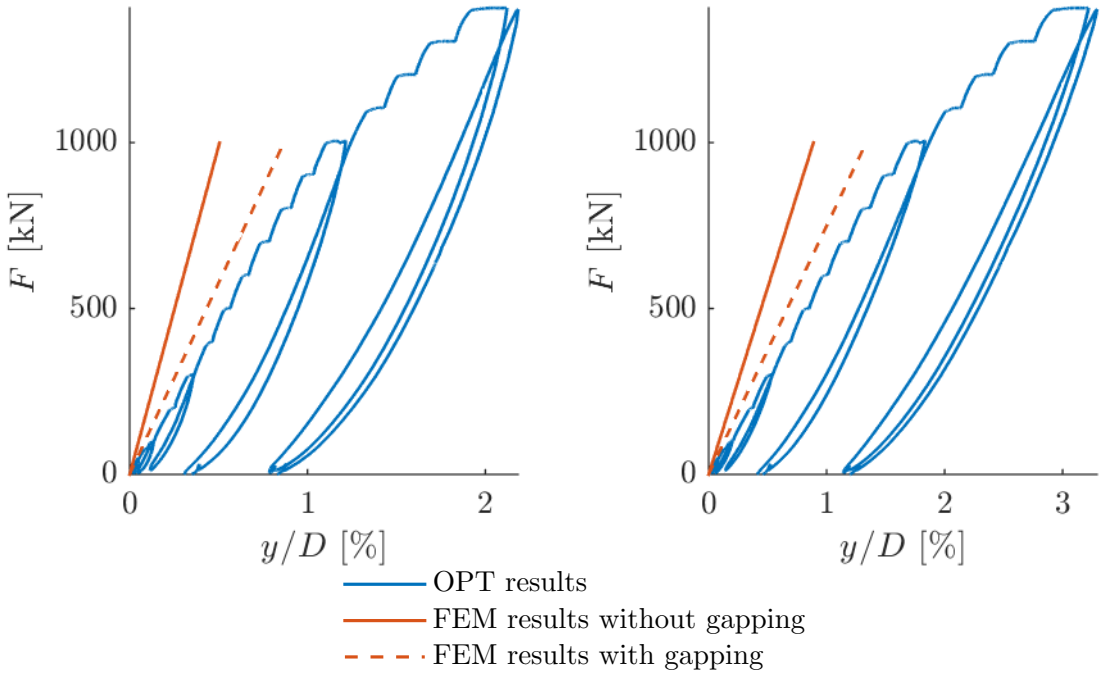

(a) Measurements at 10 cm above the ground surface

(b) Measurements at 50 cm above the ground surface

Figure 5.20.: Comparison between OPT results for pile P7 and the numerical results (with and without gapping)

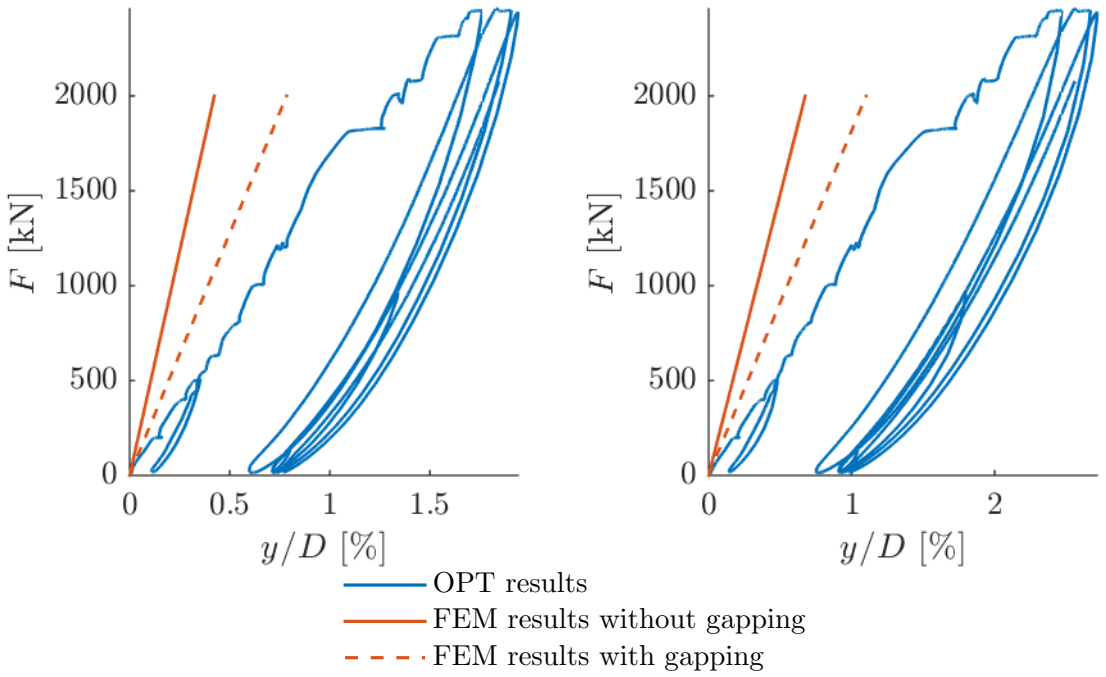

(a) Measurements at 10 cm above the ground surface

(b) Measurements at 50 cm above the ground surface

Figure 5.21.: Comparison between OPT results for pile P5 and the numerical results (with and without gapping)

5.3.3 Effects of cracks in 3D

What differs from the previous numerical simulations is that in the rock, some radial cohesive joints are added which allows accounting for the radial cracks to potentially open. The results of the 2D FEM with cohesive radial joints are used in order to guide where the cracks can potentially open and to limit the number of cohesive joints in the 3D FE model. Cohesive joints are modelled in the 3D FE model at the angles shown in Figure 5.22 all along the length of the pile. It can be noted that some radial joints are located backward the loading direction although in 2D no crack open for this range of angles, this is due to the fact that in 3D below the rotation point the loading direction is reversed. Figure 5.23 illustrates the location of the cracks that open during the loading. This result is consistent with the 2D FEM with radial joints. It can be seen that below the rotation point, some joints are damaged backward the loading direction. These numerical obersations add information from what was observed during OPT as nothing was known under the ground surface. It is to be noted that the propagation of the crack along the depth of the pile is limited and thus there is no effect of the global response of the pile as can be seen in Figure 5.24 due to the fact that the load are redistributed along the depth in 3D.

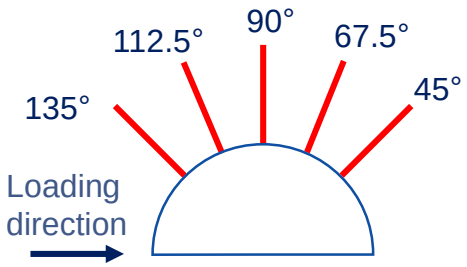

Figure 5.22.: Locations of the cohesive joints in the 3D calculation

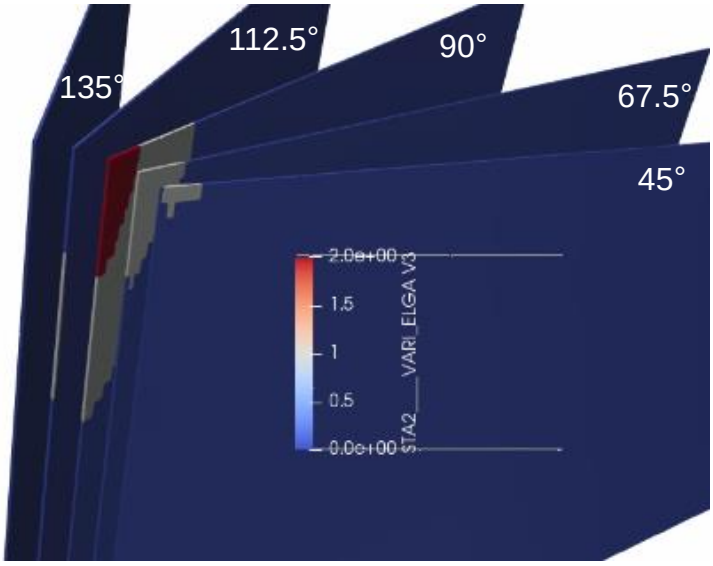

Figure 5.23.: Fracturation of the rock mass around the pile: internal variable $V3$ of the cohesive joints intact joint $V3 = 0$ (blue), damaged joint $V3 = 1$ (white) and open joint $V3 = 2$ (red)

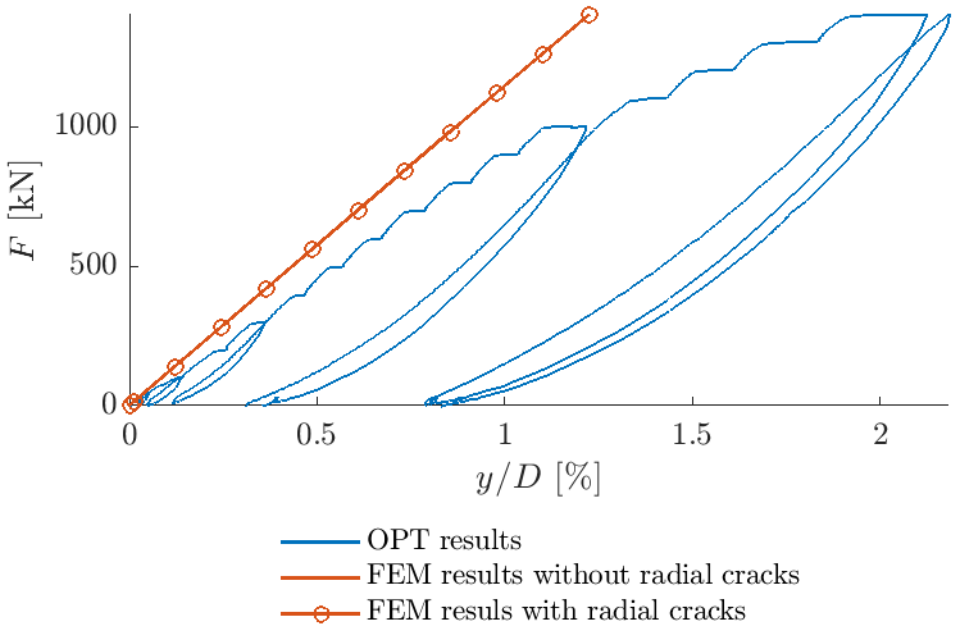

Figure 5.24.: Comparison between OPT results (at 10 cm above the ground level) for pile P7 and the numerical results with gapping (with and without radial cracks)

5.3.4 Size effects

Since the driving process induces the creation of a zone of crushed rock around the pile with a thickness observed to be closely equal to the thickness of the pile tube, this parameter may impact the global response. A sensitivity study is performed in the 3D configuration (without gapping) for a pile diameter of 0.762 m and three ratios of D/t (diameter over thickness): $D/t = 20$ (average ratio for the piles tested during OPT), $D/t = 63$ and $D/t = 109$ (the typical ratio of OWT monopiles ranges between these two values). Figure 5.25 shows the result of this sensitivity study of the pile, hence smaller thickness of the crushed zone, compensated in part by the reduced bending stiffness of the pile. For each curve the slope of the curve is shown on the graph. As the pile diameter is fixed herein, a higher ratio of D/t implies a smaller value of the thickness of the pile. On one hand, an increasing thickness of the pile wall leads to a stiffer response when considering the response in terms of moment versus rotation. This stiffness increases linearly with t/D. On the other hand, an increasing thickness of the pile wall leads to a softer response when considering the response in terms of force versus lateral displacement. This stiffness increases linearly with D/t. This influence of the thickness of the pile tube in the particular case of monopiles driven in rock needs to be accounted for in the design.

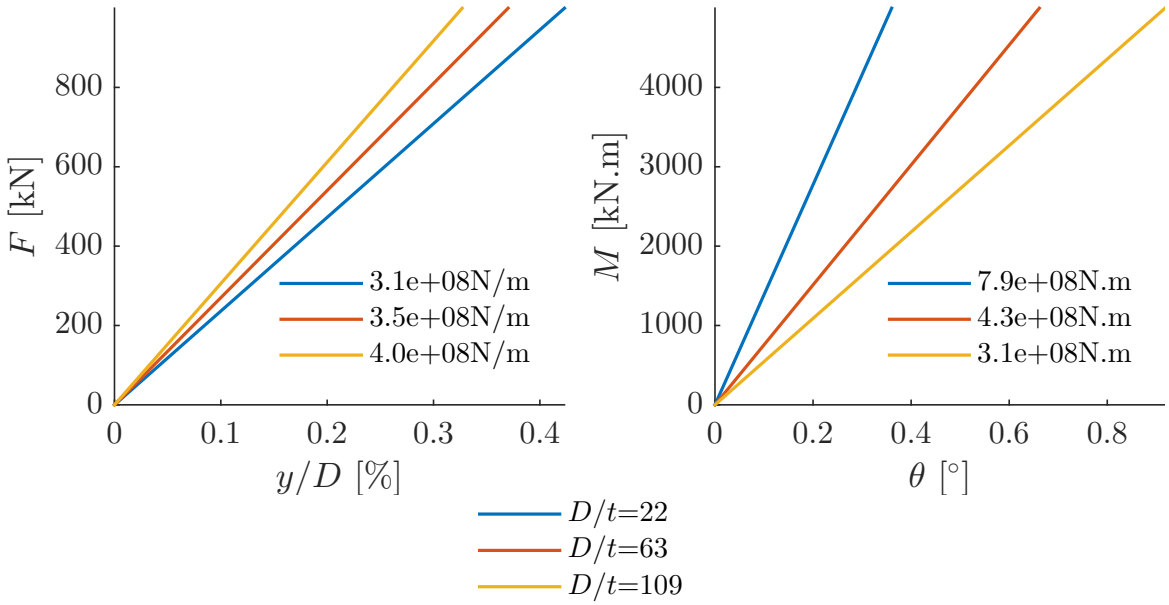

Figure 5.25.: Sensitivity study on the ratio of D/t (i.e. diameter over thickness of the pile)

5.3.5 Summary of the FEM results

Implementation simplicity and calculation speed of the 2D FEM modelling enable conclusions to be drawn on the effects of the different phenomena on the global response and permit to calibrate in an easy way the different parameters of the model. The good accordance between the numerical simulations and the experimental results provides good confidence in the modelling and a quite simple 3D FE modelling captures most of the global response. This comparison validates the transition from the 2D modelling to the 3D modelling. The 3D FE modelling allows comparison of the numerical simulations results with the results of OPT and to extend the results for other dimensions of the pile. For OWT the diameter to thickness ratio of the monopiles is much higher than for piles tested during OPT and it is shown that this can have a significant influence on the global response.

6 Conclusion and future work

6.1 Contributions

This work contributes to the research carried out on the design of monopiles for offshore wind turbines (OWT) installed in rock. Previous research programs carried out on this topic mainly refer to sands and clays. The novelty of this work is to address the behaviour of piles driven in rocks. This is motivated by the development of offshore wind farms in such ground condition, considering that the foundations contribute to about 25 - 30 % of the capital expenditure. The estimations of: the foundation stiffness, the accumulation of rotations with cyclic loading, the behaviour of the surrounding rock mass and multi-directional loading effects are identified as points of interest that need to be assessed to fulfil the aim of having a secure and optimised design.

Onshore pile tests (OPT) permitted to highlight the particularities of the rock on the response of laterally loaded piles in comparison with similar tests in other ground conditions. Regarding the evolution of the rotation accumulation at the ground surface, it appears that the rotations accumulate less in the long-term in soft rock than in loose and medium dense sands (Leblanc et al., 2010a). However, the effect of previous loading history seems more pronounced in the case of soft rock than in loose to medium dense sands. From these tests, it was observed that driving piles in soft rock leads to the creation of an annulus of crushed rock around the pile. The mechanical properties of this crushed rock are much weaker than those of the surrounding rock mass implying a significant impact on the global response of laterally loaded piles. From the field tests, the extent of this crushed rock is estimated to be equal to the thickness of the pile tube. From these tests, it also appears that both driving and loading induce cracks in the surrounding rock mass. Finally, another major observation from these tests is the creation of a gap behind the pile leading to a redistribution of stresses around the pile. These four major phenomena have been identified as relevant to be accounted for in the design.

Regarding the initial response of the laterally loaded pile, a simple model with springs in series is calibrated to fit the results of the field tests. It appears that for driven piles, the crushed rock contributes about 90 % of the total ground displacement at low to moderate loads. For drilled and grouted piles, the extent of the damaged zone due to the installation process is expected to be smaller than for driven piles. Therefore the contribution of this zone is reduced to 70 %.

Multi-directional effects are not considered in the current design procedures of OWT monopiles, but as the design gets increasingly optimised, some assumptions need to be revisited. Therefore, a new model is presented permitting the characterisation of multi-directional laterally loaded piles. The model is based on the classical $P-y$ curve approach which has been extended to include multi-directional loading. The $P-y$ curves for multi-directional loading are deduced from the $P-y$ curves of unidirectional loading by assuming equality of the stored energy of the two models. The proposed method is validated at the pile scale, based on a comparison with the model proposed by Levy et al. (2007). The comparison shows good agreement between the two approaches. When considering the effects of multi-directional loading, symmetry conditions vanish and the stiffness-matrix is no longer symmetric. Moreover, this loss of symmetry results in additional coupling effects between the direction of loading and lateral and rotational stiffness in other directions. An application example is presented to assess the impact of taking into account multi-directional effects on the natural frequency of a given OWT. This application case demonstrates that multi-directional loading leads to a reduction of a few percent of the 1st and 2nd modes frequencies. This could be (at least to some extent) a possible explanation of the shifting of the natural frequency as mentioned by Arany et al. (2015) during the first few months after installation, in addition to softening effects of the surrounding soil.

The extension of the $P-y$ curves method to account for the cyclic behaviour is presented and validated with the OPT cyclic tests results. Since creep and fatigue share important similarities, existing frameworks are used to model creep response for cyclic response, focusing on modelling cyclic accumulation that reaches a stabilised state. Thus, two Kelvin-Voigt models (one for the crushed rock and one for the rock) are calibrated in order to fit the accumulation measured during the OPT. The undertaken procedure provides good confidence in the values of the different parameters. It can be noted that this model is validated for different series of cycles with cycles period ranging from 8 to 25 s. These values are similar to period of cycles encountered for cyclic loading due to waves.

The 2D FE modelling allows separate assessment of the influence of major phenomena identified during the OPT on the global response: (i) the creation of the crushed rock annulus during the installation on the global response; (ii) the creation of gapping behind the pile; (iii) the onset and propagation of cracks; (iv) the non-linear response of the ground. From the 2D FEM modelling, it can be concluded that, by order of importance, accounting for the creation of the crushed rock and the gapping leads to substantial decrease of the lateral stiffness, radial cracks and non-linear response of the crushed rock and the rock also lead to a decrease of the lateral stiffness but to a lesser extent. The 3D FE modelling allows direct comparison of the numerical simulations results with the results of OPT. The good accordance between the numerical simulations and the experimental results provides some confidence in the modelling. A rather simple 3D model captures most of the global response. Finally, the study is extended to other pile dimensions as encountered in OWT. We show that the important parameter is the ratio of the diameter D over the thickness of

the pile wall t. The larger the D/t ratio, the smaller is the force-displacement stiffness of the pile, but the larger is the moment-rotation stiffness. This is attributed to the increase of the crushed zone around the pile, partially compensated by the reducing bending rigidity.

6.2 Future work

A major difficulty remains in the determination of the ground properties, especially under cyclic loading. In the ARSCOP ("nouvelles Approches de Reconnaissance de Sols et de Conception des Ouvrages géotechniques à l'aide du Pressiomètre") project, an in-situ characterisation campaign (dilatometer tests) was undertaken in May 2019 in the same quarry where the OPT were done with both static and cyclic loading tests. It will be interesting when the data become available to revisit the calibration of the semi-analytical model proposed in this thesis. In particular the in-situ tests will be very useful for improving the calibration of the Kelvin-Voigt model of the ground used to assess the pile response under cyclic loading. This could allow development of an up-scaling procedure for getting more reliable visco-elastic parameters of the ground at the pile scale from small scale cyclic loading tests performed in the laboratory.

Recent studies have included rotational degrees of freedom in the classical $P-y$ curves approach by adding distributed rotational springs along the pile (Byrne et al., 2015b). The multi-directional model proposed in this thesis could be extended to account for these new features and explore the effect on the frequency shift of the structure. Furthermore, cyclic modelling based on visco-elastic analogy as proposed in the thesis could be extended to multi-directional loading and validated using the numerical work done in Levy et al. (2009) and the experimental results found in Peralta (2010) and Rudolph et al. (2014).

Integrated design tools require the input of $P-y$ curves. Equivalent $P-y$ curves at various stages of cyclic loading can be obtain from the proposed cyclic modelling approach. These $P-y$ curves can be used as input in the integrated design tool for natural frequency analysis following a similar methodology as proposed by Erbrich et al. (2011)).

During this thesis, a 3D FE model was developed for piles driven in soft rocks accounting for the presence of crushed rock and gapping behind the pile. The model needs to be extended to account for rock fractures induced by pile installation and loading. The cyclic modelling approach based on visco-elastic analogy could be further validated using 3D FE computations and comparison with OPT results. For OWT, hydro-mechanical couplings could be included in the numerical model. In particular, it would be interesting to study the effects of the presence of water in the gap and in the cracks on the global response under static and cyclic loading.

Focus on some existing $P-y$ curves

A

A.1 Abbs (1983)

The method described by Abbs (1983) is adapted for carbonate rocks with unconfined compressive strength (UCS) ranging from 0.5 to 5 MPa. Figure A.1 shows typical $P-y$ curves for brittle carbonate rock using this model. The initial part is based on Reese and Welch (1975) work for stiff clays, unconfined shear strength of the rock material is used to define the shear strength. The residual frictional resistance is based on the API $P-y$ model made for sandy soils. This work was applied in weak calcarenite and gave good predictions of performance in the elastic range, but the test did not reach failure, so the method could not be compared to higher displacement. As can be seen, cyclic loading is envisaged in the formulation. However, this consists in degrading the $P-y$ curve by a constant factor, which does not depend either on the level of cyclic loading or the number of cycles.

$$P=\begin{cases}\dfrac{P_u}{2}\sqrt{\dfrac{y}{y_c}}, if\, y\leq Ay_c\\ \dfrac{P_u}{2}\sqrt{\dfrac{y}{y_c}}-0.055P_u\left(\dfrac{y_A\, y_c}{A\, y_c}\right)^{1.25}, if\, Ay_c<y\leq 6Ay_c\\ \left[D\; Sand_A\; P_{sand}\tanh\left(\dfrac{Sand_K\; z\; y}{Sand_A\; P_{sand}\; D}\right)\right], if\, y>6Ay_c\end{cases} \tag{A.1}$$

where, s_u is the undrained shear strength, z represents the depth, y is the lateral displacement, $P_u=\min[P_{us};P_{ud}]=\min\left[D\left(2s_u+\sigma'_v+2.83s_u\dfrac{z}{D}\right);11Ds_u\right]$ is the ultimate reaction defined by Reese and Welch (1975) as the minimum value between ultimate resistance for shallow depth (P_{us}) and deep (P_{ud}) failure, D is the diameter of the pile, σ'_v is the overburden pressure, ε_{50} represents the strain at one half of the maximum undrained shear strength in triaxial test, $y_c=\varepsilon_{50}D$ corresponds to displacement at 50% of ultimate resistance, A is an empirical adjustment factor determined for static loading (given by Equation A.2), $Sand_A$ is a factor to account for cyclic loading taken as 0.9, $P_{sand}=\min\left[P_{us};P_{ud}\right]=\min\left[(C_1z+C_2D)\sigma'_v;C_2D\sigma'_v\right]$ represents the ultimate bearing pressure for sand calculated using API method. C_1, C_2 and C_3 depend on the angle of friction and $Sand_K$ is the initial modulus of subgrade reaction function of internal angle of friction and relative density.

$$A=\begin{cases}0.6\ ,\ \text{if}\dfrac{z}{D}>3\\ \min\left[-0.05\left(\dfrac{z}{D}\right)^2+0.29\dfrac{z}{D}+0.2;0.6\right]\ ,\ \text{else}\end{cases} \tag{A.2}$$

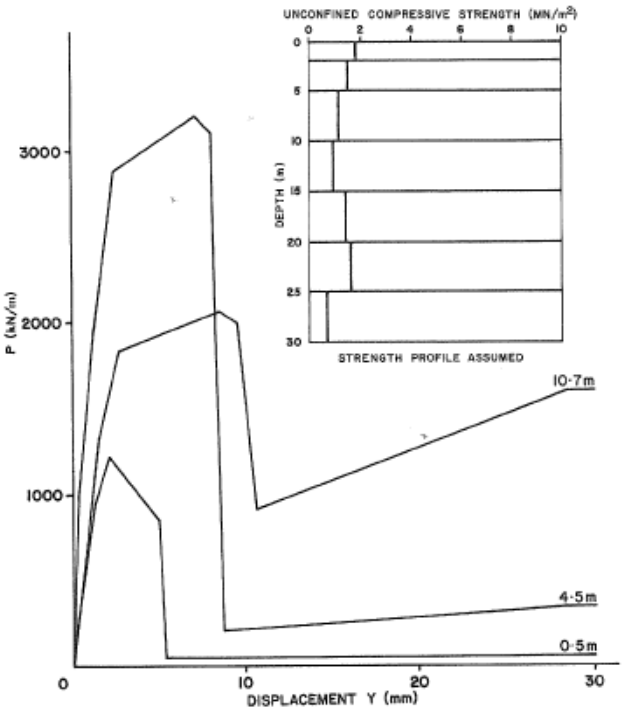

Figure A.1.: Typical p-y curves for brittle carbonate rocks (Abbs, 1983)

A.2 Fragio et al. (1985)

This $P-y$ method is based on pile load tests on bored piles in calcareous claystone with unconfined compressive strength ranging from 9 to 36 MPa. Pile slenderness ratios ranged between 12 to 18. Figure A.2 shows typical $P-y$ curves considering Fragio et al. (1985) model. The first part is linear and reflects the elastic behaviour of the rock mass (rock mass stiffness). This linear part ends when the peak lateral resistance is reached, this value is a function of the rock mass shear strength. Then, there is a horizontal part over which the peak resistance is maintained. After that, two response are considered:

- a behaviour near the surface where a wedge failure occurs (strain-softening);
- a behaviour deeper in the rock below a critical depth where a crushing flow type of failure occurs.

As can be seen, cyclic loading is not mentioned in this method.

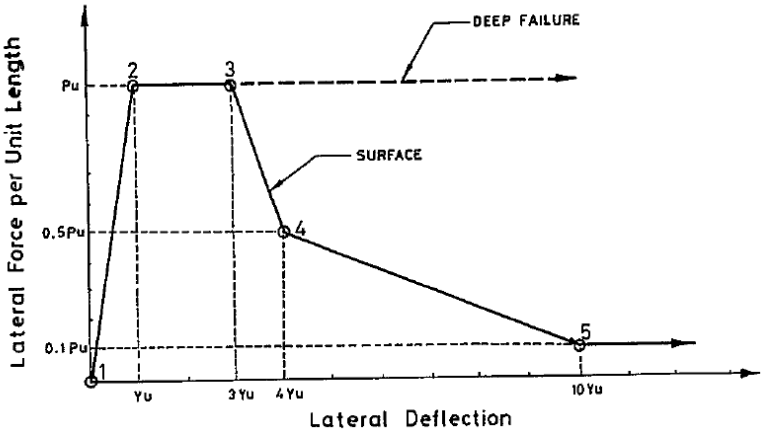

Figure A.2.: Typical shape of p-y curves for Zumaya claystone (Fragio et al., 1985)

where, $P_u = min[P_{us}; P_{ud}] = min[3\ s_u\ D; 9\ s_u\ D]$ is the ultimate resistance defined as the minimum between ultimate reaction at shallow depth and deep failure resistance, y_u represents the deflection observed in the tests at the onset of non linear behaviour, D is the diameter of the pile and s_u is the undrained shear strength.

A.3 Reese (1997)

This $P-y$ method is based on results from two tests of full scale, bored piles in rock (Nyman, 1978; Speer, 1992). Rock encountered in the two set of tests differ significantly. A brittle, vuggy coral limestone with a compressive strength of 3.45 MPa in average and RQD of zero is encountered in Islamorada. A sandstone described as very intensely to moderately fractured with a compressive strength increasing with depth from 3 to 16 MPa is found for the full-scale test at San Francisco (Reese, 1997). Pile slenderness ratios ranged between 6 to 11. Figure A.3 shows a characteristic shape of $P-y$ curve for rock considering Reese (1997) $P-y$ method. $P-y$ curves are composed of three parts. The initial part is linear, then the function is a one quarter power law. The last part is a horizontal straight line defining ultimate resistance. As may be seen, cyclic loading is not mentioned in this method. The equations of the different branches are as follow:

$$P = \begin{cases} K_{ir}\ y, y \leq y_A \\ \dfrac{P_{ur}}{2}\left(\dfrac{y}{y_{rm}}\right)^{0.25}, y \geq y_A; p \leq P_{ur} \\ P_{ur} \end{cases} \tag{A.3}$$

where, $K_{ir} = k_{ir}\ E_{ir}$ represents the slope of the initial portion, E_{ir} is the initial modulus of the rock, k_{ir} is a dimensionless constant (given by Equation A.4), P_{ur} is the ultimate resistance of the rock (given by Equation A.5), q_{ur} is the compressive strength of the rock, α_r

represents the strength reduction factor to account for the fracturing (equals to 1/3 for RQD of 100 % and increases linearly to one for RQD of 0), D is the diameter of the pile, x_r is the depth below rock surface, $y_{rm} = k_{rm}\ D$ corresponds to displacement at 50 % of ultimate resistance, k_{rm} is a constant ranging from 0.00005 to 0.0005 and y_A is the displacement at the onset of the non linear part of the response (Figure A.3).

$$k_{ir} = \begin{cases} \left(100 + \dfrac{400 x_r}{3D}\right), \text{if } \ 0 \leq x_r \leq 3D \\ 500, \text{if } \ 3D \leq x_r \end{cases} \tag{A.4}$$

$$P_{ur} = \begin{cases} \alpha_r\ q_{ur}\ D \left(1 + 1.4 \dfrac{x_r}{D}\right), \text{if } \ 0 \leq x_r \leq 3D \\ 5.2\ \alpha_r\ q_{ur}\ D, \text{if } \ 3D \leq x_r \end{cases} \tag{A.5}$$

$$y_A = \left(\frac{P_{ur}}{2\ (y_{rm})^{1/4}\ K_{ir}}\right)^{4/3} \tag{A.6}$$

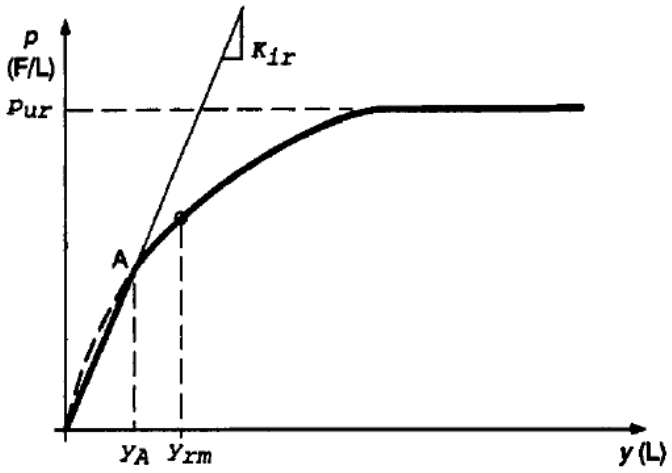

Figure A.3.: Sketch of p-y curve for rock (Reese, 1997)

A.4 Dyson and Randolph (2001)

The load-transfer curves in Dyson and Randolph (2001) model are deduced directly from series of model pile tests conducted using geotechnical centrifuge in calcareous sand. That is to say that lateral resistance of soil and lateral displacement along the pile are deduced from bending moment measurements. From this experimental curves, a generic load-transfer based on a power law model is fitted with the results. The power law is similar to that proposed by Wesselink et al. (1988). The impact of the installation method on the transfer curves has been explored. Load-transfer can be modified to take into account this effect. It can be seen that cyclic loading is not mentioned herein. Figure A.4 shows $P - y$ curves

deduced from centrifuge tests and the optimised curve deducted from experiments. The load-transfer equation obtained is:

$$\frac{P}{\gamma' D} = R\left(\frac{q_c}{\gamma' D}\right)^n \left(\frac{y}{D}\right)^m \tag{A.7}$$

where, P is the lateral resistance, γ' is the soil unit weight, D is the diameter of the pile, q_c is the cone tip resistance at the specified depth, $n = 0.72$ is a constant and m is a constant controlling the amount of curvature in the $P - y$ relationship.

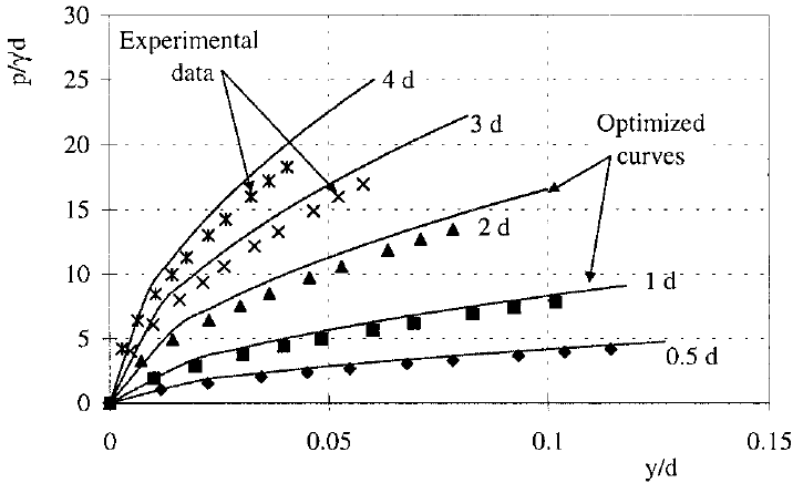

Figure A.4.: Typical experimental and optimized load-transfer curves for calcareous sand (Dyson and Randolph, 2001)

A.5 Erbrich (2004)

CHIPPER method is a new design method for laterally loaded anchor piles in weak rock. $P - y$ curves approach has been enriched with some other concepts. The theoretical basis of this model consists in finite element analysis (2D and 3D), plasticity analysis and centrifuge tests. Weak rock modelled in this article have UCS value around 400 kPa and Young's modulus of 300 MPa. The algorithm model a progressive failure at shallow depth above a chipping depth below which chipping mechanism cannot occur anymore. The effect of cyclic loading is also accounted for in the algorithm. The algorithm does not take into account a strength degradation with cycles but a shifting of lateral displacement cycle by cycle. This shifting is due to plastic displacement. Figure A.5 shows the various principles of the algorithm.

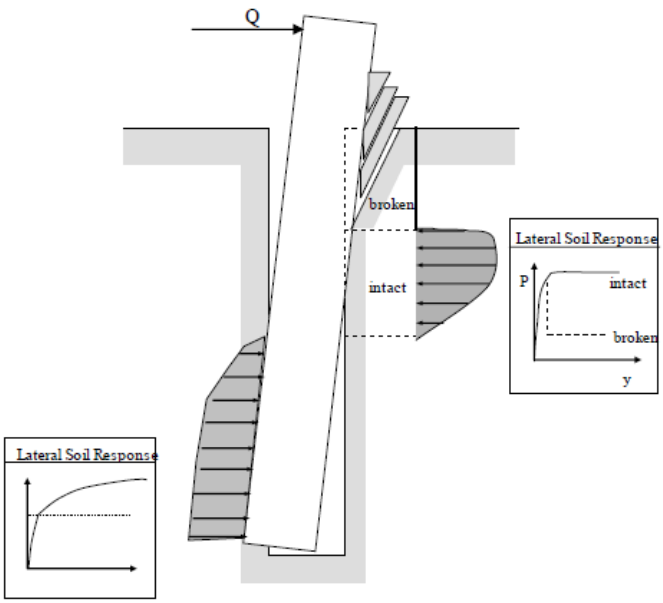

Figure A.5.: Definition of problem (Erbrich, 2004)

B

Implementation of finite difference resolution for $P-y$ curves approach

Finite difference methods (FDM) are numerical methods solving differential equations in which derivatives are approximated by linear combinations of function values at the grid point. There are several calculation schemes within this method (central, backward and forward difference), the principal calculation scheme is presented here with some possible variants. The pile is discretised into N elements, that is to say $N+1$ nodes. In the following, the discretisation is supposed to be uniform along the pile for the sake of simple presentation (same height for each element). However, a non-uniform discretisation can be used if some areas of the pile need to be refined. Nodes numbering convention used in this section is from tip to top. The nodes are numbered from 1 to $N+5$ taking into account $N+1$ nodes in the pile, two nodes above the head of the pile and two nodes below the toe of the pile. There are $N+5$ unknowns which are the lateral displacement at each node. $N+1$ equations are given with the pile equilibrium at each node (cf. Equation 2.5). Boundary conditions at the head of the pile and at the toe of the pile give four additional equations. There are $N+5$ equations to solve simultaneously for $N+5$ unknowns. A central difference scheme is used to approximate the various derivatives:

$$\begin{cases} \left(\dfrac{\mathrm{d}u}{\mathrm{d}z}\right)_i = \dfrac{u_{i-1}-u_{i+1}}{2(\Delta z)} + \mathcal{O}(\Delta z) \\ \left(\dfrac{\mathrm{d}^2u}{\mathrm{d}z^2}\right)_i = \dfrac{u_{i+1}-2u_i+u_{i-1}}{(\Delta z)^2} + \mathcal{O}(\Delta z)^2 \end{cases} \tag{B.1}$$

The three terms of the governing differential equation 2.5 are discretised as follows:

- **A term representing evolution with depth of the bending moment**, such as $\forall m \in [3; N+3]$:

$$\begin{aligned}\frac{\mathrm{d}^2}{\mathrm{d}z^2}\left(E_pI_p\frac{\mathrm{d}^2y}{\mathrm{d}z^2}\right) &= \frac{1}{h^2}\begin{bmatrix}(E_pI_p)_{m+1}\left(\dfrac{\mathrm{d}^2y}{\mathrm{d}z^2}\right)_{m+1}\\ -2\cdot(E_pI_p)_m\left(\dfrac{\mathrm{d}^2y}{\mathrm{d}z^2}\right)_m\\ +(E_pI_p)_{m-1}\left(\dfrac{\mathrm{d}^2y}{\mathrm{d}z^2}\right)_{m-1}\end{bmatrix}\\ &= \frac{1}{h^4}\begin{bmatrix}((E_pI_p)_{m-1})\,y_{m-2}\\ -2\left((E_pI_p)_{m-1}+(E_pI_p)_m\right)y_{m-1}\\ +\left((E_pI_p)_{m-1}+4(E_pI_p)_m+(E_pI_p)_{m+1}\right)y_m\\ -2\left((E_pI_p)_m+(E_pI_p)_{m+1}\right)y_{m+1}\\ +\left((E_pI_p)_{m+1}y_{m+2}\right)\end{bmatrix}\end{aligned} \tag{B.2}$$

- **A term representing evolution with depth of shear force due to axial force**, such as $\forall m \in [3; N+3]$:

$$\left(V\frac{\mathrm{d}^2y}{\mathrm{d}z^2}\right)_m = \frac{V}{h^2}\left(y_{m-1}-2y_m+y_{m+1}\right) \tag{B.3}$$

- **A term representing reaction of the surrounding ground on the pile.** Any non-linear symmetric $P-y$ curve is considered. Accurate estimation of the reaction P needs an iterative process (i numbering of the iteration). There are different ways to approximate the reaction as a linear function of the lateral displacement:

  - **with secant modulus**, the reaction is proportional to the lateral displacement, such as $\forall m \in [3; N+3]$:

$$P_m^i = E_{sm}^i\, y_m^i \tag{B.4}$$

  - **with tangent modulus**, the reaction is a linear function of the lateral displacement. The intercept of the tangent line is put in the second member of the matrix system, such as $\forall m \in [3; N+3]$:

$$P_m^i = E_{tm}^i\, y_m^i + P_{m0}^i \tag{B.5}$$

Focus on boundary conditions

Boundary conditions are expressed as linear combinations of lateral displacements. Various fixities can be considered: either deflection, rotation, shear force or bending moment can be imposed either at the head of the pile and the toe of the pile. As for differential equation, boundary conditions are expressed mathematically using the FDM with a central difference scheme. It can be noted that for pile head fixities (resp. pile toe), the subscript m should be replace by $N+3$ (resp. 3).

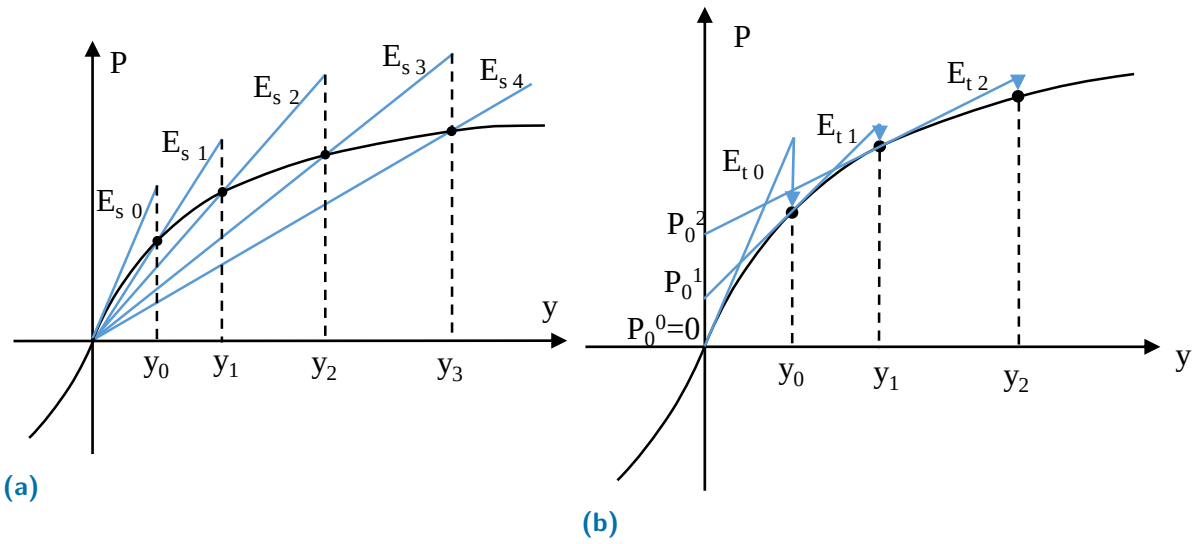

Figure B.1.: Approximation of the reaction with secant modulus (see Figure B.1a) and tangent modulus (see Figure B.1b)

- Deflection:

$$y_m = y_m \tag{B.6}$$

- Rotation:

$$\theta_m = \left(\frac{\mathrm{d}y}{\mathrm{d}z}\right)_m = \frac{y_{m-1} - y_{m+1}}{2h} \tag{B.7}$$

- Moment:

$$M_m = \left(E_p I_p \frac{\mathrm{d}^2 y}{\mathrm{d}z^2}\right)_m = \frac{(E_p I_p)_m}{h^2}\left[y_{m-1} - 2y_m + y_{m+1}\right] \tag{B.8}$$

- Shear force:

$$\begin{aligned} T_m &= \left(\frac{\mathrm{d}M}{\mathrm{d}z} + V\frac{\mathrm{d}y}{\mathrm{d}z}\right)_m \\ &= \frac{(E_p I_p)_m}{2h^3}\left[y_{m-2} - 2y_{m-1} + 2y_{m+1} - y_{m+2}\right] + \frac{V}{2h}\left[y_{m-1} - y_{m+1}\right] \end{aligned} \tag{B.9}$$

In the case of offshore wind turbine monopiles, the most relevant is to express the moment and shear at the pile head and the pile tip (Abadie, 2015).

Details of the device used during triaxial tests on the rock

C

The Sanchez cell is a triaxial apparatus. The rubber membrane used to put the rock sample inside is pierced at three locations (approximately in the middle and equally spaced around the diameter) and thin aluminum sheets are glued at these locations to ensure sealing between the sample and the pressurising chamber. This is done in order to measure the sample radial strains without measuring the deformation of the membrane. Three aluminum rings are mounted on the sample in order to support five LVDTs (three radial LVDTs and two axial ones). The accuracy of the radial LVDTs is 1 μm and 10 μm of the axial ones. The support rings are kept in contact with the membrane by metallic springs. The sample inside its membrane, the three aluminum rings and the five LVDT are shown in Figure C.1b. The confining pressure is directly applied by a volumetric servo-pump up to a maximum of 100 MPa. The axial stress is controlled by an independent axial piston, actuated by a similar volumetric servo-pump. The accuracy of the pressure measurements is 0.1 MPa. The maximum axial stress that can be reached for a 40 mm diameter sample is around 680 MPa. The temperature is regulated to 20°. Different mechanical paths can be adopted with this device, however only deviatoric and isotropic paths are done.

One difficulty that can be raised is that as the rock is quite porous and that large pores can appear on the lateral surface of the sample, under a sufficient confining pressure the membrane can "enter" into the pore and eventually pierce resulting in leakage of fluid in the sample. One solution is to choose samples that do not present large pores on their lateral surface. Another solution but not ideal is to close off the pores with resin for example but it might affects the results.

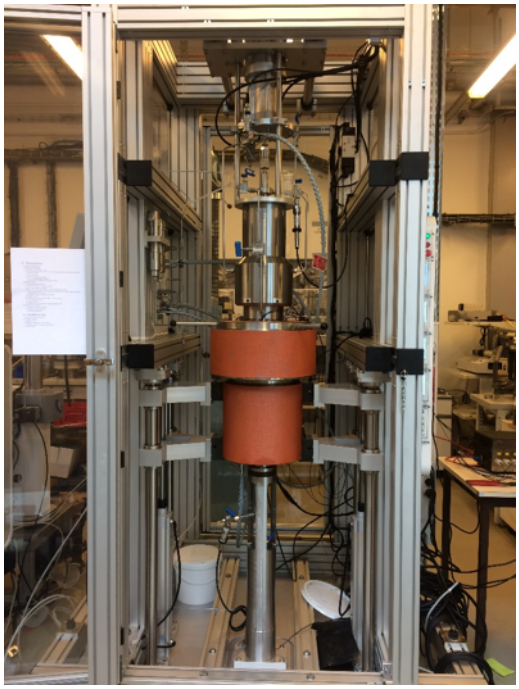

(a) Triaxial device

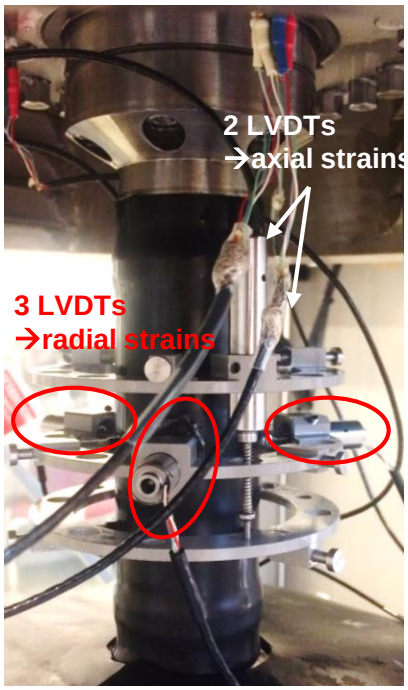

(b) Disposition of the LVDTs in the triaxial cell

Details of the calculation to deduce the $P-y$ curves of the multi-directional model

D

D.1 Linear $P-$ curves

The expression for the $P-y$ curves is given by:

$$P(y) = ky \tag{D.1a}$$

$$\tilde{P}(y) = \tilde{k}y \tag{D.1b}$$

The external work for the unidirectional model for an imposed displacement y is given by:

$$E(y) = \int_0^y P(v)\,\mathrm{d}v = \int_0^y k\,v\mathrm{d}v = \frac{k\,y^2}{2} \tag{D.2}$$

The external work for the multi-directional model for an imposed displacement y is given by:

$$\tilde{E}(y) = \sum_j \int_0^{y_j} \tilde{P}(v)\,\mathrm{d}v = \sum_j \int_0^{y\,\sin\theta_j} \tilde{k}\,v\mathrm{d}v = \frac{\tilde{k}\,y^2\,\sum_j \sin^2\theta_j}{2} \tag{D.3}$$

By setting $\tilde{E}(y) = E(y)$, the linear stiffness of the $P-y$ curve in the multi-directional model is given by:

$$\tilde{k} = \frac{k}{\sum_j \sin^2\theta_j} \tag{D.4}$$

The sum is calculated as follows:

$$\begin{aligned} \textstyle\sum_j \sin^2\theta_j &= \textstyle\sum_{j=2}^{N/2} \sin^2\left(\frac{2\pi}{N}(j-1)\right) \\ &= \frac{1}{2}\textstyle\sum_{j=1}^{N/2-1} 1-\cos\left(\frac{4\pi}{N}j\right) \end{aligned} \tag{D.5}$$

And the sum of the cosinus is calculated as follows:

$$\begin{aligned} \textstyle\sum_{j=1}^{N/2-1} \cos\left(\frac{4\pi}{N}j\right) &= \textstyle\sum_{j=1}^{N/2-1} \mathrm{Re}\left(e^{i\,\frac{4\pi}{N}j}\right) \\ &= \mathrm{Re}\left(\textstyle\sum_{j=1}^{N/2-1} e^{i\,\frac{4\pi}{N}j}\right) \\ &= \mathrm{Re}\left(-\frac{1-e^{i\frac{4\pi}{N}}}{1-e^{i\frac{4\pi}{N}}}\right) = -1 \end{aligned} \tag{D.6}$$

So $\sum_j \sin^2\theta_j = \frac{N}{4} - \frac{1}{2} + \frac{1}{2} = \frac{N}{4}$, and thus:

$$\tilde{k} = \frac{4\,k}{N} \tag{D.7}$$

D.2 Elasto-plastic $P-$ curves

The expression for the $P - y$ curves is given by:

$$P\left(y\right) = \min\left(ky, P_u\right) \tag{D.8a}$$

$$\tilde{P}\left(y\right) = \min\left(\tilde{k}y, \tilde{P}_u\right) \tag{D.8b}$$

The calculation described previously is valid for the linear part. Considering that the spring in the unidirectional model is in the plastic state leads to:

$$\begin{aligned} E\left(y\right) &= \int_0^{P_u/k} k\; v\mathrm{d}v + \int_{P_u/k}^{y} P_u \mathrm{d}v \\ &= P_u\; y - \frac{P_u^2}{2\;k} \end{aligned} \tag{D.9}$$

Considering that all the active springs in the multi-directional model reach the plastic state leads to:

$$\begin{aligned} \tilde{E}\left(y\right) &= \sum_j \int_0^{\tilde{P}_u/\tilde{k}} \tilde{k}\; v\mathrm{d}v + \sum_j \int_{\tilde{P}_u/\tilde{k}}^{y_j} \tilde{P}_u \mathrm{d}v \\ &= \tilde{P}_u\; y \sum_j \sin\theta_j - \frac{\tilde{P}_u{}^2}{2\;\tilde{k}} \left(\frac{N}{2} - 1\right) \end{aligned} \tag{D.10}$$

By setting $\tilde{E}\left(y\right) = E\left(y\right)$, it leads to (for $y \neq 0$):

$$\tilde{P}_u \sum_j \sin\theta_j - \frac{\tilde{P}_u{}^2}{2\;\tilde{k}\;y} \left(\frac{N}{2} - 1\right) = P_u - \frac{P_u^2}{2\;k\;y} \tag{D.11}$$

Passing to the limits for large displacements in the above equation leads to:

$$\tilde{P}_u \sum_j \sin\theta_j = P_u \tag{D.12}$$

The sum $\sum_j \sin\theta_j$ can be calculated as follows:

$$\begin{aligned} \sum_j \sin\theta_j &= \sum_{j=1}^{N/2-1} \mathrm{Im}\left(e^{i\frac{2\pi}{N}j}\right) \\ &= \mathrm{Im}\left(\sum_{j=1}^{N/2-1} e^{i\frac{2\pi}{N}j}\right) \\ &= \mathrm{Im}\left(\frac{e^{i\frac{2\pi}{N}} - 1}{1 - e^{i\frac{2\pi}{N}}}\right) \\ &= \frac{2\cos\left(\frac{\pi}{N}\right)\;\sin\left(\frac{\pi}{N}\right)}{1 - \cos\left(\frac{2\pi}{N}\right)} \\ &= \frac{1}{\tan\left(\frac{\pi}{N}\right)} \end{aligned} \tag{D.13}$$

And thus:

$$\tilde{P}_u = P_u \tan\frac{\pi}{N} \tag{D.14}$$

D.3 Power law $P-$ curves

The expression for the $P - y$ curves is given by:

$$P(y) = ky^m \tag{D.15a}$$

$$\tilde{P}(y) = \tilde{k}y^{\tilde{m}} \tag{D.15b}$$

The external work in the unidirectional model is:

$$E(y) = \int_0^y k\, v^m \mathrm{d}v = \frac{k\, y^{m+1}}{m+1} \tag{D.16}$$

The external work in the multi-directional model is:

$$\tilde{E}(y) = \sum_j \int_0^{y_j} \tilde{k}\, v^{\tilde{m}} \mathrm{d}v = \sum_j \frac{\tilde{k}\, y^{\tilde{m}+1} \sin^{\tilde{m}+1}\theta_j}{\tilde{m}+1} \tag{D.17}$$

By setting $\tilde{E}(y) = E(y)$ and assuming $\tilde{m} = m$ lead to:

$$\tilde{k} = \frac{k}{\sum_j \sin^{m+1}\theta_j} \tag{D.18}$$

D.4 Hyperbolic tangent $P-$ curves

The expression for the $P - y$ curves is given by:

$$P(y) = P_u \tanh\frac{ky}{P_u} \tag{D.19a}$$

$$\tilde{P}(y) = \tilde{P}_u \tanh\frac{\tilde{k}y}{\tilde{P}_u} \tag{D.19b}$$

There is no simple analytical solution of the equality of the external work. Thus, the equality of the derivative of both work input per unit length is assumed. The derivative of the external work in the unidirectional model is:

$$E'(y) = P_u \tanh\frac{k\, y}{P_u} \tag{D.20}$$

The derivative of the external work in the multi-directional model is:

$$\tilde{E}'(y) = \sum_j \tilde{P}_u \sin(\theta_j) \tanh\frac{\tilde{k}\, y \sin\theta_j}{\tilde{P}_u} \tag{D.21}$$

Passing to the limits for large displacements in the above equations leads to:

$$\tilde{P}_u = \frac{P_u}{\sum_j \sin\theta_j} = P_u \tan\frac{\pi}{N} \tag{D.22}$$

It can be noted that it is the same relationship between the ultimate reactions in both models than those found for the elasto-plastic $P-y$ curves. For displacements close to 0 we have $\tanh v \underset{v\to 0}{\sim} v$. Thus, using this methametical property of the hyperbolic tangent in Equation D.21 leads to:

$$\tilde{k} = \frac{k}{\sum_j \sin^2\theta_j} = \frac{4\,k}{N} \tag{D.23}$$

It can be noted that it is the same relationship between the initial stiffness in both models than those found for the linear $P-y$ curves.

D.5 Hyperbolic $P-$ curves

Hyperbolic $P-y$ curves can be written as follows for both models:

$$P\left(y\right) = \frac{y}{1/k + y/P_u} \tag{D.24a}$$

$$\tilde{P}\left(y\right) = \frac{y}{1/\tilde{k} + y/\tilde{P}_u} \tag{D.24b}$$

Similarly to the hyperbolic tangent function, there is no simple analytical solution of the equality of the external work. The derivative of the external work in the unidirectional model is given by:

$$E'\left(y\right) = \frac{y}{1/k + y/P_u} \tag{D.25}$$

The derivative of the external work in the multi-directional model is given by:

$$\tilde{E}'\left(y\right) = \sum_j \frac{y\sin^2\theta_j}{1/\tilde{k} + y\,\sin\theta_j/\tilde{P}_u} \tag{D.26}$$

Passing to the limits for large displacements in the above equations leads to:

$$P_u = \tilde{P}_u \sum_j \sin\theta_j \tag{D.27}$$

Thus, Equation D.14 is also for the hyperbolic model. By setting $\tilde{E}'\left(y\right) = E'\left(y\right)$ leads to:

$$\sum_j \frac{\sin^2\theta_j}{1/\tilde{k} + y\,\sin\theta_j/\tilde{P}_u} = \frac{}{1/k + y/P_u} \tag{D.28}$$

Passing to the limit for small displacement ($y \underset{}{\to} y > 00$) leads to:

$$\tilde{k} \sum_j \sin^2\theta_j = k \tag{D.29}$$

Thus, Equation D.7 is also valid for the hyperbolic model.

Details of the different parameters of the constitutive behaviour of the joints used to model gapping behind the pile

E

E.1 Calibration of the joint elements

The behaviour of the joint elements is described through five parameters among them, three are purely numerical (K_n, K_t and K) and are introduced as the penalty method is used to regularise the contact problem. For the sake of simplicity, K_n and K_t are taken equal to one another. A sensitivity study is performed in order to determine the values of these three parameters. The calibration consists in finding the values of these parameters in order to combine an independence of the response with respect to the values of these parameters and computing efficiency. This calibration is done considering the 2D modelling without crushed rock as it is the stiffest model (compared to the modelling with crushed rock). Figure E.1a shows the force versus lateral displacement curve for various values of K and fixed values of K_n and K_t. For values of K smaller or equal to 10^7 Pa/m the response is independent of K. The highest value that conducts to a converged response is chosen for numerical considerations and thus $K = 10^7$ Pa/m is considered thereafter. Figure E.1b shows the force versus lateral displacement curve for various values of $K_n = K_t$ and a fixed value of $K = 10^7$ Pa/m. For values of $K_n = K_t$ higher or equal to 10^{12} Pa/m the response is independent of the values of K_n and K_t. The smallest value that conducts to a converged response is chosen for numerical considerations and thus $K_n = K_t = 10^{12}$ Pa/m is considered thereafter. This sensitivity study is performed for various values of μ and leads to the same calibrated values of K, K_n and K_t. The thickness of the joint elements is equal to $e = 1$ mm and thus the equivalent Young's modulus of the joints is $K_n\ e = 10^6$ GPa and the equivalent shear modulus of the joints is $K_t\ e = 10^6$ GPa. These modulus values are much higher than the modulus value for all other materials in the model (steel, crushed rock and rock) and thus the underlying assumption of the penalty method is verified.

E.2 Sensitivity on the joint elements friction coefficient μ

The friction coefficient of the joint elements is a quite uncertain parameter, since it does not correspond to the angle of friction of the material around the pile but a fraction of it. The amount of the reduction of this parameter is given by some calculation standards and depends on pile installation method and the type of soil.

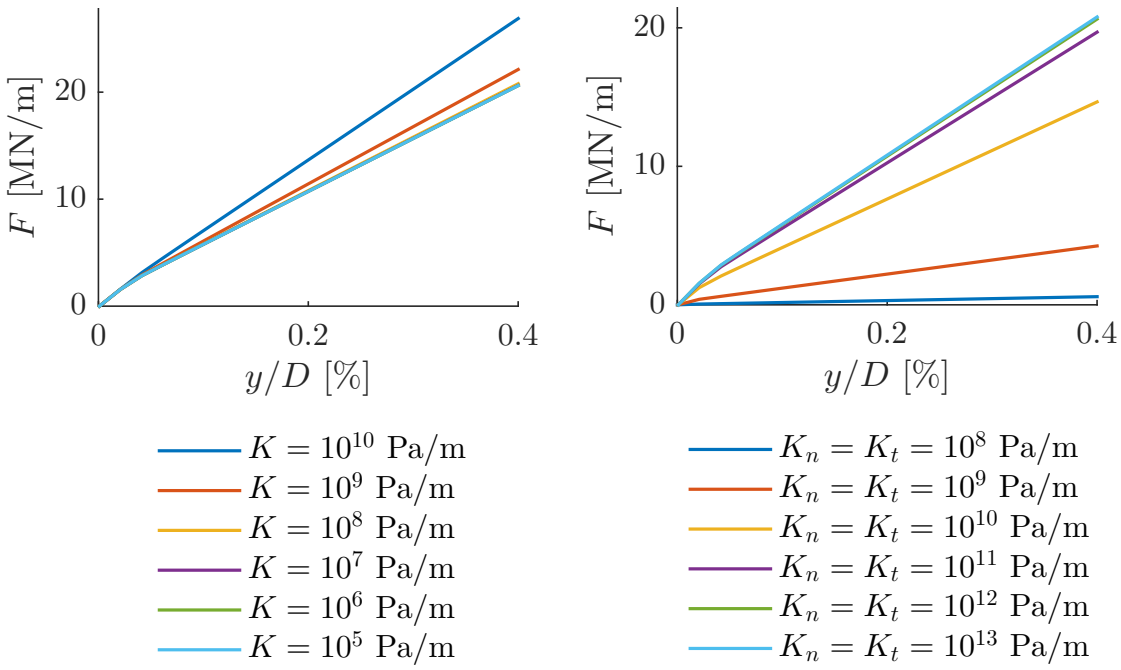

(a) K variations for $K_n = K_t = 10^{12}$ Pa/m

(b) K_n and K_t variations for $K = 10^{7}$ Pa/m

Figure E.1.: Sensitivity study of numerical parameters of the joint elements considering an adhesion equals to zero and μ equals to 0.35

This is why a sensitive study is performed on the friction coefficient. Figure E.2a shows the result of this sensitivity study. Considering a value of μ of 0.35 as the reference, a variation of ± 40 % of μ leads to a variation of ± 3 % of the global stiffness. However, even though this parameter does not influence much the global response, locally around the pile the zone where sliding occurs and where gapping occurs is impacted by this parameter as can be seen in Figure E.2b and E.2c.

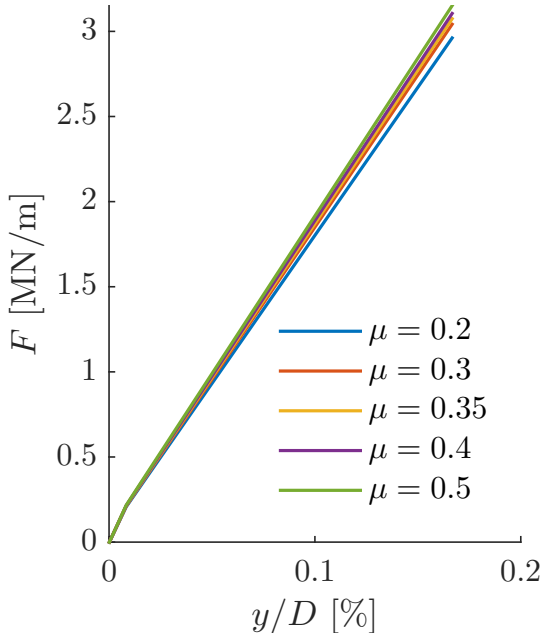

(a) Force versus displacement curve for various values of μ

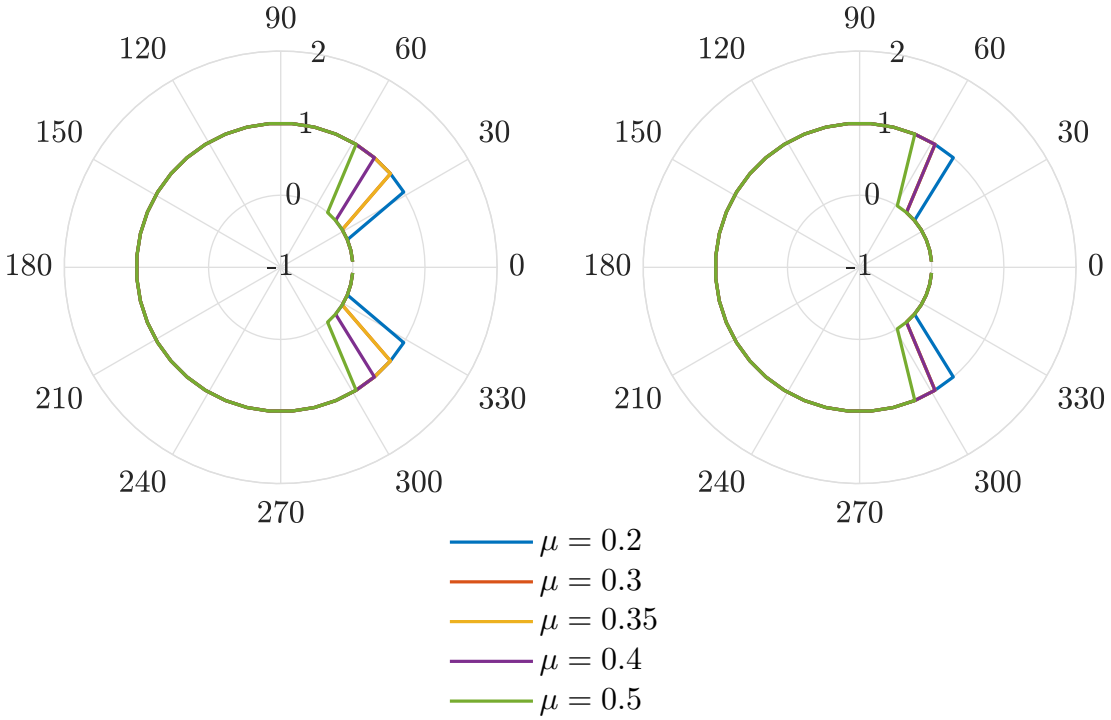

(b) Internal variable of sliding for $y/D = 0.2$ % **(c)** Internal variable of opening for $y/D = 0.2$ %

Figure E.2.: Results of the sensitivity study on the joint elements friction coefficient μ

Dependency of the 2D solution with the model size

F

For lateral loading of a cross-section of a pile, it has been identified in Baguelin et al. (1977) that the solution depends on the size of the model. This is an artefact of the 2D approach which is observed both for the analytical solution and the numerical one. We present a closed-form solution based on potential theory. These derivations are taken from the paper of Baguelin et al. (1977).
In a two-dimensional problem of isotropic elasticity in polar coordinates the Cauchy stress tensor is (with stresses in compression considered as positive):

$$\sigma = \begin{bmatrix} \sigma_r & \tau_{r\theta} \\ \tau_{r\theta} & \sigma_\theta \end{bmatrix} \tag{F.1}$$

The strain tensor can be written as (with strains in compression considered as positive):

$$\varepsilon = \begin{bmatrix} \varepsilon_r & \varepsilon_{r\theta} \\ \varepsilon_{r\theta} & \varepsilon_\theta \end{bmatrix} \tag{F.2}$$

And the strains can be linked with the displacements (assuming small strains):

$$\begin{cases} \varepsilon_r = \dfrac{\partial u_r}{\partial r} & \text{(F.3a)} \\ \varepsilon_\theta = \dfrac{u_r}{r} + \dfrac{1}{r}\dfrac{\partial u_\theta}{\partial \theta} & \text{(F.3b)} \\ 2\varepsilon_{r\theta} = \dfrac{1}{r}\dfrac{\partial u_r}{\partial \theta} + \dfrac{\partial u_\theta}{\partial r} - \dfrac{u_\theta}{r} & \text{(F.3c)} \end{cases}$$

Assuming plane strains, the relation between the stresses and the strains are written as:

$$\begin{cases} \varepsilon_r = \dfrac{1}{E'}\left(\sigma_r - \nu'\,\sigma_\theta\right) & \text{(F.4a)} \\ \varepsilon_\theta = \dfrac{1}{E'}\left(\sigma_\theta - \nu'\,\sigma_r\right) & \text{(F.4b)} \\ \varepsilon_{r\theta} = \dfrac{(1+\nu')}{E'}\tau_{r\theta} & \text{(F.4c)} \end{cases}$$

Where E' and ν' are the apparent values of the Young's modulus and the Poisson's ratio ($E' = E/(1-\nu^2)$ and $\nu' = \nu/(1-\nu)$). The equilibrium equations are automatically satisfied provided that:

$$\begin{cases} \sigma_r = \dfrac{1}{r^2}\dfrac{\partial^2 \phi}{\partial \theta^2} + \dfrac{1}{r}\dfrac{\partial \phi}{\partial r} & \text{(F.5a)} \\ \sigma_\theta = \dfrac{\partial^2 \phi}{\partial r^2} & \text{(F.5b)} \\ \sigma_{r\theta} = -\dfrac{\partial}{\partial r}\left(\dfrac{1}{r}\dfrac{\partial \phi}{\partial \theta}\right) & \text{(F.5c)} \end{cases}$$

Where ϕ is the Airy function (i.e. solution of $\nabla^2(\nabla^2\phi) = 0$). The most general Airy function is of the following form:

$$\begin{aligned} \phi \quad &= A_0\, r^2 + B_0\, r^2 \ln(r) + C_0 \ln(r) \\ &+ (I_0\, r^2 + I_1\, r^2 \ln(r) + I_2 \ln(r) + I_3)\ \theta \\ &+ \left(A_1\, r + \frac{B_1}{r} + B_1'\, r\, \theta + C_1\, r^3 + D_1\, r \ln(r)\right) \cos(\theta) \\ &+ \left(E_1\, r + \frac{F_1}{r} + F_1'\, r\, \theta + G_1\, r^3 + H_1\, r \ln(r)\right) \sin(\theta) \\ &+ \sum_{n=2}^{\infty} \left(A_n\, r^n + \frac{B_n}{r^n} + C_n\, r^{n+2} + \frac{D_n}{r^{n-2}}\right) \cos(n\theta) \\ &+ \sum_{n=2}^{\infty} \left(E_n\, r^n + \frac{F_n}{r^n} + G_n\, r^{n+2} + \frac{H_n}{r^{n-2}}\right) \sin(n\theta) \end{aligned} \qquad \text{(F.6)}$$

The terms $A_1\ r\ \cos(\theta)$ and $E_1\ r\ \sin(\theta)$ define a trivial null state of stress and are ignored. Now that the general framework of bidimensional problem of isotropic elasticity is given let us consider the case described in Baguelin et al. (1977) of a disk in translation in an elastic medium. The boundary conditions are:

- at $r = r_0$, r_0 being the outer radius of the disk:

$$\begin{cases} u_r(r_0, \theta) = C\, \cos(\theta) & \text{(F.7a)} \\ u_\theta(r_0, \theta) = -C\, \sin(\theta) & \text{(F.7b)} \end{cases}$$

- at $r = R$, R being the outer radius of the model:

$$\begin{cases} u_r(r_0, \theta) = 0 & \text{(F.8a)} \\ u_\theta(r_0, \theta) = 0 & \text{(F.8b)} \end{cases}$$

Conditions of symmetry and antisymmetry can be written as:

- Along the x-axis (i.e. $\theta = 0$ or π):

$$\begin{cases} \tau_{r\theta} = 0 & \text{(F.9a)} \\ u_\theta = 0 & \text{(F.9b)} \end{cases}$$

- Along the y-axis (i.e. $\theta = \pm\pi/2$):

$$\begin{cases} \sigma_r = 0 & \text{(F.10a)} \\ \sigma_\theta = 0 & \text{(F.10b)} \\ u_r = 0 & \text{(F.10c)} \end{cases}$$

Only four terms remain in the general form of the Airy function (Equation F.6) when considering Equations F.7, F.8, F.9 and F.10. Thus the stress field is obtained as follows:

$$\begin{cases} \sigma_r = \left[\dfrac{D_1 + 2\ F_1'}{r} - \dfrac{2\ B_1}{r^3} + 2\ C_1\ r\right]\ \cos(\theta) & \text{(F.11a)} \\ \sigma_\theta = \left[\dfrac{D_1}{r} + \dfrac{2\ B_1}{r^3} + 6\ C_1\ r\right]\ \cos(\theta) & \text{(F.11b)} \\ \tau_{r\theta} = \left[\dfrac{D_1}{r} - \dfrac{2\ B_1}{r^3} + 2\ C_1\ r\right]\ \sin(\theta) & \text{(F.11c)} \end{cases}$$

The strain field is obtained as follows:

$$\begin{cases} \varepsilon_r = \left[\dfrac{(1-\nu')D_1 + 2F_1'}{r} - \dfrac{2(1+\nu')B_1}{r^3} + 2(1-3\nu')C_1 r\right]\dfrac{\cos(\theta)}{E'} & \text{(F.12a)} \\ \varepsilon_\theta = \left[\dfrac{(1-\nu')D_1 - 2\nu' F_1'}{r} + \dfrac{2(1+\nu')B_1}{r^3} + 2(3-\nu')C_1 r\right]\dfrac{\cos(\theta)}{E'} & \text{(F.12b)} \\ 2\varepsilon_{r\theta} = \left[\dfrac{D_1}{r} - \dfrac{2\ B_1}{r^3} + 2\ C_1\ r\right]\dfrac{2(1+\nu')\sin(\theta)}{E'} & \text{(F.12c)} \end{cases}$$

The general form of the displacements is then obtained by integrating the strains:

$$\begin{aligned} u_r &= \left[((1-\nu')D_1 + 2F_1')\ln(r) + \frac{(1+\nu')B_1}{r^2} + (1-3\nu')C_1 r^2\right]\frac{\cos(\theta)}{E'} + A\cos(\theta) \\ u_\theta &= \left[((1-\nu')D_1 - 2\nu' F_1') - ((1-\nu')D_1 + 2F_1')\ln(r)\right. \\ &\quad \left. + \frac{(1+\nu')B_1}{r^2} + (5+\nu')C_1 r^2\right]\frac{\sin(\theta)}{E'} + A\sin(\theta) \end{aligned} \qquad \text{(F.13a)}$$

Where A is a constant of integration. The four unknows are determined using the boundary conditions and the compatibility of the strains. Introducing T the total applied load at $r = r_0$, the solution found in Baguelin can be deduced. The stiffness of this model $T/u_r(r = r_0)$ can be expressed as :

$$\frac{T}{u_r(r = r_0, \theta = 0)} = 8\ \pi\ E\ \frac{1-\nu}{1+\nu}\left((3-4\nu)\ \ln\left(\frac{R^2}{r_0^2}\right) - \frac{2}{3-4\nu}\frac{R^2 - r_0^2}{R^2 + r_0^2}\right)^{-1} \qquad \text{(F.14)}$$

The stiffness of the model depends directly of the size of the model and tends towards 0 when R tends to infinity.

Bibliography

Abadie, C. N. (2015). „Cyclic Lateral Loading of Monopile Foundations in Cohesionless Soils“. PhD thesis. St Catherine University of Oxford (cit. on pp. 8, 21, 27, 39, 40, 42, 167).

Abbs, A. F. (1983). „Lateral pile analysis in weak carbonate rocks“. In: *Presented at the Geotechnical Practice in Offshore Engineering* (cit. on pp. 30, 31, 57, 59, 159, 160).

Achmus, M., Kuo, Y. S., and Abdel-Rahman, K. (2009). „Behavior of monopile foundations under cyclic lateral load“. In: *Computers and Geotechnics* 36.5, pp. 725–735 (cit. on pp. 33, 34, 41, 42).

Airey, D. W. and Fahey, M. (1991). „Cyclic response of calcareous soil from the North-West Shelf of Australia“. In: *Géotechnique* 41.1, pp. 101–121 (cit. on p. 38).

API (2000). *API RP2A - Recommended practice for planning, designing and constructing fixed offshore platforms - Working stress design*. Ed. by A. P. Institute. 21st edition. Washington (cit. on pp. 42, 93, 96, 108).

Arany, L., Bhattacharya, S., Adhikari, S., Hogan, S. J., and Macdonald, J. H. G (2015). „An analytical model to predict the natural frequency of offshore wind turbines on three-spring flexible foundations using two different beam models“. In: *Soil Dynamics and Earthquake Engineering* 74, pp. 40–45 (cit. on pp. 10, 22, 23, 28, 106, 110, 115, 156).

Arany, L., Bhattacharya, S., Macdonald, J., and Hogan, S. J. (2017). „Design of monopiles for offshore wind turbines in 10 steps“. In: *Soil Dynamics and Earthquake Engineering* 92, pp. 126–152 (cit. on pp. 7, 20, 28).

Ashford, S. A. and Juirnarongrit, T. (2003). „Evaluation of pile diameter effect on initial modulus of subgrade reaction“. In: *Journal of Geotechnical and Geoenvironmental Engineering* 129.3, pp. 234–242 (cit. on p. 102).

Baguelin, F., Frank, R., and Sands, Y. H. (1977). „Theoretical study of lateral reaction mechanism of piles“. In: *Géotechique* 27.3, pp. 405–434 (cit. on pp. 28, 82, 84, 86, 88, 128, 135, 179, 180).

Berthelot, P., Puech, A., and Ropers, F. (2019). *Recommandations pou la conception et le dimensionnement des fondations d'éoliennes offshore*. Tech. rep. Comité Français de Mécanique des Sols et de Géotechnique, p. 220 (cit. on pp. 10, 18).

Bhattacharya, S. (2014). „Challenges in Design of Foundations for Offshore Wind Turbines“. In: *The institution of Engineering and Technology* (cit. on pp. 6, 10, 18).

Bhattacharya, S. and Adhikari, S. (2011). „Experimental validation of soil-structure interaction of offshore wind turbine“. In: *Soil Dynamics and Earthquake Engineering* 31.5, pp. 805–816 (cit. on p. 109).

Byrne, B. W. and Houlsby, G. T. (2003). „Foundations for offshore wind turbines“. In: *Philosophical Transactions of The Royal Society of London A : Mathematical, Physical and Engineering Sciences* 361, pp. 2909–2930 (cit. on pp. 11, 19).

Byrne, B. W., Mcadam, R. A., Burd, H. J., Houlsby, G. T., Martin, C. M., Gavin, K., Doherty, P., Igoe, D., Zdravković, L., Taborda, D. M. G., Potts, D. M., Jardine, R. J., Sideri, M., Schroeder, F. C., Muir Wood, A., Kallehave, D., and Skov Gretlund, J. (2015a). „Field testing of large diameter piles under lateral loading for offshore wind applications“. In: *16th European Conference on Soil Mechanics and Geotechnical Engineering (ECSMGE)*. Edinburgh, UK, pp. 1255–1260 (cit. on pp. 41, 52).

Byrne, B. W., Mcadam, R., Burd, H. J., Houlsby, G. T., Martin, C. M., Zdravkovi, L., Taborda, D. M. G., Potts, D. M., Jardine, R. J., Sideri, M., Schroeder, F. C., Gavin, K., Doherty, P., Igoe, D., Wood, A. M., Kallehave, D., and Gretlund, J. S. (2015b). „New design methods for large diameter piles under lateral loading for offshore wind applications“. In: *Frontiers in Offshore Geotechnics III*, pp. 705–710 (cit. on pp. 11, 41, 43, 90, 157).

Carter, J. P. and Kulhawy, F. H. (1992). „Analysis of Laterally Loaded Shafts in Rock“. In: *Journal of Geotechnical Engineering*, pp. 839–855 (cit. on pp. 20, 28, 81, 88, 146).

Cerfontaine, B. and Collin, F. (2018). „Cyclic and Fatigue Behaviour of Rock Materials: Review, Interpretation and Research Perspectives“. In: *Rock Mechanics and Rock Engineering* 51.2, pp. 391–414 (cit. on pp. 35, 37, 38).

Cho, S., Ogata, Y., and Kaneko, K. (2003). „Strain-rate dependency of the dynamic tensile strength of rock“. In: *International Journal of Rock Mechanics and Mining Sciences* 40.5, pp. 763–777 (cit. on p. 35).

Di Prisco, C. and Muir Wood, D. (2012). *Mechanical behaviour of soils under environmentally induced cyclic loads*. Vienna: Springer, p. 573 (cit. on p. 36).

DNV-GL (2014). *DNV-OS-J101: Design of Offshore Wint Turbine Structures*. Tech. rep. Det Norske Veritas and Germanischer Llyod (cit. on pp. 11, 12, 18, 24, 42, 96).

Doherty, P. and Gavin, K. (2011). „Laterally loaded monopile design for offshore wind farms“. In: *Proceedings of the Institution of Civil Engineers*. Vol. 165. 1. Institution of Civil Engineers, pp. 7–17 (cit. on pp. 12, 19).

Doherty, P., Attari, A., Murphy, G., Reig Amoras, E., Fernandez Hernando, J., Bousseau, P., De Laleu, V., Beghi, M., Sykes, R., Murphy, J., Lynch, K., Devoy McAuliffe, F., Jaksic, V., Goormachtigh, J., Tang Kristensen, J., Yanes Baonza, C., Heredero Bueno, C., and Giebhard, J. (2014). *WP Framework/Industry Challenges Report construction, deployment and installation*. Tech. rep. LEANWIND, pp. 1–114 (cit. on pp. 7, 9).

Downing, S. D. and Socie, D. F. (1982). „Simple rainflow counting algorithms“. In: *International Journal of Fatigue*, pp. 32–40 (cit. on p. 56).

Dunnavant, T. (1986). „Experimental and analytical investigation of the behaviour of single piles in overconsolidated clay subjected to cyclic lateral loads“. PhD thesis. University of Houston, TX. (cit. on p. 33).

Dunnavant, T. and O'Neill, M. (1989). „Experimental p-y model for submerged stiff clay“. In: *Journal of Geotechnical Engineering* 127.1, pp. 95–114 (cit. on p. 96).

Dupla, J. C. (1995). „Application de la sollicitation d'expansion de cavité cylindrique à l'évaluation des caractéristiques de liquéfaction d'un sable“. PhD thesis. Ecole Nationale des Ponts et Chaussées, p. 423 (cit. on p. 36).

Dyson, G. J. and Randolph, M. F. (2001). „Monotonic Lateral Loading of Piles in Calcerous Sand“. In: *Journal of Geotechnical and Geoenvironmental Engineering* 127.4, pp. 346–352 (cit. on pp. 30, 31, 33, 95, 162, 163).

Erbrich, C. T. (2004). „A New Method for the Design of Laterally Loaded Anchor Piles in Soft Rock“. In: *Offshore Technology Conference* (cit. on pp. 30, 31, 33, 34, 75, 163, 164).

Erbrich, C., O'Neill, M., Clancy, P., and Randolph, M. (2011). „Axial and lateral pile design in carbonate soils“. In: *Frontiers in Offshore Geotechnics II*. Ed. by G. &. White, pp. 125–154 (cit. on pp. 42, 125, 157).

Farmer, I. (1983). *Engineering behaviour of rocks*. Second Edi. Chapman and Hall Ltd, p. 213 (cit. on p. 38).

Fragio, A. G., Santiago, J. L., and Sutton, V. J. R. (1985). „Load Tests on Grouted Piles in Rock“. In: *Offshore Technology Conference*, pp. 93–99 (cit. on pp. 30, 31, 160, 161).

Frank, R. (1999). *Calcul des fondations superficielles et profondes*. Ed. by T. de l'Ingénieur. Presse de l'Ecole Nationale des Ponts et Chaussées, p. 144 (cit. on pp. 20, 30, 82, 83).

Guo, F., Lehane, B., and Ju, J. (2014). „Experimentally derived CPT-based p-y curves for soft clay“. In: *3rd International Symposium on Cone Penetration Testing*, pp. 1021–1028 (cit. on p. 96).

Heidari, M., El Naggar, H., Jahanandish, M., and Ghahramani, A. (2014). „Generalized cyclic p-y curve modeling for analysis of laterally loaded piles“. In: *Soil Dynamics and Earthquake Engineering* 63, pp. 138–149 (cit. on p. 42).

Houlsby, G. T., Abadie, C. N., Beuckelaers, W. J.A. P., and Byrne, B. W. (2017). „A model for nonlinear hysteretic and ratcheting behaviour“. In: *International Journal of Solids and Structures* 120, pp. 67–80 (cit. on p. 42).

Houlsby, G. and Puzrin, A. (2006). *Principles of Hyperplasticity: An Approach to Plasticity Therory Based on Thermodynamic Principles*. Ed. by Springer (cit. on p. 42).

IEC (2009). *IEC 61400-3 Wind Turbines - Part 3: Design Requirements for Offshore Wind Turbines*. Tech. rep. Geneva: International Electrotechnical Commission (cit. on pp. 18, 55).

Jonkman, J. and Musial, W. (2010). *Offshore code comparison collaboration (OC3) for IEA task 23: offshore wind technology and deployment*. Tech. rep. NREL/TP-500-48191, Golden, CO: National Renewable Energy Laboratory (cit. on p. 108).

Jonkman, J., Butterfiel, S., Musial, W., and Scott, G. (2009). *Definition of a 5-MW reference wind turbinne for offshore system development*. Tech. rep. NREL/TP-500-38060, Golden, CO: National Renewable Energy Laboratory (cit. on p. 108).

Kallehave, D., Byrne, B. W., Leblanc Thilsted, C., and Mikkelsen, K. K. (2015). „Optimization of monopiles for offshore wind turbines“. In: *Philosophical Transactions of The Royal Society of London A : Mathematical, Physical and Engineering Sciences* 373 (cit. on pp. 7, 9, 10, 19).

Knudsen, T., Bak, T., and Tabatabaeipour, S. (2012). „Detection of excessive wind turbine tower oscillations fore-afte and sideways“. In: *American Control Conference*, pp. 5795–5800 (cit. on p. 109).

Leblanc, C., Houlsby, G. T., and Byrne, B. W. (2010a). „Response of stiff piles in sand to long-term cyclic lateral loading“. In: *Géotechique* 60.2, pp. 79–90 (cit. on pp. 11, 12, 19, 21, 39, 40, 60–62, 66, 71, 155).

Leblanc, C, Byrne, B. W., and Houlsby, G. T. (2010b). „Response of stiff piles to random two-way lateral loading“. In: *Géotechnique* 60.9, pp. 715–721 (cit. on pp. 39, 42).

Lesny, K. and Hinz, P. (2007). „Investigation of monopile behaviour under cyclic lateral loading“. In: *Proceedings of the 6th International Offshore Site Investigation and Geotechnics Conference*, pp. 383–390 (cit. on p. 41).

Levy, N. H., Einav, I., and Randolph, M. F. (2007). „Effect of Recent Load History on Laterally Loaded Piles in Normally Consolidated Clay“. In: *International Journal of Geomechanics* 7.4, pp. 277–286 (cit. on pp. 24, 88, 102–104, 115, 156).

Levy, N. H., Einav, I., and Hull, T. (2009). „Cyclic shakedown of piles subjected to two-dimensional lateral loading“. In: *International Journal for Numerical and Analytical Methods in Geomechanics* 33.10, pp. 1339–1361 (cit. on pp. 24, 36, 42, 157).

Liang, R., Asce, M, Yang, K., and Nusairat, J. (2009). „p-y Criterion for Rock Mass“. In: *Journal of Geotechnical and Geoenvironmental Engineering* 135.1, pp. 26–36 (cit. on pp. 33, 34).

Lin, S. and Liao, J. (1999). „Permanent strains of piles in sand due to cyclic lateral loads“. In: *Journal of Geotechnical Engineering and Geoenvironmental Engineering* 125.9, pp. 798–802 (cit. on pp. 39, 40, 61).

Little, R. and Briaud, J. (1988). *Cyclic horizontal load tests on six piles in sands Houston Ship Channel*. Tech. rep. Research Report 5640 to USAE Waterways Experiment Station: Civil Engineering, Texas A&M University (cit. on pp. 39, 40).

Long, J. H. and Vanneste, G. (1994). „Effects of cyclic lateral loads on piles in sand“. In: *Journal of Geotechnical Engineering*, pp. 225–244 (cit. on pp. 21, 39, 40).

Matlock, H. and Ripperger, E. (1956). „Procedures and instrumentation for tests on a laterally loaded pile“. In: *8th Texas Conference on Soil Mechanics and Foundation Engineering*. Austin, TX., pp. 1220–1086 (cit. on p. 33).

Mayoral, J., Pestana, J., and Seed, R. (2005). „Determination of multidirectional p-y curves for soft clays“. In: *Geotechnical Testing Journal* 28.3, pp. 253–263 (cit. on p. 24).

Mayoral, J. M., Pestana, J. M., and Seed, R. B. (2016a). „Modeling clay-pile interface during multi-directional loading“. In: *Computers and Geotechnics* 74, pp. 163–173 (cit. on pp. 24, 25).

– (2016b). „Multi-directional cyclic p-y curves for soft clays“. In: *Ocean Engineering* 115, pp. 1–18 (cit. on pp. 24, 25).

McCarron, W. O. (2016). „Bounding surface model for soil resistance to cyclic lateral pile displacements with arbitrary direction“. In: *Computers and Geotechnics* 71, pp. 47–55 (cit. on pp. 24, 25).

Mezazigh, S. and Levacher, D. (1998). „Laterally loaded piles in sand: slope effect on P-y curves“. In: *Canadian Geotechnical Journal* 35.3, pp. 433–441 (cit. on p. 33).

Muir Wood, A., Mackenzie, B., Burbury, D., Rattley, M., Clayton, C., Mygind, M., Wessel Andersen, K., LeBlanc Thilsted, C., and Albjerg Liingaard, M. (2015). „Design of large diameter monopiles in chalk at Westermost Rough offshore wind farm“. In: *Frontiers in Offshore Geotechnics III*. Taylor & Francis Group, pp. 723–728 (cit. on p. 43).

Page, A., Grimstad, G., Eiksund, G., and Jostad, H. (2018). „A macro-element pile foundation model for integrated analyses of monopile-based offshore wind turbines“. In: *Ocean Engineering* 167, pp. 23–35 (cit. on p. 28).

Page Risueno, A., Jostad, H., and Saue, M. (2013). „Application of an undrained and partially drained cyclic accumulation model for monopile design“. In: *Proceedings of the 5th International Young Geotechnical Engineers' Conference*, pp. 205–208 (cit. on p. 42).

Passon, P. (2006). *Memorandum derivation and description of the soil-pile-interaction models*. Tech. rep. IEA-Annex XXIII Subtask 2, Stuttfart, Germany: Endowed Chair of Energy (cit. on pp. 108–110).

Pender, M. J. and of Auckland. School of Engineering, U. (1993). *Aseismic pile foundation design analysis*. University of Auckland, p. 230 (cit. on p. 146).

Peralta, V. P. (2010). „Investigations on the Behavior of Large Diameter Piles under Long-Term Lateral Cyclic Loading in Cohesionless Soil“. PhD thesis. Leibniz University (cit. on pp. 21, 24, 157).

Poulos, H. G. (1971). „Behavior of laterally loaded piles: I- Single piles“. In: *Journal of the Soil Mechanics and Foundations Division*, pp. 711–731 (cit. on pp. 146, 147).

Poulos, H. G. and Davis, E. H. (1980). *Pile foundation analysis and design*. Wiley (cit. on p. 28).

Poulos, H. G and Hull, T. (1989). „The role of analytical geomechanics in foundation engineering“. In: *Foundation Engineering: Current principles and practices* 2, pp. 1578–1606 (cit. on pp. 12, 19, 20, 82, 83).

Puech, A. and Garnier, J. (2017). *Design of Piles Under Cyclic Loading: SOLCYP Recommendations*. Ed. by ISTE and Wiley, p. 452 (cit. on pp. 19, 21, 42, 57, 61).

R7.01.16 (2013). *Integration of the elastoplastic mechanical behaviors of Drucker-Prager, associated (DRUCK_PRAGER)and non-aligned (DRUCK_PRAG_N_A) and postprocessings*. Tech. rep. (cit. on pp. 129, 130).

R7.01.25 (2016). *Laws of behavior of the joints of stoppings: JOINT_MECA_RUPT and JOINT_MECA_FROT*. Tech. rep., p. 31 (cit. on pp. 131–133).

Rakotonindriana, M. H. J. (2009). „Comportement des pieux et des groupes de pieux sous chargement latéral cyclique“. PhD thesis. ENPC (cit. on p. 40).

Randolph, M. F. (1981). „The response of flexible piles to lateral loading“. In: *Géotechnique* 31.2, pp. 247–259 (cit. on pp. 20, 146).

Randolph, M. F. and Houlsby, G. T. (1984). „The limiting pressure on a circular pile loaded laterally in cohesive soil“. In: *Géotechnique* 34.4, pp. 613–623 (cit. on p. 102).

Reese, L. (1997). „Analysis of Laterally Loaded Piles in Weak Rock“. In: *Journal of Geotechnical and Geoenvironmental Engineering* 123.11, pp. 1010–1017 (cit. on pp. 12, 30, 31, 95, 161, 162).

Reese, L. and Van Impe, W. (2011). *Single Piles and Pile Groups Under Lateral Loading*. Ed. by C. Press, p. 508 (cit. on p. 29).

Reese, L. and Welch, R. (1975). „Lateral loadings of deep foundations in stiff clay“. In: *Journal of Geotechnical Engineering Division* 101.7, pp. 633–649 (cit. on pp. 33, 93, 159).

Rodrigues, S., Restrepo, C., Kontos, E., Teixeira Pinto, R., and Bauer, P. (2015). „Trends of offshore wind projects“. In: *Renewable and Sustainable Energy Reviews* 49, pp. 1114–1135 (cit. on p. 5).

Rosquoët, F. (2004). „Pieux sous charge latérale cyclique“. PhD thesis. Ecole Centrale de Nantes (cit. on pp. 32, 33, 40).

Rudolph, C., Bienen, B., and Grabe, J. (2014). „Effect of variation of the loading direction on the displacement accumulation of large-diameter piles under cyclic lateral loading in sand“. In: *Canadian Geotechnical Journal* 51.10, pp. 1196–1206 (cit. on pp. 24, 157).

Schafhirt, S., Page, A., Eiksund, G. R., and Muskulus, M. (2016). „Influence of Soil Parameters on the Fatigue Lifetime of Offshore Wind Turbines with Monopile Support Structure“. In: *Energy Procedia*, pp. 347–356 (cit. on pp. 10, 22).

Shadlou, M. and Bhattacharya, S. (2016). „Dynamic stiffness of monopiles supporting offshore wind turbine generators“. In: *Soil Dynamics and Earthquake Engineering* 88, pp. 15–32 (cit. on pp. 28, 146).

Su, D. (2012). „Resistance of short, stiff piles to multidirectional lateral loadings“. In: *Geotechnical Testing Journal* 35.2 (cit. on pp. 24, 88, 99, 115).

Su, D. and Yan, W. (2013). „A multidirectional p-y model forlateralsand-pileinteractions“. In: *Soils and Foundations* 53.2, pp. 199–214 (cit. on pp. 24, 25, 96, 99).

Taborda, D. M. G., Zdravković, L., Potts, D. M., Burd, H. J., Byrne, B. W., Gavin, K., Houlsby, G. T., Jardine, R. J., Liu, T., Martin, C. M., and McAdam, R. A. (2019). „Finite element modelling of laterally loaded piles in a dense marine sand at Dunkirk“. In: *Géotechnique* Accepted, pp. 1–47 (cit. on p. 97).

Taborda, D., Zdravkovic, L., Kontoe, S., and Potts, D. (2014). „Computational study on the modification of a bounding surface plasticity model for sands“. In: *Computers and Geotechnics* 59, pp. 145–160 (cit. on p. 34).

Velarde, J. (2016). *Design of Monopile Foundations to Support the DTU 10 MW Offshore Wind Turbine*. Tech. rep. (cit. on pp. 8, 34).

Wesselink, B., Murff, J., Randolph, M., Nunez, I., and Hyden, A. (1988). „Analysis of centrifuge model test data from laterally loaded piles in calcareous sand“. In: *Engineering for calcareous sediments*. Ed. by Balkema. Rotterdam, The Netherlands, pp. 261–270 (cit. on pp. 93, 162).

Wilson, D. W. (1998). „Soil-Pile Superstructure Interaction in liquefying sand and soft clay“. PhD thesis. University of California Davis (cit. on p. 33).

WindEurope (2019). *Offshore Wind in Europe windeurope.org Key trends and statistics 2018*. Tech. rep. Brussels: WindEurope, pp. 1–40 (cit. on pp. 5–8).

Xiao, J. Q., Ding, D. X., Xu, G., and Jiang, F. L. (2009). „Inverted S-shaped model for nonlinear fatigue damage of rock“. In: *International Journal of Rock Mechanics and Mining Sciences* 46.3, pp. 643–648 (cit. on p. 38).

Xue, J., Gavin, K., Murphy, G., Doherty, P., and Igoe, D. (2016). „Optimization technique to determine the p-y curves of laterally loaded stiff piles in dense sand“. In: *Geotechnical Testing Journal* 39.5 (cit. on pp. 32, 33).

Yang, K. and Liang, R. (2007). „Methods for deriving p-y curves from instrumented lateral load tests“. In: *Geotechnical Testing Journal* 30.1, pp. 31–38 (cit. on p. 32).

Zdravkovic, L., Taborda, D. M. G., Potts, D. M., Jardine, R. J., Sideri, M., Schroeder, F. C., Byrne, B. W., Mcadam, R., Burd, H. J., Houlsby, G. T., Martin, C. M., Gavin, K., Doherty, P., Igoe, D., Muir Wood, A., Kallehave, D., and Skov Gretlund, J. (2015). „Numerical modelling of large diameter piles under lateral loading for offshore wind applications“. In: *Frontiers in Offshore Geotechnics III*, pp. 978–1 (cit. on pp. 33, 34).

Zdravković, L., Taborda, D. M., Potts, D. M., Abadias, D., Burd, H. J., Byrne, B. W., Gavin, K., Houlsby, G. T., Jardine, R. J., Martin, C. M., McAdam, R. A., and Ushev, E. (2019). „Finite element modelling of laterally loaded piles in a stiff glacial clay till at Cowden“. In: *Géotechnique* Accepted, pp. 1–40 (cit. on p. 97).

Zhang, Y. and Andersen, K. H. (2019). „Soil reaction curves for monopiles in clay“. In: *Marine Structures* 65, pp. 94–113 (cit. on pp. 21, 82).

Zhao, J. (2010). „Applicability of Mohr-Coulomb and Hoek-Brown strength criteria to the dynamic strength of brittle rock.“ In: *International Journal of Rock Mechanics and Mining Sciences* 37.7, pp. 115–1121 (cit. on p. 35).

List of Figures

List of Tables